Die Sheet Hydroforming of a Complex Shaped AA2024-W Aircraft Skin Panel – From Concept to Final Component

by

Jean-Pierre Louis Serfontein

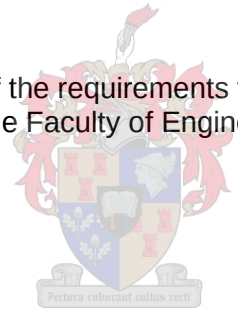

Thesis presented in partial fulfilment of the requirements for the degree of Master of Engineering (Engineering Management) in the Faculty of Engineering at Stellenbosch University

Supervisor: Prof. Oliver Damm

Co-supervisor: Prof. Natasha Sacks

March 2021

Declaration

By submitting this thesis electronically, I declare that the entirety of the work contained therein is my own, original work, that I am the sole author thereof (save to the extent explicitly otherwise stated), that reproduction and publication thereof by Stellenbosch University will not infringe any third party rights and that I have not previously in its entirety or in part submitted it for obtaining any qualification.

Date: 12 February 2021

Abstract

Blanks and press tools are traditionally manufactured by conceptualising a design based on knowledge and experience. Designs are compensated through a "trial-and-error" process until the manufacturing solution has been validated. The use of manufacturing simulations has aided engineers to design and manufacture components. Simulated manufacturability studies are becoming standard practice worldwide. The purpose of this research is to evaluate and validate the simulation of die sheet hydroforming of a complex-shaped aluminium alloy aircraft skin panel. The capability of ESI Group's PAM-STAMP 2G forming simulation software package and the procedure used in taking a component from concept to a realised part were assessed. A case study was conducted to evaluate and validate the simulation. The objective was to conceptualise the sheet metal blank and tooling and characterise the sheet metal blank material properties. Then, using simulation, the feasibility, and then manufacturability of the blank and tool concepts were evaluated. Finally, the concept was validated by manufacturing and inspecting the component. These steps defined the forming process conceptualisation cycle. ESI Group PAM-STAMP 2G was validated in a quantitative before-and-after field experiment.

From the case study, several concepts were developed and evaluated digitally using the forming process conceptualisation cycle. Nine concepts were conceptualised. The final concept was selected for manufacturing and tool proofing. Four components were manufactured and inspected using standard metrology methods on a coordinate measuring machine. The components were found to meet the design requirements. The simulation process did not account for an installation condition; hence the unclamped inspection configuration was used. A lack of correlation between the simulation result and the manufactured components were found and required further investigation. An added simulation operation stage improved the alignment of the simulation result and the nominal surface, in turn, improved inspection within the simulation package. A slight improvement in the correlation between the simulation and the manufactured component was found.

A simulation model validation study was conducted with a friction study to determine the dependency of the system on this parameter. The validation study showed a better correlation of the simulation result to the manufactured component at a higher friction coefficient. The friction coefficient was varied from 0.15 to 0.55, with 0.5 the best performing result. The four components were three-dimensional (3D) scanned and assessed using 3D metrology methods. The final surface profile deviation between the simulation and the manufactured component was 7.18 mm. The findings of this study showed two gaps in the simulation of die sheet hydroforming of complex-shaped panel-type aluminium alloy components. The omission of friction physics of the rubber-to-metal interface as the simulation under predicts distortion. Second is the lack of effective metrology inspection methods for assessment of the final predicted shape of the component within a commercial simulation software package.

Opsomming

Tradisioneel word ru-stukke en persgereedskap vervaardig deur ’n ontwerp te konseptualiseer wat op kennis en ondervinding gebaseer is. Ontwerpe word deur ’n proses van ‘leer en probeer’ gekompenseer, totdat die vervaardigingsoplossing gestaaf is. Die gebruik van vervaardigingsimulasies help ingenieurs om komponente te ontwerp en te vervaardig. Gesimuleerde vervaardigbaarheidstudies is besig om wêreldwyd die standaard praktyk te word. Die doel van hierdie navorsing is om die simulasie van die stempelplaathidrovorming van ’n aluminiumallooi-vliegtuighuidpaneel met ’n ingewikkelde vorm te evalueer en te staaf. Die vermoë van die ESI Groep se PAM-STAMP 2G programmatuurpakket vir vormingsimulasie en die prosedure wat gevolg word om ’n komponent van konsep tot by gerealiseerde onderdeel te neem, was geevalueer. ’n Gevallestudie is uitgevoer om die simulasie te evalueer en te staaf. Die doelwit was om die plaatmetaalru-stuk en gereedskap te konseptualiseer en die plaatmetaalru-stuk se materiële eienskappe te karakteriseer. Met behulp van simulasie is eers die lewensvatbaarheid en daarna die vervaardigbaarheid van die ru-stuk- en gereedskapskonsepte toe geëvalueer. Ten slotte is die konsept gestaaf deur die onderdeel te vervaardig en te inspekteer. Hierdie stappe omskryf die konseptualiseringsiklus van die vormingsproses. PAM-STAMP 2G programmatuurpakket vir simulasie is deur ’n kwantitatiewe voor-en-ná-veldproef gestaaf.

Uit die gevallestudie is verskeie konsepte met behulp van die konseptualiseringsiklus van die vormingsproses ontwikkel en digitaal geëvalueer. Nege konsepte is gekonseptualiseer. Die laaste konsep is vir vervaardiging en gereedskapstoetsing gekies. Vier onderdele is vervaardig en met behulp van standaard metrologiese metodes op ’n koördinaat-meetmasjien geïnspekteer. Die onderdelle het aan die ontwerpvereistes voldoen. Die simulasieproses het nie vir ’n installasie kondisie voorsiening gemaak nie; dus is die konfigurasie vir ’n inspeksie van die onderdeel sonder vasklamping gebruik. Daar was ’n gebrek aan korrelasie tussen die simulasieresultaat en die vervaardigde onderdele en dit het verdere ondersoek vereis. ‘n Bykomende simulasiefase het die ooreenkoms tussen die simulasieresultaat en die nominale oppervlak verbeter, wat weer die inspeksie binne die simulasiepakket verbeter het. Daar was ’n minimale verbetering in die korrelasie tussen die simulasie en die vervaardigde onderdeel.

’n Stawingstudie van die simulasiemodel is met ’n wrywingstudie gedoen, om die stelsel se afhanklikheid van hierdie afbakening vas te stel. Die stawingstudie het ’n beter korrelasie tussen die simulasieresultaat en die vervaardigde onderdeel teen ’n hoër wrywingskoëffisiënt getoon. Die wrywingskoëffisiënt is tussen 0.15 en 0.55 gewissel, met 0.5 wat die beste resultaat gelewer het. Die vier onderdele is driedimensioneel (3D) geskandeer en met behulp van 3D- metrologiese metodes geassesseer. Die finale oppervlakprofielafwyking tussen die simulasie en die vervaardigde onderdeel was 7.18 mm. Die bevindings van hierdie studie lig probleme uit met die simulasie van die stempelplaathidrovorming van paneeltipe aluminiumallooi-onderdele met ingewikkelde vorms. Die weglaat van die wrywingfisika van die rubber-op-metaal-koppelvlak, aangesien die simulasie te min verwringing voorspel. Die tweede is die gebrek aan doeltreffende metrologiese inspeksiemetodes vir assessering van die finale voorspelde vorm van die onderdeel in ’n kommersiële programmatuurpakket vir simulasie.

Acknowledgements

The author would firstly like to thank his project advisors, Professor Dimitri Dimitrov, Professor Oliver Damm, and Professor Natasha Sacks, for their academic guidance and leadership roles in the presented study. Without their assistance in the fields of manufacturing processes and material sciences, this project would not have been possible. The advisors granted the author the freedom to make the project his own and perform experiments and observations on his own accord.

The support and funding from Aerosud Aviation (Pty) Ltd and the South African Department of Trade Industry and Competition through the Technology and Human Resources for Industry Programme.

To my family for their undying support and, specifically my wife, Meg and my daughters, Mia and Giorgia, who have loved, encouraged and believed in me throughout each endeavour I choose to pursue.

To my father-in-law, Mr Geoffery Ward, who assisted me with professionally editing my thesis.

Finally, to my colleagues at Aerosud Aviation (Pty) Ltd, specifically Mr Wouter Gerber and Mr Johan Botha, for their support and guidance during the design and manufacturing phase of the study.

A portion of the research has been published and presented at the 2019 International Conference on Competitive Manufacturing (COMA 19). Serfontein, J.L., Dimitrov, D., Gerber, W. 2019. Composite and Metallic Forming Manufacturability Criteria for Incorporation into Material Selection Methodology. Processing of Advanced Materials I, in *International Conference on Competitive Manufacturing,* 337 – 345. Stellenbosch University, South Africa.

Table of Contents

List of Figures

List of Tables

Nomenclature

AA	Aluminium Alloy
CAD	Computer-Aided Design
CAE	Computer-Aided Engineering
CMM	Coordinate Measuring Machine
CNC	Computer Numeric Control
CPU	Central Processing Unit
DOE	Design of Experiments
FEM	Finite Element Model
FLC	Forming Limit Curve
FLD	Forming Limit Diagram
IGS	Initial Graphics Exchange Specification
IR	Infrared
NURB	Non-Rational B-Spline
OML	Outer Mould Line
SHF-D	Die Sheet Hydroforming
SHF-P	Punch Sheet Hydroforming
SHF-T	Tube Sheet Hydroforming
STL	Stereolithography

Chapter 1: Introduction

1.1. Background

Product design in the early stages requires a more quantitative process to ensure the outcome from a simulation study will meet expectations. Function, aesthetic and cost are typical factors considered in the design process. However, the manufacturability of a sheet metal component is one of the main factors considered but is limited to engineering knowledge. The current practice to conceptualise the sheet metal blank and tooling is to propose a design, proceed to manufacture after a review process, and, finally proceed with tool proofing (Altan and Tekkaya (Vol 1) 2012). If the final form of the component does not meet expectation, the tooling concept and possibly the sheet metal blank will be reworked, or a complete redesign is required. These actions are the traditional/conventional manufacturing process which is dependent on the trial-and-error methodology (Yershov et al. 2012).

Post-processing methods are required to rework the component within the design tolerance. Reworking metal components can be conducted with ease and is a well-established practice, but costs are added to the component that can be omitted. If the component deviates significantly from the nominal design and cannot be reworked, it is scrapped, and a new component will need to be manufactured (Dirikolu and Akdemir 2004).

The use of manufacturing simulations has aided engineers and designers to improve the blank and tooling concepts. Manufacturing simulations provide a comprehensive perspective of what can be expected from the proposed design and whether to proceed or redesign. Simulation allows for the review of the concept without manufacturing a tool or pressing a trial part. In addition, optimisation studies can be conducted to attain the most suitable blank and tool geometries (Hatipoğlu and Alkaş, 2016). As with any simulation package, two key factors must be considered to ensure the results attained are acceptable. Firstly, knowledge of the simulation package, specifically, the mathematical principles and how they may have been simplified from reality. The sheet forming packages conduct implicit, non-linear simulations which give more accurate results in comparison to a linear static solution. The second factor is the material properties (ESI Group. 2018).

Die sheet hydroforming is conducted on a fluid cell press and is a forming process more than 50 years old (Carlsson and Vrijhof 2018) (Bell 2020). The process requires only a female die tool, compared to the male punch tool required for stamping processes. A pressurised fluid takes the role of the male punch tool. The fluid is contained within a high-pressure chamber and is separated from the blank and tooling using a rubber diaphragm bladder. Sacrificial rubber pads are also typically used to protect the diaphragm bladder. Limitations of die sheet hydroforming on a fluid cell press are the high cycle time and equipment costs due to the high pressures fluid cells must operate at compared to stamping presses. These limitations make sheet hydroforming ideal for the aerospace industry due to low manufacturing volumes and high-value selling price of components (Altan and Tekkaya (Vol 1) 2012).

The benefits of die sheet hydroforming and a female tool die is the free bulging effect allowing for uniform in-plane strain stretching, in contract to the high local deformation experienced in conventional stamping. Because of the uniform loading distribution of the die sheet hydroforming, the process is an alternative for low-formability components and aluminium alloys (Altan and Tekkaya (Vol 1) 2012) (Lee et al. 2015). Thus, the die sheet hydroforming process is an exceptional candidate as an alternative manufacturing process for the complex shaped aluminium alloy components.

Much of the research investigating die sheet hydroforming and state of the art simulation software packages are limited to simple, shaped components. The shapes are typically singe-edge flanged components compared to a sizeable complex shaped panel-type component. (Hatipoğlu et al. 2007),

(Chen et al. 2015), (Păunoiu el. al. 2015), (Leacock et al. 2016), (Păunoiu et al. 2019) and (Zhang et al. 2019). The die sheet hydroforming simulation process is aligned to flanged and tube components. Many commercial simulation software packages have scripted processes to automatically set-up the various operations that make up a forming process. The current procedures apply loading directly to the blank and omit the need for modelling the rubber diaphragm and bladder, as well as the friction coefficients for metal-to-rubber interface (ESI Group. 2018).

1.2. Problem Statement

Blanks and press tools are traditionally manufactured by conceptualising a design based on knowledge and experience. Designs are adapted and compensated (distorted from the nominal surface definition) to realise adequate components through a “trial-and-error” process until the manufacturing solution has been validated. Components manufactured by inadequate blank and tooling can be post-processed through rework but adds costs and should be omitted to maximise profits. The introduction of commercial simulation software packages to evaluate the manufacturability of the design solution before blanks and tools are manufactured. Thus reducing, or even omitting, unnecessary adaptations and rework of components manufacture from inadequate blank and tooling. A benefit of die sheet hydroforming with female die tools is uniform in-plane stretching of the component due to the free bulging effect. Aircraft skin panel component has been selected for this case study and will be manufactured in aircraft-grade 2024 aluminium alloy. The component is currently manufactured using a conventional stamping process, which does not yield desired results, even with a compensated stamping die set.

Stamping, crash forming, tube gas and hydroforming processes are well-established in most manufacturing simulation software packages. Current research into sheet hydroforming is limited to small, simple flanged and dome components, and tube and punch sheet hydroforming. Manufacturing simulation software packages make use of scripted and pre-defined set-up procedures for sheet hydroforming. Will a manufacturing simulation software package effectively evaluate and validate conceptualised blank and tooling to manufacture a sizeable complex shaped aluminium alloy aircraft panel using die sheet hydroforming?

1.3. Research Objectives

Given the research question proposed in the problem statement, the following research objectives are provided to answer this question:

1. Design and simulate blank and tooling concepts for manufacture by die sheet hydroforming based on the aircraft skin panel manufactured by conventional stamp forming.

2. Determine which is the best performing blank and tooling concept, by comparing the simulation results with the nominal surface of the aircraft skin panel.

3. Manufacture the conceptualised blank and tooling and manufacturer the aircraft skin panel on a fluid cell press.

4. Dimensionally inspect the manufactured aircraft skin panel against the nominal surface using typical metrology methods and equipment.

5. Determine the accuracy of the simulation software package’s ability to predict the final aircraft skin panel by comparing it with the manufactured component.

1.4. Scope and Limitations

1.4.1. Scope

The scope of work for this study is to investigate die sheet hydroforming of a complex shaped aircraft skin panel manufactured in aluminium alloy. The component will be manufactured from AA2024-W temper condition 2 mm clad sheet or -O temper condition 2 mm sheet. A key part of the investigation is the die sheet hydroforming tool, and initial flat blank shape design will be conceptualised using Dassault Systeme CATIA V5 Computer-aided Design Software Package. The tool and blank will be simulated using ESI Group PAM-STAMP 2G forming simulation software package only to validate the design digitally, before proceeding to tool proofing and press trials. The capability of PAM-STAMP, to simulate accurately the die sheet hydroforming of a large complex shaped aluminium alloy aircraft component will be assessed. Based on the findings, additions to the procedures used to conduct a forming feasibility and manufacturability assessment, and effectively assess the simulation output will be provided and validated the presented study.

1.4.2. Limitations

The list of limitations that pose risks to the completion of the study:

1. Access to simulation material properties is limited, and material characterisation experiments are required for aluminium alloy (AA) 2024 in a post-heat solution treated temper condition. Due to the cost and time to complete a characterisation campaign, only the AA2024-W temper condition could be completed. Aerosud Aviation provided material properties in AA2024-O temper condition. The concern was material properties availability where an alternative material that significantly differs from AA2024-W could not be sourced. The difference between -W and -O temper conditions did not impact the final findings of this study.

2. Due to the size of the component and tooling selected for the case study, only the Quintus Technologies fluid cell press at Denel Aerostructures can be used for the study.

3. The ESI Group PAM-STAMP 2G scripted hydroforming pressure loading is applied to the sheet metal blank only and cannot be altered to be applied to any other defined elements. If loading is applied to hyperelastic rubber elements, a constant pressure will be used.

4. Tooling compensation based on a simulation optimisation study cannot be conducted and incorporated into the final tooling design concept. For tooling to be manufactured, it must be a parametric solid body geometry. PAM-STAMP outputs the compensated tool surface in STL format, which requires advanced CAD design knowledge and experience to model the compensated surface correctly. Conducting the redesign within the time frame available to complete this research and the risk the design will not be adequate to manufacture warrants the use of a nominal surface profile tool concept. This limit may impede the component from meeting the design tolerance but will not compromise the evaluation of the simulation software package.

1.5. Contribution of the research

The research will contribute to the development of digital manufacturing, specifically die sheet hydroforming. The automotive and aerospace industries will benefit the most from this study. The trial-and-error design process is still commonly used throughout the industry, especially in South Africa. An effective process to design, simulate, evaluate and validate a tool and blank will significantly aid manufactures in reducing costs and becoming more competitive locally and internationally.

Chapter 2: Literature Review

Metallic forming processes have been used extensively in the aircraft and automotive industry, and have been well-studied and understood academically (Chen et al. 2014), (Hatipoğlu and Alkaş, 2016). Thus, the literature presented will reinforce known topics applicable to the die sheet hydroforming forming manufacturing process, material characterisation, the finite element simulation of the process, and validation and correlation of the manufactured component and simulation results using metrology inspection.

2.1. Die Sheet Hydroforming Manufacturing Process

Metal forming is the process of transforming a specified material into a useful component. The material usually begins in a flat, shapeless form, termed the sheet metal blank. Forming is one of six manufacturing processes, separated from primary shape processing, subtractive processes, additive processes, material treatment, and joining (Altan and Tekkaya (Vol 1) 2012). Within the forming manufacturing process, Solfronk and Sobotka (2011) indicated sheet metal forming as one of the most widely-spread technologies for metallic part production and how it enables part production with different shapes, as well as size variation. Metal forming processes are classified into three groups (Altan and Tekkaya (Vol 1) 2012):

1. Bulk-forming: forgings, extrusion, rolling, and drawing
2. Sheet forming: brake forming, deep drawings, stretch forming
3. Hybrid forming: drawing and ironing, and bending and coining

Aircraft skin panels and ribs and automotive bodies are examples of components that are manufactured from sheet metal and manufactured by the processes classified in group 2. Stamping and sheet hydroforming are the two manufacturing processes used by the aerospace and automotive industry to manufacture sheet metal components. Figure 2.1 depicts a typical stamp forming press machine.

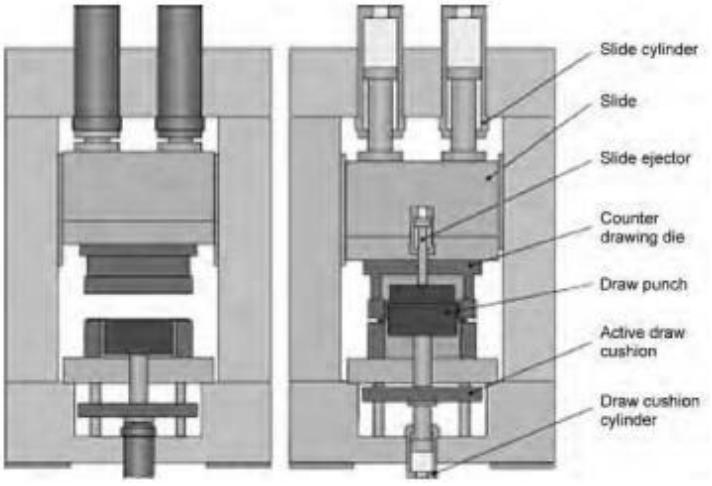

Figure 2.1: Schematic of a hydraulic press with a draw cushion and die set, with components labelled (Altan and Tekkaya (Vol 1) 2012)

Stamp forming made use of a rigid punch and die tooling, whereas the hydroforming process used a fluid medium to pressurise one side of the component which forced it against a shaped tool that was either a male or female type. The component contoured the tool, taking the desired shape of the component (Altan and Tekkaya (Vol 2) 2012), Lee et al. (2015), (Hatipoğlu and Alkaş, 2016). The variant of hydroforming investigated was sheet hydroforming, with tube forming the other.

Sheet hydroforming is further split into two subcategorised based on the type of tool, which is either a punch or die. Punch sheet hydroforming is a hydromechanical process and typically used for components that can only be manufactured by being deep-drawn. Die sheet hydroforming is a high pressure forming process, further classified into single or double blank based on the number of blanks required to manufacture the component. (Altan and Tekkaya (Vol 2) 2012) (Lee et al., 2015) (Bell et al., 2020). Typical components manufactured by die sheet hydroforming are flanged component and some shallow, deep-drawn components. Figure 2.2 depicts the classification of sheet hydroforming processes. Other types of hydroforming of sheet metal blanks were conducted on rubber forming presses (Dirikolu and Akdemir 2004), where hydrostatic pressure is applied to the blank using a solid silicon rubber medium. Although rubber forming is in a strict sense, no a sheet hydroforming process (Altan and Tekkaya (Vol 2) 2012).

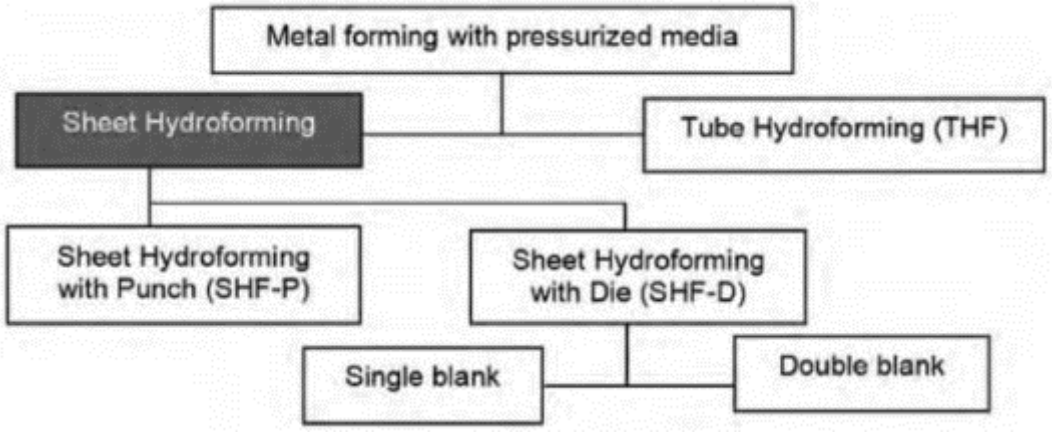

Figure 2.2: Classification of sheet forming processes using liquid media (Altan and Tekkaya (Vol 2) 2012)

To illustrate each of the four hydroforming processes, Figure 2.3 depicts differences between each the respective processes.

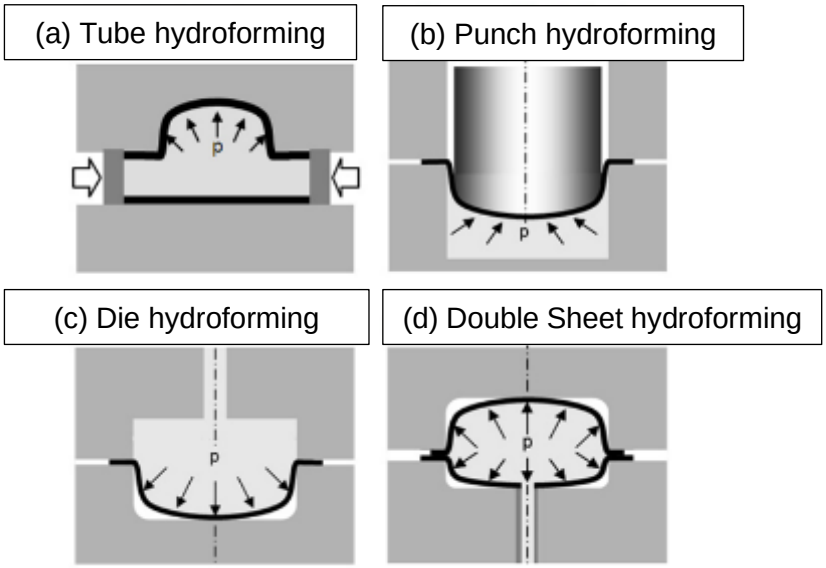

Figure 2.3: (a) Tube Hydroforming (b) Water punch hydroforming (c) Water die hydroforming (d) Double sheet hydroforming (Tolazzi 2010)

Die sheet hydroforming is used on the fluid cell or flexform press machines, where the blank is formed against the female die. The press ram is oil and a flexible rubber diaphragm, which replaces the solid punch used in conventional stamp forming. Under the oil pressure, the rubber diaphragm conforms to the shape of the tool and holds the blank over the die cavity. A single rigid die tool is required and can be more cost-effective, compared to a standard stamp forming tool and die sets. (Altan and Tekkaya (Vol 2) 2012), (Lee et al. 2015). Figure 2.4 provides a cross-sectional view of a fluid cell press. Tools are loaded onto the tray and shuttled into the press chamber. Sacrificial throw pads are placed above the blank to protect the rubber diaphragm during forming.

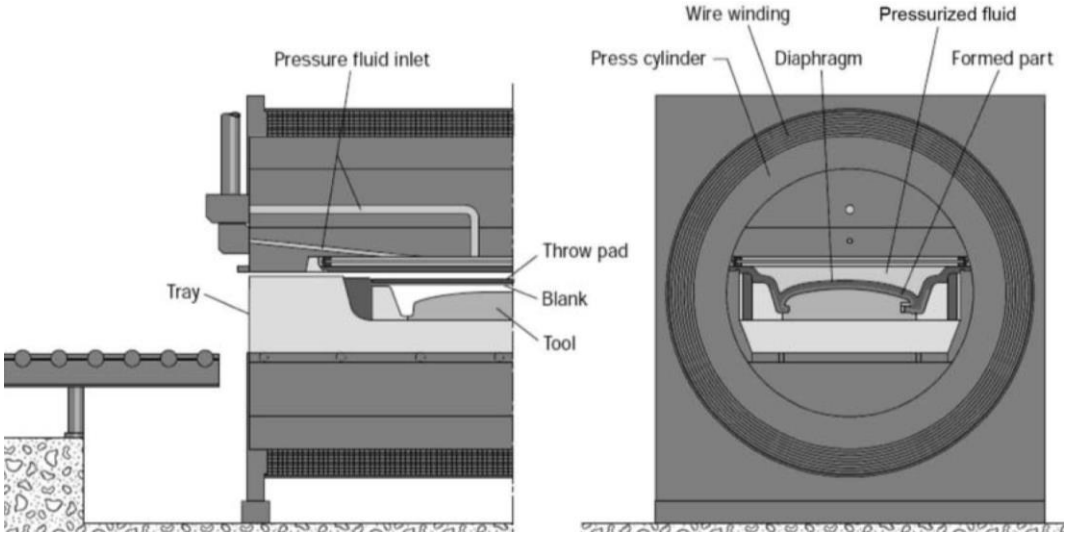

Figure 2.4: Flexform fluid cell press (Altan and Tekkaya (Vol 2) 2012)

2.1.1. Advantages

The advantages of die sheet hydroforming process are good surface finish, good dimensional stability, low tooling cost and less tool wear (Lee et al. 2015).

Better formability is exhibited by die sheet hydroforming compared to conventional stamp forming due to the free bulging effect. As the sheet is drawn into the die cavity by the fluid medium, a uniform in-plane strain distribution throughout the sheet is experienced as opposed to the high local deformation that is imposed by the corners of a rigid punch in stamping processes. The improved formability makes die sheet hydroforming a viable alternative to low formability materials (Altan and Tekkaya (Vol 2) 2012).

As die sheet hydroforming is typically a cold-forming process, the sheet goes through higher levels of work hardening compared to other processes. Cold forming operations require higher forces (typical operating condition for hydroforming machines) than forming at elevated temperatures. Forming at elevated temperatures improves the formability but increases the cost dramatically (Bell et al. 2020). As the accuracy of die sheet hydroforming is high and accommodates low formability materials, even with low manufacturing cycles and volumes, it is a significantly beneficial manufacturing process.

As the die sheet hydroforming process only requires one tool, and a soft medium forms the blank, tooling costs are dramatically reduced compared to conventional stamping tools. Firstly, fewer tools need to be manufactured and maybe simpler without the need for a die set for alignment of the punch and die tools. In die sheet hydroforming, the female die tool is placed on the fluid cell press tray without the need to fix it in place. Second, is tool wear, which is also reduced due to the softer forming medium compared to a rigid punch (Lee et al. 2015) (Altan and Tekkaya (Vol 2) 2012).

Die sheet hydroforming exhibits good surface quality as one surface interfaces with the rubber throw pads and diaphragm compared to stamping tools with both sides interfacing rigid metal tool faces. The softer rubber surface and high applied pressure reduce the probability of tool marks and sidewall wrinkles (Altan and Tekkaya (Vol 2) 2012).

Complex shaped and featured components require multiple stamping stages to be manufactured using conventional forming processes, whereas die sheet hydroforming allows for single operations. Special features such as undercuts, in-process trimming, cutting & hydropiercing can be incorporated but is still possible in stamping process tooling (Altan and Tekkaya (Vol 2) 2012) (Bell et al. 2020). Fewer forming operations reduces manufacturing costs and time.

Lee et al. (2018) made use of the unique features of die sheet hydroforming tooling with in-situ trimming, as shown in Figure 2.5. Steps 1 to 3 of the forming process are the typical straight or curved edge flanging. Steps 4 and 5 are the in-situ trimming stages. The blank is formed into the open undercut cavity and because of the sharp edge the blank shears off.

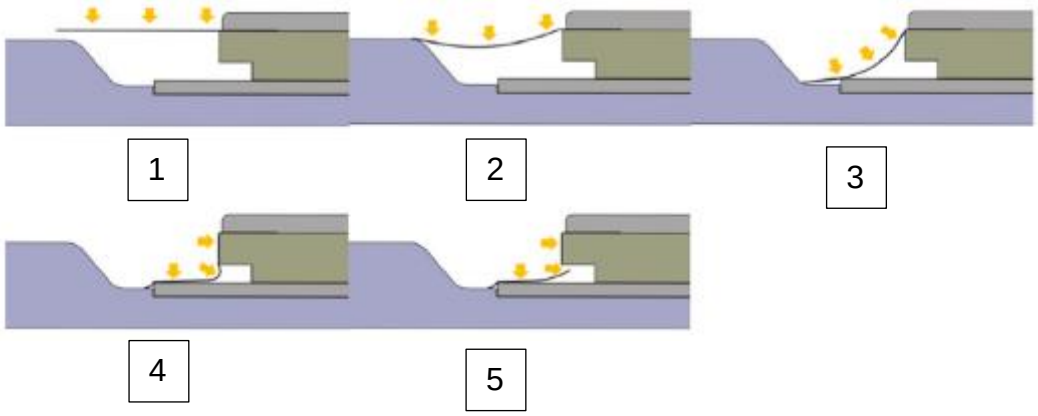

Figure 2.5: Process description of rubber-diagram forming (Lee et al. 2018)

2.1.2. Disadvantages

Die sheet hydroforming has several advantages and a few disadvantages compared to competing manufacturing processes. The most notable disadvantage of the die sheet hydroforming process is the cost of equipment and low cycle times. High ram forces resulted in a higher machine cost compared to stamping press machines. High cycle times lower the quantity of product produced. Recovery of these costs was achieved in higher-value quality products (Altan and Tekkaya (Vol 2) 2012). Bell et al. (2020) found the capital investment for equipment to be roughly 30% higher than conventional stamping machines. In addition, typical cycle times for die sheet hydroforming is around 20 to 60 seconds instead of a few seconds in conventional cold forming operations.

Component definition in terms of sharp corners is a pitfall of die sheet hydroforming. Bell et al. (2020) stated that in order to achieve sharp radii, pressure intensifiers are required. Altan and Tekkaya (Vol 2) (2012) denoted higher pot pressures were required to form sharp corners. Pot pressure depends on the sheet material thickness and the smallest corner radius in the die geometry. Typically, second forming operations are required to achieve the sharp radii definition in die sheet hydroforming.

As materials are inherently work hardened during the die sheet hydroforming process, the ductility of the material is sacrificed. This is a disadvantage of most cold forming processes, assuming the component requires a specific degree of ductility. Post heat treatment operations are used to improve ductility (Bell et al., 2020).

It is the author's opinion that die sheet hydroforming has the disadvantage in its ability to control the blankholding loading during the forming process. Stamping tools have a double-acting cylinder, with the second cylinder used for holding a blank to control the flow of the material and thus in-plane strain imposed as the component is drawn into the die. Die sheet hydroforming does not allow for controlled blankholding without well-designed tooling.

2.1.3. Manufacturing Defects

Manufacturing defects reduce the aesthetic qualities of a component and must be minimised or avoided altogether. Wrinkling and fracture defects are the typical flaws in evidence on formed components (Abedrabbo et al., 2005). Other defects include tearing, springback and other geometric and surface defects (Kadkhodayan and Moayyedian 2011). Wrinkles in formed metal components can be treated as a recoverable defect, unlike fracture. “Wrinkling occurs when the compressive stresses go beyond a certain value during forming” (Kadkhodayan and Moayyedian 2011). Prevention of defects is essential to ensure dimensional accuracy and acceptable aesthetics (Elangovan et al. 2010). In the case of wrinkling, the clamping and holding tools can “iron” out the wrinkles, but only if used correctly. Component type and geometry can be limited due to wrinkling and fracture defects. Wrinkling is deemed acceptable if it lies outside the component’s trimmed zone (Abedrabbo et al., 2005). Altan and Tekkaya (Vol 2) (2012) list the following as the common defects in die sheet hydroforming:

- Excessive thinning leading to fracture
- Flange wrinkling
- Sidewall wrinkling
- Excessive bulging leading to fracture
- Surface marks

To illustrate three common sheet metal forming defects, Figure 2.6 shows tearing, wrinkling, and springback.

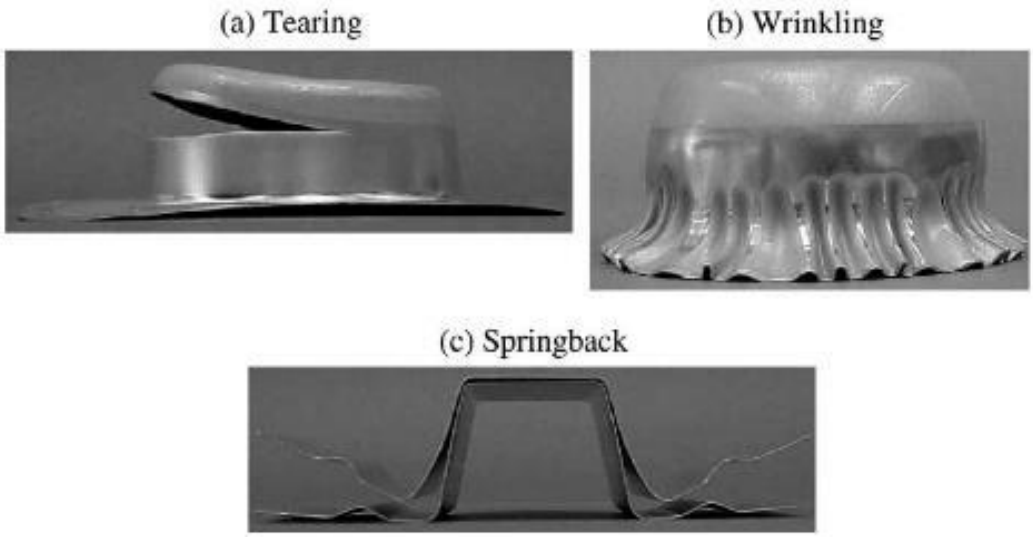

Figure 2.6: Problems in sheet metal forming (Hsu et al. 2002)

In addition to wrinkling, fracture and surface defects, Zhang et al. (2019) describes springback as one of the main defects in die sheet hydroforming. Simulation software packages are used to provide insight to the tooling such that tooling can be compensated to account for springback. Chen et al. (2014) conducted a study focusing on the experimentation and simulation of spingback of straight

edge flanging of aluminium alloy by die sheet hydroforming. The ability to overcompensate the tool with an undercut is a benefit to straight edge flanging. Chen et al. (2014) found that the PAM-STAMP simulation results agreed well with the experiments and is an effective method to predict and perfect the real case. Yoshida et al. (2013) classifies typical springback mechanisms as six distinct types and are presented in Figure 2.7. Panel buckling torsion springback is most applicable to aircraft panels and car auto bodies. The mechanism is a result of uneven in-plane stresses. Sufficient in-plane stretching must be achieved to minimise panel buckling distortion in formed panel structures (Yoshida et al. 2013). The free bulging effect is uniform in-plane strain distribution seen throughout the sheet as the sheet is drawn into the die cavity by the fluid medium. Analogous to an inflated balloon, the rubber membrane of the balloon experiences uniform in-plane stretching as air is pumped into it, and it expands due to the rising pressure within. The sheet undergoes the same stretching in sheet hydroforming when the blank is clamped along its edges and drawn into the tool die cavity. Arguably, the free bulge effect of die sheet hydroforming is seen as the right forming mechanism to minimise panel buckling torsion springback.

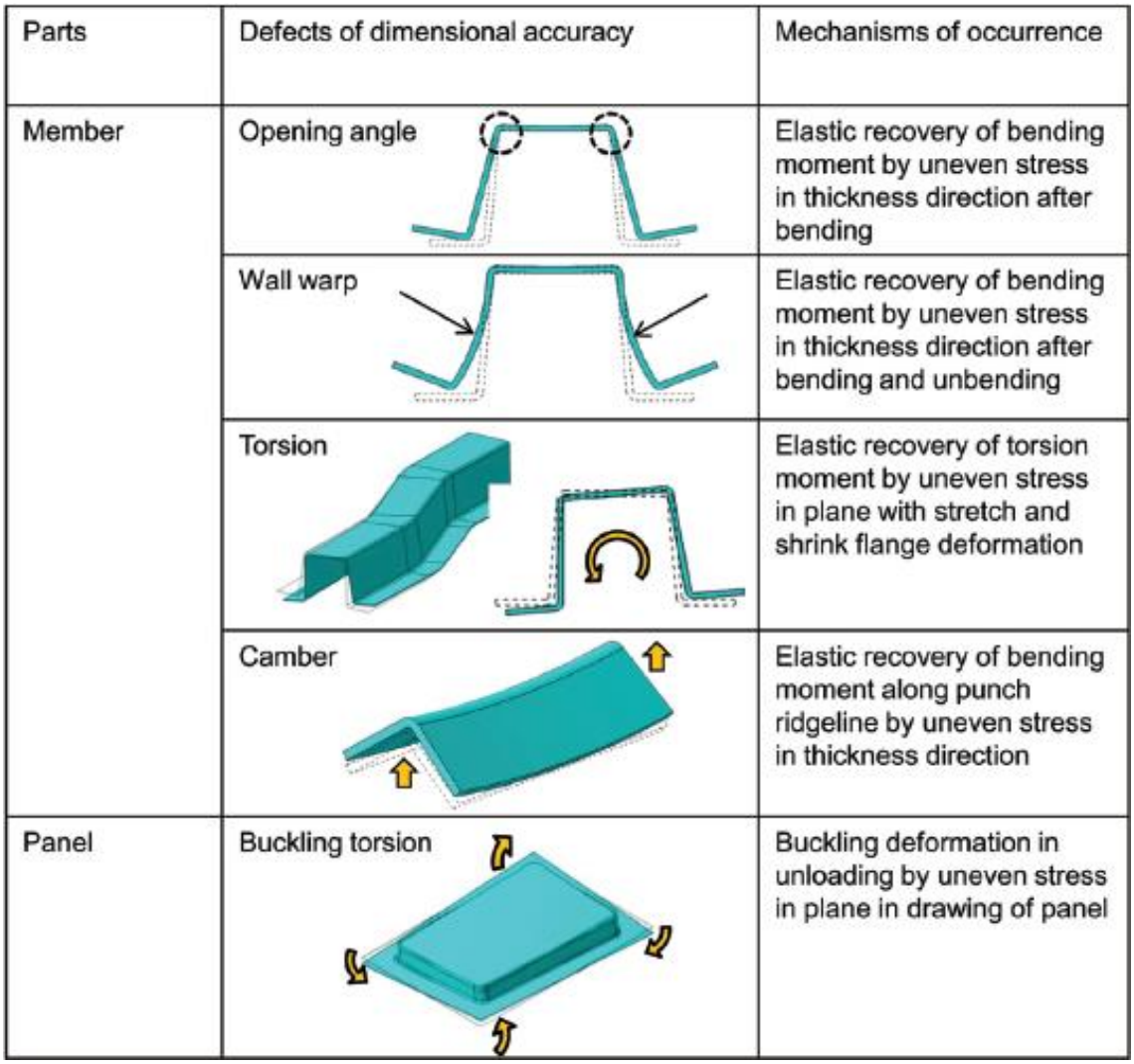

Figure 2.7: Classification of typical springback problems and its mechanisms of occurrence (Yoshida et al. 2013)

The study conducted by Solfronk et al. (2016) investigate the accuracy the material mathematical models had on predicting accurately stamped springback. The authors evaluated two yield criteria, the Hill 48 and the Vegter in combination with isotropic and kinematic hardening laws in PAM-STAMP. It was found that yield criterion had little influence on the springback, due to low deformation

in high strain areas. More complicated components, that experience a greater degree of deformation, would benefit from the more advanced yield criterion. Kinematic hardening models have a definitive influence when predicting the springback. Thus spring-back prediction rests in the selection of the deformation hardening model and that the yield criterion does not influence the result as much.

Defects can be prevented with the correct design procedures and knowledge to conceptualise the manufacturing tools and sheet metal blanks. Simulation aids in identifying areas where defects will result and provides designers and engineers with the necessary information to make the correct design changes (Abedrabbo et al., 2005, Altan and Tekkaya (Vol 2) (2012)). Altan and Tekkaya (Vol 2) (2012) provides the following as the steps involved in FEM simulation:

1. CAD – Creating geometry for the blank and tooling is the first step.
2. Material Properties – Accurate material data is necessary to predict the material flow.
3. Friction coefficients – This is a required input parameter.
4. Influence of temperature and heat transfer coefficients – Materials at elevated temperatures are strain-rate sensitive and are considered in the warm and hot forming processes.

The omission of defects improves the formability confidence of the design. ErtUrk and Kazazoglu (1982) defined formability as “the amount of deformation that can be given to a specimen without fracture or necking in a given process”. Altan and Tekkaya (Vol 1) (2012) define several formability terms:

- Stretching (stretchability) – the ability of the material to stretch without failure biaxially.
- Bending (bendability) – the ability of the material to bend around a corner radius by 90° along a straight line.
- Bending under stretching – a standard deformation mode, based on the combination of bending and stretching limits.
- Stretching at the edge – the ability of the sheet material edges to avoid failure during the forming and trimming processes.
- Deep drawing (drawability) – the ability of the material to be drawn to the desired shape.

2.2. Material Characterisation

The success of any FE analysis is dependent on proper understanding or material properties and friction (Hatipoğlu and Alkaş, 2016). This section covers material properties, friction, plasticity yield criterion, flow stress hardening laws, and forming limit diagrams which are essential for any numerical analysis to account for strain path change effects ensuring the accuracy of prediction (Thuillier et al. 2009).

2.2.1. Material Properties

Aluminium alloys are the most widely used metals in the aerospace industry for their strength-to-weight benefits compared to that of steel. The most widely used sheet metal used in the manufacture of aircraft panels and ribs was AA2024 (Niu 2011). Aluminium alloys are still widely used material in the aerospace industry, even though composite materials (carbon and glass-reinforced plastic) are beginning to be used more predominantly in modern airframes. Apart from fabrication, other characteristics that are considered when a material is selected are (MMPDS-07 2012) (Niu 2011):

- Static and fatigue strength
- Fracture toughness and crack growth rate
- Availability and cost
- Corrosion and embrittlement
- Compatibility with other materials

- Environmental stability

Alloys are materials created primarily from the pure base material and lower quantities of other elements. Aluminium alloy sheets are produced in wrought by rolling process. The four-digit naming system specifies the major alloying elements and the assignment of the specific alloy. The 2 series aluminium alloys are copper (Cu) based with low quantities of Magnesium (Mg), Manganese (Mn), Silicon (Si) and Lithium (Li). Table 2-1 shows the elements used along with aluminium (Al) that makes up AA2024.

Table 2-1: Wrought Aluminium Alloy 2024 Elemental Breakdown (Dowling 2007)

Identification	Principle Alloying Elements, typical % by weight		
	Cu	Mg	Mn
AA2024	4.4	1.5	0.6

The specific elements and their quantities in the alloy gave AA2024 its good strength, fatigue and corrosion attributes. Excellent properties and creep resistance as elevated temperatures. In addition to the bare aluminium plate or sheet, aluminium alloys sheet is supplied in clad form. Cladding is a thin coating of pure aluminium bonded to the aluminium alloys during the rolling process. Cladding provides added corrosion protection and is typically between 2.5 – 5 % of the total sheet thickness (Dowling 2007) (MMPDS-07 2012) (Niu 2011).

Aluminium alloys are nonferrous metals, which unlike steels which strengthen during quenching and tempering due to martensitic structures, are strengthened by precipitation hardening. Precipitation hardening is the following steps: solution heat treatment, quenching and age hardening (Dowling 2007). Aluminium alloys are manufactured in four tempers (Niu 2011):

- O – annealed
- F – as fabricated
- H – strain hardened
- T- heat treated

The -T3 and -T4 tempers have high toughness, whereas -T6 and -T8 tempers have high strength. The -O temper condition cannot be used in aircraft structures and must be heat solution treated to after being formed into the desired shape (MMPDS-07 2012). In terms of fabrication characteristics, the formability of -T3 sheet material is low in comparison to -O condition. Hijazi et al. (2004) conducted a study to determine the FLD using digital image correlation of AA2024-O. Two sheet thicknesses were characterised, 0.81 mm and 1.25 mm, using the Nakajima test, conducted in accordance with ISO 12004-2. The study showed that the limiting strains increased with increasing sheet thickness. Fallah et al. (2018) investigated the effects of natural ageing treatment on mechanical, microstructural and forming properties of AA2024 sheets. The T3 temper is solution heat-treated, cold-worked and naturally-aged to a suitable stable condition as received from the supplier. Solution heat treatment is achieved by heating to a temperature of 495°C and holding long enough to allow constituents to enter solid solution and cooling rapidly enough to hold the constituents in solution (MMPDS-07 2012).

The -T3 temper condition is removed if the material is heat-treated again. Due to the low formability of -T3, once heat treated, the formability improves, as shown in the study conducted by Fallah et al. (2018). From the heat treatment process specification ABP 3-1119 (2005), the AA2024 clad sheet

is processed to -W temper condition by heating in a furnace for 23m30s±30s at 495±5°C, quenching in water which is no warmer than 40°C for 3m±1m within a delay of 12s after exiting the furnace.

After heat treatment and quenching, the sheet is in -W temper condition, which is an unstable temper and ages naturally at room temperature. The material naturally ages from -W temper condition to -T42 temper condition after being cold-worked by press forming (MMPDS-07 2012). The formability of the sheet significantly improves in W temper condition, but the time to press after heat solution heat treatment is limited. Fallah et al. (2018) showed that the 0.81 mm thick AA2024-T3 sheet's formability decreased as the material began to age to a harder T42 condition.

2.2.2. Plasticity yield criterion laws

There are several plasticity laws/yield criteria, namely Hill 48, Hill 90, Barlat 89, Barlat 91, Barlat 2000, Vegter yield locus Lite and Yoshida 6th order. The listed laws are anisotropic yield criteria, whereas Tresca and Von Mises are isotropic yield criteria (ESI Group 2018, Sister and Slota 2016). Sheet metals exhibit anisotropic characteristics due to the rolling process and resulting in the different behaviour in the three directions, rolling, transverse and thickness. "A surface represents a yield criterion in 3D space. Inside the yield surface, the material is in an elastic state, and outside of the yield surface it is in a plastic state" (Altan and Tekkaya (Vol 1) 2012).

The yield locus for the Hill 48 and Hill 90 material cards are the simplest to create and mostly used with an isotropic hardening law (Sister and Slota 2016). The Hill 48 yield criterion is based on the von Mises yield criterion for orthotropic materials and assumes a plane stress state. Hill 90 overcomes this limitation but requires five additional parameters that are determined from a balanced biaxial test (Solfronk et al. 2016, Altan and Tekkaya (Vol 1) 2012). The equi-biaxial test is a bulge test. A circle-shaped disk is clamped at the edges and forced to bulge using a liquid medium until failure. The major and minor strain of the sheet is measured using an optical measuring device that has a minimum of two cameras (ESI Group. 2013).

The proportional yield limit is determined by conducting tensile tests as per ASTM E 8M. Plasticity strain r ratios in 0°, 45° and 90° relative to the sheet rolling direction and the difference in yield limit for each direction are required to generate the Hill 48 yield locus. The plasticity strain r ratio is calculated from the tensile test conducted as per ASTM E 8M and calculated as per ASTM E 517. The ratio is based on width strain (ε_w) divided by the thickness strain (ε_t) (ESI Group. 2013, Sister and Slota 2016). The Barlat criterion is a more general anisotropic yield criterion and is most applicable to aluminium alloys. The material properties required to establish a Barlat criterion is the same as those required for Hill 90 with one additional r-value. The r-value is expressed as the strain rate in the minor direction divided by the strain rate in the major direction.

The Barlat 2000 yield locus is described by eight coefficients that are determined from the various tests already mentioned (Altan and Tekkaya (Vol 1) 2012, Barlat et al., 2003). Figure 2.8 illustrates the differences between Hill 48, Hill 90, and the Barlat 2000 plasticity laws. The graph shows the normalised yield locus of each yield criterion against a reference stress value. The graph of the criteria was created using the ESI Group Esimat-wizard excel tool (ESI MAT-WIZARD, 2020). Both the Hill 48 and Hill 90 criterion maintain the oval-shape, which is similar to the locus of the Von Mises criterion. The Barlat 2000 shape is noticeably different in the regions that describe in-plane strain state (Altan and Tekkaya (Vol 1) 2012). What this indicated was that the Hill criterion required higher loading, compared to Barlat, to deform the component plastically where in-plane strain was concerned.

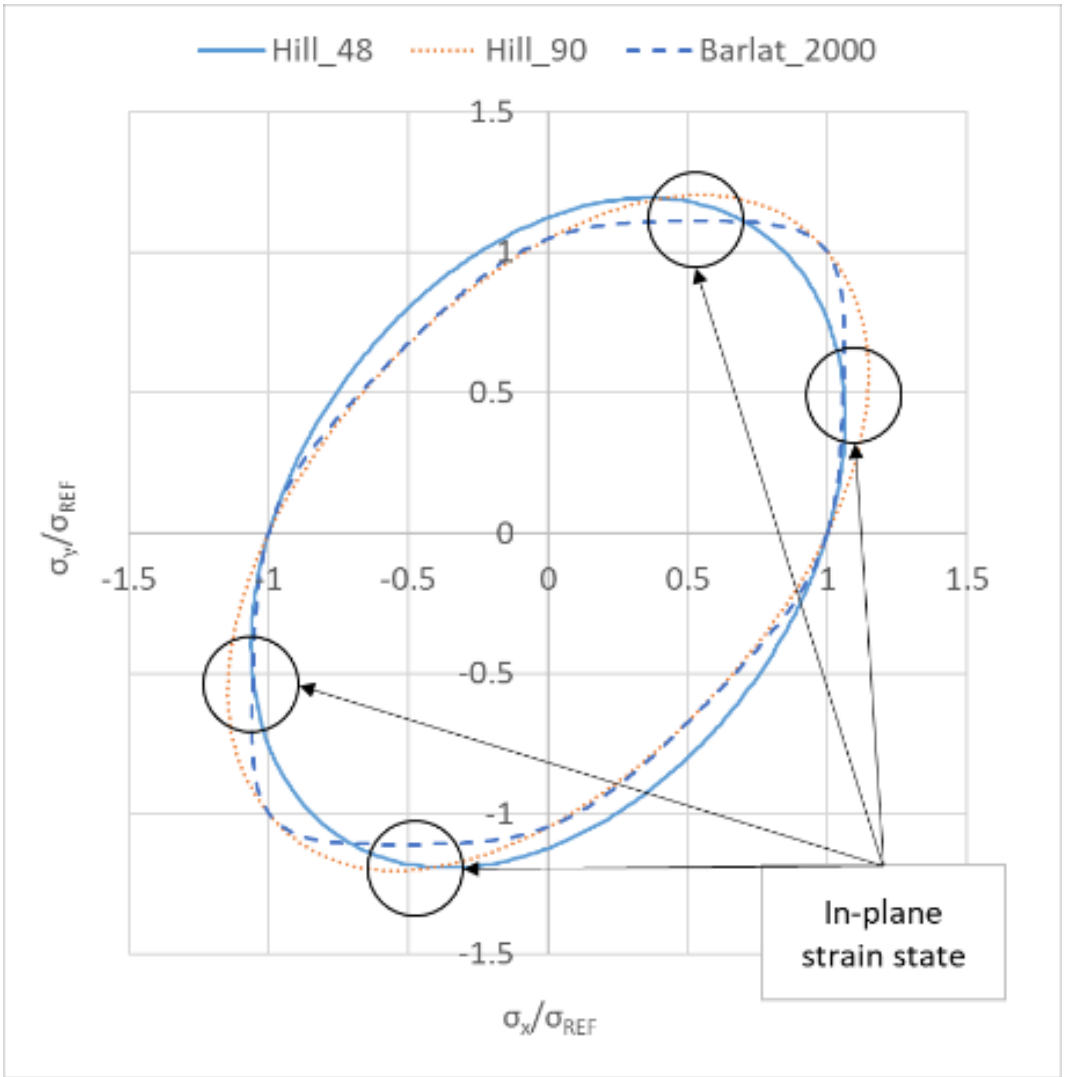

Figure 2.8: Normalised yield locus comparison of Hill 48, Hill 90 and Barlat 2000

The Vegter yield locus is more complicated than any of the other yield loci. It is based on uniaxial tensile, plane strain, shear and biaxial (compression) tests. Interpolation of the results is conducted, using the Bezier interpolation function. Compared to Hill 48 and Hill 90, the Vegter yield locus material card is stated to provide more accurate simulation results (Solfronk et al. 2016) and is evident in Figure 2.9. Similar to the Barlat 2000 yield locus, the Vegter_Lite, Vegter_2017, and Yoshida_6th_order yield loci are significant improvements on the Hill 48 and Hill 90 criterion. More testing is required and, hence, more costly, compared to the required number of tests for the other material cards. The complete Vegter yield locus law requires 17 parameters from 9 test. The Vegter lite law was developed to reduce the number of tests as it requires eight parameters from four tests. As conducted for the Hill 48 material card, three tensile tests are conducted. The Vegter Lite only requires the bulge test to be conducted (ESI Group. 2013, Solfronk et al. 2016).

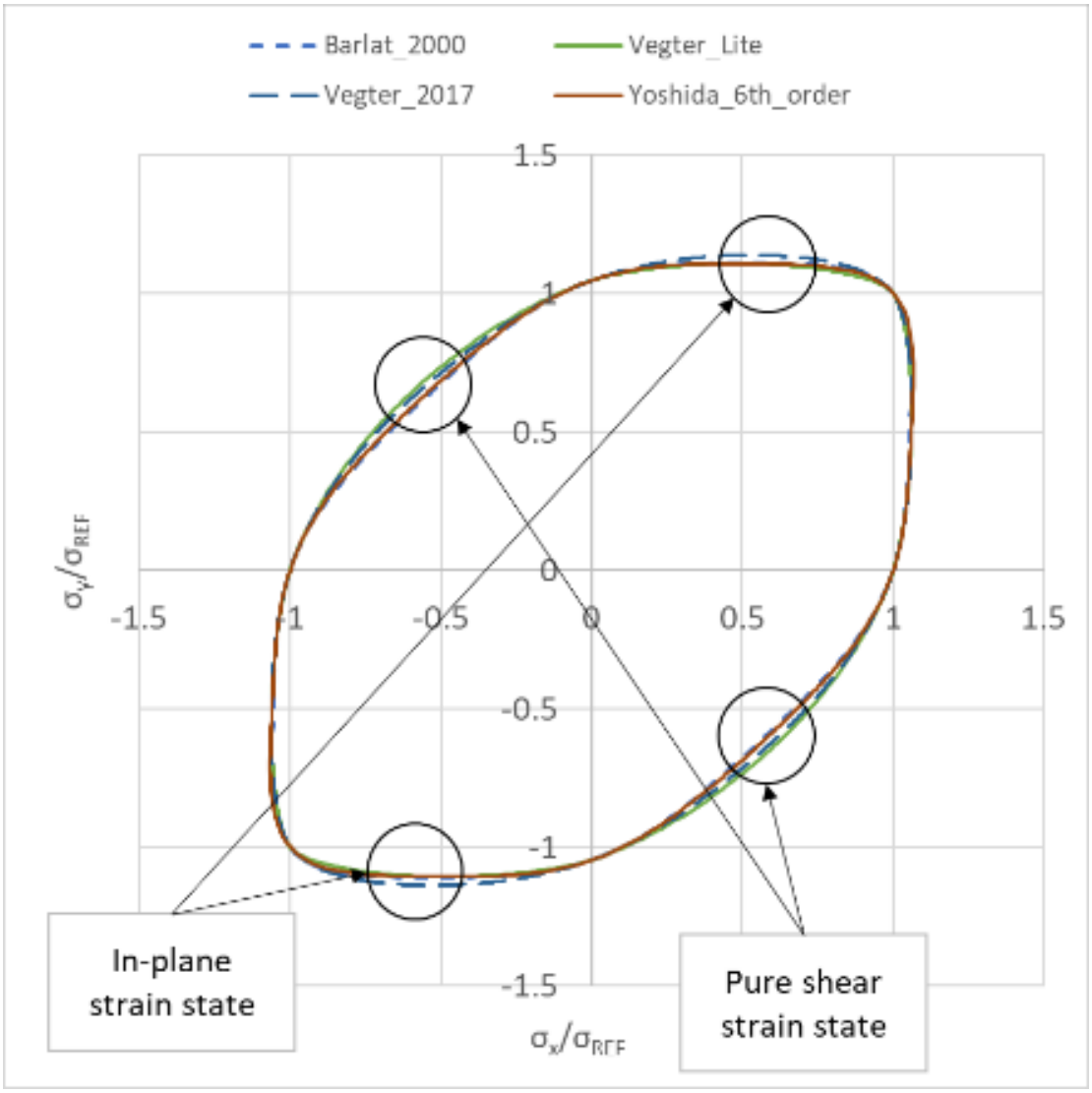

Figure 2.9: Normalised yield locus comparison of Barlat 2000, Vegter_Lite, Vegter_2017, and Yoshida_6th_order

Figure 2.9 illustrates the differences between the Barlat 2000, the Vegter_Lite, Vegter_2017, and Yoshida_6th_order yield plasticity laws. The graph shows the normalised yield locus of each yield criterion against a reference stress value. The graph of the criteria was created using the ESI Group Esimat-wizard excel tool (ESI MAT-WIZARD, 2020). The Barlat 2000, the Vegter_Lite, Vegter_2017, and Yoshida_6th_order yield loci shapes are noticeably similar and deviate in two regions. The first describes the in-plane strain state, and the second is the pure shear strain state (Altan and Tekkaya (Vol 1) 2012). What this indicates is the Barlat 2000, the Vegter_Lite, and Yoshida_6th_order yield criterion requires higher loading compared to Vegter_2017 to plastically deform the component, but only marginally. Similar to arguments for Hill 48 and Hill 90, compared to Barlat 2000, this may result in a load that is much greater than is required to manufacture the component, and may result in inadequate results, compared to the simulation result. However, it is marginal, compared to what may be expected in comparison to Hill 48 and Hill 90 yield criterion. Altan and Tekkaya (Vol 1) (2012) describes the pure shear strain state as a condition where loading applied in y-axis stress tensor is equal to negative the x-axis stress tensor ($\sigma_y = -\sigma_x$) in a plane stress state ($\sigma_z = 0$). With reference to the FLD and zones 5 and 6, this describes the strain state where wrinkling is expected.

2.2.3. Flow stress hardening laws

Yield criterion describes the state of the material in the elastic region of the stress-strain / stress flow curve. Beyond this yield locus limit, the material will deform permanently and is in the plastic region of the stress-strain / stress flow curve. Hardening laws govern the strength of the material in the plastic zone. If the material is stretched past its yield limit, it will be permanently deformed. All materials have a maximum tensile stress failure limit. Once reached, the material will begin to neck and thin at a localised area until failing if stretching is continued Altan and Tekkaya (Vol 1) (2012). Solfronk et al. (2016) found that the kinematic hardening model reveals much better matching with the experiment compared to an isotropic law. The minimal difference between the Vegter yield criterion and Yoshida kinematic hardening law and the use of Hill 48 and Yoshida kinematic hardening law. This perspective showed that the kinematic hardening law was more influential on the results compared to the plasticity hardening law.

A flow stress curve is a typical stress-strain curve that describes the materials characteristic behaviour when subjected to a load. Figure 2.10 depicts the typical flow stress or stress-strain curve. Young's Modulus (E) is the slope in the elastic region that is from zero to the proportional limit. Rp is the proportional limit yield stress, based on the proportional limit force (Fp), and the original area of the test specimen (A_o). Unloading the material will not result in permanent deformation. Yield is defined at the 0.2 % strain for all metals. Rm is the maximum tensile stress, based on the maximum tensile force (Fmax) and A_o. Ag is the strain in the material at maximum tensile stress. A is the strain limit of the material where failure occurs.

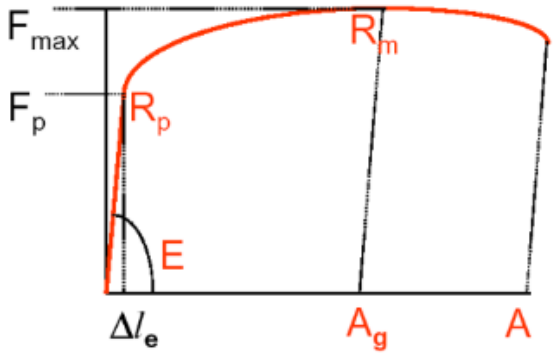

Figure 2.10: A typical stress strain-strain curve (ESI Group 2018)

The Krupkowsky Law, also known as the Swift law (Solfronk et al. 2016, Altan and Tekkaya (Vol 1) 2012, Sister and Slota 2016) is input into PAM-STAMP 2G using three constants: n, K and ε_0 in the following formula.

$$\sigma = K(\epsilon_0 + \epsilon_p)^n \quad (1)$$

σ is the flow stress [Pa]

K is the strength or material coefficient [Pa]

n is the strain hardening exponent [ ]

ϵ_0, ϵ_p are elastic and plastic strain respectively [mm/mm]

PAM-STAMP 2G makes use of six hardening laws: Holloman, power law, Krupkowsky, Yoshida Kinematic Law, Swift Hockett-Sherby Law, and a point list based on tensile test data (ESI Group 2018). If a material characterisation campaign cannot be conducted, the Krupkowsky hardening law is mostly utilised. It is an isotropic hardening law that can be generated from uniaxial tensile or equi-biaxial bulge test data (Solfronk et al. 2016) (ESI Group, 2020).

With tensile or equi-biaxial test data, the n, K and ε_0 constants can be derived from Rm, Rp and Ag. Tensile testing is the simplest means of testing, compared to the required equipment to conduct equi-biaxial testing. Altan and Tekkaya (Vol 1) (2012) provide a comparison of the flow curves from tensile and the equi-biaxial bulge test. The strain limit of the tensile test is lower compared to that seen in equi-biaxial bulge test. Thus, when using tensile data, extrapolation is required to reach the true strain limits the material can sustain.

Altan and Tekkaya (Vol1) (2012) explanation for an isotropic hardening law is stated as: “The metal continues to yield plastically with further loading when the equivalent stress calculated using the yield criterion exceeds the flow stress at the current plastic strain”. Essentially, an isotropic hardening law will not predict the orthotropic or anisotropic hardening behaviour the material exhibits. The Bauschinger effect describes this behaviour. When a component is unloaded or experiences reverse loading, isotropic yielding predicts higher stresses than that of the experiment. Thus, isotropic laws are nonconservative when predicting springback (Altan and Tekkaya (Vol1) (2012). The Krupkowsky law is an isotropic hardening law, typically accepted for FE simulation (Lee et al. 2015).

Altan and Tekkaya (Vol1) (2012) explanation for a kinematic hardening law states “the initial yield surface translates in the stress space with further loading without changing its size to model the strain-hardening behaviour in the multiaxial stress state. Hardening laws result in yielding at low stress during the reverse loading compared with experiments”. Hence, it, too, is deemed insufficient to model the material behaviour during unloading. The more advanced Yoshida law is a kinematic hardening law.

A mixed hardening law, a combination of the isotropic and Prager’s kinematic hardening laws, states that “the yield surface expands in shape uniformly and translates in the stress space”. The mixed hardening law predicts the Bauschinger effect, but cannot model the nonlinear transient behaviour at the start of plasticity during reverse loading.

Nonlinear hardening laws introduced by Armstrong and Frederick (1996) better describes the transient Bauschinger effect. The most advanced hardening law is the Yoshida-Uemori kinematic hardening law (Yoshida and Uemori, 2003). Kinematic hardening laws provide a more accurate result compared to the Krupkowsky law when predicting springback of a component. Assuming linear conditions does not represent the true nature of material behaviour in the plastic region. The Yoshida-Uemori model better predicts the unloading and reverse loading behaviour, and has been shown to provide predictions that were the closest to the experimental data compared to all the hardening laws (Altan and Tekkaya (Vol 1) 2012).

To summarise the differences between the models, the isotropic law is seen as a purely linear flow curve that will overpredict the stress state of the material and underpredict the springback state of the simulated component. Work hardening effects that are inherent to the forming process due to the large strain state of the material are not accounted for in this model. The kinematic and mixed hardening laws do a better job than the isotropic hardening law, as they more accurately predict the Bauschinger effect, but still lack the effectiveness of the Yoshida-Uemori model. The non-linear hardening law is the most effective at predicting the springback of the component, as it accounts for the change in modulus of elasticity during the cyclic loading and hardening of the material during the manufacturing process. The downfall is the cost of testing and the number of tests that must be conducted. An isotropic material card is by far the cheapest to create from a simple tensile test. The

Yoshida-Uemori hardening law has ten material parameters that must be derived from uniaxial tensile, uniaxial and cyclic uniaxial tensile testing, compared with the single test for a Krupkowsky law (Altan and Tekkaya (Vol 1) 2012, Yoshida and Uemori, 2003). To illustrate the large-strain cyclic plasticity, the Yoshida-Uemori model describes the stress-strain responses in reverse deformation. An extract from Yoshida and Uemori (2003) is presented in Figure 2.11. In comparison to Figure 2.5, a significant difference in the final springback of the component can be expected from the two models.

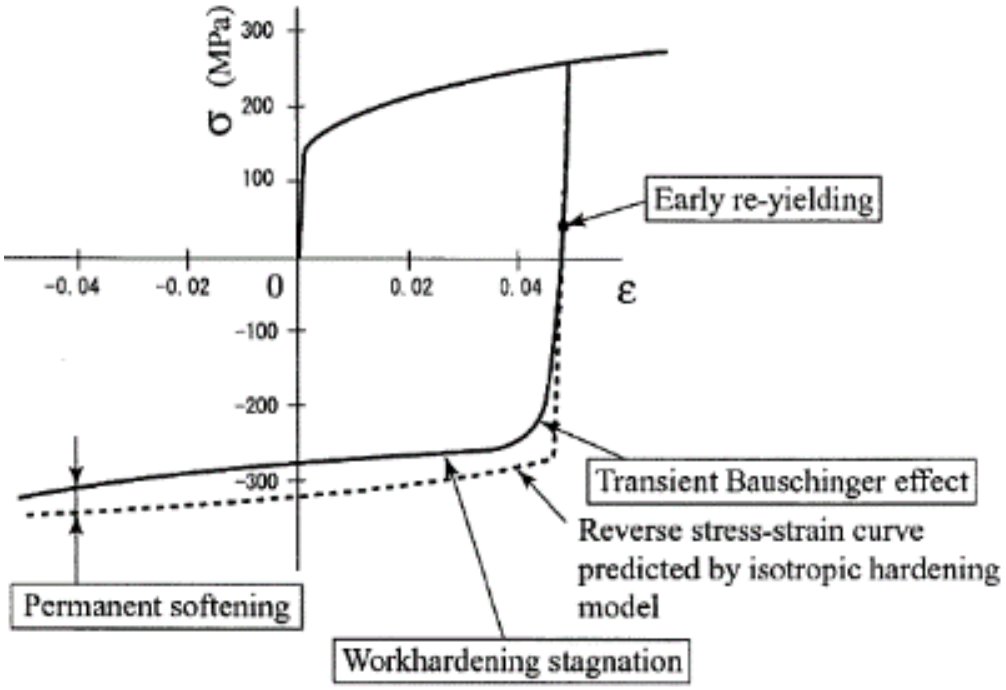

Figure 2.11: An example of a stress-strain response in a forward-reverse deformation (experimental data of in-plane tension-compression of SPCC) (Yoshida and Uemori, 2003)

2.2.4. Forming Limit Diagrams (FLD)

Metal forming defect assessment is conducted using the forming limit diagram (Narayanasamy and Sathiya Narayanan 2008). The FLD is a useful indicator that defines the formability or workability of sheet metal. Pearce (1982) described the FLD as “an immense aid in the production of sound pressings and the diagnosis of press shop failures”. The FLD was developed in the 1960s from the works of Gorton M. Godwin and Stuart Keeler. Keller was responsible for the right-hand side of the FLD, and Godwin for the left-hand side. The FLD is “an empirical limit line and has brought and still brings many benefits to press-shop practice” (Pearce 1982). The work of Pearce (1982) preceded the digital age of computer design and simulation. The FLD is the quintessential tool used in the manufacture of the formed metal component (Samuel, 2004).

Kumar et al. (2016) stated “the FLD is used during the design stage of any new sheet metal component for tooling shape & optimising manufacturing parameters. In the sheet metal industry, it is widely used and considered as one of the most important tools to determine the formability of sheet metal component (Samuel, 2004). Every thickness and type of sheet metal have a unique FLD which defines its formability, strain limit and forming regions”. Extensive testing is required to establish an FLD (Pearce 1982, Altan and Tekkaya (Vol 1) 2012).

The standard test methods established to determine FLDs are ASTM E 2218-2 and ISO 12004-2. With reference to ISO 12004 parts 1 and 2, two standardised test methods are defined, the Nakajima and the Marciniak Test. The Nakajima test makes use of a 100 mm diameter hemispherical punch

that forms circular blanks with different circular recesses on either side. The recess in the blanks ensures the complete strain state of the material can be exhibited, that is from uniaxial to equiaxial.

The Marciniak test is similar to the Nakajima test except for the flat-faced cylindrical punch. In addition, a circular hole in the bottom reduces the effect of friction (Altan and Tekkaya (Vol 1) (2012). It must be stressed that FLDs are based on true strains and not engineering strains. Figure 2.12 (a) and (b) are extracts from Altan and Tekkaya (Vol 1) (2012) and the PAM-STAMP user manual (ESI Group 2018), respectively. Figure 2.12 shows the typical definition of a forming limit curve (FLC). The minor strain is plotted on the x-axis, whereas the major strain is on the y-axis. The PAM-STAMP user manual describes the various regions of the FLD as six distinct zones.

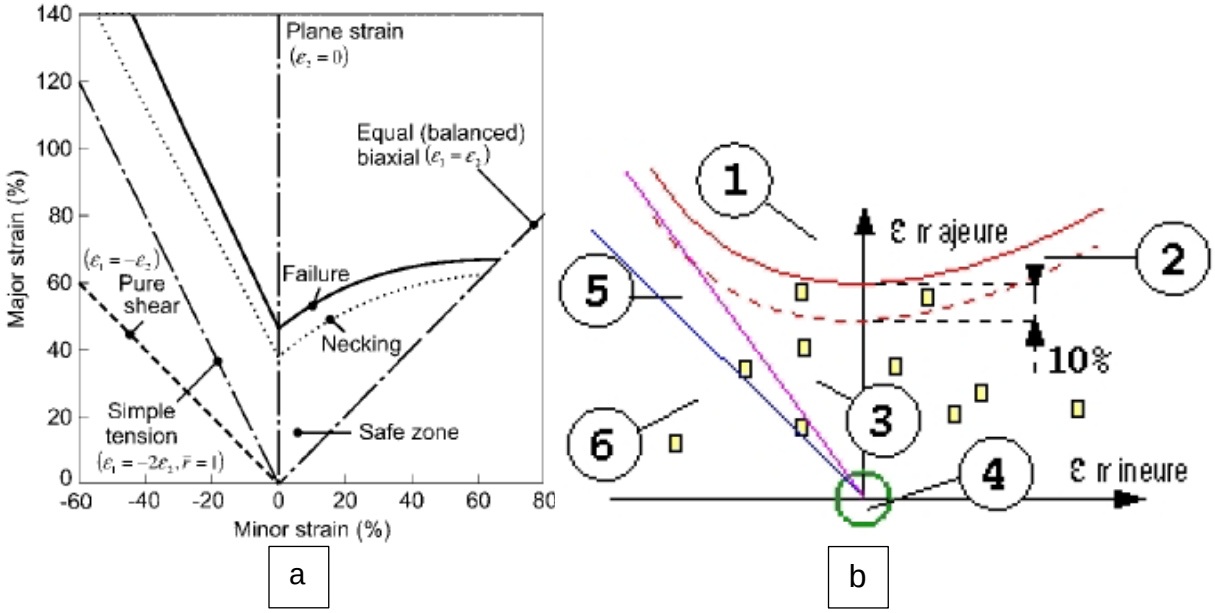

Figure 2.12: (a) FLC (Altan and Tekkaya (Vol 1) 2012) (b) FLD zone quality definition ESI Group PAM-STAMP 2G Simulation Software Package (ESI Group 2018)

PAM-STAMP plots each element's strain state per zone of the diagram:

- Zone 1 is above the failure limit of the material and represents cracks.
- Zone 2 is between the failure line and the necking line. PAM-STAMP prescribes an offset of 10% but can be modified.
- Zone 3 is the safe zone which defines the regions where sufficient in-plane stretching has occurred. In this region, the sheet has deformed past the yield point, and, will retain the desired shape. It is also not stretched too excessively, resulting in fracture. The higher the degree of stretch, the lower the degree of springback.
- Zone 4 is the region where insufficient stretching is experienced. In this zone, the material has not exceeded the yield stress limit and, thus, will not retain any permanent deformation. The radius of the zone 4 can be modified but is typically retained at the yield limit of 0.2% (0.002 logarithmic true strain).
- Zone 5 indicates a tendency for wrinkling.
- Zone 6 simply indicates a strong wrinkling tendency (ESI Group, 2018).

An approximate FLD can be created based on the Keeler-Brazier equation but is deemed to give nonconservative results (Altan and Tekkaya (Vol 1) 2012, ESI Group 2018). The PAM-STAMP user's guide makes an important note that the Keeler-Brazier equation cannot be used with aluminium. Without an FLD, formability assessment is limited as an approximate for aluminium cannot be used.

Figure 2.13 shows the FLD with the FLC extracted from the Hijazi et al. (2004) and Fallah et al. (2018) studies. The figure shows the poor formability of AA2024-W compared to AA2024-O condition. The O temper condition 2 mm curve is extrapolated from the 0.81 mm and 1.25 mm curves, based on the linear relation between the two curves. Thus, for this study, the O temper condition material is offset from the 1.25 mm curve by 1.122947894.

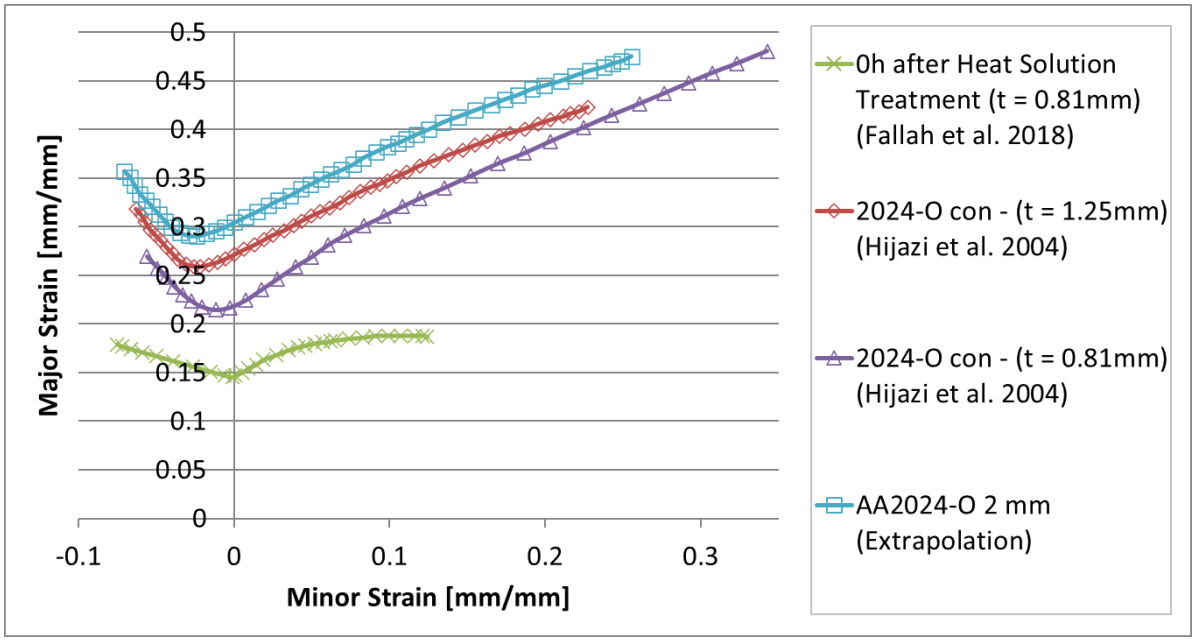

Figure 2.13: AA2024-W and -O temper condition FLD

In the absence of an FLD, various plots are available to assess the formability of the concept. The use of the thinning of the material indicates areas of high tensile stress, which can result in necking or, finally, fracture. Wrinkling will occur due to compressive stresses and is visually evident in the simulation results if the mesh element size is small enough (ESI Group 2018).

2.2.5. Friction

Friction, as described by Altan and Tekkaya (Vol 1) (2012), was one of the most important factors that must be considered in any forming process. Friction was controlled or lowered by introducing a lubricant. Both the friction and the lubricant were influenced by the two materials that were interfaced, the surface finish of the respective surfaces, temperature, sliding velocity, contact pressure, and characteristics of the lubricant. Friction must be characterised by testing in laboratory conditions using tribological test equipment. (Altan and Tekkaya (Vol 1), 2012))

Several sources were explored to assess how other researchers have dealt with friction in their forming simulations. Dirikolu and Akdemir (2004) investigated the rubber-pad forming process. Rubber-pad forming is a type of hydroforming, except it is conducted with a hyperelastic material, unlike an incompressible fluid. Thus the modelling of hyperelastic elements was required, and the friction coefficient for the rubber-to-metal interface important. The simulation package used for the Dirikolu and Akdemir (2004) study was ANSYS. The friction coefficients used were 0.2 and 0.1 for lubricated rubber-to-metal and metal-to-blank, respectively. The values were based on previous literature, and it is not clear if the friction coefficients were determined by testing or not. The component was a circular disk 80 mm in diameter. The effect of friction was explored, with two simulation studies conducted. The rubber-to-metal and metal-to-metal friction coefficients of 0.1 and 0.3 were used in the first simulation. The rubber-to-metal and metal-to-metal friction coefficients were then altered to 0.3 in the second simulation study. The component's Von Mises stresses were found to lessen in the second study with higher friction coefficients.

Kang et al. (2004) conducted a comparative study on stamping and hydroforming of an automobile fuel tank. Fuel tanks are large complex shaped components. The authors did not indicate the model used to mathematically represent the rubber nor the friction coefficients for the simulation even though they are both noted as important parameters.

The Hatipoğlu et al. (2007) study investigated die sheet hydroforming. Values of 0.2 and 0.9 were used for the friction coefficients between the metal-to-metal and rubber-to-metal interfaces, respectively. The friction coefficients were based on test data from a previous study. The authors explored straight edge flanging to validate defects such as springback and wrinkling.

Chen et al. (2014) and Chen et al. (2015) conducted die sheet hydroforming of straight and curved edge flanging, respectively. In both studies, the authors used a friction coefficient of 0.1 for every contact surface. The friction coefficient was based on previous studies that were related to stamp forming. Chen et al. (2014) found that the springback of flanged components in the rubber forming process was smaller than that of stamping owing to the friction force. This is in contrast to Hatipoğlu et al. (2007) who found the friction did not influence the defect definition and was based on flange length, and material rolling direction. Forming pressure had an affected but only up to a limit. Chen et al. (2015) agreed with the findings from the Hatipoğlu et al. (2007), where increasing the applied pressure controlled and reduced wrinkling in the flanged component.

Leacock et al. (2016) was an industrial application study on die sheet hydroforming. The study aimed to omit the modelling of the rubber throw pads and diaphragm to show it was possible to model the flex forming process without it. The component selected for the study was more complex but was still a curved edge flanged component. Figure 2.14 depicts the complex aircraft frame component from the Leacock et al. (2016) study. Leacock et al. (2016) made use of a friction coefficient of 0.15, which was only applied to the metal-to-metal interface. Leacock et al. (2016) found it was possible to model the flex forming process without the rubber provided accurate material characterisation was conducted.

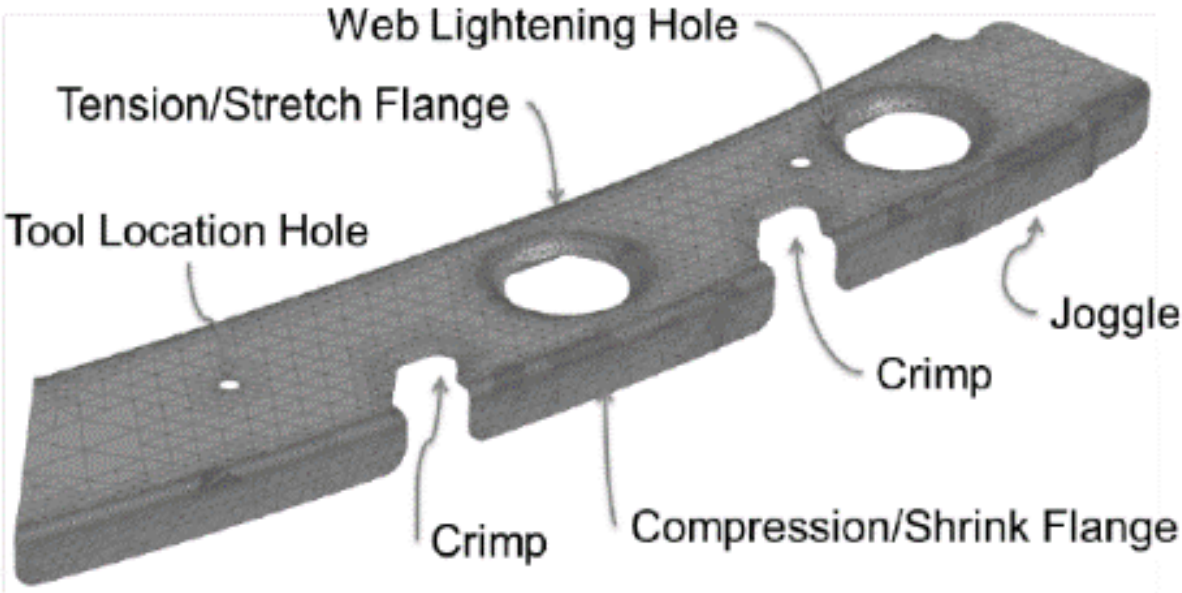

Figure 2.14: Complex aircraft frame component (Leacock et al. 2016)

The component investigated by Lee et al. (2018) is depicted in Figure 2.15. Figure 2.15 (a) and (b) depicts the forming die tool and blank designs. Figure 2.15 (c) depicts the nominal component design. Lee et al. (2018) used a friction coefficient of 0.1. The friction coefficient was based on literature and was not tested. Due to the results witnessed in the study, Lee et al. (2018) conducted a variable friction simulation study varying the friction coefficient in the following increments: 0.02,

0.06, 0.1, 0.15, 0.2, and 0.3. Friction coefficients were selected based on values observed during the manufacturing trials. Lee et al. (2018) found a direct relationship between friction and the time required to fracture. Friction was seen to significantly increase the tensile stress in the blank in the curved section of the form. Thus, Lee et al. (2018) concluded that “increased friction leads to more rapid specimen failure during flexible forming”. Arguably, this finding of Lee et al. (2018) contradicts the findings of Dirikolu and Akdemir (2004).

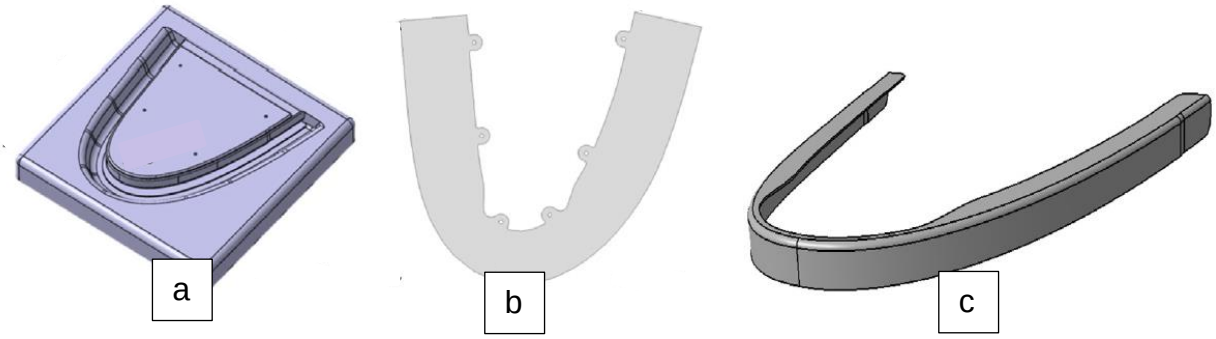

Figure 2.15: (a) Forming die for rubber-diaphragm forming; (b) schematic of the blank sheet; (c) final aircraft component (Lee et al. 2018)

The Păunoiu et al. (2019) study used a friction coefficient of 0.1 for the metal-to-metal interface, and 0.15 for the rubber-to-metal interface based on literature. Hyperelastic rubber elements were modelled. The Muñoz-Rubio et al. (2019) was a pure simulation-based optimisation study which aimed to provide a validated solution to form aluminium alloy AA2024-T3 temper condition. The objective of the study was to provide optimal forming parameters. The optimal friction coefficients predicted to ensure the manufacture of the component for the pressure load of 60 MPa was 0.1 for the metal-to-metal interface and 0.5 for the metal-to-rubber interface. Figure 2.16 illustrates the shape of the component investigated in the Muñoz-Rubio et al. (2019) study. The width of the curved section of the component is 25 mm. The Păunoiu et al. (2019) and Muñoz-Rubio et al. (2019) studies are unlike the other studies as the components are drawn and not flanged.

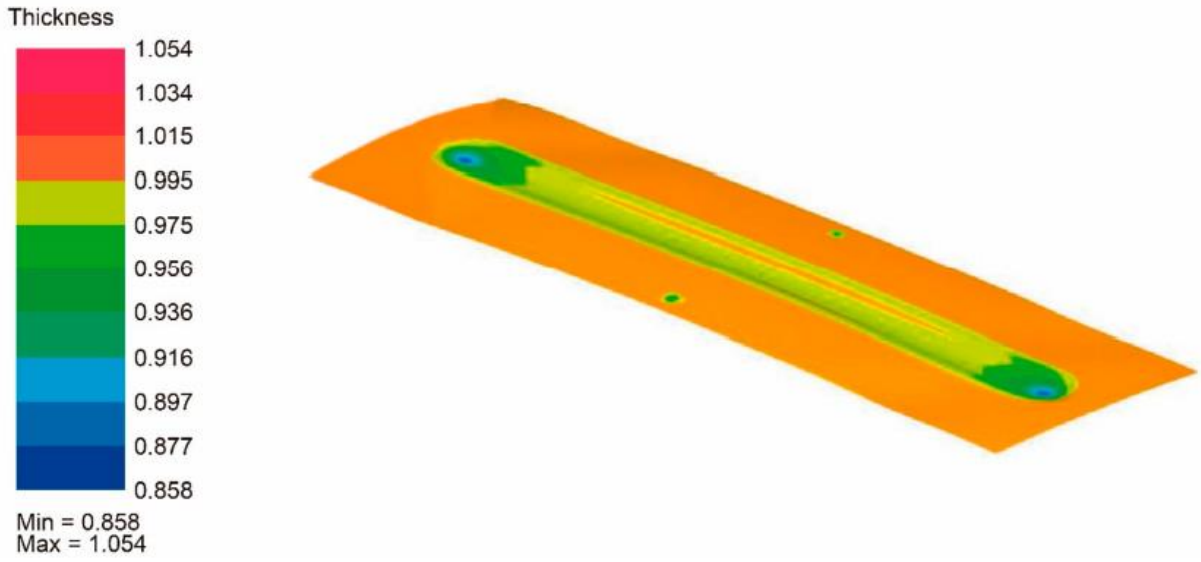

Figure 2.16: Simulation of the minimum thickness t_{min} (mm) in the stamping area (Muñoz-Rubio et al. 2019)

Zhang et al. (2019) investigated a method to design die profiles to manufacture complex curved flanged components. The material selected for the study was aluminium alloy AA2024-W temper condition. The rubber throw pad and diaphragm were modelled using the Mooney – Rivlin hyperelastic material law. The friction coefficients used were 0.3 for the metal-to-metal interface, and 0.15 for the rubber-to-metal interface. The friction coefficients were based on results from a previous study which provided no evidence as to where the coefficients were sourced.

The several studies presented have shown fairly low values for the rubber-to-metal friction coefficient were used. Majority of the components in the respective studies were straight and curved edge flanged components. The friction coefficients for those studies were lower than 0.3 with Hatipoğlu et al. (2007) the only authors that made use of a high friction coefficient of 0.9 for the rubber-to-metal interface. The Muñoz-Rubio et al. (2019) and Păunoiu et al. (2019) studies were the only deep-drawn type components studied. Muñoz-Rubio et al. (2019) conducted a theoretical study and showed the optimum friction for the component to meet the nominal design surface profile was 0.5.

Considering the lack in clarity around the friction coefficients employed by researchers in die sheet hydroforming, the study of Gómez et al. (2013) was reviewed as it investigated the effects of dry interfaces, water, oil, and wear debris on the friction coefficient of rubber against steel. The two configurations of interest from the study are the dry and lubricated conditions. The rubber throw pads are typically covered with talcum powder to reduce the friction between the rubber-to-metal interface and not a typically lubricated. The Gómez et al. (2013) study found for the dry condition that the friction varied widely between 0.6 and 1.2. In contrast, the oiled condition which gave friction coefficients below 0.2. Based on the Gómez et al. (2013) findings, the throw pads in die sheet hydroforming would experience high friction compared to the low 0.2 friction coefficients of lubricated interfaces.

To summarise, the influence of friction on straight and curved edge flanged components was not significant. Where there was a flat surface area, like the component in the Muñoz-Rubio et al. (2019) study, the influence rubber had on the formed component was evident. Friction has a significant influence on the stress and strain distribution of a component, but not the forming limit strain. Where panel type structures are concerned, friction plays a significant role (Kumar et al. 2014).

2.3. Finite Element (FE) Simulation

2.3.1. Commercial Forming Simulation Software Packages

The maturity of finite element (FE) code to perform forming manufacturing operations, and provide the ability to predict and optimise a blank and tool concept substantially reduces time and material wastage inherent in the conventional “trial-and-error” process which can be an expensive concept study (Yershov et al. 2012). Forming simulation tools have been adopted by the automotive industry extensively and are becoming a common practice in industry (Frącz et al. 2013).

The most significant advantage of a simulation study was cost-benefits. Yershov et al. (2012) highlighted “the ability to significantly conserve material by reducing wastage, shortened the time required for component finishing and lowered labour costs”. Yershov et al. (2012) showed no evidence of how the actual component compared to the simulation result, but the publication provides a detailed procedure of how a PAM-STAMP simulation and optimisation study was set-up.

Several commercial FEM simulation packages are available with only a few dedicated to manufacturing. The list below provides an overview of the FEM codes used by various authors over the last two decades to investigate stamping and all types of sheet hydroforming:

- ABAQUS: Hosseinzade et al. (2009), Ziaeipoor et al. (2014), Bagherzadeh et al. (2015), Lee et al. (2018), Păunoiu et al. (2019).
- ANSYS: Dirikolu and Akdemir (2004).
- AUTOFORM: Leacock et al. (2016), Carlsson and Vrijhof (2018).
- DYNAFORM: Lang et al. (2012), Frącz et al. (2013).
- LS-DYNA: Lang et al. (2004), Lang et al. (2005), Lang et al. (2008), Abedrabbo et al. (2005), Hatipoğlu et al.(2007).
- MSC MARC: Samuel (2004), Hatipoğlu et al.(2007), Baosheng et al. (2012).
- STAMP3D: Hama et al. (2007).
- PAM-STAMP: Ahmetoglu et al. (2004), Lee and Chun (2005), Chen et al. (2014), Chen et al. (2015), Zhang et al. (2019), Muñoz-Rubio et al. (2019).

The packages not listed above are ALTAIR HYPERFORM, Simufact Forming (Part of the Hexagon group), and Hexagon Forming Technologies (FTI). These packages do not accommodate sheet metal hydroforming as they focus on stamping and forging. (Altair Hyperform™, 2020), (Hexagon Forming Technologies, 2020), (Hexagon Simufact Forming, 2020).

2.3.2. Simulation Fundamentals and Element Types

All of the above simulation packages made use of either the explicit and implicit algorithm solving techniques. Non-linearity in structural mechanics was characterised into three types (Cook et al. 2002):

- Material non-linearity where the material property was a function of the state of stress or strain.
- Contact non-linearity where the gap between adjacent components may open or close, the contact area between parts changes as the contact forces change, or there was sliding contact with frictional forces.
- Geometrical nonlinearity where deformations were large enough such that equilibrium equations written with respect to the deformed structural geometry. Also, in terms of loading, which may change direction such as the case where pressure inflates a membrane.

A linear solution simply made use of hook's law where:

$$KX = F \quad (2)$$

K is the stiffness matrix the system [N/mm]

X is the displacement matrix of the system [mm]

F is the force matrix of the system [N]

Typically, applied external forces were the knowns, and the displacement and internal forces of the system were determined by solving the inverse stiffness or compliance matrix [K^{-1}]. A linear analysis was typically not time-dependant, except when considering a thermal or thermal-mechanical analysis which may be both time and temperature-dependant (Cook et al. 2002).

Non-linear systems that fall into any or all of the three types listed above made use of the complete equation of motion, which was also a time-dependent analysis.

$$M\ddot{X} + D\ddot{X} + KX = F(t) \quad (3)$$

K is the stiffness matrix the system [N/mm]

X is the displacement matrix of the system [mm]

$\dot{X}$ is the velocity matrix of the system [mm/s]

$\ddot{X}$ is the acceleration matrix of the system [mm/s²]

F is the force matrix of the system [N]

Depending on the problem to be solved, stamping or a springback, an explicit or implicit analysis was used. For an explicit solution, the system was assumed to have no damping with structure expected to undergo large displacements or loading over a defined time frame. The nodal velocities determined by the known acceleration and displacement. At time t_0 the displacement is known, and from the reduced equation of motion formula, the acceleration is computed from the internal and external forces. The explicit algorithm searches for the nodal velocity and displacement for the next time increment t_1. The time step (Δt), which is the difference between t_1 and t_0, is kept small to ensure the stability of the computation, accuracy and convergence (ESI Group, 2018).

In an implicit analysis, the simulation was assumed to be static using an incremental method based on loading or kinematics. Dynamic effects were neglected, and thus, the velocity and accelerations set to zero. Unlike the explicit method, when an applied load was prescribed, the nodal displacement cannot be solved explicitly (Cook et al. 2002). The solver computed the solution using linear iterations known as Newton-Raphson iterations with a defined convergence criterion. The tangent stiffness was computed and defined as the change in load with respect to the change in displacement (ESI Group, 2018). The slope of the force (P) versus displacement (u) plot, which was not known at the outset of the analysis, is shown in Figure 2.17 (a). The modified Newton-Raphson method, depicted in Figure 2.17 (b), made use of the same tangent stiffness instead of updating computing a new stiffness in each iteration. Figure 2.17 illustrates softening curves. Whereas, a hardening curve slopes upwards.

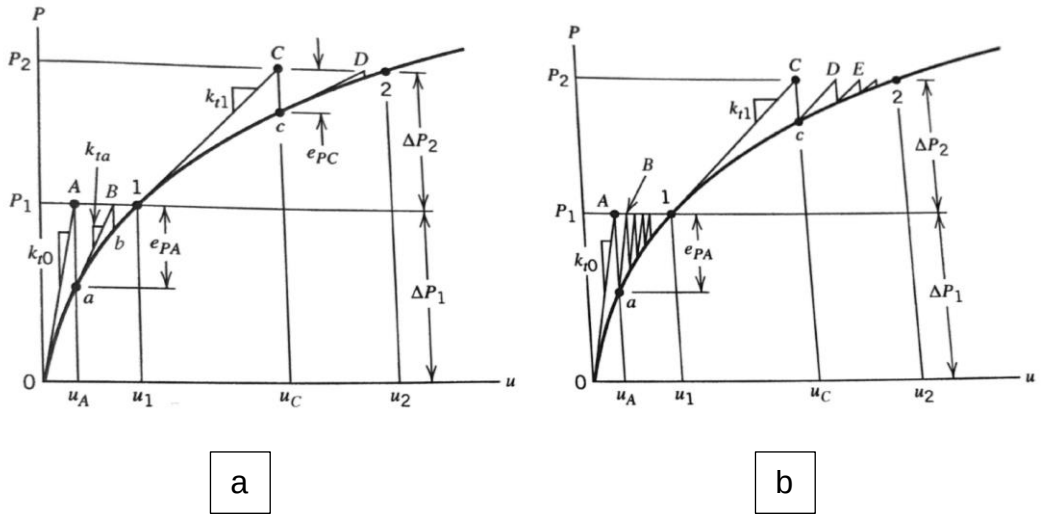

Figure 2.17: Iterations to convergence at each load level P_1 and P_2. (a) Newton-Raphson iterations (b) Modified Newton-Raphson iterations (Cook et al. 2002)

A single matrix inversion may take several seconds or minutes to compute. Large finite element models may take a few hours to invert the stiffness matrix. In a non-linear simulation, multiple matrix inversions must be computed, resulting in several hours or days required to reach a converged solution. Several methods were available to compute the matrix inversion, namely the direct, preconditioned conjugate gradient (PCG), iterative, MUltifrontal Massively Parallel sparse (MUMPS) Direct, and MUMPS Direct Out of Core methods. MUMPS direct is the ESI direct solver and thus the default solution.

Two typical convergence criteria are force and displacement. It was difficult to satisfy the force convergence criterion because of local force imbalances, but have little effect on the overall structural behaviour (Cook et al. 2002). PAM-STAMP made use of the displacement and energy convergence criterion. For displacement, the default convergence tolerance was 0.01 for springback and 0.1 for gravity. The energy convergence tolerance was 0.01 for springback.

Typically, finite elements used for a forming simulation analysis were shell type elements. Rigid body solid elements are used for tooling bodies. Whereas, the blank was modelled using deformable elasto-plastic shell elements. Both triangular 3-node and quadrilateral 4-node elements were used with the 4-node element type the dominant as it had bi-linear interpolation polynomial and shell hourglass control compared to the 3-node only having one-degree interpolation polynomial. For through-thickness stress distribution that resulted from plasticization, PAM-STAMP made use of the gauss rule and five integration points. The greater the number of integration points, the more CPU time required to compute a solution. The gauss rule weights the distribution of the integration points to improve result quality as opposed to a uniform distribution. In terms of shell element types, several are available, but the default used in PAM-STAMP was Belytschko-Tsay. Belytschko-Tsay elements are simple and efficient and were based on the concept of uniform reduced integration. For shock and vibration-based analysis, the Hughes-Tezduyar element type was proposed. Also, when excessive hourglassing was observed. Hourglassing was rarely witnessed and resulted in the degeneration of the mesh, as shown in Figure 2.18. Hourglassing was controlled by three options, the elastic modulus, the plastic modulus, and viscosity. Elastic and plastic modulus were based on the selected material. For viscosity, the anti-hourglass stresses were determined proportionally to the generalised strain velocities and did not have cumulated effects as in the stiffness formulation. The elastic modulus is the default setting for hourglass control (ESI Group, 2018).

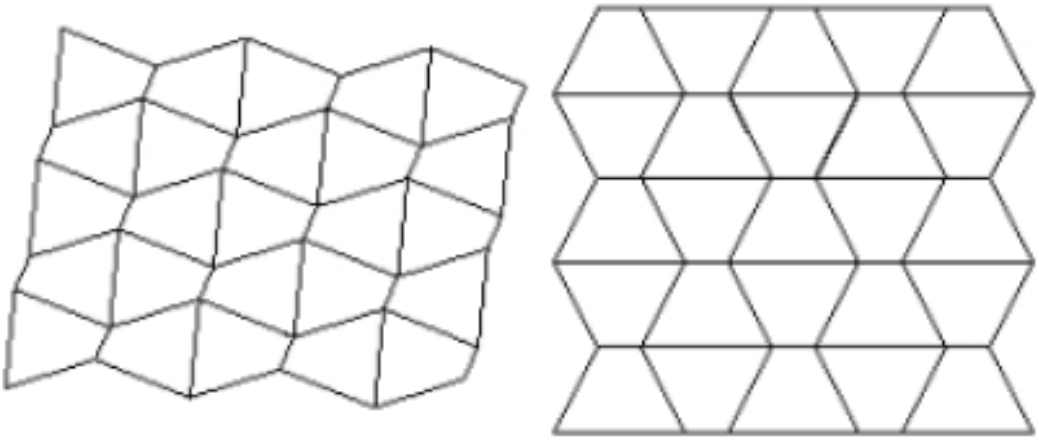

Figure 2.18: Element hourglassing effect

The Belytschko-Wong-Chiang element type was based on a better kinematic field with the shear strains calculated by nodal projection. The projection allows for a six degree of freedom shell element useful in warped configurations. In the case where an advanced implicit computation was selected, the Batoz Q4 gamma element was used. The element improves the accuracy of warping cases. Four integration points were required providing greater accuracy but came with a higher CPU time cost (ESI Group, 2018).

FE simulation made use of Coulomb's law to mathematically describe the physics of friction. In PAM-STAMP, when an element from a solid body, such as the tooling, applied a normal force to a node on the deformable sheet metal blank, a tangential force opposite to the direction of sliding resulted. This tangential force was friction, described by the friction coefficient (μ) multiplied by the normal force (N) (ESI Group, 2018).

The ESI Group (2018) examples of coulomb's friction coefficients are:

1. 0.05 was defined as excellent sliding.
2. 0.1 to 0.15 was conventional values, with 0.15 for accurate contact and 0.15 for penalty contact.
3. 0.2 was defined as rough surface contact.

2.3.3. Forming Simulation Modelling

ESI Group (2018) described tooling surfaces as accurate contact with a lower friction coefficient typically used. A definition for a rubber tool surface was not provided. Within the several options to define friction, a user-defined friction subroutine may be used to define a specific friction behaviour.

The six options are (ESI Group, 2018):

1. Constant: Single value
2. Function of pressure
3. Function of velocity
4. Function of pressure and velocity
5. Function of pressure, velocity and temperature
6. User-defined

Any forming manufacturing process is described as stages or operations, not including other processes like joining and painting. The Yershov et al. (2012) study conducted a stamp forming simulation in PAM-STAMP to manufacture a tray. Five stages were defined: clamping, stamping, loading removal and springback, a second stamping pass, and final springback.

In the case of the fluid cell forming process, a standard macro was available. Although, the macro available as a standard module to set-up a hydroforming manufacturing stage was based on the more widely used tube and punch hydroforming processes. Sheet hydroforming process steps were hydroforming, springback, and trimming. Additional stages are added depending on the number of tooling stages.

PAM-STAMP has predefined forming stages that are assigned using macros. Process macros enable the software to automatically create stages that during the data set-up of a standard simulation, allowing for efficiency and improved productivity. Non-standard and new processes will require development and validation before adoption. Through extensive literature research, the most widely studied die sheet hydroforming process was related to tube and punch hydroforming and not die hydroforming. The punch was modelled as a solid body, whereas the fluid represented the punch in die sheet hydroforming. The die sheet hydroforming process made use of silicon rubber throw pads and a diaphragm to contain the fluid. The recommended PAM-STAMP procedure to conduct a fluid cell forming simulation does not allow for automatic set-up of the rubber elements and application of the defined pressure load of the fluid on these elements. Pressure can only be applied to hyperelastic elements as a constant (ESI Group. 2018).

A punch sheet hydroforming process is the inverse of a die sheet hydroforming process. The rubber membrane contains the fluid when the punch is below the blank and the fluid above. In the case where the fluid is below the punch, literature has shown a rubber diaphragm is not used to contain the fluid. The punch above the fluid configuration was seen to be the most common and was the most commonly researched sheet hydroforming process compared to die sheet hydroforming. The punch was forced into the fluid, whereas the fluid moves around the die tool in die sheet hydroforming. In punch sheet hydroforming, the rubber diaphragm and the friction between the rubber-to-metal interface was not a concern (Zhang et al. 2003), (Ahmetoglu et al. 2004), (Lang et

al. 2004), (Lang et al. 2005), (Lee and Chun (2005), (Abedrabbo et al. 2005), (Hama et al. 2007), (Lang et al. 2008), (Hosseinzade et al. 2009), (Baosheng et al. 2012), (Lang et al. 2012), (ZiaeiPoor et al. 2014), (Bagherzadeh et al. 2015). Arguably, this is the reasoning for its lack of development and maturity in the simulation of sheet hydroforming.

Dirikolu and Akdemir (2004) investigated the computer-aided modelling of a flexible forming process using ANSYS but was not related to die sheet hydroforming and was a rubber forming process as discussed previously. Dirikolu and Akdemir (2004) modelled hyperelastic solid elements that made use of the Mooney-Rivlin material law to represent the material properties of rubber mathematically. The Mooney-Rivlin material law is the standard hyperelastic material used in most FE simulations. Hyperelasticity is based on a strain energy density, whose derivative with respect to strain determines the 2nd Piola-Kirchhoff stress tensor. The strain energy density is dependant on two material parameters that determine the material response. The two parameters are determined through experimental testing (Dirikolu and Akdemir 2004) (ESI Group. 2018). The Dirikolu and Akdemir (2004) study found that a variation in the rubber hardness had no impact on forming stresses predicted in the blank.

The Hatipoğlu et al. (2007) study was one of the first die sheet hydroforming investigations. Two simulation packages were used, LS-DYNA and MSC MARC. Solid hyperplastic elements were modelled to represent the diaphragm, along with the blank and a solid body die. The modelling definition from the Hatipoğlu et al. (2007) study is shown in Figure 2.19. An implicit solution was used for the loading, and an explicit solution for the unloading as implicit solution did not converge correctly for the unloading stage. Hatipoğlu et al. (2007) made use of 2D shell elements to model the blank and rubber diaphragm. 3D solid elements were not used as the author found the computation time for the simulation to solve was extensive and could not be used with hardware available at the time. The author also made used of symmetry to halve the size of the model, which saves on computation time. The material used in the study was AA2024-T3 clad sheet in three thicknesses, 1.0, 1.6, and 2.0 mm. The Ludwick Equation represented the flow curve for the sheet metal.

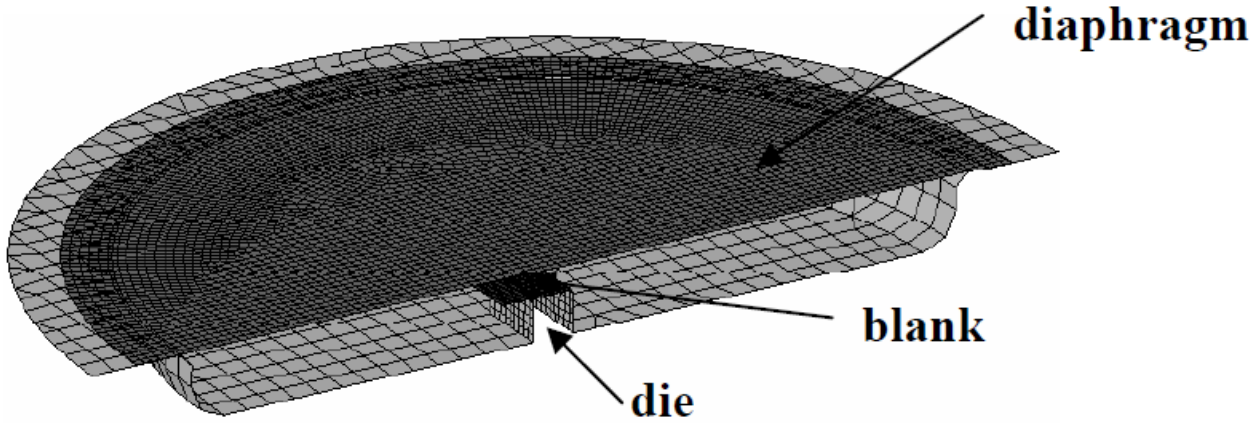

Figure 2.19: Bodies in the finite element model (Hatipoğlu et al. 2007)

Chen et al. (2014) and Chen et al. (2015) conducted a study investigating the springback of flanged straight and curved edged components, respectively. PAM-STAMP was used in both studies. The simulation model for the Chen et al. (2014) study, with and without the diaphragm rubber, is depicted in Figure 2.20 (a) and (b), respectively. Chen et al. (2015) studied the formability of three aluminium alloys, AA2024-O, AA7075-O and AA2024-T3, all 1.0 mm in thickness. Chen et al. (2015) found that the -O temper condition materials had fewer wrinkles compared to AA2024-T3 temper condition.

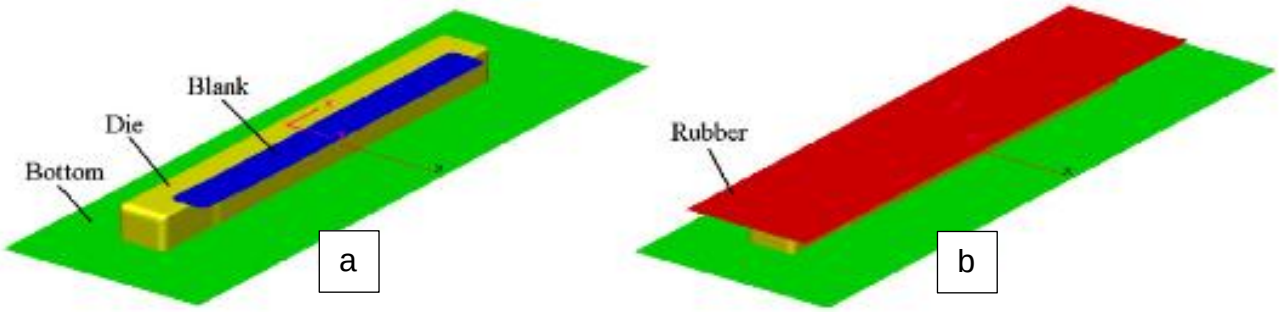

Figure 2.20: Simulation model. (a) Without rubber and (b) with rubber (Chen et al. 2014)

Chen et al. (2014) noted the importance of mesh size, where the size of the sheet metal blank elements had a direct influence on the stress field after forming, especially concerning the sheet contacting the fillets and radii of the tool. Chen et al. (2014) ensured the simulation maintained a 5:1 element size ratio, which was at least 5-7 elements in the blank across the radius of the tool edge. The radius of the tool was 3 mm. Thus the minimum blank element size was 0.5 mm. This is an important modelling rule that must be used to ensure good result resolution. The blank was modelled using 2D shell elements. Typically, the bottom and tool are also modelled using 2D shell elements as rigid bodies. The author provided no detail of the element type used for the rubber except the Mooney-Rivlin material law was utilised. From Figure 2.20 B, it appears 2D shell elements were used to represent the rubber throw pads. The Barlat 89 plasticity yield criterion law was used for the sheet metal blank. The authors did not specify the flow stress hardening law. However, the material properties presented indicated the Krupkowsky Law was implemented.

Leacock et al. (2016) conducted an industrial study on the formability of a complex shaped aircraft frame component manufacture in AA7075-O, that was heat solution treated and naturally aged 30 minutes before forming. Thus, the component was formed in the -W temper condition. The study was conducted in AUTOFORM. The material laws used for the sheet metal blank were BBC2005 yield criterion law and Hockett-Sherby (Krupkowsky) isotropic hardening law.

Rubber was not modelled as the purpose was to present a methodology for die sheet hydroforming of an aerospace frame component without the computational cost and complexity of including rubber. Pressure loading was applied directly to the sheet metal blank and was justified on the basis that the rubber applied a hydrostatic pressure loading. As the bladder was not modelled, the friction condition of the rubber-to-metal interface was not incorporated. The authors only state that a friction coefficient of 0.15 was applied.

Leacock et al. (2016) found that it was possible to accurately model die sheet hydroforming without modelling the rubber provided an accurate material characterisation and the use of anisotropic material laws. In addition, the author noted the use of through-thickness stresses at the bend radius, which is zero for the in-plane stress assumption, improved the predicted springback. Leacock et al. (2016) findings are contradictory to Solfronk et al. (2016). Leacock et al. (2016) had made use of an isotropic hardening law and stated it was acceptable in predicting the springback, whereas as Solfronk et al. (2016) deemed the kinematic hardening law an essential in predicting accurate springback.

Lee et al. (2018) made use of ABAQUS/Explicit version 6.12 simulation software package to investigate plastic deformation and failure in aluminium alloy AA2024-O temper condition, 1.0 mm in thickness. Two rubber pads were simulated as solid 3D elements, as shown in Figure 2.21.

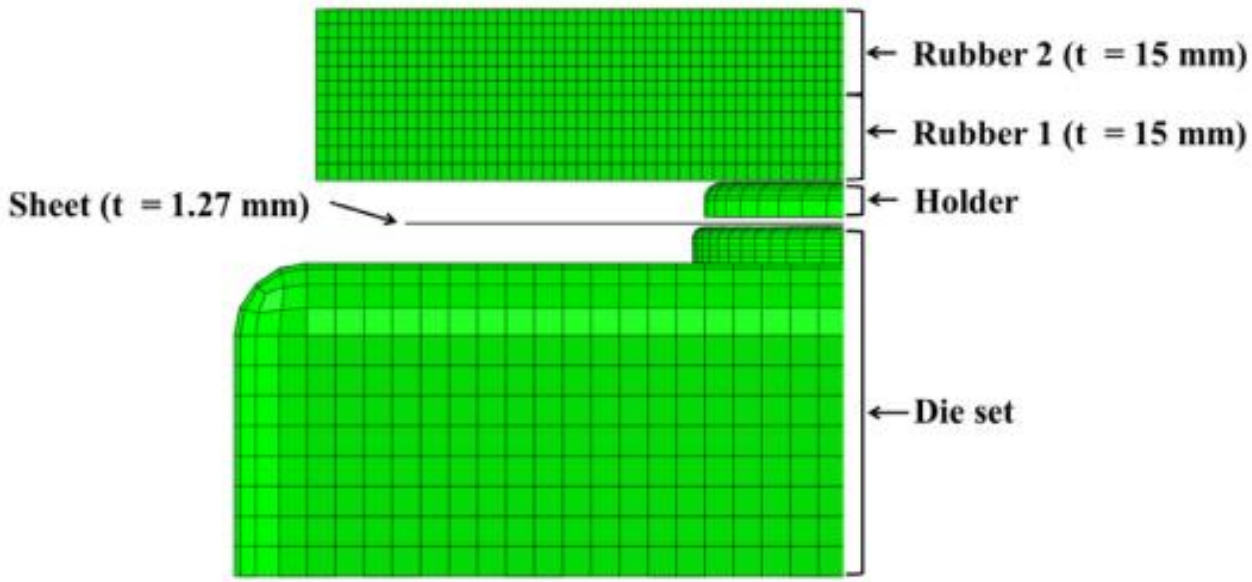

Figure 2.21: FE model for rubber-diaphragm forming (Lee et al. 2018)

The rubber elements were modelled using solid 3D continuum elements (C3D8R) and made use of the Mooney-Rivlin material law for the rubber. A uniform pressure for the duration of the forming cycle was applied to rubber 2's elements.

The sheet metal blank was modelled using 2D shell elements. The material laws used in the Lee et al. (2018) study was Hill 48 and the Swift (Krupkowsky) isotropic hardening law. Given the year the study was conducted, the author should have made use of more advanced material laws.

Although Lee et al. (2018) used dated and inaccurate material laws for plasticity and hardening, a ductile fracture model was used to model the fracture of the component. The Lee et al. (2018) study made use of in-situ trimming features, to shear off the excess material to final form during the manufacturing process. The ductile fracture model was used to predict the trimming stage of the forming process without a trimming operation.

The purpose of the Carlsson and Vrijhof (2018) demonstration was to show a correlation between die sheet hydroforming and simulation for ultra-high-strength steels and other difficult materials. The authors made use of AUTOFORM. The rubber pads and diaphragm were not modelled. The basis for not modelling the rubber was the low stiffness of the rubber diaphragm compared to the sheet metal. The material laws and friction coefficients used in the study were not published. However, the authors stated, "there was a close correlation between experimental and simulated values when the pressure-dependent friction model was used". Figure 2.22 depicts the sizable complex shaped component of the Carlsson and Vrijhof (2018) study. A simulation model set-up was not provided. The sheet dimensions for the experiments were 140x620mm².

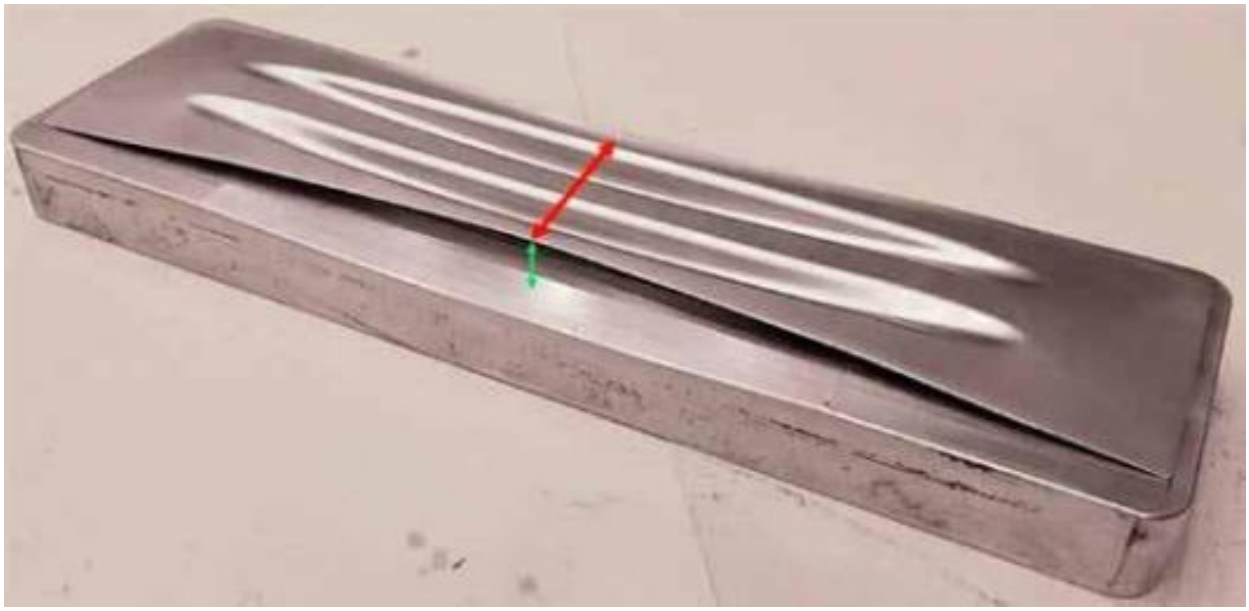

Figure 2.22: Flexformed beam on the tool. Red = minimum waist width, green = springback from the tool (Carlsson and Vrijhof. 2018)

Păunoiu et al. (2019) investigated a 160 mm diameter dome structured component, as shown in Figure 2.23. The components were simulated in the ABAQUS simulation software package. The grade of aluminium alloy used for the study was not stipulated. The authors found inaccuracies in the hyperelastic modelling of the rubber, with simulation results not matching what was experienced during press trials. Certain components fractured and were associated to the low formability of the aluminium alloy (Păunoiu et al. 2019).

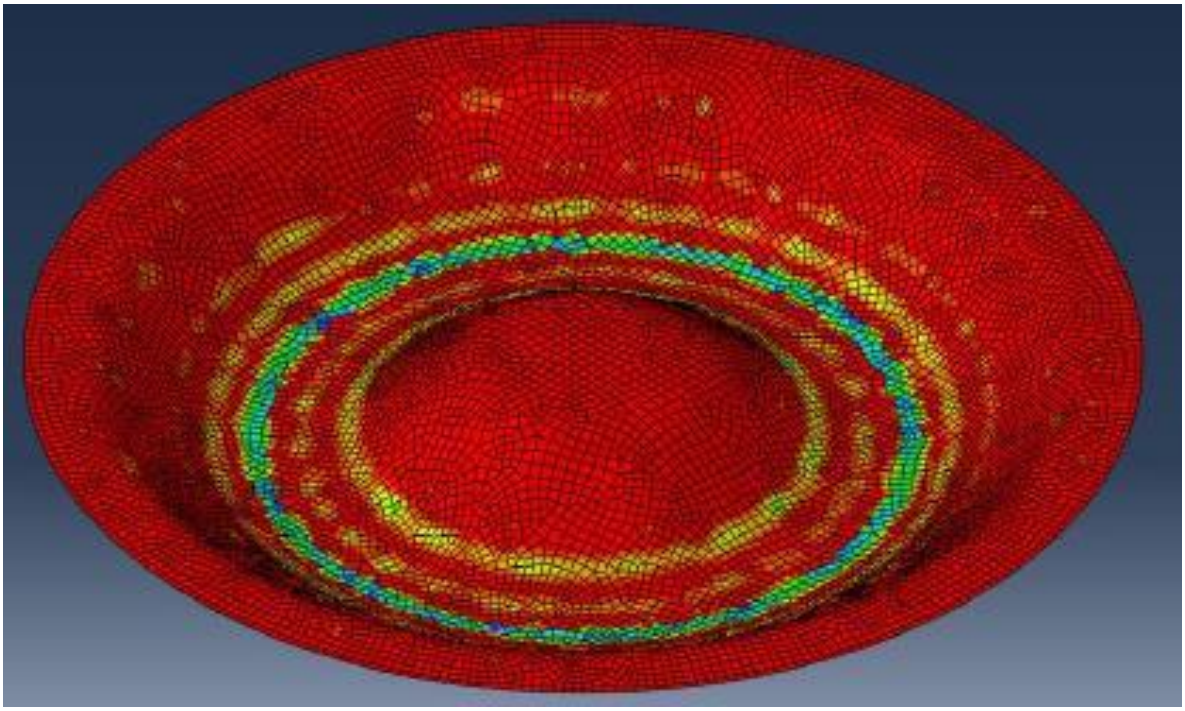

Figure 2.23: Complex auto body part (Păunoiu et al. 2019)

The Muñoz-Rubio et al. (2019) study was conducted in PAM-STAMP. Hyperelastic solid elements were modelled to include the rubber throw pads and diaphragm. The optimal friction coefficients were predicted through a design of experiments (DOE) approach. Thus, parameters were altered until the component was the same as the nominal sensing surface. The material properties used were Hill 48 and an isotropic hardening laws. For the hypothetical study, the material properties were acceptable to validate the Taguchi's Robust Design Method (a multi-objective optimisation algorithm). A forming limit curve was also created for the purposed of assessing the components, but no FLD results were published. Shell elements were used to model the sheet, rubber diaphragm, and the die. The material properties for the hardening law (K, n, E) were altered along with the rubber-to-metal and metal-to-metal friction coefficients. Arguably, the alteration of the material properties should have remained fixed as these were based on tests. Varying the friction properties was a sensible approach.

The component (a) and simulation set-up (b) from the Zhang et al. (2019) study are depicted in Figure 2.24. Similar to the previous studies, a curved edge flanged component was manufactured by die sheet hydroforming. The authors made use of CATIA V5 and PAM-STAMP to design and simulated the blank and tooling, respectively. The die and station surfaces were meshed with 2D shell elements, 0.5 mm in size. 0.1 mm 2D shell elements were used for the blank and rubber. The corner radius of the component was 3 mm. Zhang et al. (2019) maintained a 6:1 radius to element length ratio. Unlike the findings of previous authors, Zhang et al. (2019) denoted that the increase in pressure had little effect on the springback. Zhang et al. (2019) compensated the tool design, which resulted in low springback results.

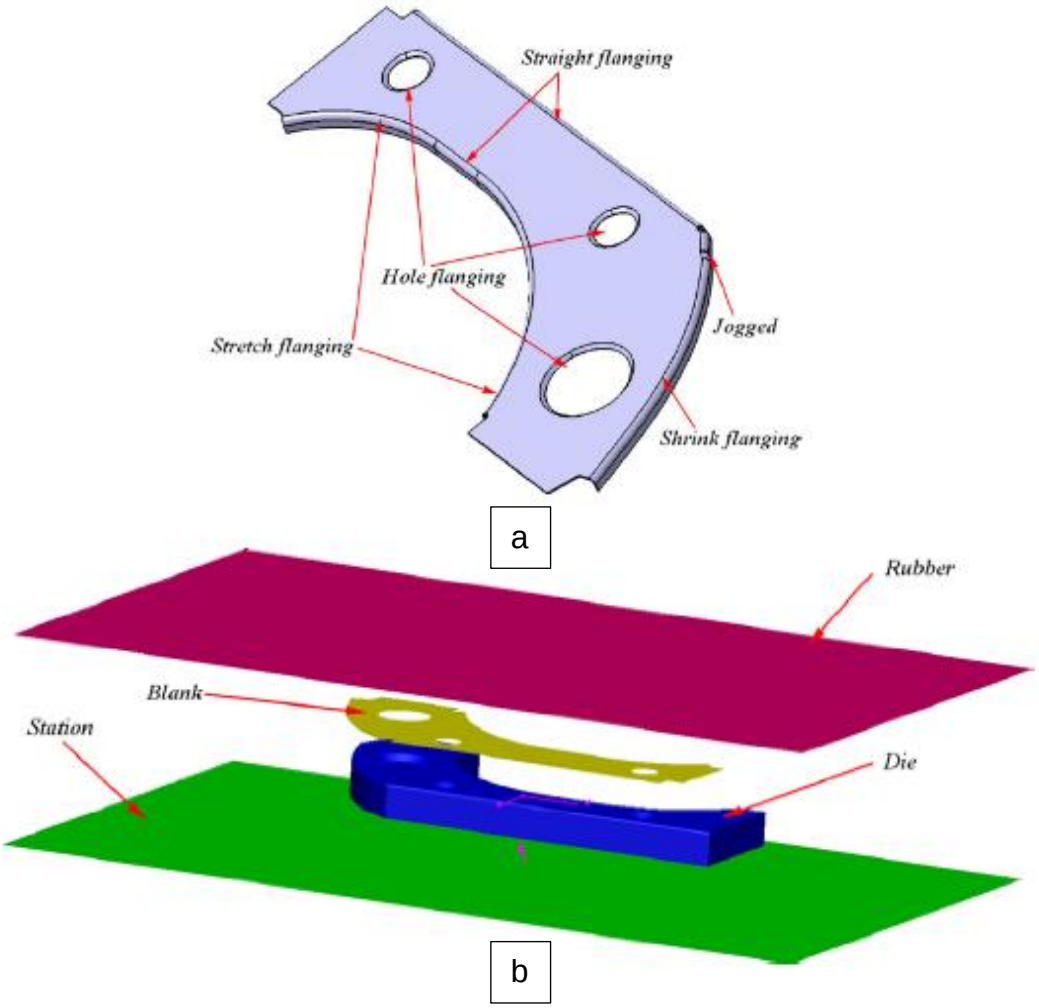

Figure 2.24: (a) Curved flanged part, (b) Simulation Model (Zhang et al. 2019)

Of all the studies in die sheet hydroforming, the following authors included rubber: Kang et al. (2004), Hatipoğlu et al. (2007), Chen et al. (2014), Chen et al. (2015), Lee et al. (2018), Păunoiu et al. (2019), Muñoz-Rubio et al. (2019), Zhang et al. (2019). Including rubber not only required additional testing to determine the material properties and friction coefficients (if tests were conducted), but the solid 3D elements are computationally expensive and take time for the simulation to solve. Older studies showed problems due to the available hardware of the time but became less of an issue with fasters computers. Even so, the simulation of rubber hyperelastic elements does result in costly computation time.

The Leacock (2016) and Carlsson and Vrijhof (2018) studies did not incorporate rubber elements. The main benefit was reduced computation time as the pressure was applied directly to the blank. Characterisation of the rubber was not required, which was a saving to the project. The respective studies validated that rubber hyperelastic elements are not required for die sheet hydroforming simulation studies.

The components in all the studies were simple straight or curved edged components that were flanged compared to the geometries of Carlsson and Vrijhof (2018), Păunoiu et al. (2019) and Muñoz-Rubio et al. (2019) that were more complex shaped as they had compound curves. Flanging by sheet hydroforming on a fluid cell press is by far the most effective manufacturing method. Unlike stamped flanged components, which typically suffer large springback distortion as undercut tools cannot be accommodated. The components from the Carlsson and Vrijhof (2018), Păunoiu et al. (2019) and Muñoz-Rubio et al. (2019) studies were drawn into the die. It can be concluded that it is possible to simulate die sheet hydroforming without the need for a rubber diaphragm.

2.4. Metrology Inspection

Metrology is defined as the “study of measurement”, and inspection is defined as the “critical examination of a product to determine its conformance to applicable quality standards and specifications” McGraw-Hill (2003). Thus, metrology inspection is the practice of inspecting components at various stages of the manufacturing process to ensure it meets design requirements. Metrology inspection is conducted using two techniques which are defined as either contacting or non-contacting (Curtis & Farago, 2013).

Contact systems are coordinate measuring machines (CMM) which are characterised by a bridge structure that supports the vertically mounted arm-with-probe. The probe tip makes contact with the component’s surface and a measurement taken in terms of the coordinate measured and the difference with respect to the nominal coordinate (Curtis & Farago, 2013).

Non-contacting systems are optical measurement machines (OMM) such as laser scanners that capture the geometrical features of the object. Other optical equipment includes microscopes and optical measurement projectors. 3D scanners capture 1000’s of points on the surface of the component without making physical contact (Curtis & Farago, 2013).

CMM and OMM equipment are tools that are used to capture accurate measurements of the component. For formed components, the inspection strategy of either contacting, non-contact, or inspection fixtures may be employed. Inspection fixtures are typically utilised in serial production to validate on component level. In contrast, a detailed inspection is carried out for first article inspection of individual components or the final product assembly. Inspection fixtures validate the form of the component against a calibrated surface profile. The component must be clamped in the inspection tool with minimal force to validate the installation condition without excessive stresses imposed on the assembly. In addition, once clamped, a component is checked for any raised regions from the inspection tool interface. Simulation correlation using both the contacting and inspection fixture methods was explored. The use of non-contact inspection methods was introduced, and its

correlation with simulation results. In the following sections, an outline of contact and non-contact methods is provided.

2.4.1. Coordinate Measuring Machine (CMM)

There are several advantages of CMM (Metrology World, 2020) (Curtis & Farago, 2013) (Paulk et al. 1995):

1. Repeatability. Once a component has passed the first article inspection, the same program can be used again and again, which also lowers set-up time.
2. Time-saving. CMM can be done quickly, but only after the initial set-up is completed and measurement is automatically conducted for the same components.
3. Measurement Accuracy. The Alpha image is a gantry-style CMM has ultra-high accuracy of 0.1 µm given the size of the machine at 2500 x 8000 x 1500 mm^3. The maximum error in the full volume is 40 µm.
4. Reduced Operator Influence. As it is a computer-controlled machined, and as the program is created and used again, the possibility of operator error is reduced.
5. Managed. Detailed measures of the software process and product quality are collected. Both the software process and products are quantitatively understood and controlled.
6. Optimised. Continuous process improvement is enabled by quantitative feedback from the process and from piloting innovative ideas and technologies.

Disadvantages of CMM (Metrology World, 2020) (Curtis & Farago, 2013) (Paulk et al. 1995):

1. Cost of equipment. CMM equipment, whether it be portable or fixed, small or large scale, the machinery carries a high cost.
2. Less Portable. CMM is available in portable versions but is less accurate than a fixed set-up.
3. Unreachable surfaces. The probe cannot reach some surfaces or points. Thus, these items must be constructed.
4. Skilled programmers and operators. CMM can be complicated and requires skilled individuals to program the CMM operation and operators to conduct the assessment.

The studies of Leacock et al. (2016), Karaağaç (2016), Păunoiu et al. (2019), and Zhang et al. (2019) made use of CMM to assess the final form of the component. Leacock et al. (2016) measured the manufactured components using a Renishaw Cyclone touch-probe scanner whilst supported on a screw-jack fixture. The screw-jack fixture is shown in Figure 2.25.

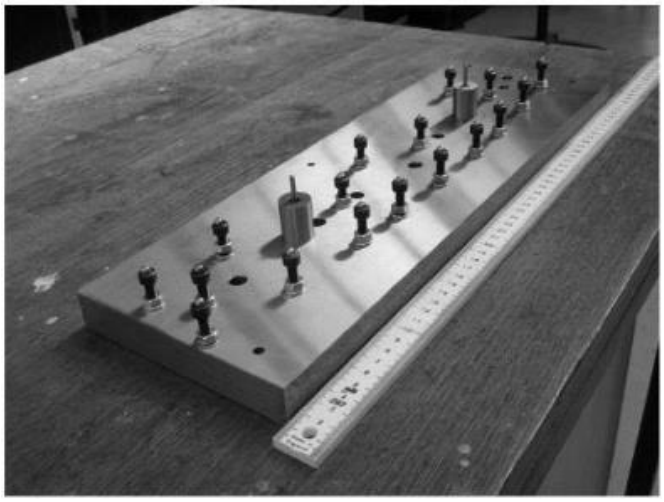

Figure 2.25: support fixture for measurement used in the validation study (Leacock et al. 2016)

The springback angle of the flange at several points along its edge was measured. The measured values were compared to the nominal desired component. In the Leacock et al. (2016) study, the measured deviation and simulation deviation are both presented, as shown in Figure 2.26, to illustrate the correlation between the results. As the author made use of CMM to inspect the component, a line graph was used to present the differences between the simulated and manufactured component. The comparison was stated to show a good correlation in the overall prediction of springback in the compression flange results (Leacock et al. 2016). The correlation assessment was the differences between the experimental line and the model line, as shown in Figure 2.26.

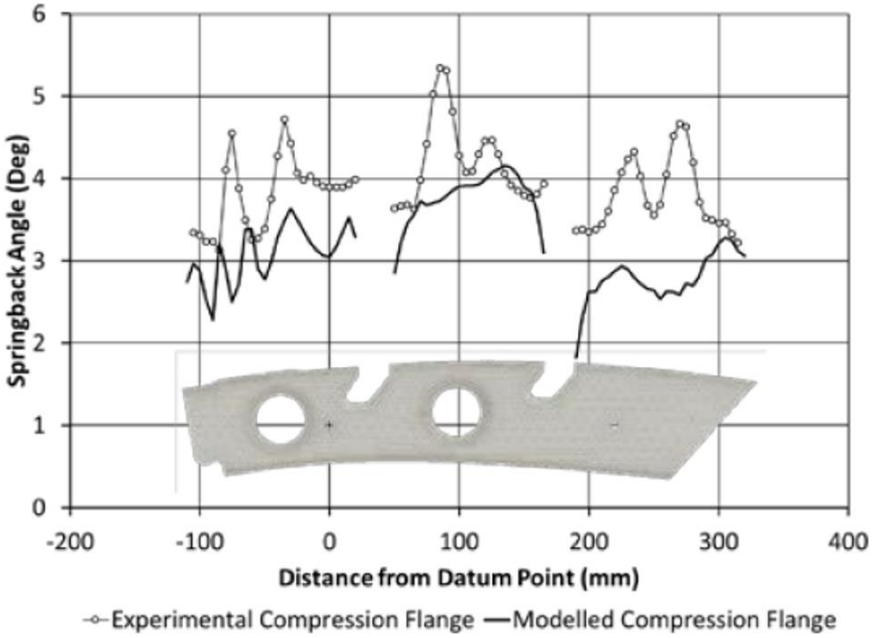

Figure 2.26: Springback angle for the compression flange (Leacock et al. 2016)

Karaağaç (2016) conducted a die and punch sheet hydroforming study on V-bend plates to investigate springback. The angle of the formed specimens was calculated using CMM, as shown in Figure 2.27.

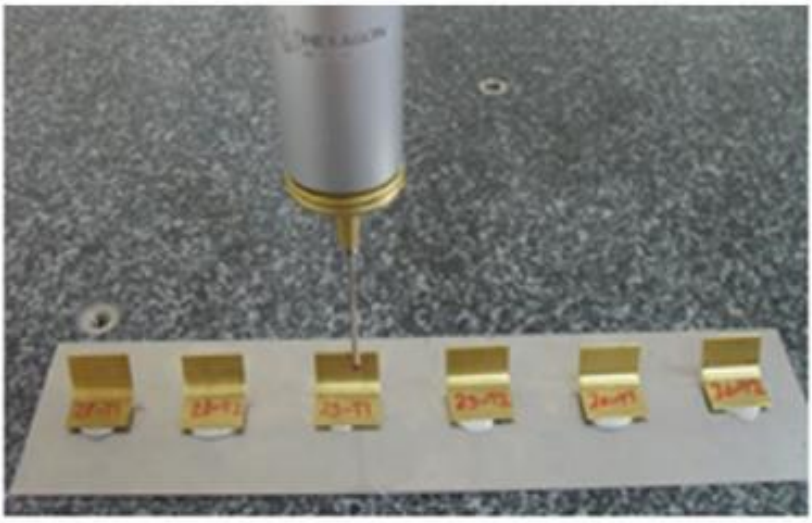

Figure 2.27: Measurement in the CMM (Karaağaç 2016)

A typical plot of the results from the Karaağaç (2016) study is depicted in Figure 2.28. The x-axis was the respective die angles while the y-axis plotted a single measured angle for various holding times. Similar to the Leacock et al. (2016) study, a line graph must be used to present the captured CMM results. Karaağaç (2016) did not conduct a simulation and used this presentation method to illustrate the difference between each die angle and the influence of how long the component is held under pressure during the forming process

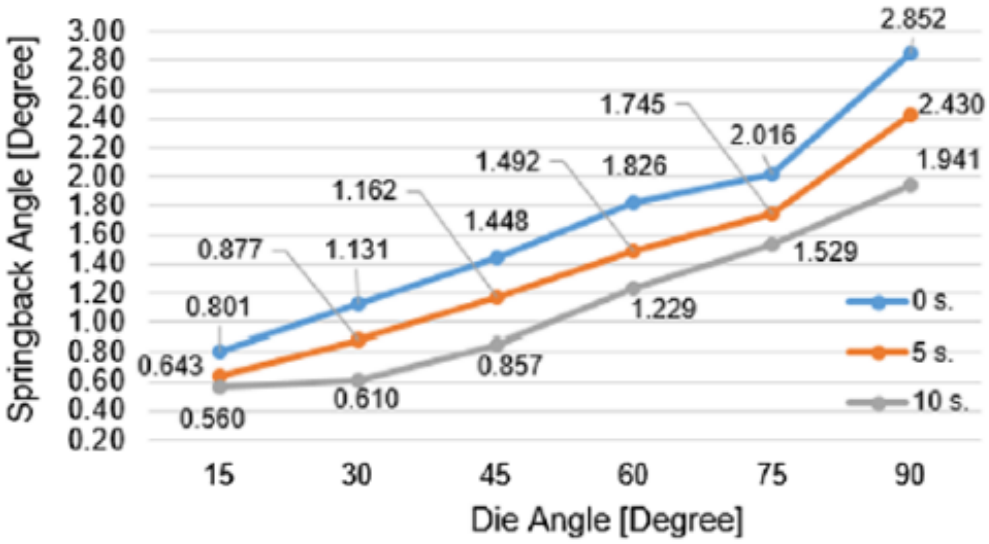

Figure 2.28: Measurement in the CMM (Karaağaç 2016)

The Păunoiu et al. (2019) component was more complex than those of Leacock et al. (2016) and Karaağaç (2016). Figure 2.29 depicts the CMM height gauge equipment measuring one of the die tools used to manufacture a component.

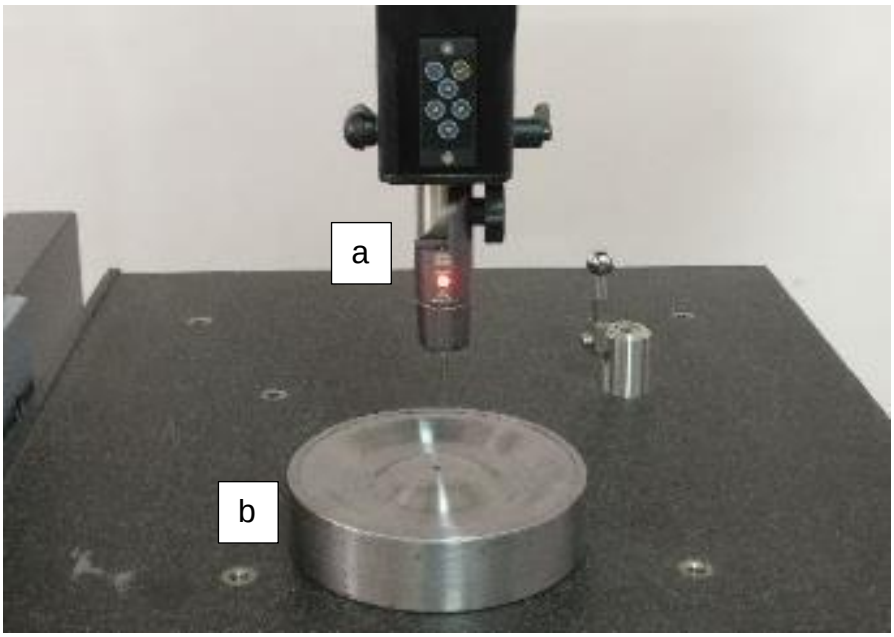

Figure 2.29: (a) Height gauge, Tesa Micro Hite 3D, (b) die tool (Păunoiu et al. 2019)

Păunoiu et al. (2019) first measured the dies to account for inaccuracies that may have resulted from the machining of the tools. Several points were measured to define a point cloud profile, which was then imported into ABAQUS, to manipulate the mesh surface. The components were then manufactured and measured using the same equipment. A comparison between the simulation results and the component was conducted. Figure 2.30 depicts the centre line measurement of the component, the die tool, and the difference between them. The diagram shows the deviation between the part and the desired nominal shape in the radius zones. Like the previous authors, Păunoiu et al. (2019) made use of a line graph to present the results.

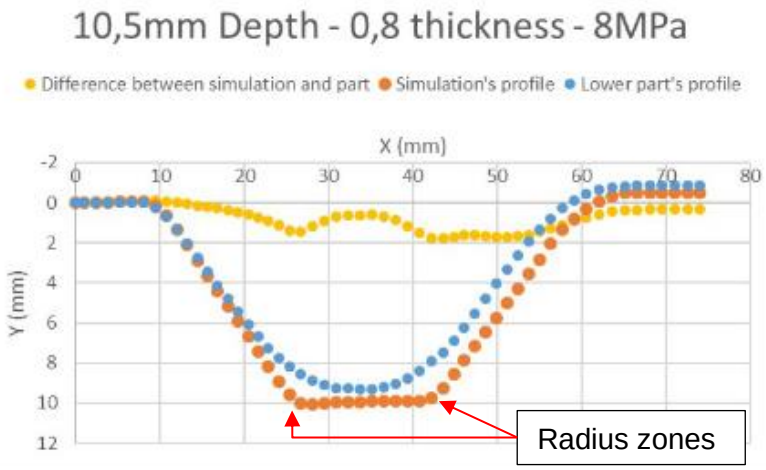

Figure 2.30: Comparison diagram between simulation and the part for 8 MPa pressure loading (Păunoiu et al. 2019)

The study conducted by Zhang et al. (2019) explores curved edge flanged components, similar to the component investigated by Leacock et al. (2016). Zhang et al. (2019) made use of CMM to inspect the manufactured components. Figure 2.31 depicts the results of Zhang et al. (2019), which showed the difference between the manufactured component's measurements and the same points taken from the simulation. Zhang et al. (2019) made use of a line graph plot to show the parts had conformed to the nominal design due to the correlation between the curves.

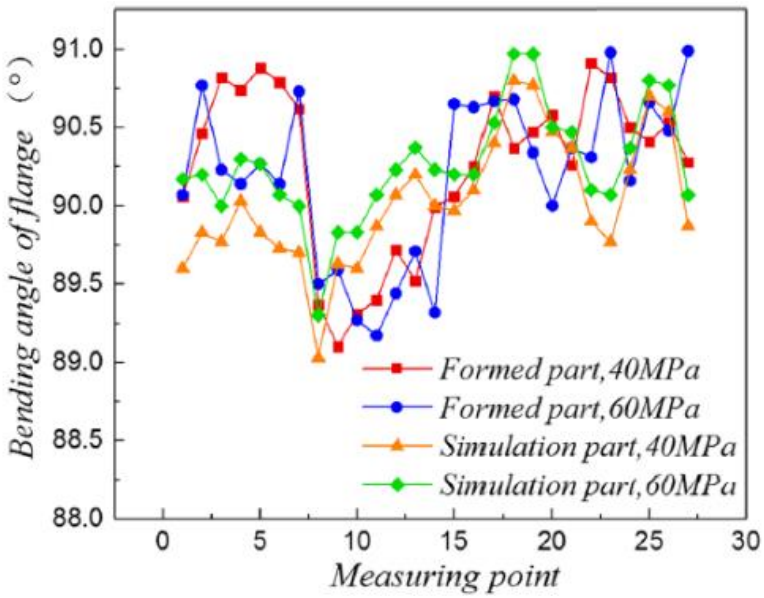

Figure 2.31: Manufacturing and simulation flange angle comparison (Zhang et al. 2019)

Leacock et al. (2016), Karaağaç (2016), Păunoiu et al. (2019), and Zhang et al. (2019) all used CMM to measure the performance of their respective components against the nominal design. CMM measures a single programmed point in 3D space. Multiple points were measured to provide more detail to perform calculations to determine a surface profile or edge curve. The authors have created plots of measured points versus flange bend angle or distance from a defined coordinate in a specific axis to provide comparison trends between what was predicted in the FEM and what was measured from the actual component. The closer the trends, the better the simulation was at predicting the final component. No statistical investigations were conducted to assess the similarity of the FEM and measured curves in any of the studies.

A downfall of using CMM is a large number of points are required to describe a surface or line accurately. The number of points required increases substantially with the complexity of the surface shape. Taking fewer points using CMM may result in missed detail.

2.4.2. Optical Measuring Machines (OMM)

There are several advantages of OMM (Kutz, M. 2013) (Metrology World, 2020):

1. High resolution. The latest developments in optical sensors have provided exceptional resolution capabilities.
2. High measurement accuracy. An improved resolution has resulted in high measurement accuracy. Laser scanners provide the best accuracy for measurement that competes with CMM systems.
3. High scanning speeds. Optical measurement machines outpace CMM measurement significantly.
4. Lower cost. Compared to CMM, 3D scanners are far cheaper and modular in size.
5. CAD model generation. Due to the level of detail captured by optical measurement systems, generation of 3D CAD models of the component can be created. This allows for the comparison of the scanned component with the nominal design.

Disadvantages of OMM (Metrology World, 2020) (Kutz, M. 2013):

1. Higher costs in computing power. OMM captures much more data than CMM. The high-resolution images and data points captured require powerful computers to handle the data and present to the user in a reasonable time. Such powerful machines are costly.
2. Large datasets. Depending on the scanning strategy and the size of the component, a large quantity of measurement data can be captured. The data must be processed (computer power) and storable.
3. Data capture can be compromised. Optical measurement is a non-contact system and thus realise on good reflection of the light source back into the optical sensor. Shiny surfaces are difficult to scan using white light or laser scanners without dulling the surface with talcum powder.

Optical measurement is beneficial when evaluating complex-shaped components and simulation result comparisons. Schneider el at. (2008) validated numerical forming manufacturing simulation results by optical measurement of the tools and component. Unlike CMM, optical measurement systems are capable of captured millions of points provided a significant amount of detail compared to CMM (Curtis & Farago, 2013).

Schneider el at. (2008) made use of the GOM 3D metrology optical measurement equipment and software, the ATOS camera system and the Argus software package. The GOM ATOS and ARGUS systems were used complete measurement of an existing tool. The aim of the study was not to validate a conceptualised tool but was conducted to showcase the capability of the GOM optical

measurement equipment. The GOM ARGUS software package was used to evaluate the formed component. The simulation of the forming process was conducted, using the LS-DYNA FE solver.

The procedure followed was:

1. Import the FE data into the GOM Argus software package.
2. Import the measurement data.
3. Transform the measurement data to the coordinate system of the FE.
4. Create comparison points.
5. Compare displacement and strain.

In step three, the effective alignment of the simulation result with the formed component was conducted. The author chose a best-fit alignment and reference point system (RPS) registration against the borderlines of the initial simulation. Schneider el at. (2008) found the procedure showed a direct numerical comparison of forming simulations with the experimental formed components. The correlation was accomplished based on the difference of full-field strain and shape information. Figure 2.32 illustrates a geometric comparison of the simulated component compared to the actual component. Schneider el at. (2008) used this comparison method to validate the simulations software packages capability to predict the final state of the component after springback.

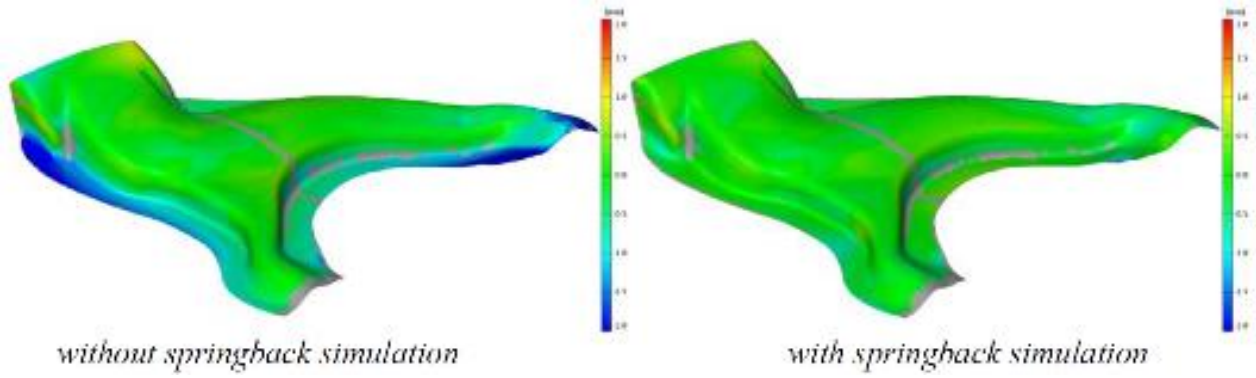

Figure 2.32: Geometric deviation of simulation to measurement (Schneider el at. 2008)

The study conducted by Solfronk and Sobotka (2011) concluded that PAM-STAMP simulation results and measurements from the formed component are agreeable. Advantages of the GOM ARGUS software was it enabled the user to:

- Optimise tooling surfaces
- Have conducted proper parameter selection
- Ensure the dimensional stability of the stamping
- Ensure compliance of thickness tolerances
- Ensure minimal deformation
- Critical zones that were susceptible to wrinkling and fracture were defect-free.

A disadvantage of the GOM ARGUS system was the surface of the stamping must be prepared with a regular point mesh grid whose displacements after deformation are evaluated (Solfronk and Sobotka 2011). This process cannot be used for industrial production and thus is only applicable to qualification and validation of the manufacturing in preparation for a first article inspection. Figure 2.33 depicts the large sheet metal component covered in a regular point mesh grid pattern.

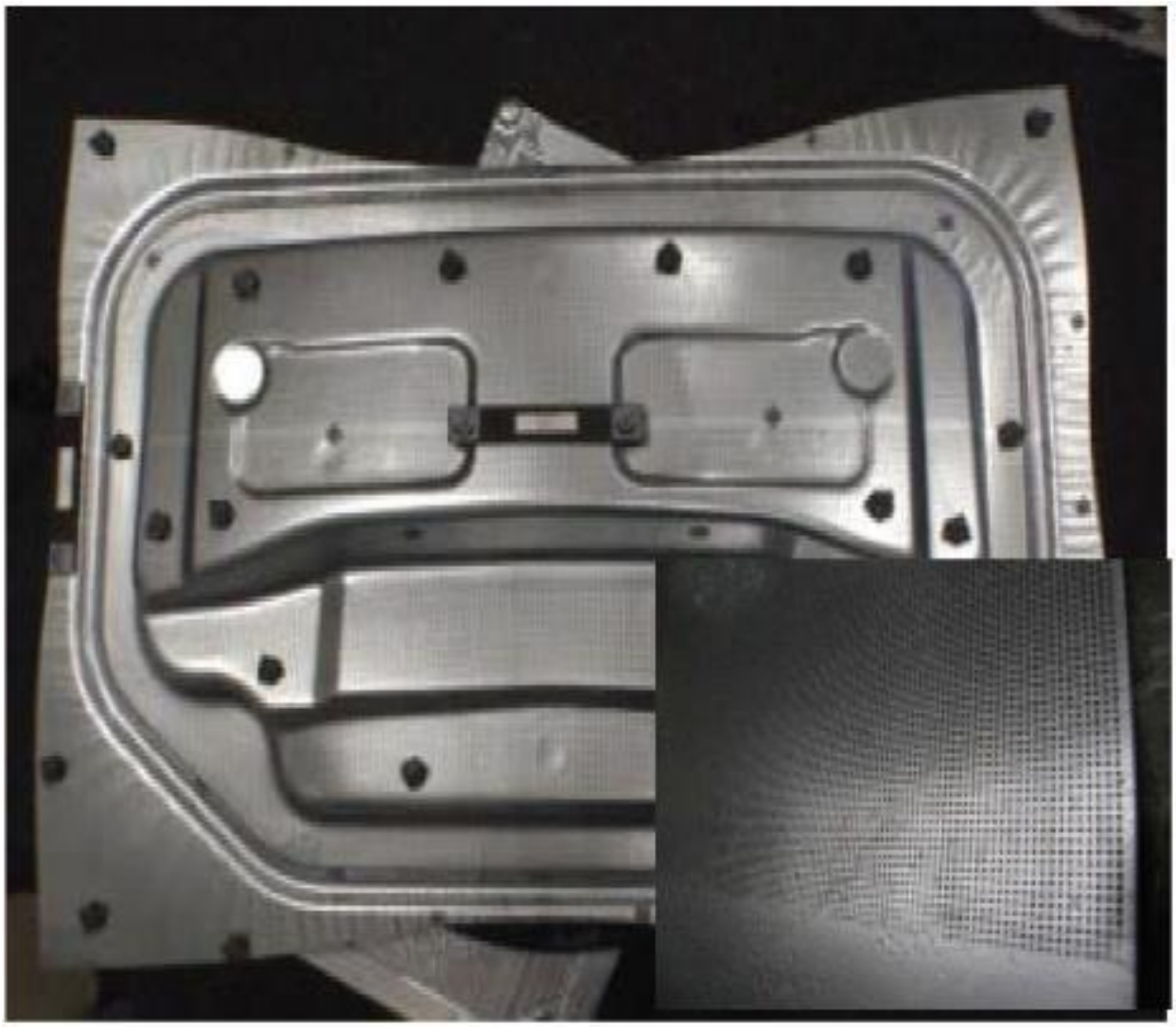

Figure 2.33: Large sheet metal component covered in a regular point mesh grid (Solfronk and Sobotka 2011)

Frącz et al. (2013) investigated the use of photogrammetric systems for verification of the simulation results from a sheet metal forming manufacturing process. The GOM ARGUS optical measuring system was used to determine the real values of the analysed draw piece strains, construction of a real FLC, and comparisons of the draw piece shape with the theoretical CAD model. The study showed the benefits of using optical measuring equipment to verify computer simulation results directly. The software package used to conduct the manufacturing simulation study was DYNAFORM. The authors denote the drawback of the measuring equipment was accuracy, especially of small radii, and was attributed to the ARGUS system requiring a mesh grid pattern.

The drawbacks of the system may not be practical for the industrial application of the GOM ARGUS metrology software package but certainly showed useful in validating the simulation results. The latest developments from GOM allowed scanned point cloud data to be imported from any scanning equipment. The point cloud was then used to create a facetted mesh surface (GOM Software, 2019). The nominal surface geometry of the component was then imported into the software package, and an assessment of the two surfaces conducted similar to the processes of Schneider el at. (2008), Solfronk and Sobotka (2011), and Frącz et al. (2013).

2.4.3. Alignment

Alignment is the relative positioning of components with respect to one another (McGraw-Hill, 2003). Hexagon defined best-fit alignment as “a set of measured points or a set of actual feature centroids to match, as closely as possible to its nominal location or theoretical counterpart” (Hexagon, 2020). Both Hexagon and GOM made use of the least square algorithm to align the two sets of points. One set of points are transformed such that the sum of the squared distances between matching points in the two sets was minimal. GOM Software (2019) defined best-fit as a local alignment which must be used after an initial alignment was completed. The initial or global alignment brought the two bodies into close proximity. Best-fit is then used to improve on the global alignment. Use of best-fit without an initial alignment may result in an inadequate alignment, especially if the two bodies are severely distorted compared to one another. A datum structure is typically defined on the component drawing set and is used for alignment and metrology inspection purposes. Three datum features are used to adequately describe the space and orientation an object occupies: a plane, a line and point GOM Software (2019). A plane is defined by three points and a line by two points.

Reference Point System (RPS) alignment is based on a given set of reference points on each of the two components. Each body is referred to as the nominal and the actual bodies. The effective direction, X, Y and Z for each linked RPS point must be defined. The effective direction is the translational degree of freedom that is constrained. RPS is a local alignment that follows an initial or global alignment GOM Software (2019).

Three initial or global alignments are available in the GOM software package, namely original, 3-2-1, and 3-point alignment. In the case where the data was scanned, the original alignment will not be a suitable option as the component will be oriented in a completely different location to the nominal component. In the case of a simulation result, which was typically modelled on the same coordinate system as the CAD model, an original alignment is acceptable. 3-2-1 alignment is based on the principle: three points are chosen to define a plane, two points are chosen to define the line relative to the plane. The final point selected is chosen to define the origin of the coordinate system. The two bodies are then aligned based on the coordinate system. 3-point alignment was a much simpler alignment method; three points are chosen on the nominal, and the corresponding set of points are chosen on the actual body (GOM Software 2019). The three points of the respective bodies are then brought as closely as possible to one another, enforcing the alignment of the two components. Alignment, especially with respect to the defined datum structure, ensures a standardised measuring practice is followed irrespective how well or poor a component has been manufactured. The same must be applied in FE simulation to ensure the simulation is assessed correctly.

Chapter 3: Approach and Methodology

3.1. Research Design

The objective of this study was to conceptualise the sheet metal blank and tooling and to characterise the sheet metal blank material properties. Then, using a manufacturing simulation software package, the capability of the blank and tool concepts to manufacture the component was evaluated. Finally, the concepts were validated by manufacturing and inspecting the component. The simulation software package ESI Group PAM-STAMP 2G was validated in a quantitative before-and-after field experiment. The component selected for the study was manufactured in metal from the conceptualised tools and blanks. Tooling and blank designs were taken from the conceptualisation stage through to final acceptance for proofing digitally, using Computer-Aided Design (CAD) and Computer-Aided Engineering (CAE) tools. Components were manufactured and measured, initially using coordinate measuring machine (CMM) and later three-dimensional (3D) scans using optical measuring machines, which were compared to the nominal design and the simulation result.

3.2. Research Instruments

For digital modelling and simulation, the following software packages were used:

1. Dassault Systeme CATIA V5 CAD modelling software package, 2018 release.
2. ESI Group PAM-STAMP 2G version 2018.0.1 metal forming simulation software package
3. GOM Inspect 3D metrology software package, version 2018.

List of hardware used for the study:

1. Denel Aerostructures Quintus Technologies fluid cell press

   The metallic aircraft skin panel was manufactured using Denel Aerostructures' Quintus Technologies fluid cell press. The fluid cell press has a press bed size of 1.1 x 4 m and a pressing capacity of 100MPa.

2. Aerosud Aviation Romer Absolute Arm RA-7525 SI

   The Romer Absolute Arm RA-7525 SI is a high-precision 3D scanning device. It has a measuring range of 2.5 m, point repeatability of 20 µm, and a volume accuracy of ± 29 µm.

3. Aerosud Aviation Alpha Image

   The Alpha image is a gantry-style CMM. Equipment specifications: Ultra-high-resolution reader (0.1 µm) with a measuring stroke of 2500 mm in the x-axis, 8000 mm in the y-axis, and 1500 mm in the z-axis. The maximum error in the full volume is 40 µm.

3.3. Research Data

The data that was collected during the case study was comprised of:

- CAD and Simulation data
- Manufactured metal components
- Metrology data

CAD and simulation data was comprised of a digital representation of the component that was manufactured from the conceptualised tool and blank. The simulation component was assessed against the nominal 3D model for dimensional deviations to determine if the blank and tools were acceptable concepts. Actual components were manufactured using the chosen tooling and blank concepts. Metrology data was gathered through CMM and 3D laser scanning tools. The final components were measured and compared with the nominal design and the simulation result to determine deviations.

3.4. Forming Process Conceptualisation Cycle

Based on the simulation steps and inputs adapted from Altan and Tekkaya (Vol 2) (2012), the forming process conceptualisation cycle depicted in Figure 3.1 was defined and applied.

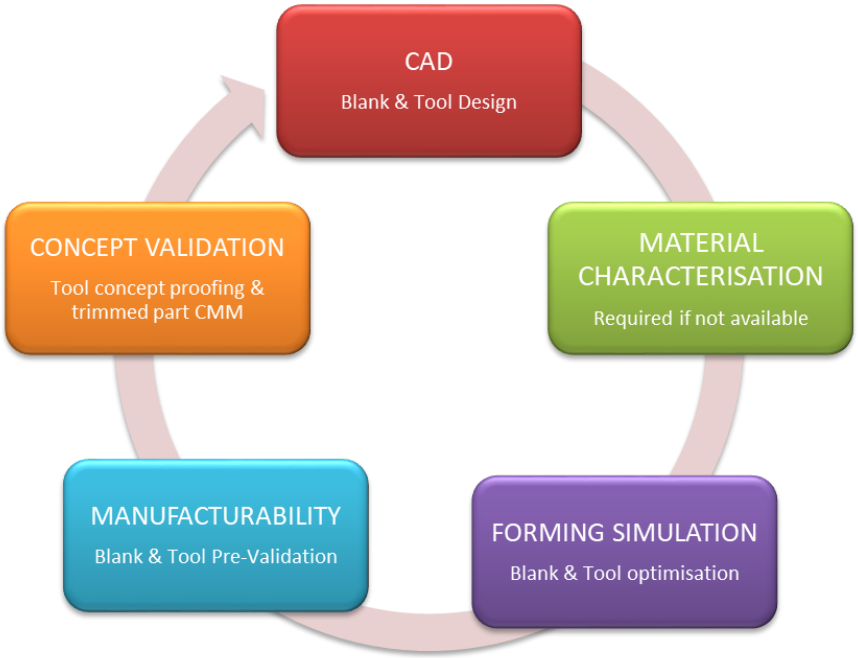

Figure 3.1: Forming process conceptualisation cycle (Serfontein et al. 2019)

The process cycle was a means to effectively conceptualise and assess a blank and tool design, taking a concept form a CAD model to the final realised component. At the heart of the process was FE simulation which aided in optimising and verifying the blank and tooling concepts without a “trial-and-error” process.

3.4.1. Computer-Aided Design (CAD)

The purpose of the CAD phase was the creation and preparation of a surface from which the sheet blank and tooling 3D models are designed and used to conduct a forming simulation study. The models if accepted, were used to manufacture the actual blanks and tools. From the 3D model of the component, a surface was extracted, termed the outer mould line (OML). The OML was the nominal surface upon which a comparison was conducted to assess the conformance of the manufactured component.

A plane was then either created or selected from the axis coordinate system. The OML surface was manipulated by translation and rotation transformations such that the OML surface was equidistant from the plane. Typically, the corners of the OML surface were used to assess if it was equidistant to the plane but may change depending on the component’s curvature.

The OML surface was prepared in this way to ensure it was in a natural position with gravity taken into account. If the component were angled in the tool, additional alignment and holding fixtures would be required to prevent the blank from sliding. Also, if the component was to be manufactured by a deep-drawn forming process, depending on the depth, the corners may be prone to cracking. Overall, the component surface should be prepared to account for flaws and defects in the tooling from the beginning with the evolution of the blank and tooling design driven by the simulation results.

Once the final surface was created, the blank and tools were conceptualised. The initial blank was a projection of the final surface onto the plane defined previously. The projection surface resulted in a flat blank and was termed the unfolded surface. The edges of the unfolded surface were extended (in-plane of the surface) at least 25 mm which allowed for trimming to the desire component.

The tool was conceptualised based on the forming process. Similar to the blank, the OML surface was extended by 25 mm. The edge extension was tangential to the surface and followed the surface contour. The extended tool surface was then used to create an extruded solid body. The length of the extrude was dependant on the depth of the fluid cell press. The sides of the extruded body are then drafted 15° and the corners filleted with a 10 mm radius.

It is important to ensure sharp edges and corners are omitted using radii and fillets. Radii and fillets cannot be less than 10 mm, these dimensions are too small and will not omit the sharp corner. Figure 3.2 depicts the blank and tool geometry that was created by following the described process.

Once the models were created, they were then saved into Initial Graphics Exchange Specification (.igs or IGS) file format such they could be imported into the CAE software package. As the blank was flat, it can be imported into the simulation software package as either a surface or a curve from which the FE mesh was created (ESI Group 2018).

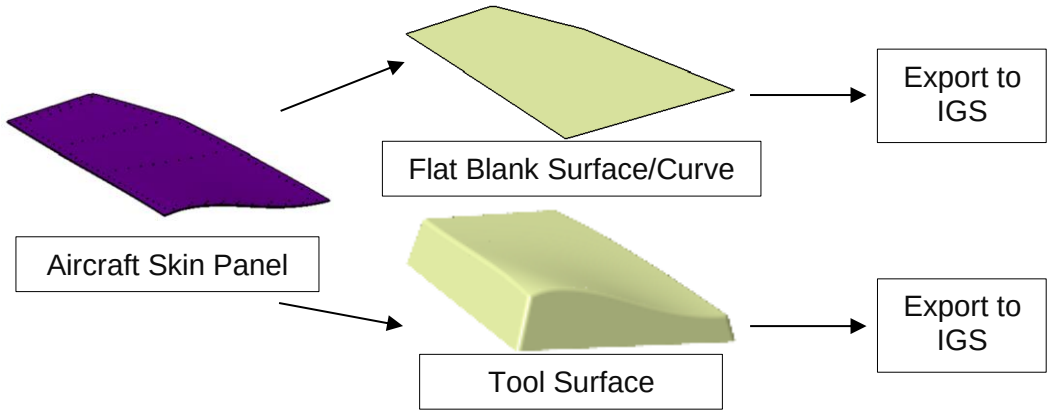

Figure 3.2: Tool and blank surface geometry creation

In addition to the blank and tool, a trim curve was created. A trim curve was the boundary line of the final component. The trim curve was exported into an IGS file format, as shown in Figure 3.3.

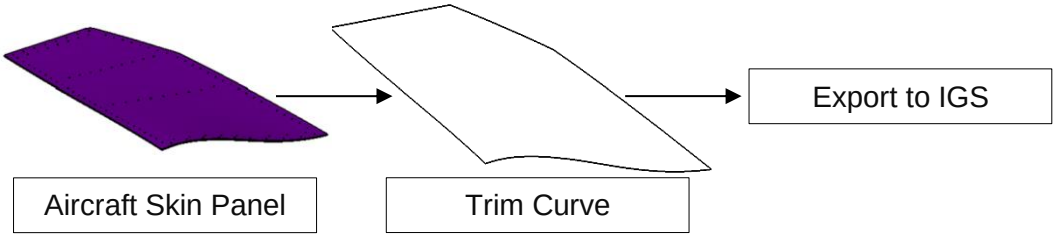

Figure 3.3: Trim curve creation

3.4.2. Material Characterisation

The material characterisation phase covers the material properties and other parameters required to conduct the simulation. Material properties are captured in a material card comprised of the following (ESI Group 2018):

1. Material properties (Modulus of elasticity, Poisson's ratio and density)
2. Plasticity law/yield criteria
3. Hardening law
4. Forming limit diagram
5. Friction coefficients based on pressure and velocity (Optional)

The two most widely used unit types are Megapascals [MPa] or Gigapascals [GPa] (ESI Group, 2018).

For MPa units:

- Displacement in millimetres [mm]
- Time in seconds [s]
- Velocity in millimetres per second [mm/s]
- Mass in tons [ton]
- Temperature in degrees Celsius [°C]
- Force in Newtons [N]

For GPa units:

- Displacement in millimetres [mm]
- Time in milliseconds [ms]
- Velocity in meters per second [m/s]
- Mass in kilograms [kg]
- Temperature in degrees Celsius [°C]
- Force in kilonewtons [kN]

Test standards and parameters:

- Modulus of Elasticity (E) [MPa] or [GPa] determined in accordance with ASTM E111 or EN ISO 6892-1
- Poisson ratio (ρ) [ ] determined in accordance with ASTM E132
- Density (ρ) [ton/mm^3] or [kg/mm^3]
- Plastic anisotropy coefficient in accordance with ASTM E 517 / ISO 10113
- The exponent of strain hardening in accordance with ASTM E 646 / ISO 10275
- Experimental Forming Limit Curve in accordance with ISO 12004-2

Friction is not a material property, but rather a property of two components interfacing one another. Typically, friction is defined as a coefficient for the duration of the forming process. The friction coefficient will vary from material to material and is further influenced by the lubricant used. The use of variable friction coefficients that are dependent on the pressure and velocity can be accommodated in PAM-STAMP but must be determined by experimental testing (ESI Group, 2018).

The material properties, FLC, and friction testing were conducted at the Technical University of Liberec (TUL), Faculty of Mechanical Engineering, Department of Engineering Technology, section of Metal Forming and Plastics, Republic of Czech (TUL, 2020) in collaboration with ESI Group.

The tensile and compressive testing was conducted on an Instron Ceast 9350 dynamic test equipment. Figure 3.4 (a) shows the dynamic test apparatus fitted with an epsilon extensometer for strain measurement. Figure 3.4 (b) shows the standard dog-bone style uniaxial test sample geometry. Uniaxial tests provided the mechanical properties, the plastic anisotropy coefficients and exponent of strain hardening used to determine the plasticity and hardening law properties.

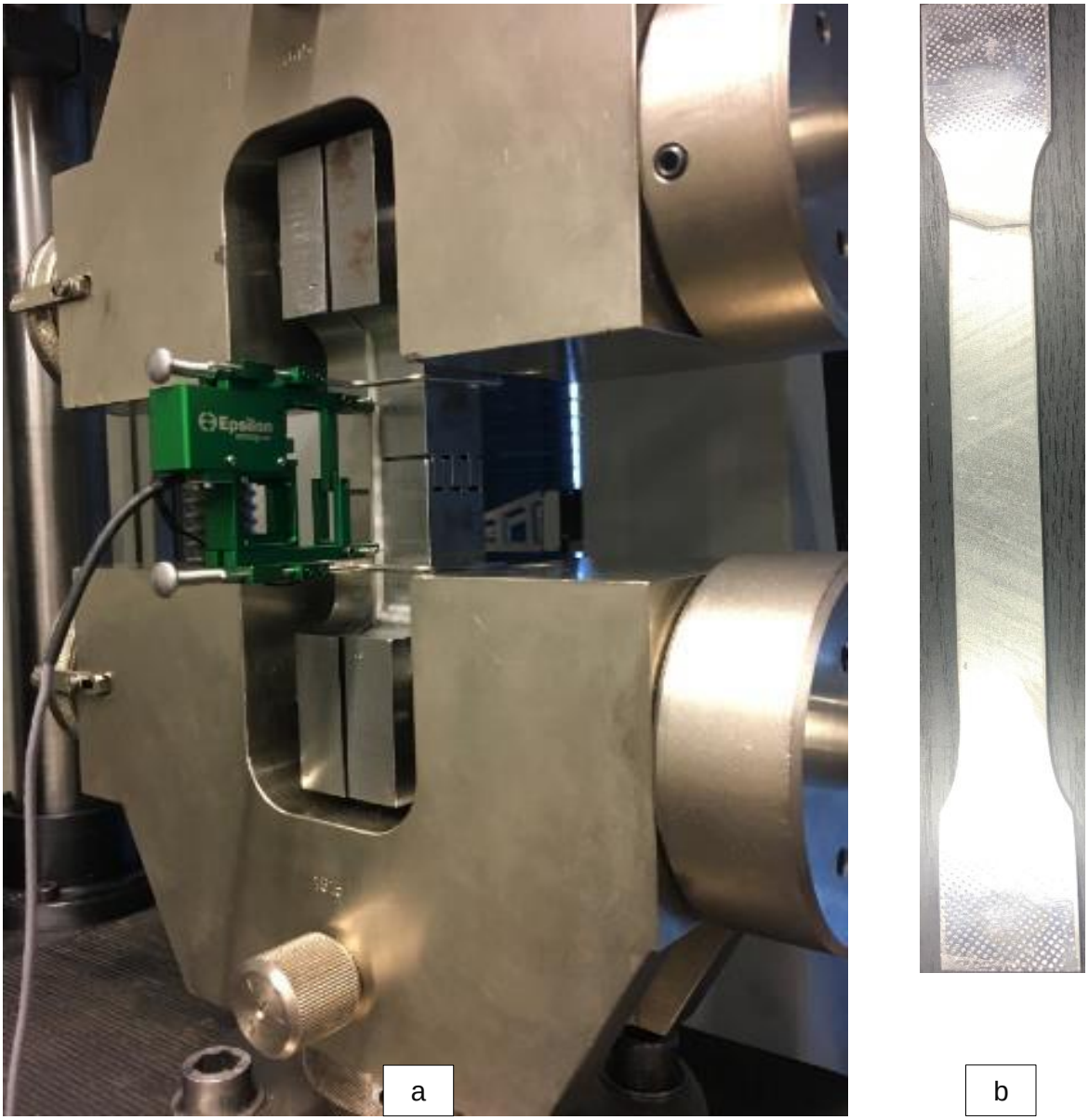

Figure 3.4: (a) Instron Ceast 9350 dynamic test apparatus (TUL, 2020) (b) Uniaxial dog-boned style test sample

FLC testing was conducted using equipment developed at the TUL mechanical testing and tribology laboratory, see Figure 3.5 (a). In addition to the FLC testing, a hydraulic bulge test was conducted for equi-biaxial test data. Both tests are optically based and are conducted using the GOM ARAMIS test and measurement system. Figure 3.5 (a) shows the FLC test samples that ranged from the narrowest width sample to the complete circular disk.

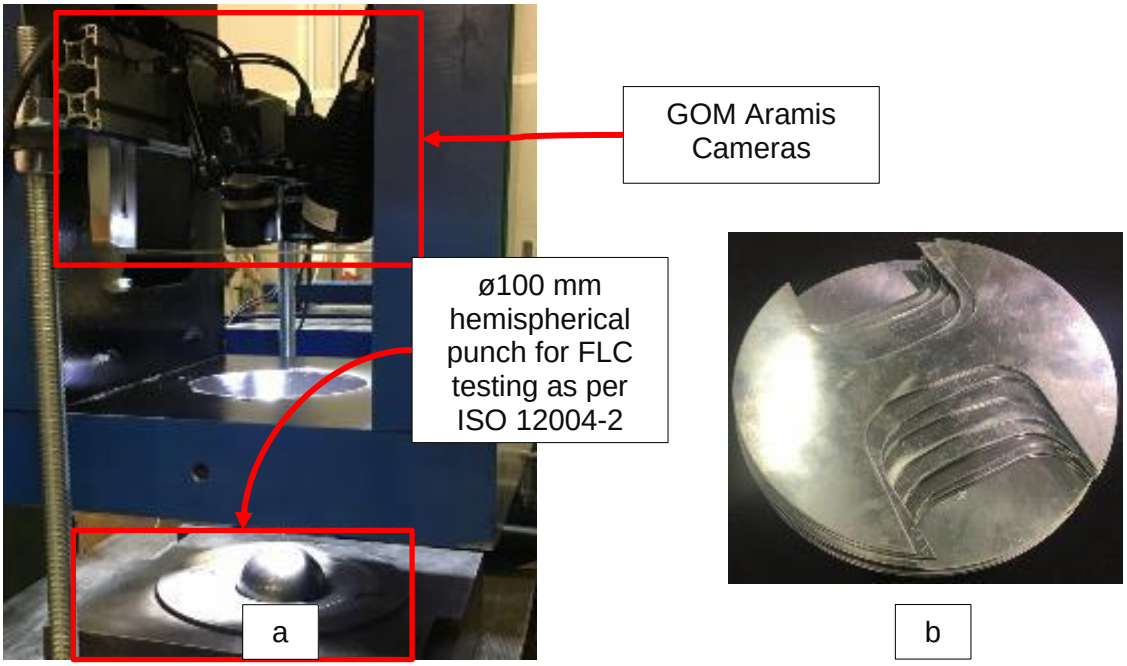

Figure 3.5: (a) Forming Limit Curve Testing equipment with GOM Aramis camera system (TUL, 2020) (b) Forming Limit Curve Test Samples

The equipment used for conducting friction testing was the SOKOL 400 tribological testing machine, as shown in Figure 3.6 and Figure 3.7. The SOKOL 400 allowed for varying the speed with a constant pressure applied to the test sample, whilst the friction force was measured (TUL, 2020). The purpose of this test was to characterise the friction between the blank and the tool with the desired lubricant included to provide a complete variable friction profile.

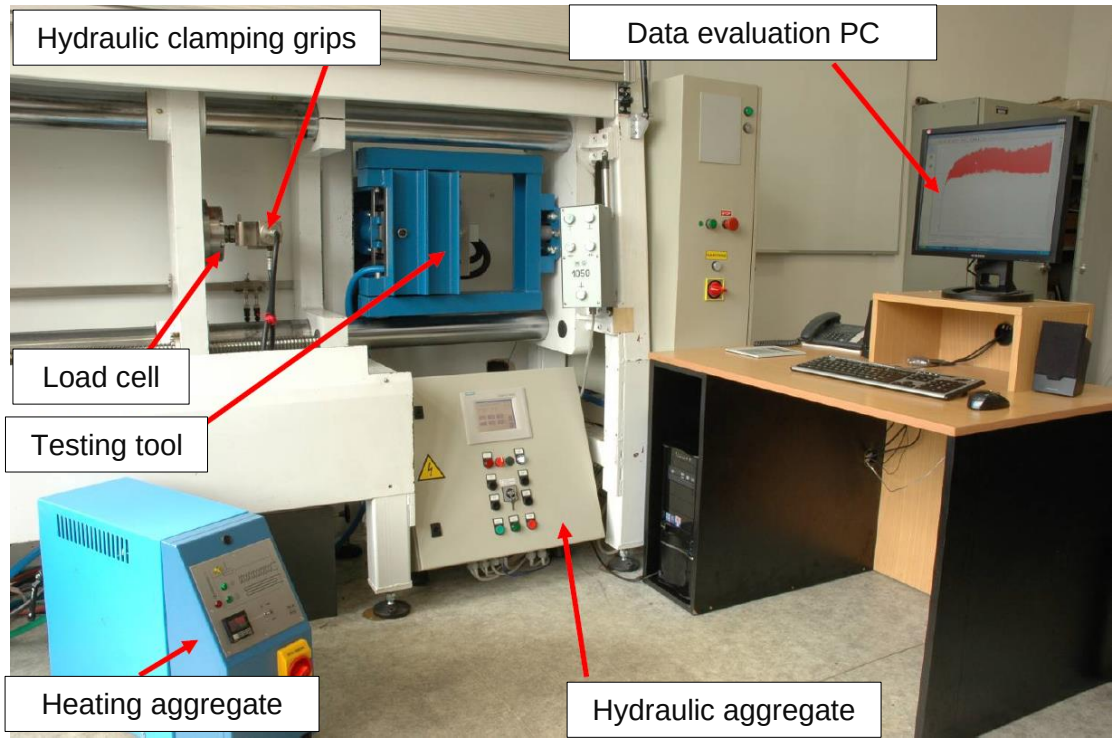

Figure 3.6: SOKOL 400 - friction testing device (TUL 2020)

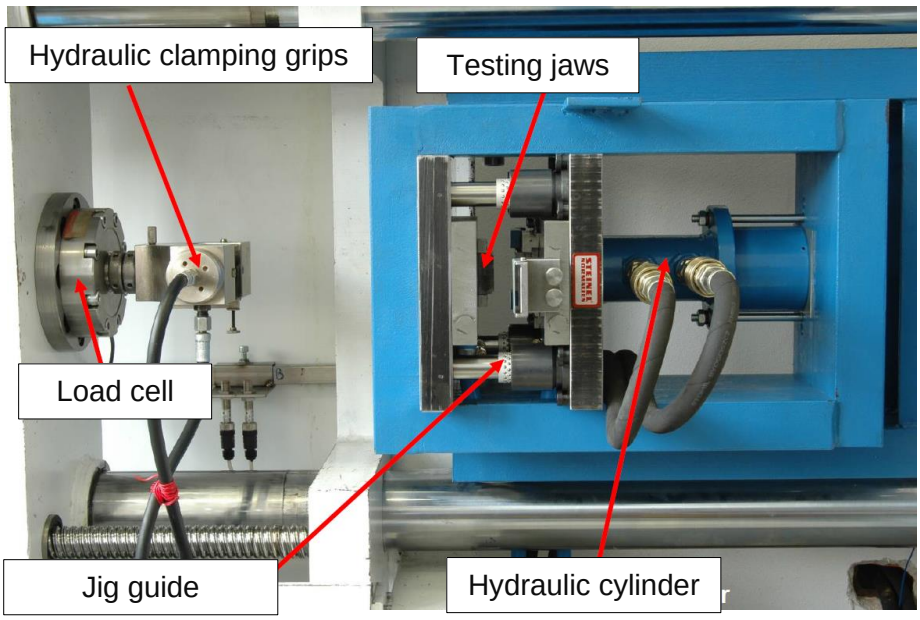

Figure 3.7: SOKOL 400 - friction testing tool breakdown (TUL 2020)

The SOKOL 400 testing parameter's ranges are listed below:

- Feed velocity 1 – 400 mm/s
- Contact pressure 0.5 – 83 MPa
- Temperature 5 – 98 °C
- Jaw contact areas 4000 mm² (20 x 20 mm)
- Maximum data scanning frequency 10 kHz (routinely 2 kHz)
- Maximum specimen length 1200 mm
- Specimen width 44 mm

Figure 3.8 depicts the two-dimensional (2D) drawings of the friction clamps used in the SOKOL 400 tribological test machine. It is important that the clamps are manufactured from the same material as the tool.

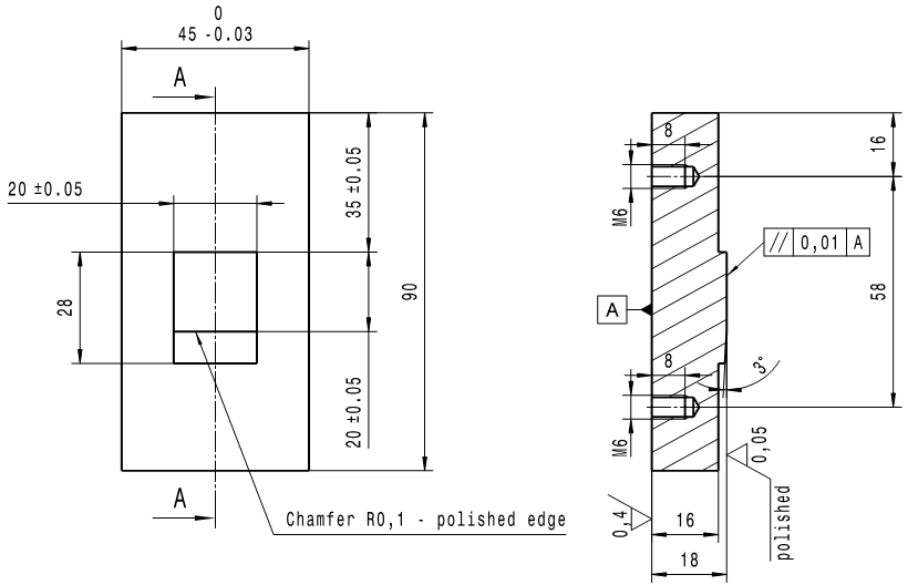

Figure 3.8: 2D drawings of the friction clamping jaws used in the SOKOL 400 tribological test machine (TUL, 2020)

3.4.3. Forming Simulation

With the geometry prepared and material properties known, the forming simulation phase followed next. This phase was a feasibility study of the conceptualised design. Feasibility assessed the degree of how well-suited the tool and blank were to manufacture the component. Mesh element size was typically coarse with five elements across the smallest tool radius. A level three mesh refinement was used to refine the mesh where required. Mesh refinement was activated in areas where the blank interfaces the tool.

The simulation time step was based on the smallest blank element size and increased with mesh refinement. Hence, the simulation will run in a shorter time frame than that of a fine mesh used in the manufacturability study. The blank and tool surface geometry and the trim curve are imported into the PAM-STAMP, where it was automatically meshed, as shown in Figure 3.9.

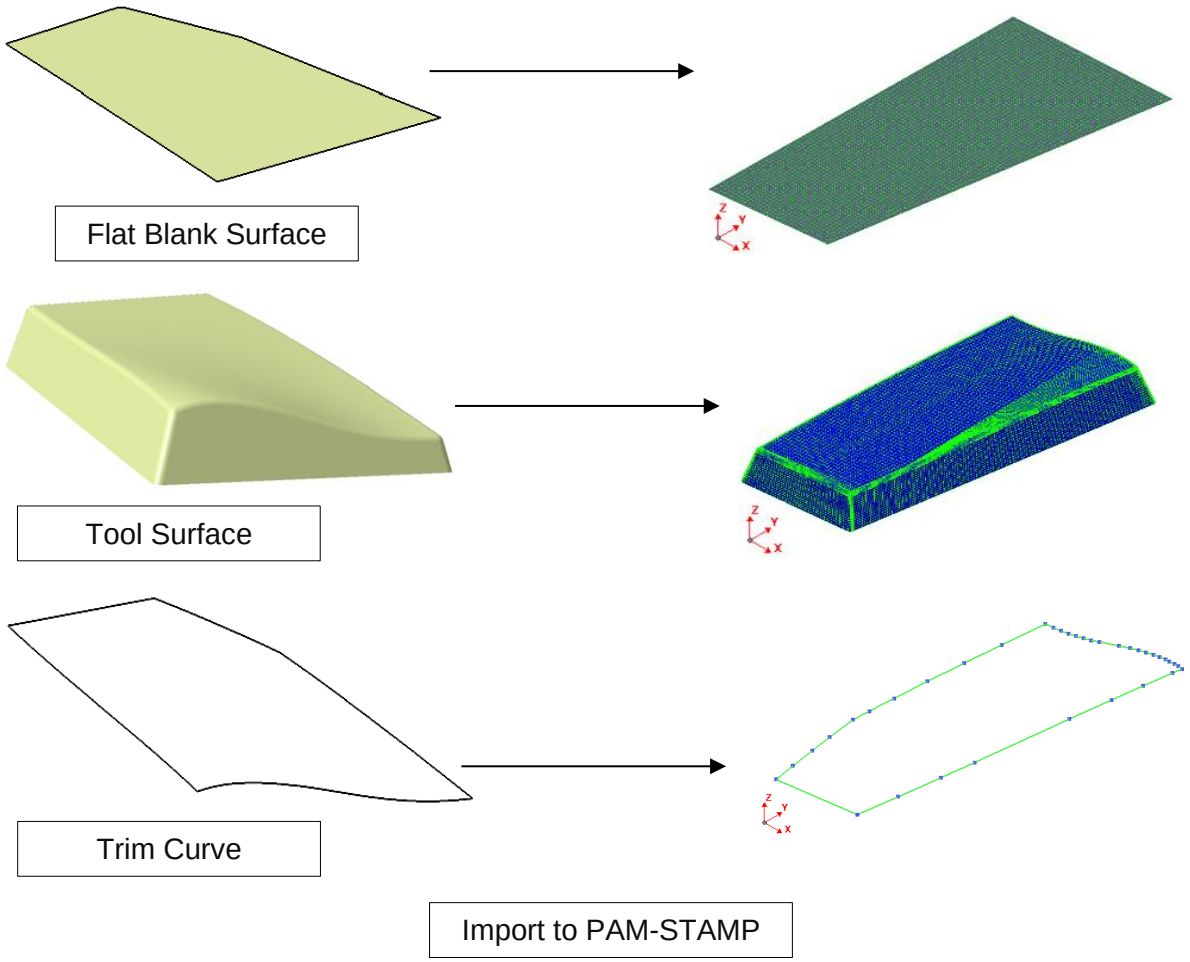

Figure 3.9: Blank and tool surface geometry and trim curve import into PAM-STAMP 2G

The surface geometries are discretised into a quadrilateral and triangular shell 2D elements. Quadrilateral elements were the main element types with triangular elements used, where necessary. 1D bar elements defined the trim curves. Figure 3.10 depicts the blank, the tool and the trim curve FE model assembly in PAM-STAMP after the blank and tool surfaces, and the trim curve has been imported and meshed.

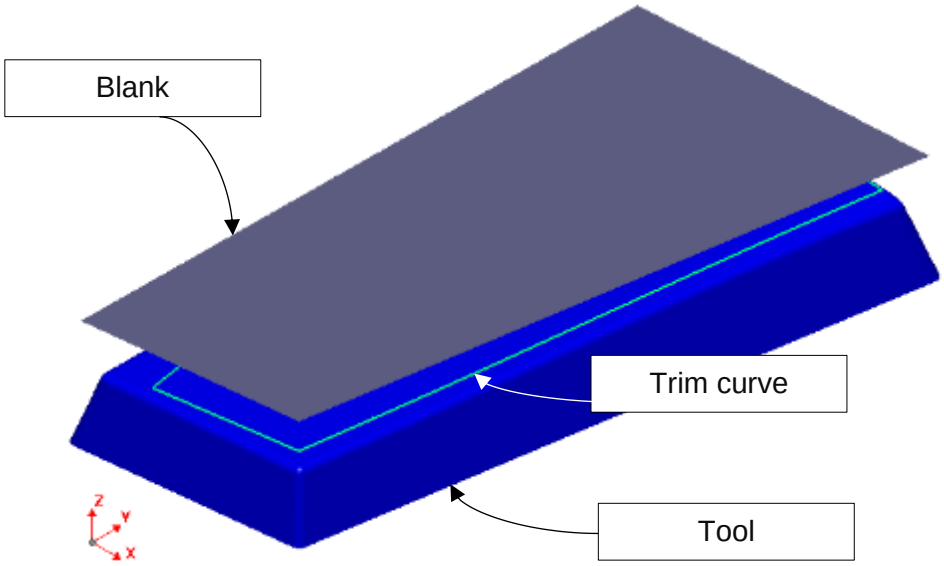

Figure 3.10: Blank, tool and trim curve assembly set-up PAM-STAMP 2G

The following stages of the manufacturing process were used in the following order:

OP 1 – Forming stage

OP 2 – Springback stage

OP 3 – Trim and springback stage

In the case of multi-stage tool operations, OP 1 and 2 were repeated before proceeding to OP 3. Another key activity in this phase was optimisation studies. In PAM-STAMP 2G, the following optimisations can be conducted (ESI Group, 2018):

1. Blank contour optimisation
2. Trimming line optimisation
3. Die compensation

The blank contour and trimming line optimisation operations optimise the initial blank and then the trimming curves in intermediate stages, respectively. Die compensation was an automatic method of correcting a die shape to compensate for the effects of springback. Die compensation made use of a multi-stage module which allowed for the creation of some tools during a full chain process (ESI Group, 2018).

The die compensation optimisation tool was used in the presented study. The tool die was optimised to provide the most accurate final form after springback. From the first stage forming process through to the springback stage, the complete forming process was considered during the optimisation study.

The following checks were performed to validate the blank and tool concept was acceptable to proceed to a detailed manufacturability simulation. The FLD, zone quality overlay was reviewed to assess the component for defects (wrinkling and cracking), and that enough in-pane stretching was achieved. The FLD zone check was also checked at the end of the complete process to confirm no wrinkles or cracks occurred. The distortion of the component was validated against the desired component surface and was imported into PAM-STAMP. The surface derived by simulation was compared to the nominal shape of the component by means of a surface distortion plot. The maximum distortion and the shape were determined based on a distortion plot.

3.4.4. Manufacturability

The manufacturability phase investigated the concept in greater detail. This phase was identical to the forming simulation phase, with the exception of the mesh element size finer compared to the mesh size used in the feasibility simulation phase, but maintaining the five elements across the smallest radius rule. Typically, a kinematic material property card was used, as it provided a more accurate form and springback compared to the isotropic material card. Typically, element refinement was not used in this phase due to the refined mesh structure already imposed. The use of a finer mesh resulted in longer simulation times. As simulations are prone to errors and mistakes made by the engineer, many of the problems that could arise are corrected in the feasibility phase before proceeding to the manufacturability phase. The acceptance criteria for the manufacturability phased was the component must experience sufficient in-plane stretching as shown on an FLD, and minimal springback. The simulated surface must have a low degree of springback when compared to the nominal design, ideally within the design tolerance requirements.

3.4.5. Concept Validation

Once a concept was accepted from the manufacturability phased, the tooling and blank concept were manufactured. Press and trimming trials are constructed to manufacture first article components. These components are inspected using CMM or OMM equipment and software to compare the final form to the design. If the surface profile of the component was within the design tolerance requirements, the blank and tooling were accepted for serial production.

Chapter 4: Case Study

4.1. Introduction

The component used for the metallic case study was an aircraft skin panel that was manufactured by stamp forming from AA2024. The AA2024 sheet was purchased in -T3 temper condition from the supplier. The sheet was solution heated treated to -W temper condition (a softened state that improves the formability of the sheet metal) after which it was formed and left to naturally age to the -T42 temper condition. Figure 4.1 depicts the 3D and 2D images of the aircraft skin panel used in the presented study. A key geometric feature of the aircraft skin panel was the s-shaped edge feature. The component was a geometrically complex surface panel which gradually transitioned from a flat plate to a complex curved surface. The complex surface made this component a good candidate for the case study. Single and double edge flanged and domed components are typically researched and easier to manufacture compared to a complex shaped component. The work of Hatipoğlu et al. (2007), Lee et al. (2015), Chen et al. (2015), Păunoiu el. al. (2015), Leacock et al. (2016), Păunoiu et al. (2019) and Zhang et al. (2019) have been discussed in great detail in Section 2.3.

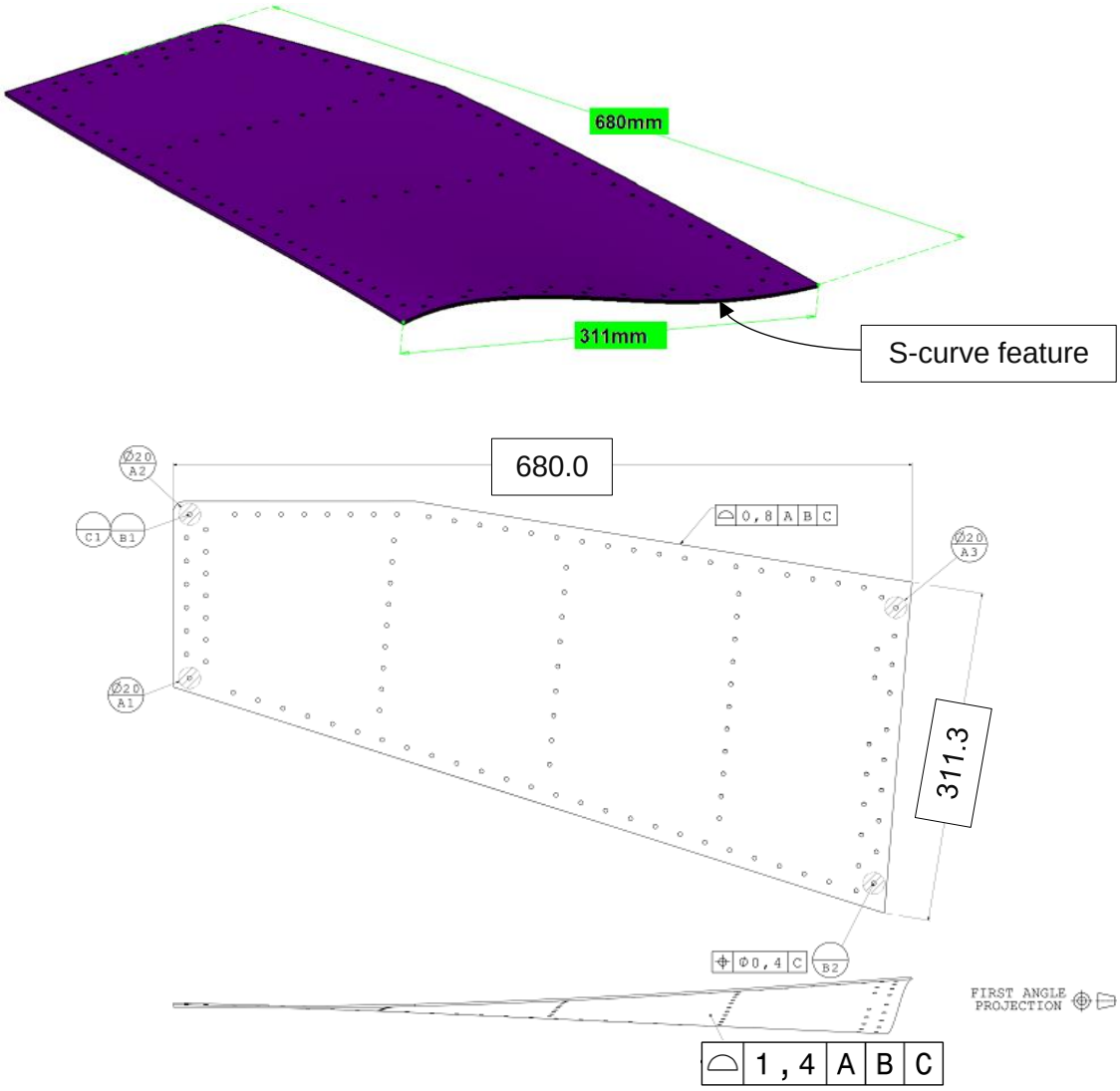

Figure 4.1: 3D and 2D images of the aircraft skin panel

The 2D drawing, shown in Figure 4.1, contains critical dimensional requirements of the component. The balloons A, B, and C define the datum structure of the component. Three points define the plane structure, which is designated as datum A. Two points define a line structure, which is designated as datum B. Finally, a single point for location, which is designated as datum C. A surface profile tolerance of 1.4 mm was defined with respect to the A, B, and C datums. This datum structure was used to align the component in a standardised way for proper inspect.

The component did not meet the 1.4 mm surface profile dimensional requirement using male matched metal stamp forming tooling and had to be manually adjusted to final form. The case study investigated an alternative manufacturing process, using a Quintus fluid cell press. The development of the appropriate tool and blank through manufacturability assessment using PAM-STAMP 2G forming simulation package was the focus of the study. The objective of the case study was to demonstrate the capability of PAM-STAMP to conduct a die sheet hydroforming simulation.

4.2. Computer-Aided Design

The objective of the CAD phase was to create and prepare the component OML surface such that it was suitable to import into the simulation software package. The approach used was to create the geometry in accordance with the approach defined in Section 3.4.1. The OML surface was created with each blank and tool design created from this initial surface. An offset plane was defined from the component based on the coordinate system at the component's centroid. The distances of the furthest points of the component to the offset plane were measured, as shown in Figure 4.2. The four corners (labelled 1 to 4) of the component had different heights to the defined plane.

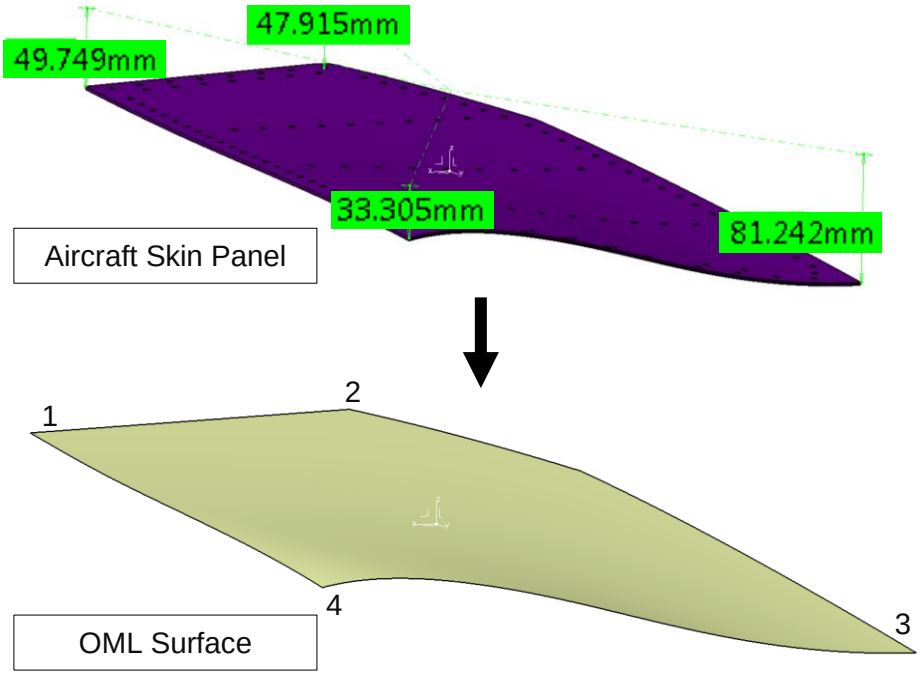

Figure 4.2: Perpendicular distances to a reference plane and the OML surface

Through two rotational transformations, each corner was made equidistant to the offset plane. As depicted in Figure 4.3, a line between points 2 and 4 was created. A second surface was created by rotating 4.25° about line 2-4. Points 1 and 3 are equidistant from the offset plane and measured 60.765 mm and 60.601 mm, respectively.

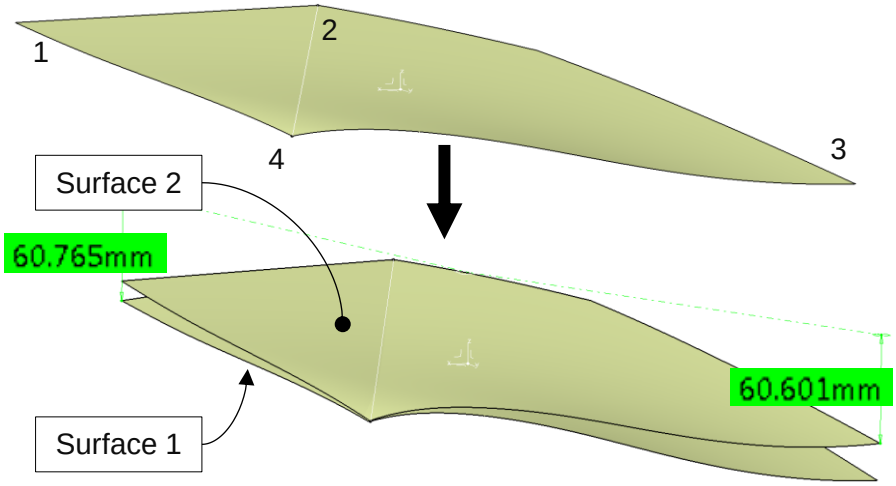

Figure 4.3: Second surface - rotated to equalise corners 1 and 3

The process was repeated for points 1 and 3. A line between points 1 and 3 was created. A third surface was created by rotating 1.8° about line 1-3. Points 2 and 4 are equidistant from the offset plane and measured 42.574 mm and 42.853 mm, respectively. Figure 4.4 depicts the third and final desired surface.

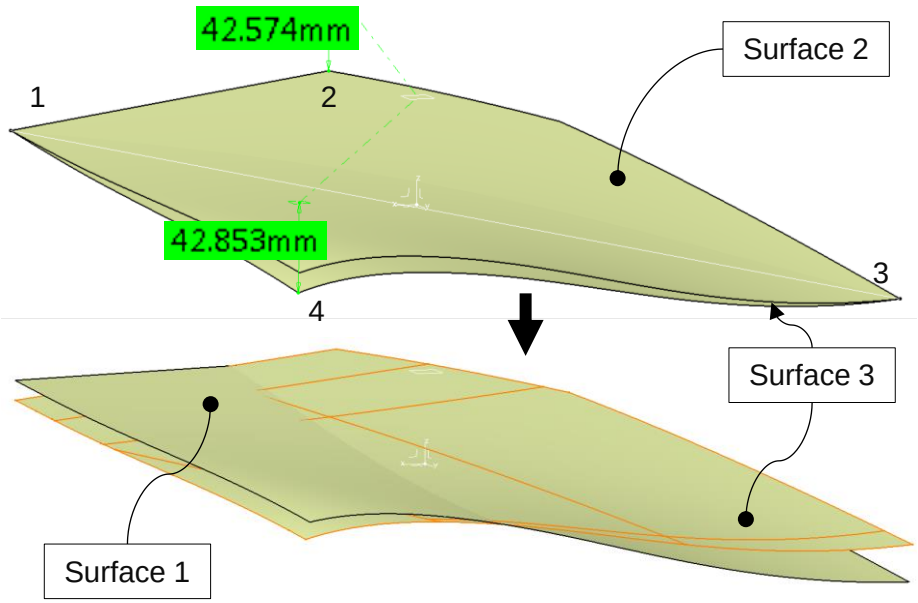

Figure 4.4: Third surface - rotated to equalise corners 2 and 4

The final OML surface was used to create all the concepts with adaptations based on the findings from the previous blank and tool concept's simulation study. The CAD phase was revisited for each blank and tooling conceptualisation. Only Concept-1's design process will be discussed in detail. All blank and tooling concepts are created in a similar way. Initial blank concepts were based on the OML surface. Later, the blanks were based on the tool geometry. Figure 4.5 shows the process followed to create the blank for Concept-1.

An outline of the OML surface, defined previously, was created and projected onto an offset plane. The projected OML surface outline was then offset outward resulting in the final blank outline. The angular segment of the component was omitted to make a rectangular blank. Having retained the angular segment may have unwanted results. The final blank outline was finally enclosed into a surface, not depicted in Figure 4.5.

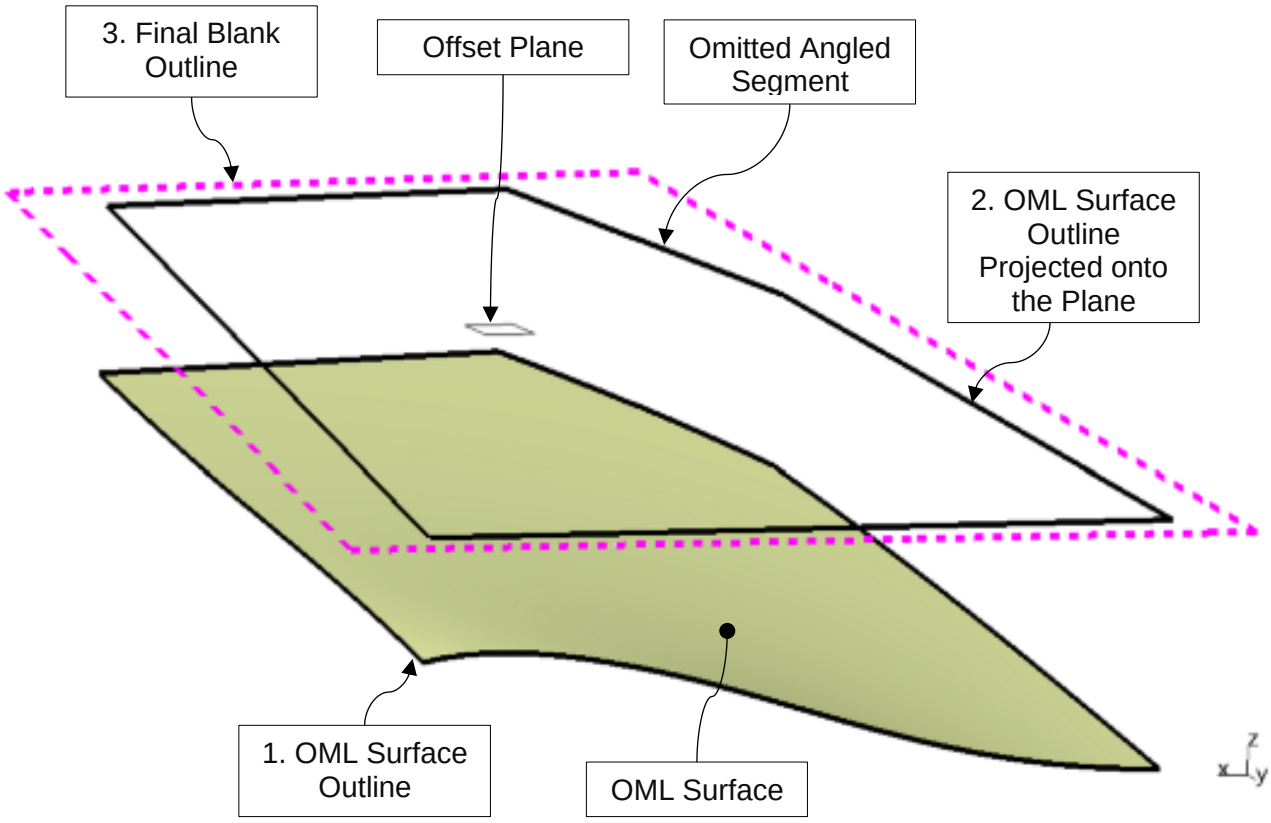

Figure 4.5: Concept-1 blank design sequence

With the blank conceptualised, the tool was then created based on the OML surface. Figure 4.6 shows Concept-1's tool design. The edges of the OML surface are extended outward tangential to the curvature of the OML surface. The angular segments of the component were omitted in the tool as well. The tool surface was extruded downward to create a solid body with a minimum thickness of 50 mm. The edges received a 20 mm radius to omit sharp corners that may result in unwanted cracks in the blank and may also damage the fluid cell press. The sides of the tool were drafted with a 15 ° angle relative to the vertical surface. Undercut surface and sharp edges used in the fluid cell press tool are utilised in cases where the blank was trimmed during the forming process. These features were not utilised in the manufacture of this component.

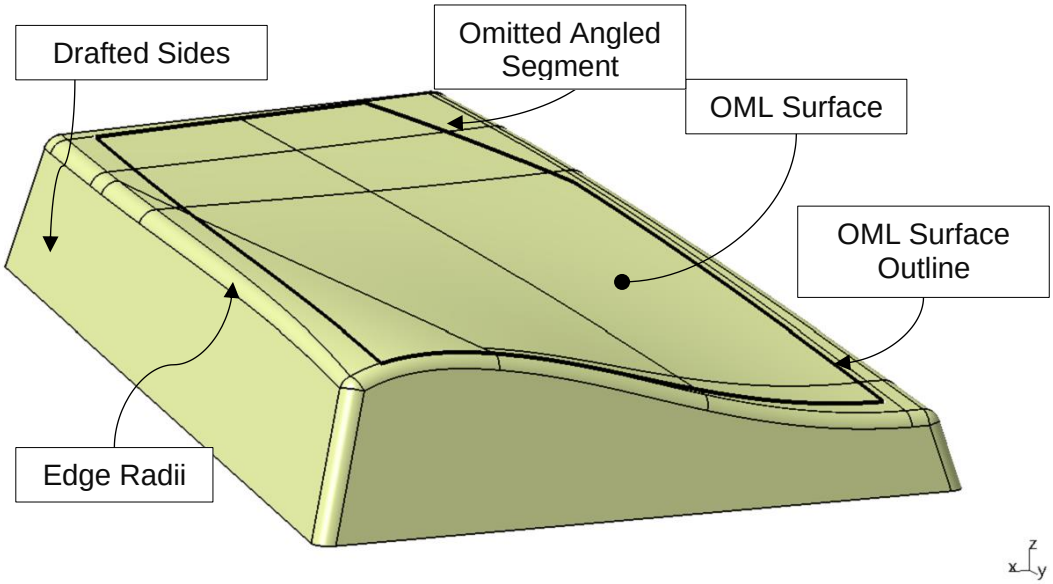

Figure 4.6: Concept-1 tool design

With a conceptualised blank and tool available, the data was prepared for the simulation phase. As outlined in Section 3.4.1, the blank surface, tool surface and OML surface outline were exported into IGS file format and imported into PAM-STAMP.

4.3. Material Characterisation

Limited aluminium alloy materials were available in the ESI Group PAM-STAMP material properties database (ESI Group 2018). AA2024 clad sheet in 2 mm thickness in the -W or -O temper conditions were not available in the PAM-STAMP database. Hence, a material characterisation test campaign was conducted in collaboration with ESI Group (Republic of Czech) and the Technical University of Liberec to characterise AA2024-W 2mm clad sheet. The data cannot be published as it is confidential, proprietary information.

The several PAM-STAMP material cards were realised from the material characterisation campaign for AA2024-W 2 mm thickness are listed below:

- Vegter yield locus lite plasticity law / Krupkowsky isotropic hardening law
- Vegter yield locus lite plasticity law / Yoshida-Uemori kinematic hardening law
- Vegter yield locus lite plasticity law / Yoshida-Uemori kinematic hardening law with variable Young's modulus
- A forming limit curve of the 2mm AA2024-W @30 minutes after heat solution treatment
- Variable friction curves dependant on pressure and velocity

The AA2024-O and -T3 2 mm thickness material cards were the Barlat 2000 plasticity law / isotropic hardening law. These two materials were characterised in a separate study at Aerosud Aviation. The data cannot be published as it is confidential, proprietary information. Figure 4.7 illustrates a normalised yield locus comparison of the Barlat 2000 for the AA2024-O and -T3 sheets, and the Vegter_Lite for the AA2024-W sheet. With reference to the literature presented in Section 2.2, the only deviation between the two yield loci was the pure shear strain state.

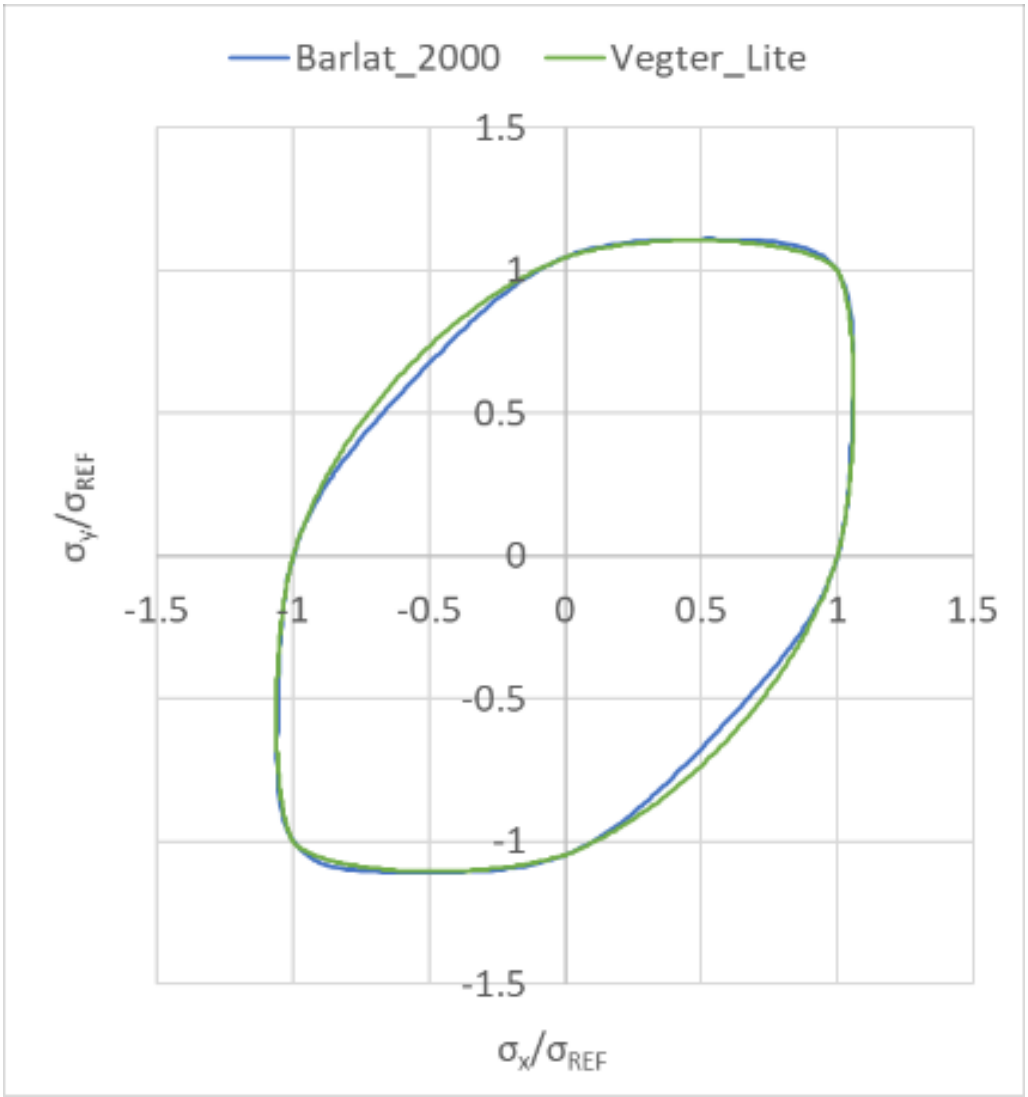

Figure 4.7: Normalised yield locus comparison of Barlat 2000 and Vegter_Lite

Figure 4.8 illustrates the normalised hardening flow curves for the -O, -W, and -T3 temper conditions of AA2024 2 mm thick sheet. Unlike the yield loci, the plastic state of the materials defines their respective formability compared to one another. The flow curve depicted in Figure 4.8 shows AA2024 in -T3 temper condition was the least formable of the three tempers and was the reason for heat solution treatment of the material to improve its formability. The lower the stress state of the material, the lower the forces and energy required to deform the component. AA2024 in -O temper condition had the best formability of the three tempers.

Even though the -O temper condition material had a lower energy requirement to deform into the desired component, it will be more susceptible to failure as AA2024-O was 60% weaker in mechanical strength than AA2024-T3, as seen in Figure 4.8. An additional disadvantage of the -O temper condition material was it had to be heat solution treated after forming, as it cannot be used in that temper condition due to the strength limitations. Post solution heat treatment can have dire effects on the form with the material having an unknown springback effect. A restrike forming stage may be required. The further heat treatment and restrike manufacturing stages of -O temper condition material will not be investigated in the presented study with only the final form of the component being the desired result.

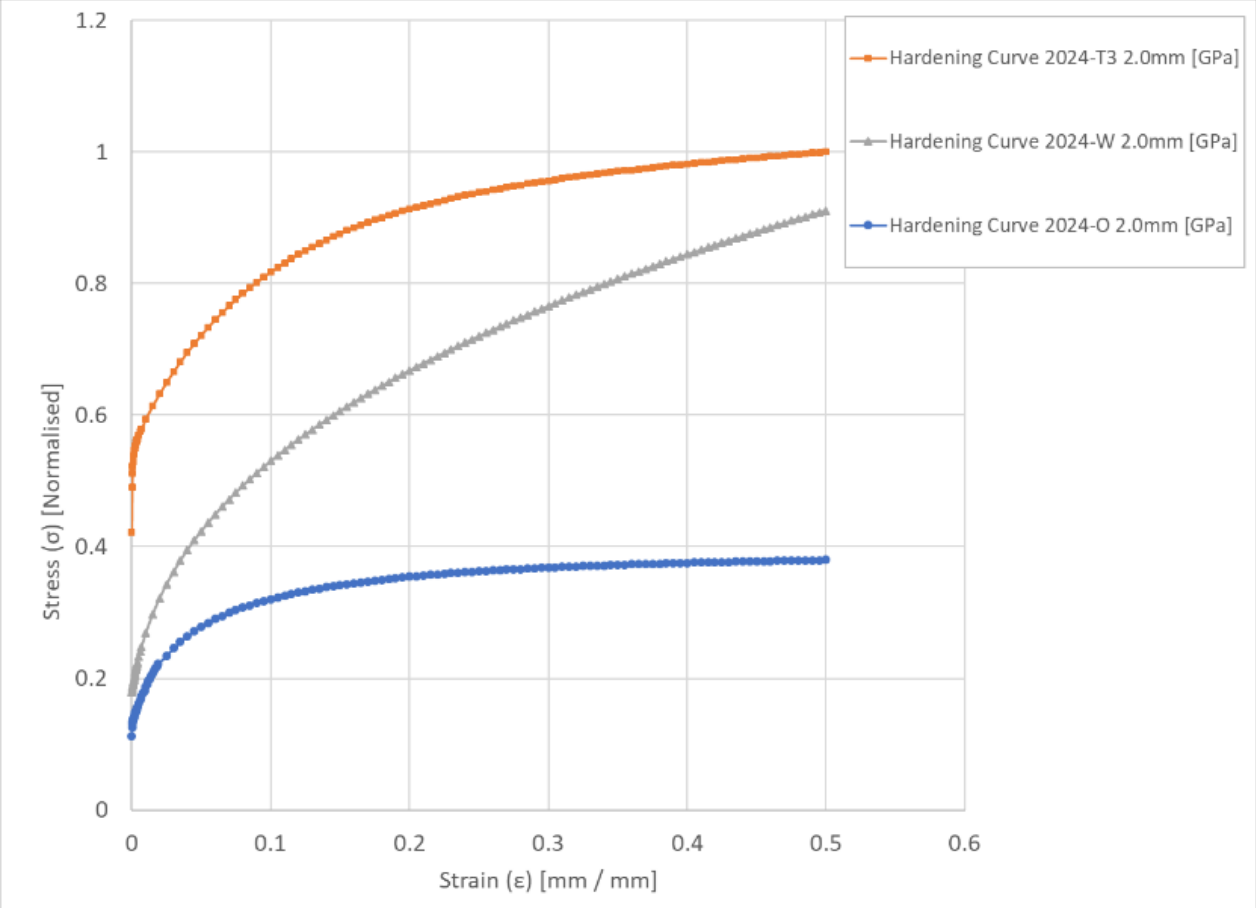

Figure 4.8: Normalised hardening curve comparison of AA2024 2 mm thickness in -O, -W, and -T3 temper condition

Forming limit curve (FLC) tests were conducted at the TUL mechanical testing and tribology laboratory. Figure 4.9 (a) shows a snapshot of the GOM ARAMIS test and measurement software GUI with the result from one of the six different FLC test samples (Figure 4.9 (b)). Several samples of each test sample geometry were tested for the creation of a single FLC curve.

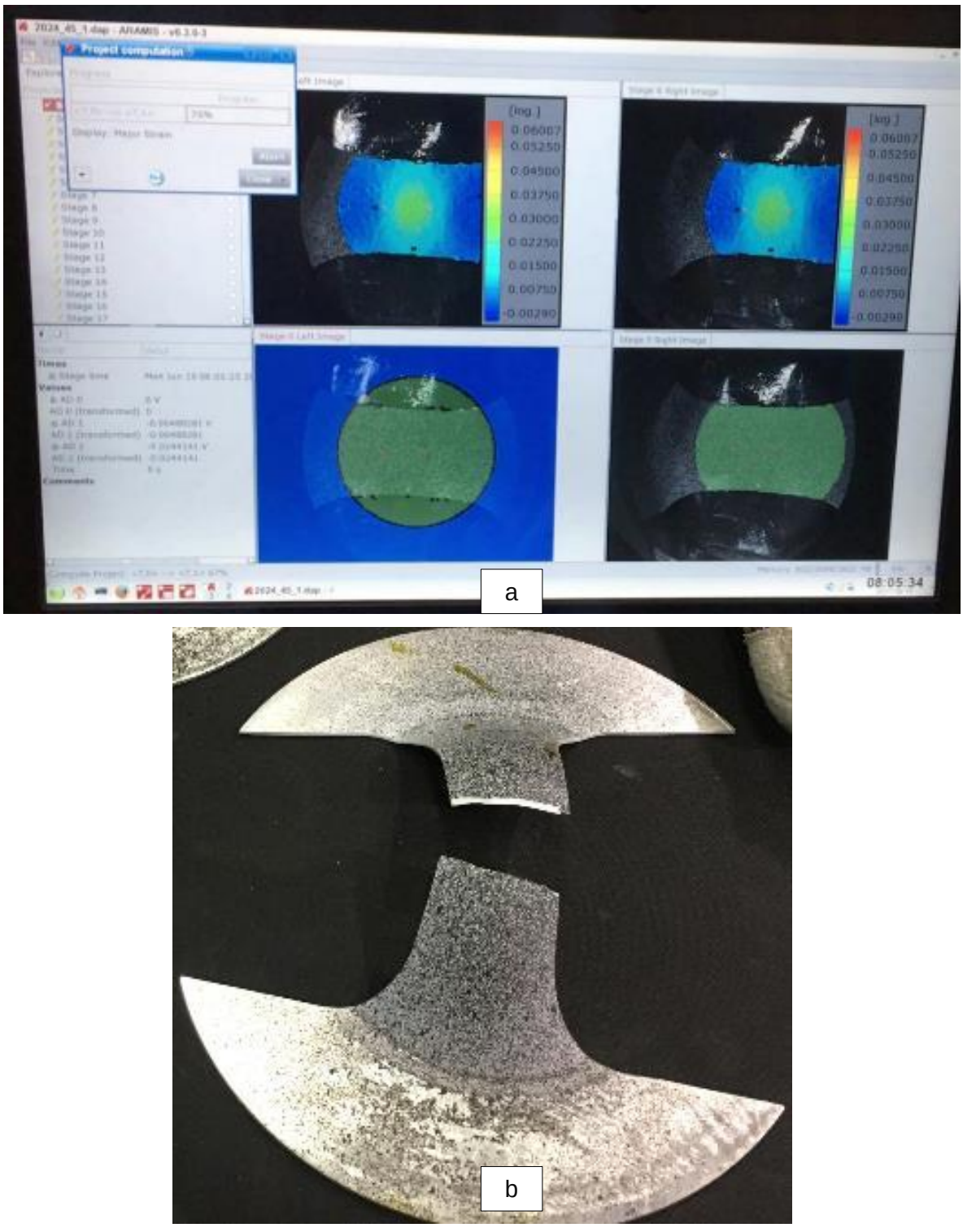

Figure 4.9: (a) Forming Limit Curve Test captured and evaluated using GOM Aramis test and measurement system (b) one of the size tested sample types for FLC characterisation

Figure 4.10 depicts the forming limit diagram (FLD) for AA2024-W and -O 2 mm thick sheet. The -W temper condition FLC, was tested whereas the -O temper condition FLC was extrapolated from literature (see Section 2.2.4). It was evident that the -O temper condition formability was far greater than -W temper condition as the degree of strain experience before rupture of is much greater.

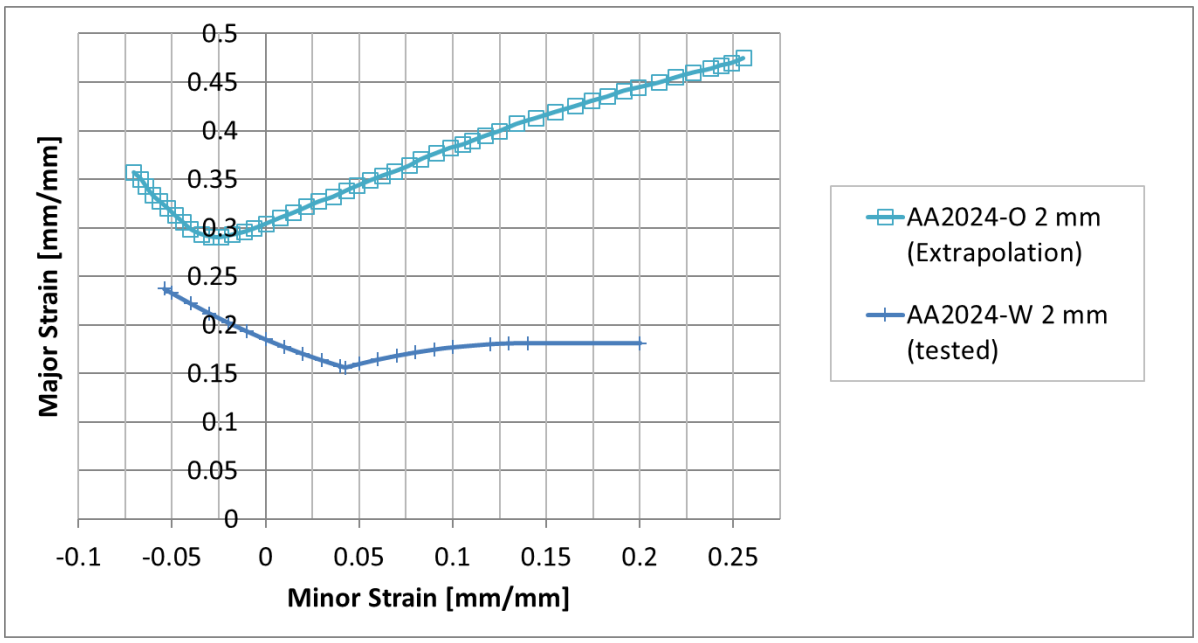

Figure 4.10: FLD with the AA2024-W 2 mm tested forming limit curve and the extrapolated AA2024-O 2 mm curve

The final parameter required was friction. A variable friction coefficient based on pressure and velocity was characterised, but only for the metal-to-metal interface. The rubber-to-metal interface was not conducted. The lubricant chosen was petroleum jelly (which is a synthetic lubricant), as it could be applied in constant layer and is a cheaper alternative to the more costly lubricants.

The clamps and test sample strips used for friction testing on the SOKOL 400 testing machine are depicted in Figure 4.11 (a) and (b), respectively. The testing was carried out at ambient environmental conditions. The sliding velocities [m/s] were: 0.01, 0.05, 0.1, 0.2, and 0.4, for the applied pressure [GPa] range of: 0.001, 0.005, 0.01, and 0.04. A test sample was required for each velocity/pressure point. Thus, base on a minimum of 20 test samples, 120 test samples tested all overall.

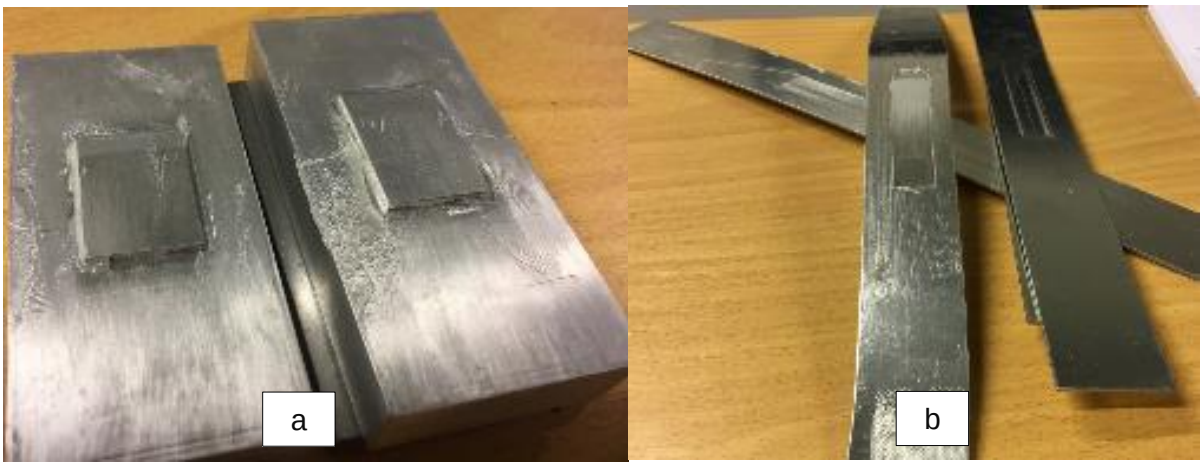

Figure 4.11: (a) Friction clamping jaws for friction testing in the SOKOL 400
(b) Typical friction test samples – 1200 x 44 mm

Figure 4.12 illustrates the variable friction coefficient for a metal-to-metal interface lubricated with petroleum jelly, based on pressure and sliding velocity. The data was published with Aerosud Aviation's permission. The friction coefficient varies from a minimum of 0.15 to a maximum of 0.192. Where this data was not utilised in simulation, a friction coefficient of 0.15 was assumed.

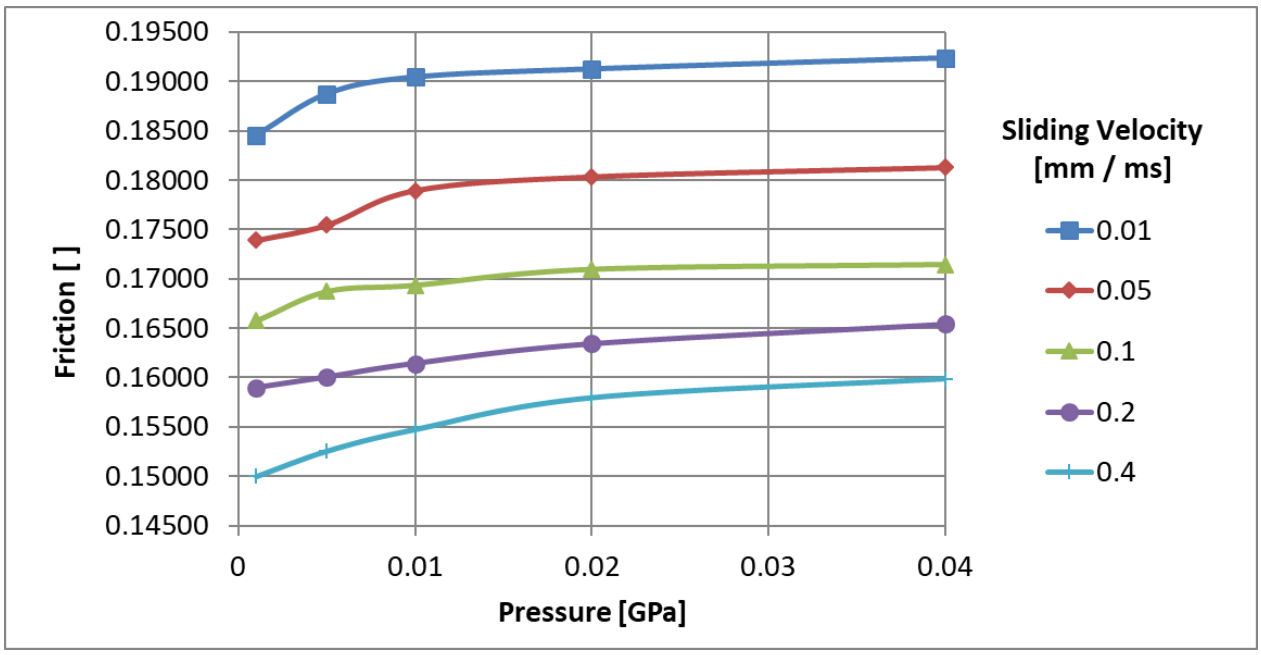

Figure 4.12: Metal – metal lubricated with petroleum jelly, variable friction coefficient based on pressure and sliding velocity

With the material characterised, the simulation investigation could proceed. As the cycle was circular, indicating phases will be revisited until a solution was found. The material characterisation phase was conducted once unless a change was made to the blank material, tooling material, or the lubricant.

4.4. Forming Simulation

4.4.1. Parameter Definition

Due to the set-up procedures within PAM-STAMP, pressure can only be applied to the blank. Simply meshing the silicon rubber pads and applying pressure to it as opposed to the blank was not possible without in-depth knowledge and experience of adapting the solver input deck or standard procedures defined in PAM-STAMP.

An attempt to set-up this type of model with the ESI Groups PAM-STAMP team was attempted but abandoned due to time and complexity. The Mooney-Rivlin law was used for rubber pad simulation, with volume tools (ESI Group 2018). Based on the literature presented in Sections 2.2.5 and 2.3, it was concluded that the modelling of the rubber elements would also require additional testing to characterise both the friction physics and the rubber material properties. Friction is mathematically modelled using Coulomb's friction law, the true physics of sliding rubber in the simulation is simplified. Thus, adding to the computational time of the simulation with little benefit.

The standard fluid forming parameters used for this study are depicted in Figure 4.13. The maximum pressure that was applied by the fluid cell press selected to conduct the forming trial was 0.08 GPa. The autostop criteria selected was contact area, and the maximum fluid pressure time interval set to 1. Contact area is defined as the whole blank, making contact with the tool. The maximum pressure interval is the time, after maximum pressure or the contact area criterion is reached, the applied pressure is held for before the process ends. Even though the maximum pressure that can be applied was 0.08 GPa, the simulation stopped at a lower pressure, when the autostop criteria were met.

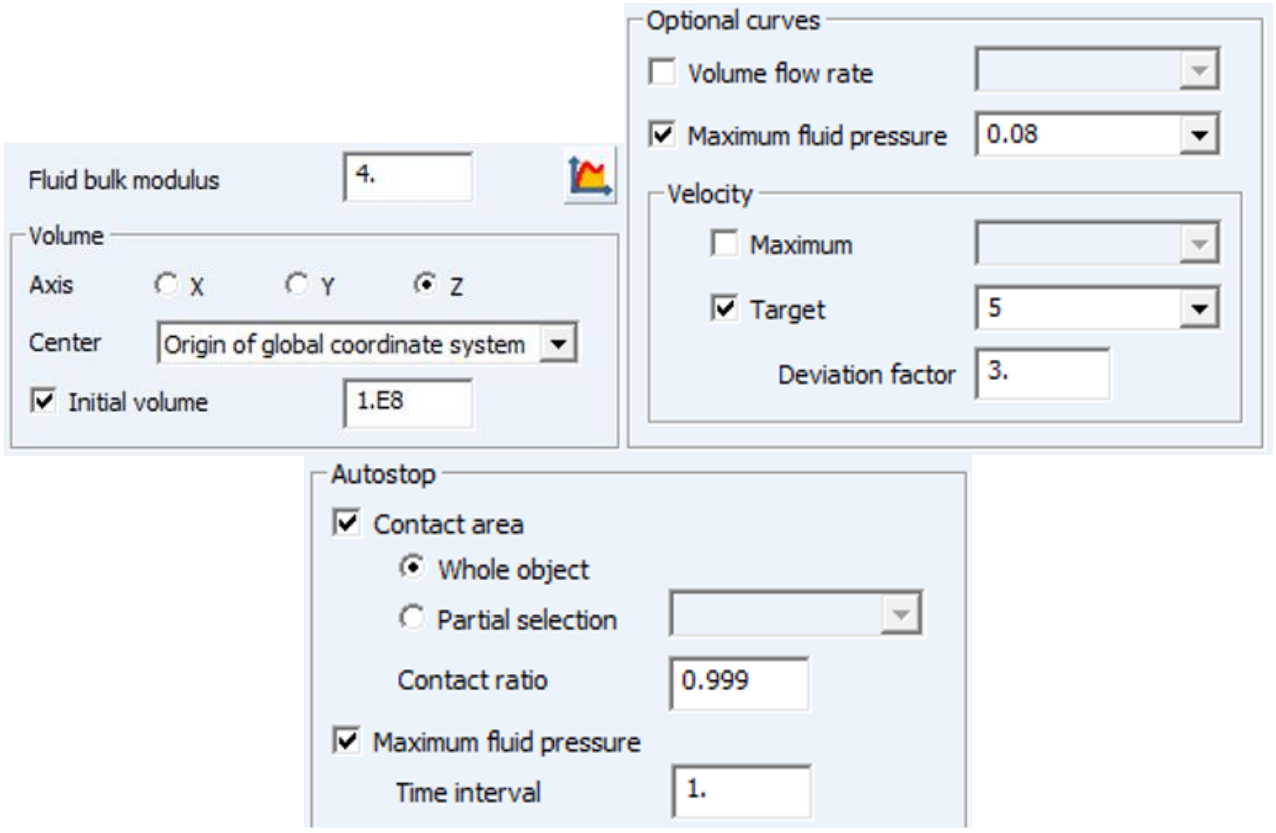

Figure 4.13: PAM-STAMP fluid forming parameters

The pressure was applied over time, and was based on the velocity of the fluid flowing into the system. This is the PAM-STAMP pressure based criterion. A velocity of 5 m/s was specified, resulting in a pressure vs time curve, as shown in Figure 4.14.

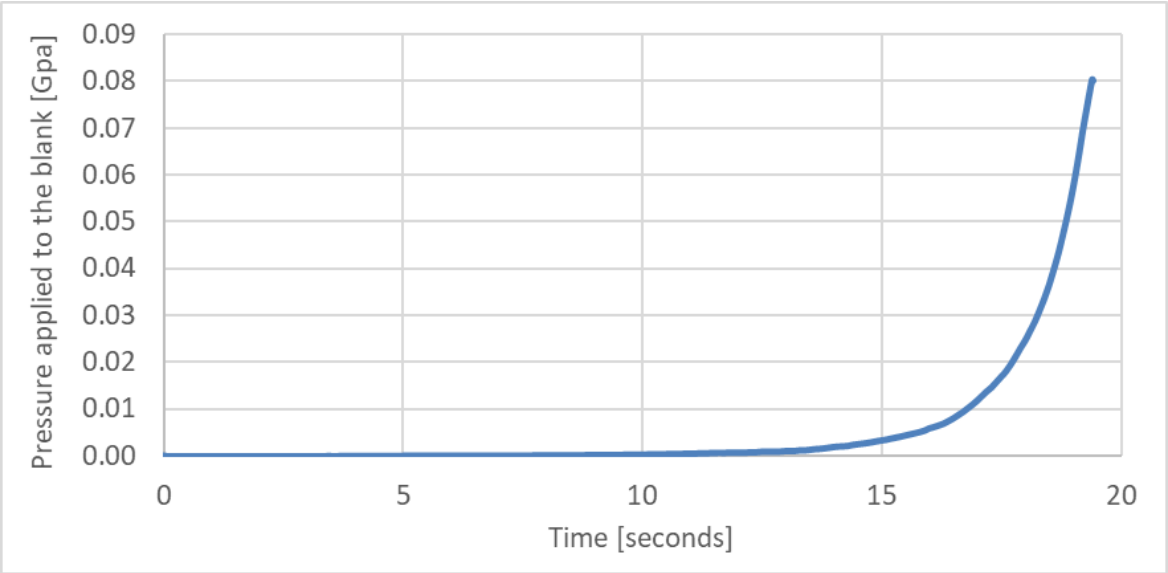

Figure 4.14: Fluid cell pressure applied to the blank vs time

Friction coefficients were defined in Section 4.3. Of the six options available in PAM-STAMP, the friction coefficient was kept constant, or it was varied as a function of pressure and velocity.

After the forming stage was completed, the springback and trimming stages were conducted. The simulation manufacturing stages, as discussed in Section 3.4.3, are as followings:

Single stage manufacturing operations:

OP 1 – Forming stage

OP 2 – Springback stage

OP 3 – Trim and springback stage

Two stage manufacturing operations:

OP 1 – Pre-forming stage

OP 2 – Springback stage

OP 3 – Second forming Stage

OP 4 – Trim and springback stage

4.4.2. Concept-1 through 8 Evolution Summary

This subchapter summarises the design evolution of the blank and tool concepts starting with Concept-1 and concluding with Concept-8. Concept-9 was the chosen concept and is presented in Section 4.5. Concepts 1 through 8 are presented in greater detail in Appendix A. Each concept was evaluated for in-plane stretching using an FLD zone quality plot, a springback pre- and post-overview, and finally, a distortion plot where the final simulation shape and desired shape were compared.

Concept-1 was the simplest, and, possibly, the most cost-effective design solution in comparison to any of the other concepts. The concept never passed the feasibility phase as there was a lack of in-plane stretching in the blank, and the final shape sprung back close to the initial blank shape. The final shape deviated from the nominal surface with a maximum displacement of 26.757 mm (maximum distortion less the minimum distortion). The desired s-shaped curve was not achieved. Figure 4.15 depicts Concept-1 and Concept-2 and the stark difference between them. Concept-1 was designed similarly to the stamping process, whereas Concept-2 was designed to deep draw the blank after the blank's edges draped over the sides of the tool. The draped edges were expected to increase the in-plane stretching.

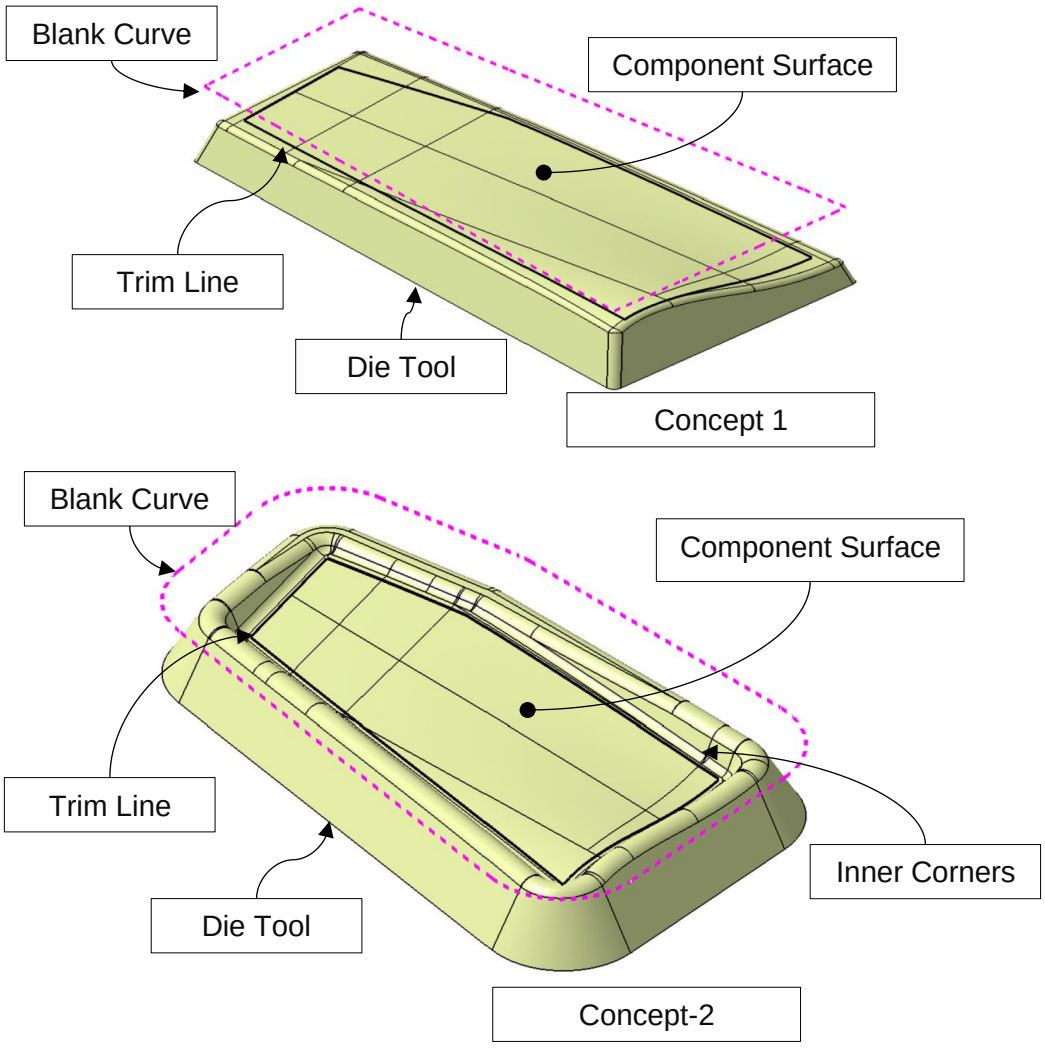

Figure 4.15: Concept-1 and Concept-2 Tool and Blank Comparison

The Concept-2 blank, unlike the process followed for Concept-1's blank, was the outline of the base of Concept-2's tool. Constraining the edge of the blank improved the in-plane stretching but only marginally compared to Concept-1, as seen in Figure 4.16. Concept-2's final distortion showed significant improvement compared to Concept-1, with a maximum distortion of 11.964 mm compared to the nominal surface. The s-shaped curve feature was also achieved and with an edge deviation of 2.462 mm. Further improvement was sought, and thus, Concept-2 was rejected, and another solution attempted.

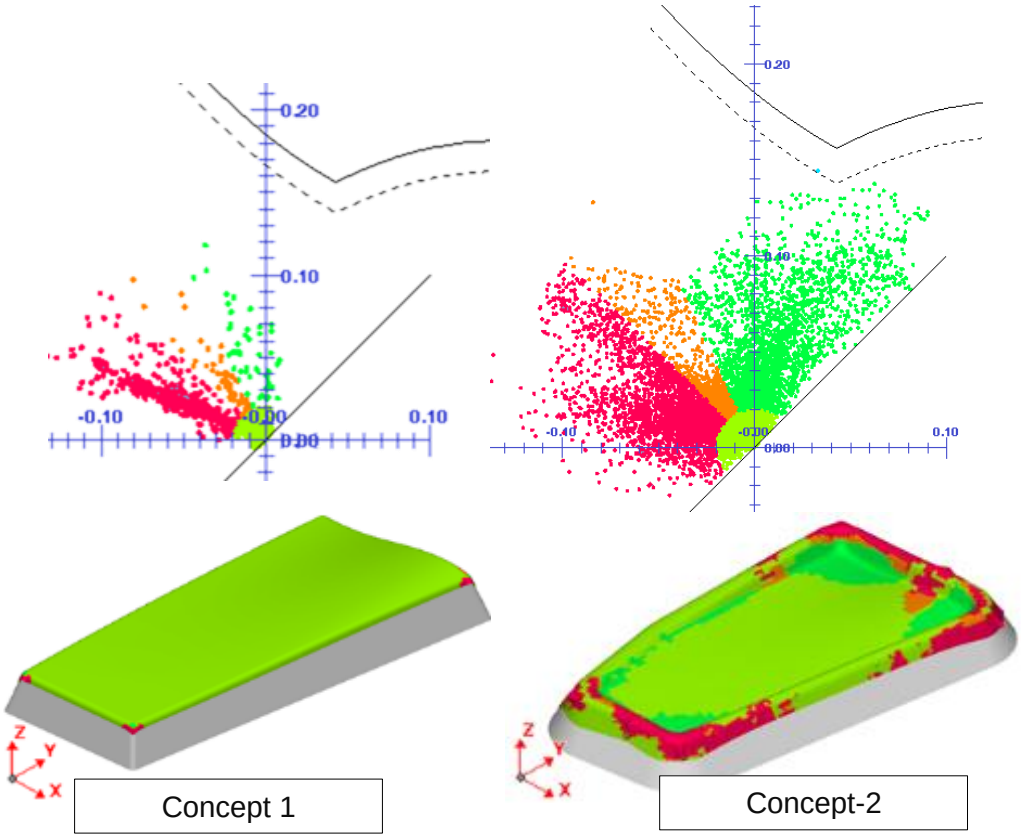

Figure 4.16: Concept-1 and Concept-2 FLD zone quality plot Comparison

The strategy for Concept-3 was to increase the draw depth to increase the in-plane stretching that was witnessed in Concept-2. The added draw depth was accomplished by means of a two-stage forming process. The blank was the outline of the base of Concept-3's tool, similar to Concept-2. The first tool created a pre-formed blank with edges that draped over the second stage tool. The pre-formed definition increased the edge restraint, and thus increased the in-plane stretching of the blank.

Concept-3 showed a further 57% improvement, compared to Concept-2 with a distortion of 5.132 mm compared to the nominal surface. The s-shaped curve was also achieved with a deviation of only 1.235 mm. However, the concept was rejected as the FLD zone quality plot (see Figure 4.17) predicted cracking near the component. PAM-STAMP only presents cracking based on the stress and strain state and not as physical separation of the finite elements. For this reason, the relaxation that would be witnessed in cracking areas was not accurately simulated, and thus the result cannot be accepted as a possible solution.

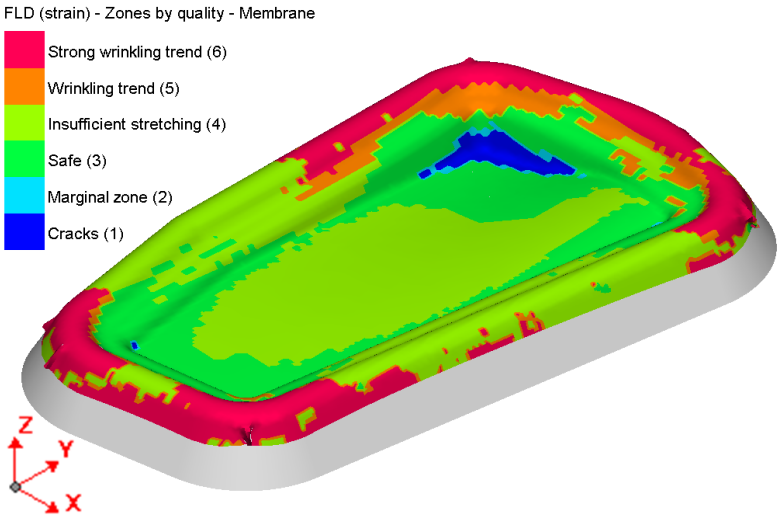

Figure 4.17: Concept-3 FLD zone quality plot

The strategy for Concept-4 was to reduce the draw depth such that cracking would be omitted. Similar to concept's 2 and 3, the Concept-4 blank was the outline of the base of Concept-4's tool. The larger overhanging blank was considered to increase edge restraint in a similar way to Concept-2 and 3. The additional feature in this concept was a draw valley which was assumed to draw the sheet further once the blank made contact with the inner tool surface. The blank was drawn into draw valley and assumed to increase the in-plane stretching. In-plane stretching was improved marginally, but the blank was predicted to crack in the draw valley, as seen in Figure 4.18. Even though Concept-4 did not form without cracking, which renders this concept void, the s-shaped curve was achieved with almost zero deviation. Even with cracking predicted, the s-shaped curve was achieved as the software package did not account for rupture with element splitting. Had the elements split, a greater degree of springback would be witnessed. The blank distorted severely on the opposite side to the s-shaped curve with a distance of 17.656 mm.

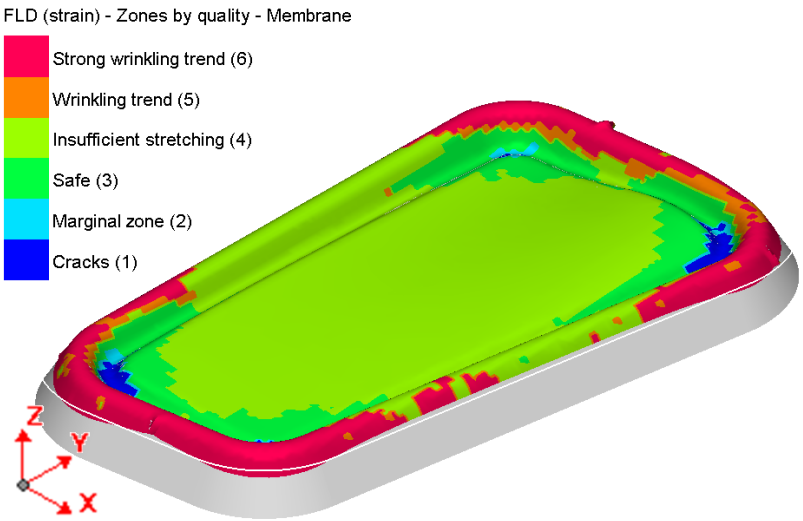

Figure 4.18: Concept-4 FLD zone quality plot

Up to the completion of Concept-4, Concept-3 was the best performing concept thus far without considering the cracking witnessed in two of the concepts. Concept's 2, 3 and 4 maintained a similar outline shape for both the blank and the tool with the internal sections altered. The strategy for Concept-5 was to investigate the feasibility of several blank and tool designs. Three tools and four blanks were conceptualised to investigate alternative shapes to those used previously.

Tool concepts 2 and 4 had shallow draw depths, while Concept-3 had a deep draw depth. Concept-5 tool A was designed with a much deeper draw depth than any of the previous concepts. Concept-5 tool A's draw depth was increased by 59.3% and 35.1%, compared to Concept-2 and 3, respectively. Due to the blank designs used with Concept-5 tool A, cracking was not predicted as these blanks do not drape over the tool like the previous concepts. Figure 4.19 depicts Concept-5's tool A design and the outlines of blank A and B. Compared to concepts 2, 3 and 4, Concept-5 tool A was designed with straight edges and a flat top surface.

The outer tool radii of Concept-5 tool A were smaller than the previous concepts. Concept-3 outer radii were 30 mm, whereas Concept-5 tool A had outer radii of 10 mm. The smaller radii had the potential to affect the way the blank was constrained as it was assumed to bend around a smaller radius more severally than a larger radius, and thus increasing the in-plane stretching.

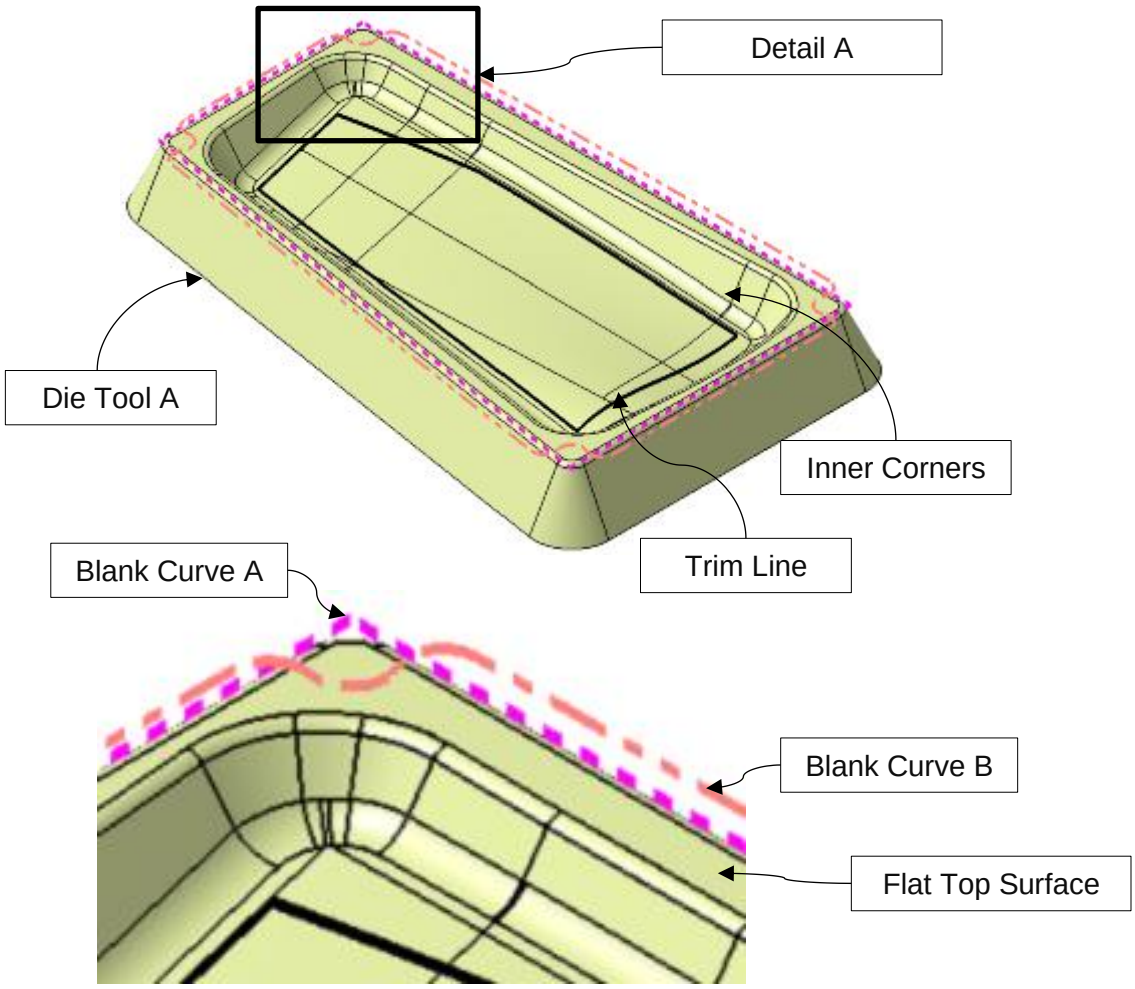

Figure 4.19: Detailed view of Concept-5's Tool A and Blank A & B

The previous blank concepts were designed with large overhangs and a continuous edge. The continuous edge feature of blank concepts 2, 3 and 4, and the lack of locating features in concepts 2, 3 and 4 tools, would result in difficulties aligning the blank on the tool identically to the simulated forming process. For the blank to align with the tool easily and accurately, it had to interface with defined features incorporated into the tool design. Alignment features were erroneously not considered for the initial concepts. Concept-5's blanks A and B were designed with the intent to improve alignment with the tool.

Concept-5 blank A formed on tool A performed poorly with little in-plane stretching and large distortions to a maximum of 20.512 mm compared to the nominal surface. Concept-5 blank B formed on tool A performed even worse, as the final component was predicted to have wrinkling as seen in Figure 4.20. Wrinkling was predicted to severely distort the formed component as the simulation showed that the component might have a predicted distortion of 23.88 mm from the nominal surface. Both Concept-5's tool A configurations with blank A and B were rejected as design solutions.

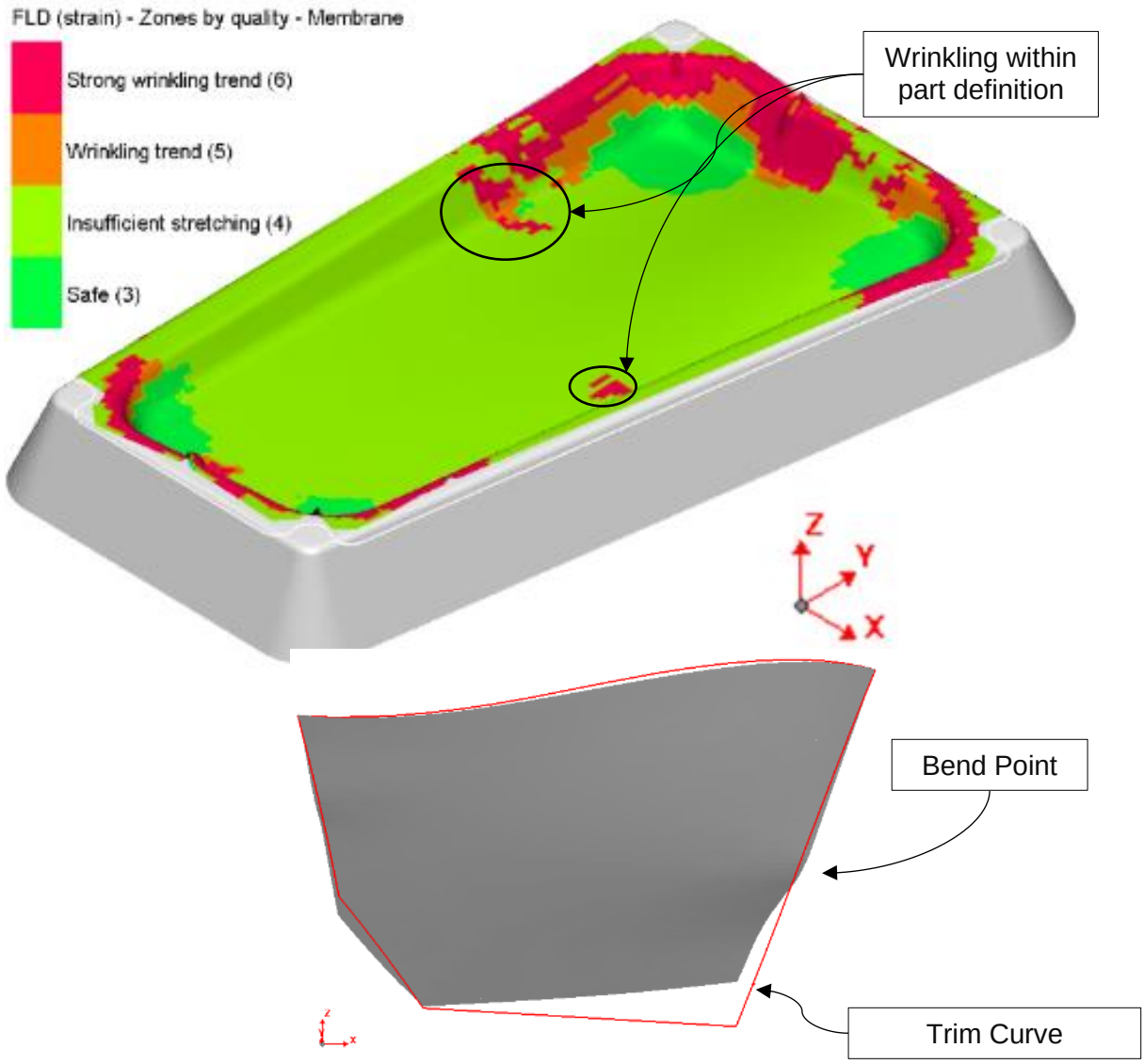

Figure 4.20: Detailed view of the lack of alignment features

Concept-5 tool B was designed to have curved segments. In addition, the distance from the inner corners to the edge of the final component in tool A was close, whereas this distance was made larger in tool B. The curved segment design was introduced to omit the wrinkling seen in the Concept-5 tool A and blank B configuration. Blank B was retained and used with tool B to investigate its feasibility to omit wrinkling. Blank C was introduced with a much larger overhang, compared to blank B, but the overhang compared with concepts 2, 3 and 4 was much smaller. Concept-5's tool B, blank B and Blank C are depicted in Figure 4.21

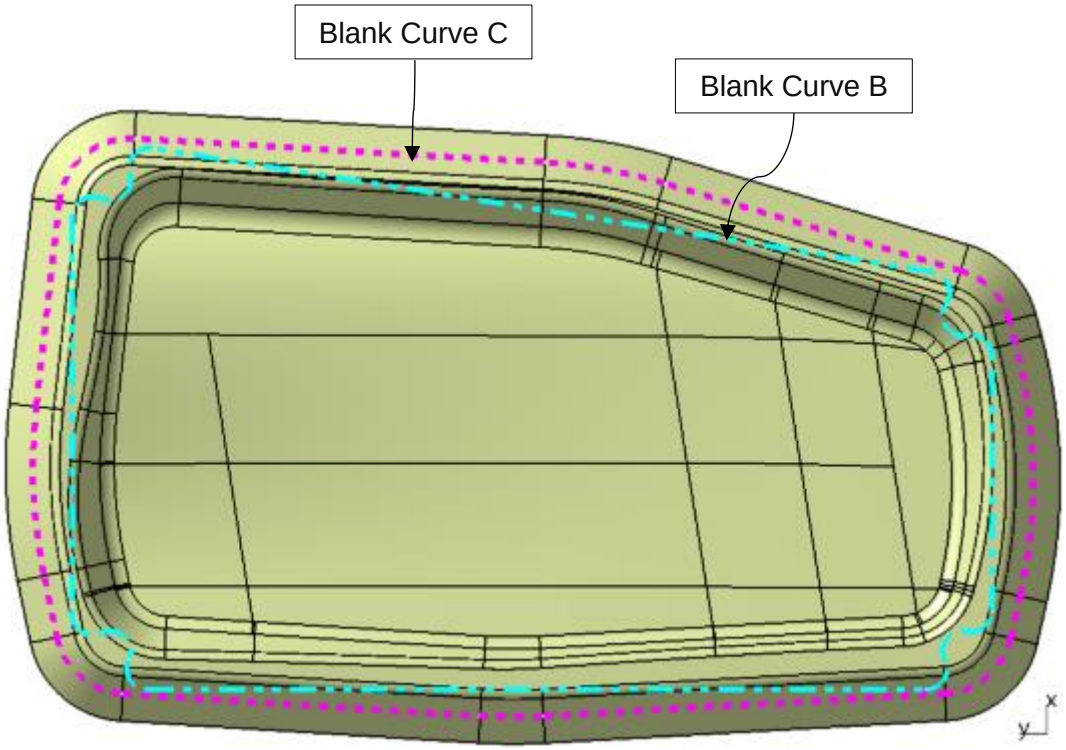

Figure 4.21: Concept-5 tool B, blank B and C top view

Concept-5 tool B did not show an improvement for either blank B or C, compared to any of the concepts attempted thus far. Both blank B and C configuration for tool B showed excessive distortion and almost no in-plane stretching. In an attempt to recover the poor performance of this concept, tool C was designed with the same outline definition as tool B, except the outer section was reduced by 16 mm as shown in Figure 4.22.

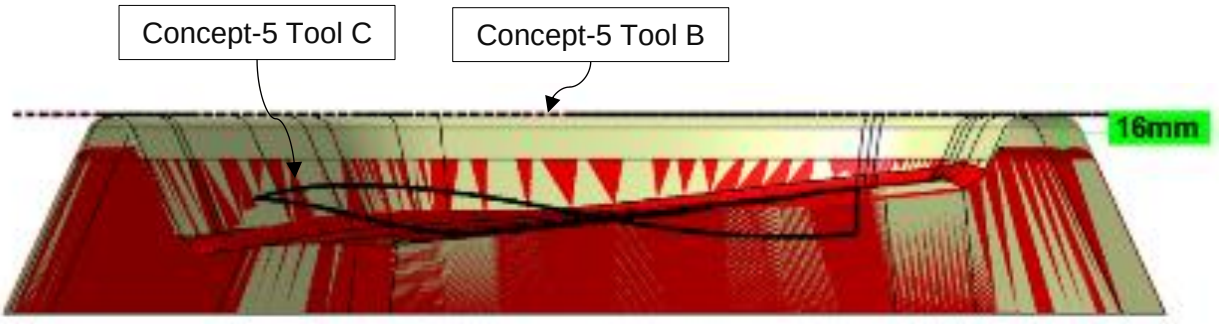

Figure 4.22: Concept-5 tool C height reduction compared to tool B

The change in height resulted in the draw depth of tool C becoming less than tool B. Blank D was designed with a small overhang and traced the outer edge of tool C's upper rim as shown in Figure 4.23. The blank saw little in-plane stretching and cracking was predicted. The concept was rejected due to excessive distortion of 26.067 mm from the nominal surface and cracking.

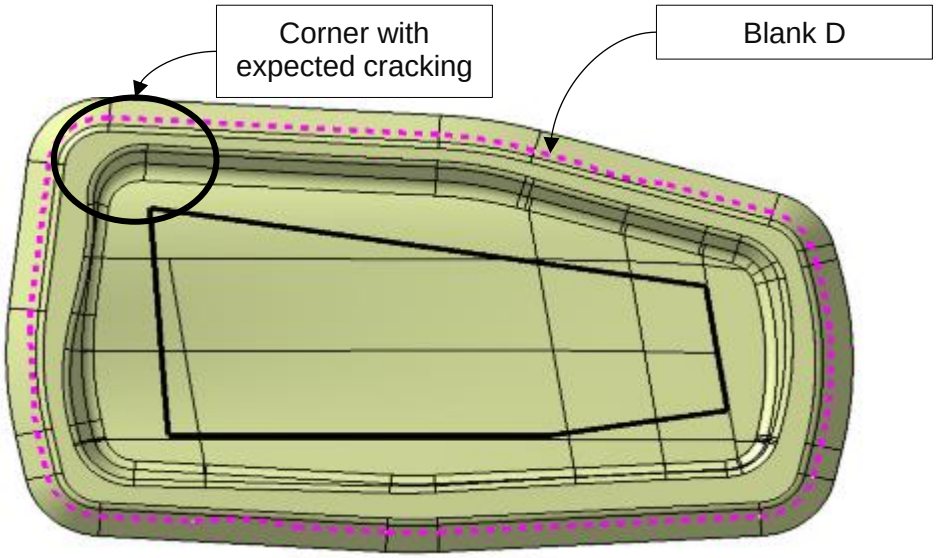

Figure 4.23: Concept-5 tool C and blank D top view

Building on the findings thus far, Concept-6 was designed with a deeper draw depth and large overhangs, as these features had shown promising results. The draw depth of Concept-5 tool A and the overhang lengths of the blank from Concept-2, 3 and 4 were used to conceptualise the Concept-6 design. In addition, the flat top surface was utilised with edge radii of 10 mm. Unlike the emphasis in Concept-5 to ensure alignment of the blank during manufacturing, Concept-6's blank did not utilise this necessary feature. Alignment features were omitted to assess the capability of the tool. Concept-6 is presented in Figure 4.24.

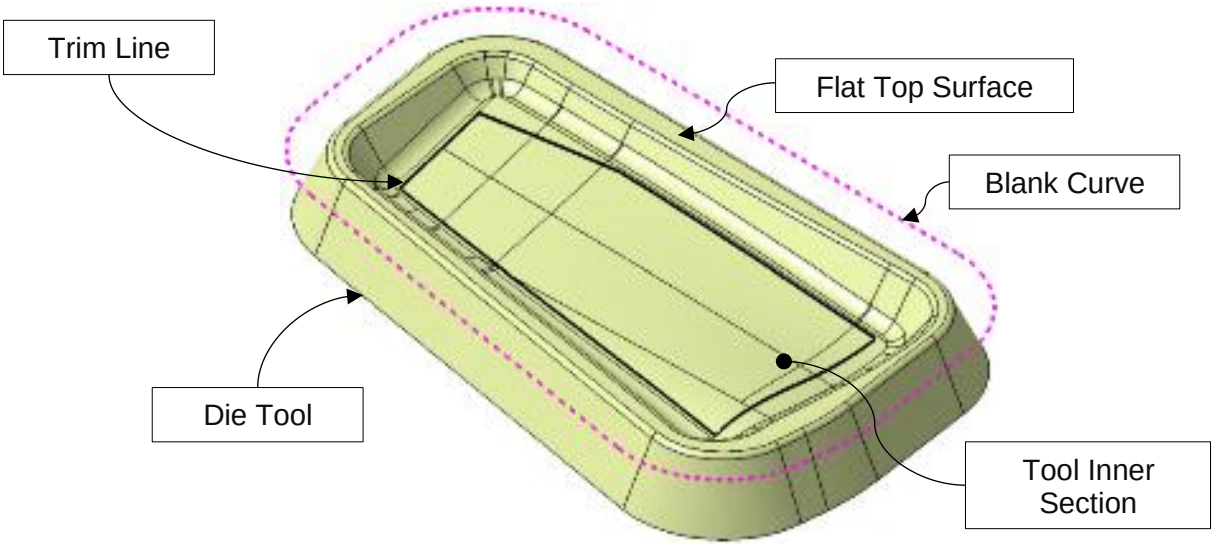

Figure 4.24: Concept-6 blank and tool definition

Concept-6 performed marginally worse than Concept-3 with a maximum distortion of 7.472 mm. The concept showed no signs of cracking, but in-part wrinkling was predicted in the same location as seen in the Concept-5 tool A and blank B configuration. The s-shape curve showed a predicted distortion of 1.067 mm. The intent was to achieve a final distortion within the 1.4 mm surface profile tolerance. Thus, the concept was rejected in pursuit of a better performing concept.

The promising result of Concept-6 was used in the development of Concept-7. The distance from the final part to the inner corner was increased to omit possible wrinkling in the component. As there was no cracking seen in the previous concept, the draw depth remained the same. However, due to the s-shape curve, the form was predicted to crack in the same place as was predicted in the Concept-5 tool B, blank C and Concept-5 tool C, blank C configurations. The blank size was much larger than the tool to drape over the sides. The blank was based on the tool's base outline, as done in concepts 2, 3, and 4. The inner and outer sections of the tool model were separated to conduct an optimisation study. The two surfaces were split to allow the inner tool section to be altered by the tool compensation optimisation study, and the outer section of the tool was unchanged maintaining the form of the tooling. Concept-7 is presented in Figure 4.25.

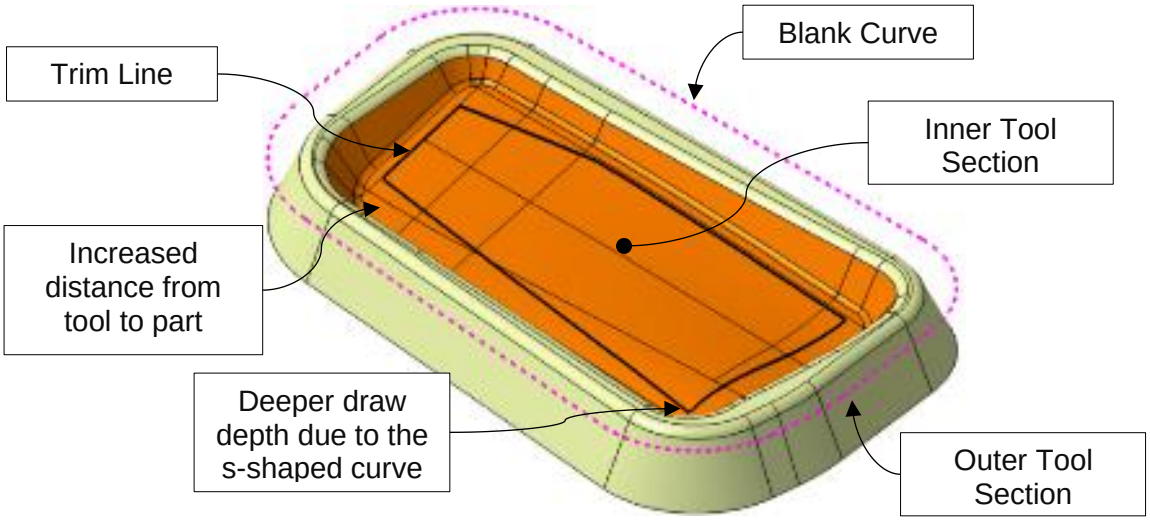

Figure 4.25: Concept-7 blank and tool definition

The simulation was conducted with the Vegter isotropic, and the Vegter kinematic material cards. Both showed very similar results with predicted cracking and wrinkling in the same regions. The only difference was the predicted final distortion of the respective simulated components. The tool compensation optimisation study improved the form as cracking was reduced significantly. However, wrinkling in the same region was witnessed. Overall, the maximum distortions were 4.621 mm and 7.415 mm for the Vegter isotropic and the Vegter kinematic material cards, respectively. The optimised tool showed a maximum distortion of 3.671 mm compared to the nominal surface.

The Concept-7 tool exhibited a form not witnessed in any of the other concepts. The Vegter isotropic material form had a much larger central bulge than that of the Vegter kinematic material. The optimisation study was predicted to correct for this bugle and thus reduced it significantly. Even with an improvement in the final form of the component, Concept-7 and the optimised tool were rejected. The blank and tool designs were not suitable as a manufacturing solution without accurate alignment features. In addition, the compensated tool was output in an STL ASCII geometry format which would need to be parameterised for it to be manufactured.

All the concepts showed a similar trend with the blank bottoming out before the overhang edges formed completely. For Concept-8, Concept-5's blank B definition was revisited. The overhang size of Concept-5 blank B was extended and function similarly to a flanging operation. Thus, the extended overhang features are termed flanges. Concept-8 is presented in Figure 4.26. Three investigations were conducted using the Concept-8 blank and tool design:

1. A single-stage tool concept
2. A two-stage tool concept pre-forming the flanges in the first stage
3. Investigate blankholder force required to get complete in-plane stretching

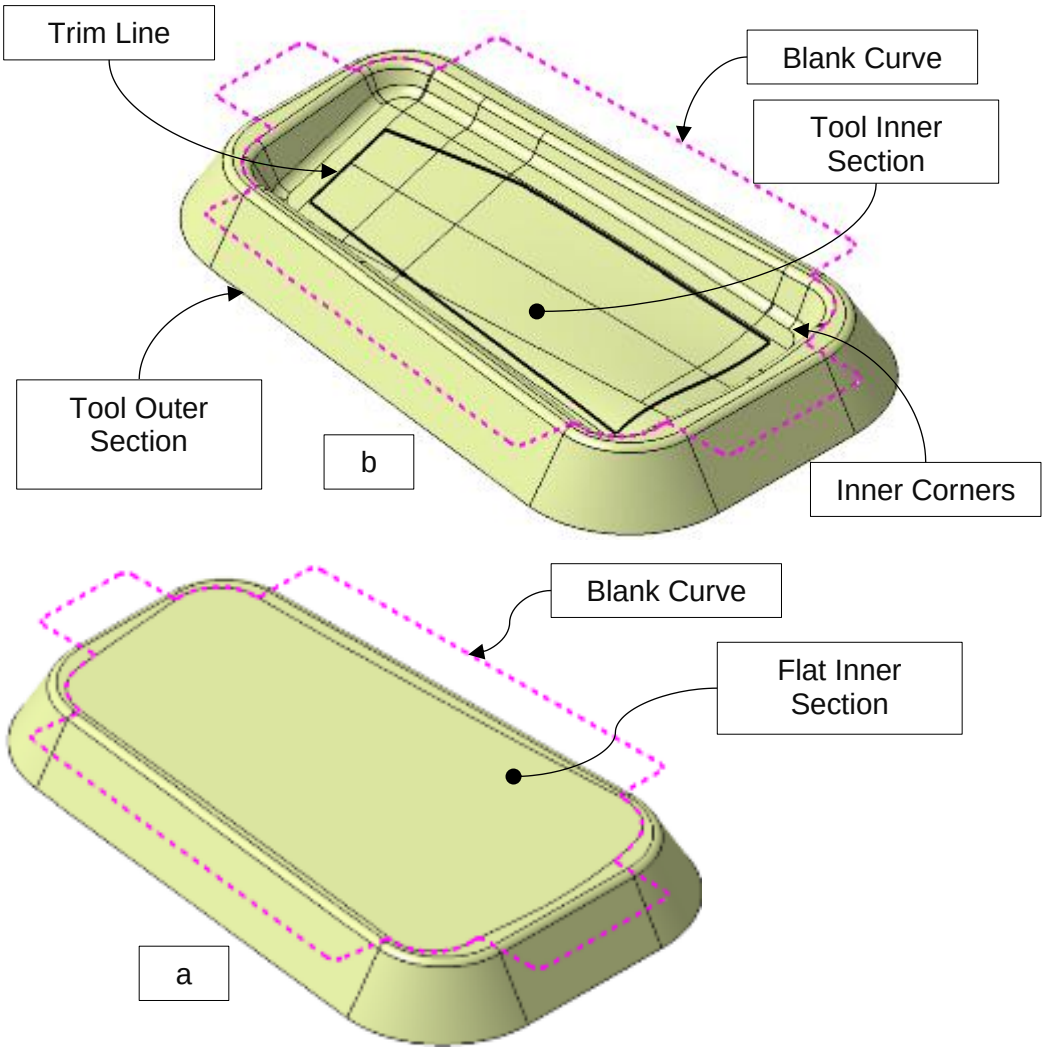

Figure 4.26: Concept-8 blank and first (a) and second (b) stage tool definition

The single stage process made use of the second stage tool with one pressing. The two stage process made use of the first stage tool to pre-form the blank with the second stage tool pressing the component into its final form.

The third investigation of Concept-8 made us of blankholders, as shown in Figure 4.27. The purpose of this investigation was to simulate different blankholding forces, which increased the blanks edge restraint condition and then access the predicted in-plane stretch and springback of the component.

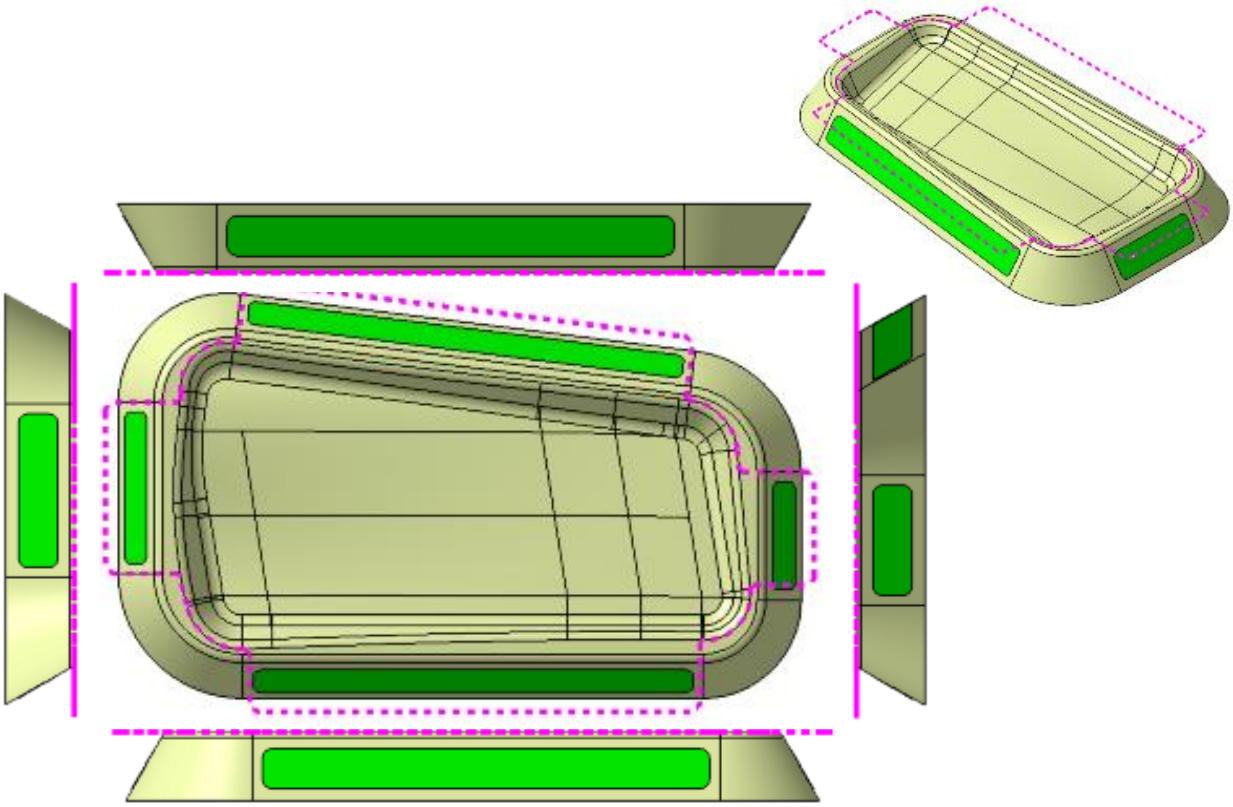

Figure 4.27: Concept-8 blank and tool with blankholders

The single stage pressing of Concept-8 showed promising results. No wrinkling or cracking was witnessed in the component. In-plane stretching was negligible except in the corners. The predicted distortion of the final component was 15 mm from the nominal surface. The s-shaped curve feature of the tool was well defined but was predicted to distort by 3.397 mm. The single stage resulted in the flanges coming into contact with the sides of the tool once the blank bottomed out. The blank bottoming out does not allow for the flanges to be restrained, which were predicted to improve the in-plane stretching in the blank.

The second stage investigation began with the flat-topped first stage tool and a flat blank. In the first stage forming process, the flanges of the blank are folded over the edge of the tool. The second stage tool was then activated in the simulation with the blank positioned automatically above it. The flanges are now already in contact with the tool sides with the inner portion of the pre-formed blank still flat. As the pressure was increased, the friction was expected to increase, similar to how a blankholder functions. As the pressure was extremely low at the beginning of the forming process and only increased exponentially in last 5 seconds (see Figure 4.14 in Section 4.4.1), the applied loading to the flanges was not high enough to restrain the blank, and thus the two stage process for Concept-8 did not provide an improvement compared to the single stage pressing.

The in-plane stretching witnessed in the second stage forming process for Concept-8 was almost identical to the single stage. The blank displacement of the two stage pressing was of 12.292 mm, compared to 15 mm for the single stage. The s-shaped curve feature was well defined compared to the single stage pressing, with a deviation of 1.756 mm.

The intent, starting with Concept-2, was to improve the in-plane stretching by restraining the edges of the blank. The final investigation of Concept-8 would provide insight into how effective blankholders would be in increasing in-plane stretching of the blank. The flat blank was pre-forming using the first stage tool, the second stage tool was then activated, and the pre-formed blank

positioned as conducted in the second investigation. The blankholders were then activated and pressed against the side of the tool, holding the blank's flanges down at a specified force. Starting with 50 kN, then 100 kN, and increasing in intervals of 100 kN until 1000 kN. 250 kN and 750 kN blankholder forces were also applied. As the blankholder force was increased, so the degree of in-plane stretching increased until almost the entire blank was within the safe zone or zone 3. Minor cracking was predicted for the 1000 kN scenario. Figure 4.28 presents some of the FLD zone quality plots for the 200, 700, and 1000 kN blankholder forces (see Appendix A.10, Figure A.79 and Figure A.80 for all the blankholder force's FLD zone quality plots).

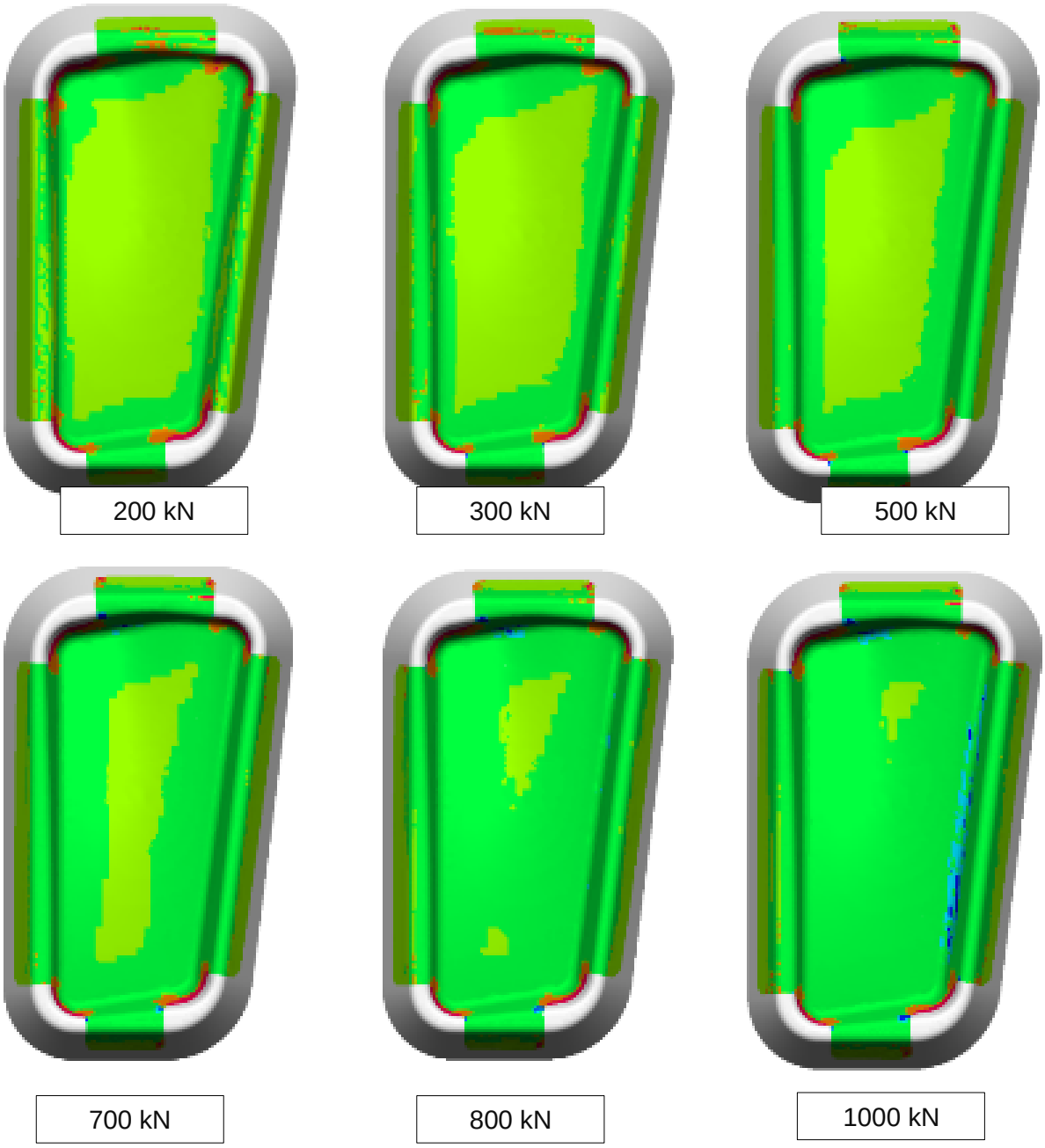

Figure 4.28: Concept-8 FLD results for the varied blankholder force investigation

Figure 4.29 is a bar graph chart of the simulated blankholder forces versus the predicted distortion of the final component. The only anomaly was the 50 kN force, which predicted a lower distortion compared to the 100 kN force. The main purpose of the investigation was to access how the distortion would trend as the blankholder force was increased. The optimum loading was 700 kN, after which the springback regressed with an increase in blankholder force. The 700 kN blankholder force scenario predicted the maximum distortion of the blank to be 1.585 mm compared to the nominal surface.

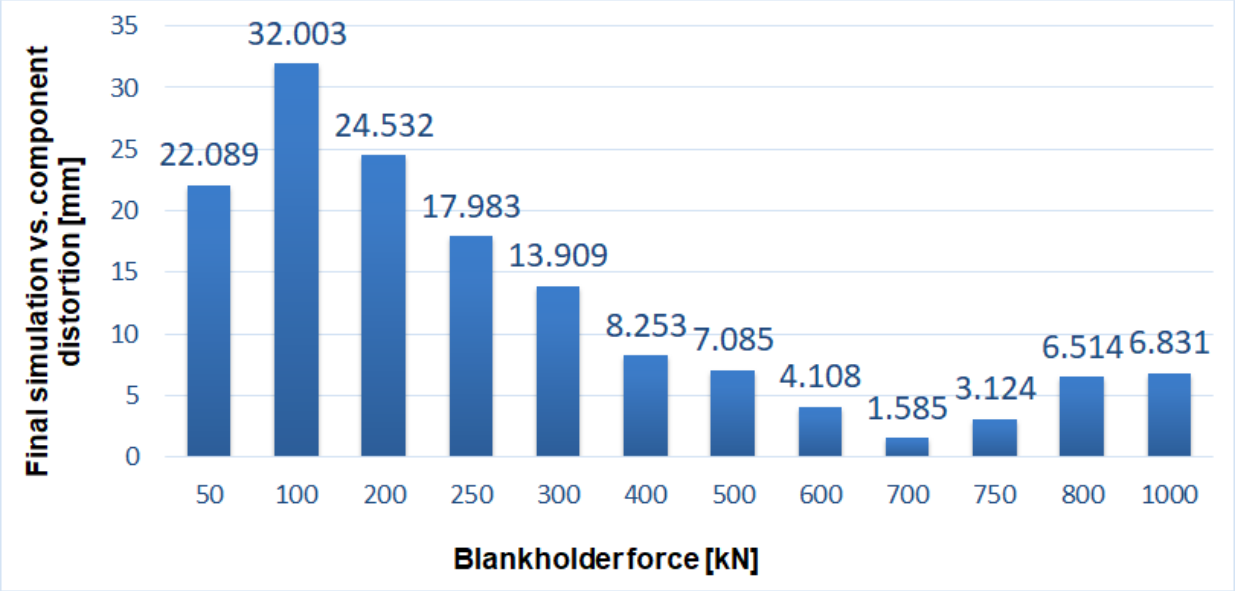

Figure 4.29: Concept-8 blankholder force vs final simulation form distortion

The exceptional result of Concept-8 with pre-loaded blankholders was still rejected as it was not feasible. The disadvantage of the fluid cell forming press was the lack of blankholding mechanisms compared to a typical stamp forming process. The blankholders for Concept-8 would need to be bolted to the sides of the second stage tool using sixteen M16 bolts on the longer edge, and torque tightened to at least 135 Nm.

AA2024-W aluminium alloy sheet after heat solution treatment will naturally age quickly after removal from the refrigerator. Thus there is limited time to get the pre-formed blank and blankholders correctly fastened down. Ensuring the several bolts are all applying the correct loading is too a time-consuming process, aside from the difficulty of ensuring the correct pressure is applied uniformly. A tightening sequence will need to be followed as the bolts, the blankholders and blank deform under the localised pressure the bolts apply. The pre-loaded bolt will be relaxed as the next one is fastened into position.

Assuming the torque tightening each bolt has provided the pressure loading (without some form verification), the time taken to complete all four sides of the tool will likely exceed time limit in which the -W temper conditioned blank must be pressed within. The disassembly of the blankholders to prepare the next blank must be taken into account too. The solution will be time-consuming and thus only applicable to extremely low production rates, with the risk of the blank being pressed in a much harder condition than what is intended. Even though the concept was rejected, the results from Concept-8 provided significant insights on how to proceed with conceptualising Concept-9.

In total, 12 forming simulation feasibility studies were conducted. From Concept-1 to 8, understanding the fluid cell forming process and the design requirements for tool and blank was established. The blank and tool design changes from Concept-1 to Concept-8 are summarised in Figure 4.30 and Figure 4.31, respectively.

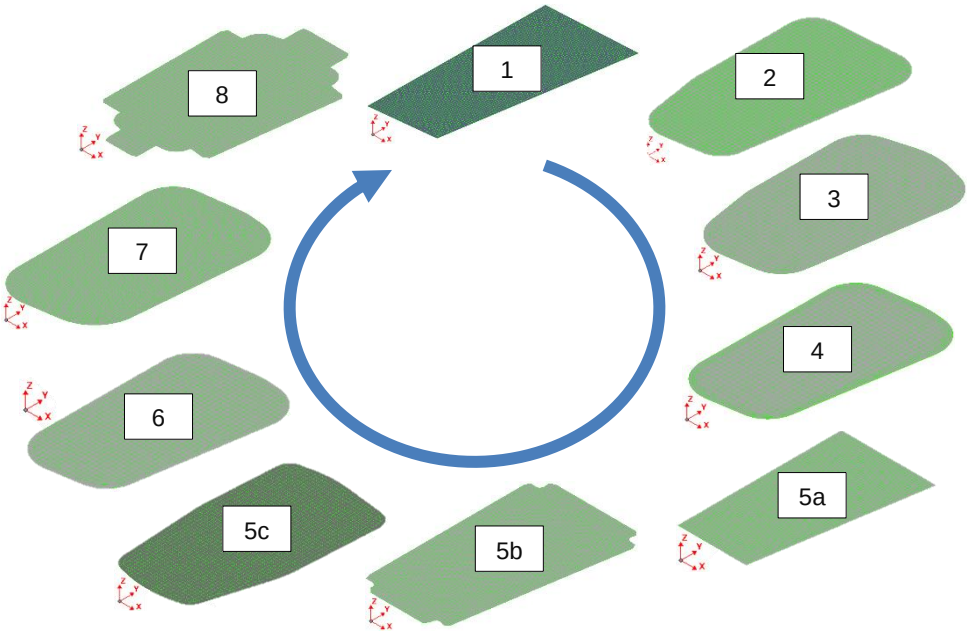

Figure 4.30: Blank design evolution

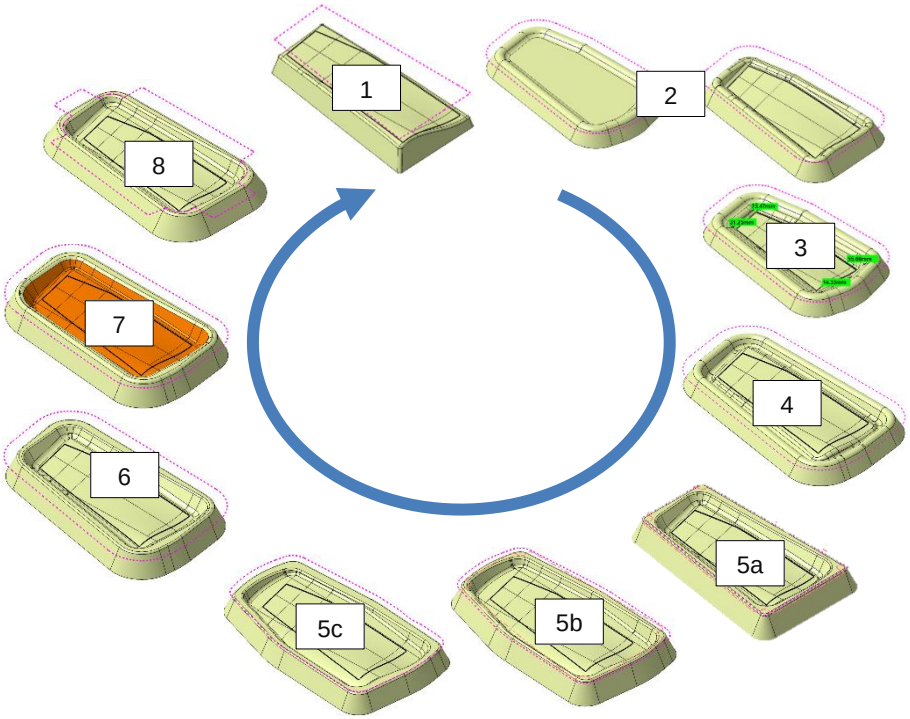

Figure 4.31: Tool design evolution

4.5. Manufacturability

Based on the results from all the concepts (see Appendix A), Concept-9 was designed to meet the following criteria:

1. Large overhang blank flanges
2. Optimal tool draw depth
3. Two-stage tooling to create a pre-form blank to increase restraint loading
4. A blank alignment mechanism on the tool

The tool and blank designs from Concept-7 and the findings from Concept-8 were used to develop Concept-9. The blank corners were rounded tangential to the flange edge. This design feature omitted the stress concentrations that resulted in the corners of Concept-8. The first stage tooling had blank alignment features that allowed for quick and accurate alignment of the blank on the tool, a key feature that was lacking in all previous concepts. By restraining the edges of the blank, a blankholder feature was introduced. The first stage pre-formed the blank flanges, allowing for natural alignment and holding of the blank during the second stage forming process. Holding rollers were proposed to increase the holding force on the blank edges in addition to the pre-formed flanges. Hydropiercing was introduced for the final trim location punch hole features to be created. The location points on the formed part are for accurate alignment in a computer numerically controlled (CNC) milling machine.

A tool compensation optimisation study similar to what was conducted for Concept-7 was not implemented for Concept-9 for two reasons. The compensated tool from Concept-7 was output in an STL ASCII geometry format which would need to be re-designed into a parametric solid body geometry for it to be manufactured. Due to the advanced CAD design knowledge and experience required to model the compensated surfaces adequately, within the time frame available for this research, the optimisation study was not conducted for Concept-9. In addition, had Concept-9 been manufactured with compensation, and the component did not meet the design requirements, what would have caused this deviation would essentially create more variables that would need to be validated.

The lack of compensation to the tool surface did not affect the outcome of the study, as the simulation and the manufactured component would be compared against a common surface profile. This validated the simulations capability to accurately predict the form of the component, irrespective of the final component meeting the design tolerance specification or not.

Figure 4.32 depicts the first and second stage tooling and blank designs for Concept-9.

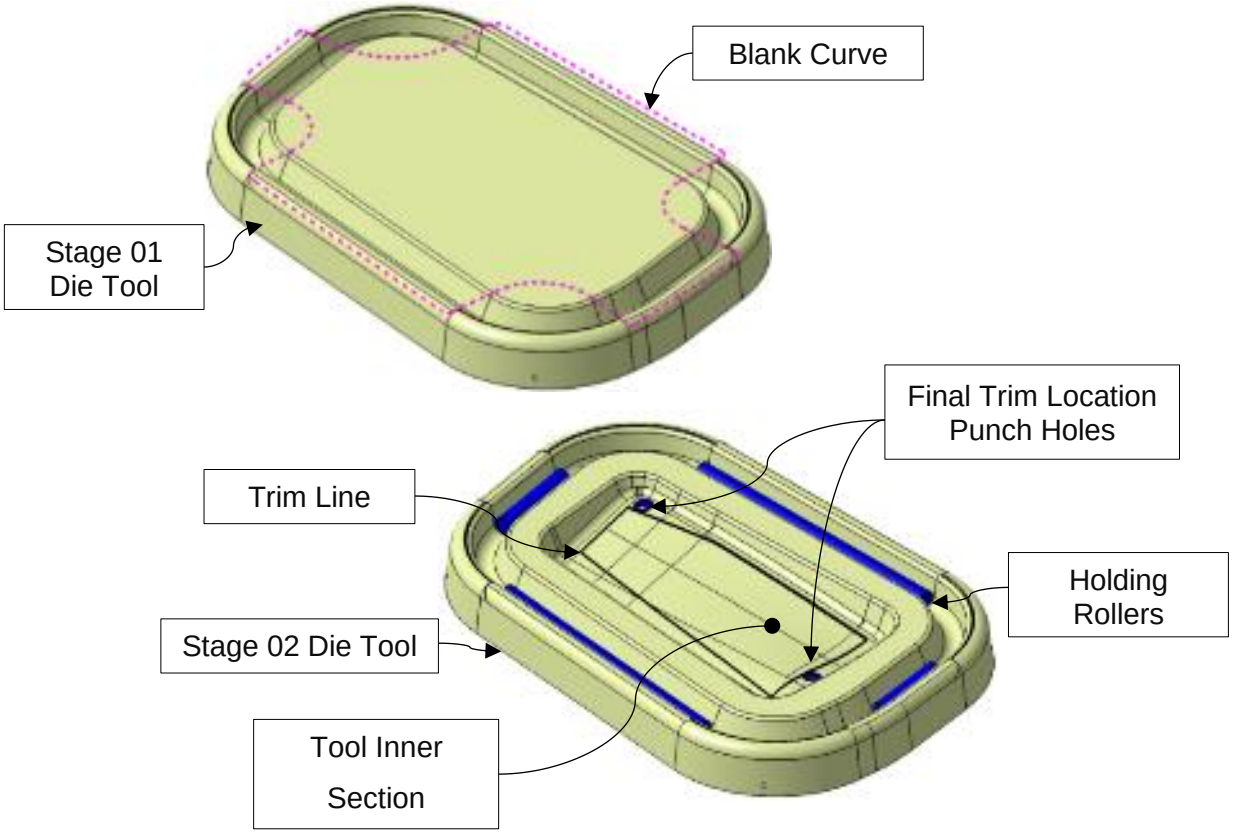

Figure 4.32: Concept-9 first and second stage tools and blank

Figure 4.33 depicts the top and side view of Concept-9's stage 1 tool and blank. The minimum edge radius of the tool was 10 mm. The blankholder feature was drafted with an angle of 25° on the inner face and 10° on the outer face. The depth of the feature was 30mm with a bottom radius of 22 mm.

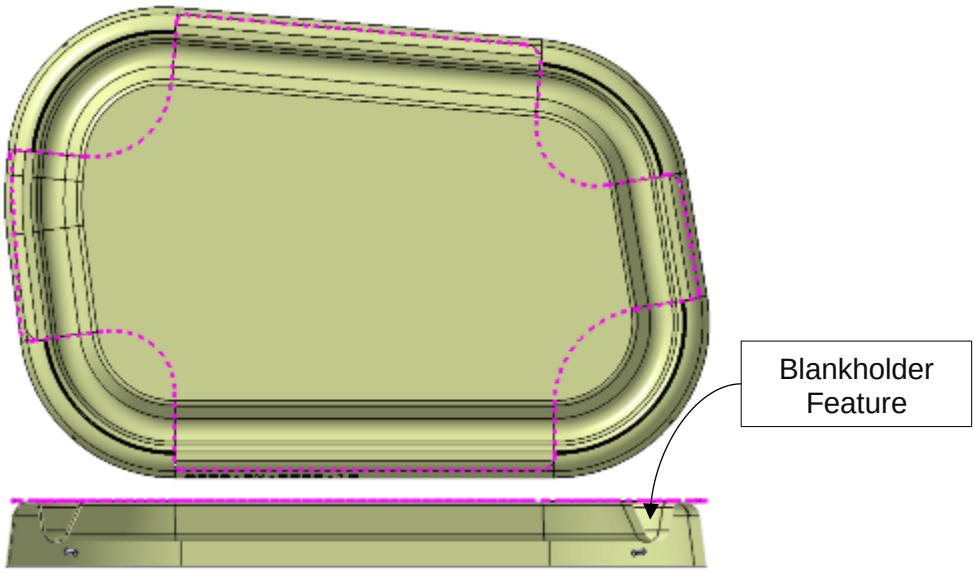

Figure 4.33: Concept-9 stage 1 tool and blank – top and side views

Figure 4.34 depicts the top and side view of Concept-9's stage 2 tool and the holding rollers. The rollers had a diameter of 40 mm. Like the draw depth of Concept-7, the draw depth of Concept-9 was 37mm.

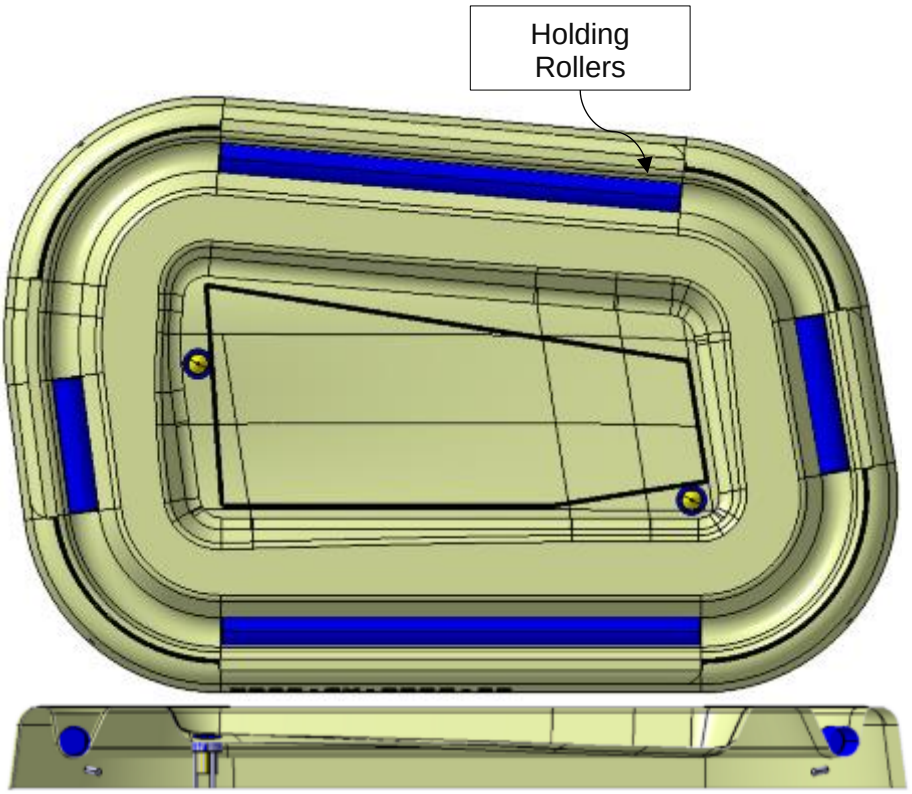

Figure 4.34: Concept-9 stage 2 tool – top and side views

Figure 4.35 depicts Concept-9's blank mesh and a detailed view of the edge definition. The mesh element size for the blank was 8 mm. Due to the tight radius of the blank. The flanges are meshed with a level 3 refinement to ensures the edge definition is captured accurately. The sheet metal rolling direction was in the y-axis.

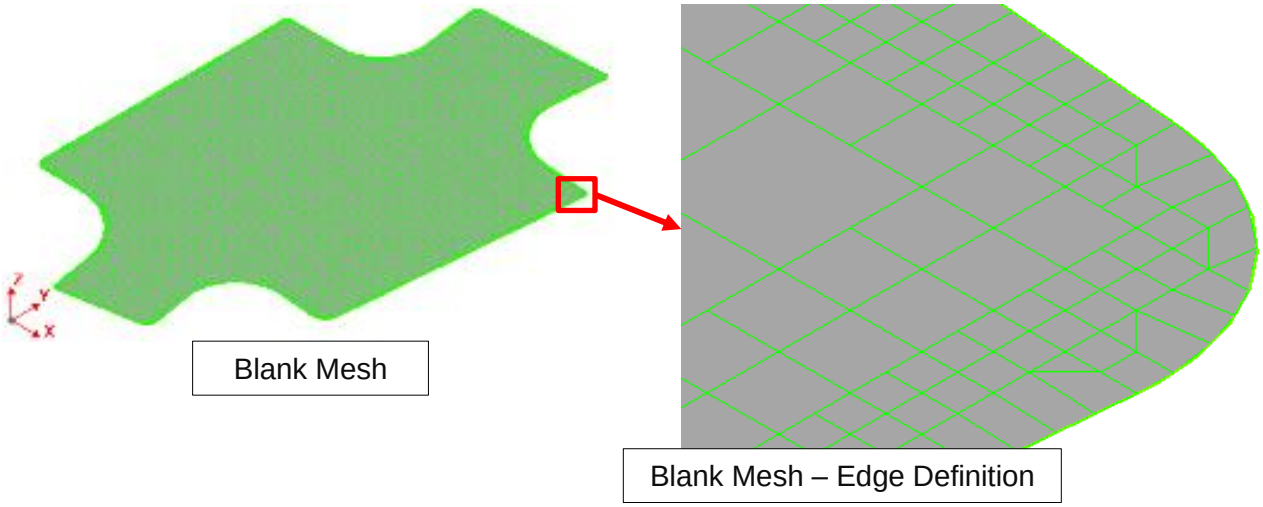

Figure 4.35: Concept-9 Blank Mesh and detailed edge definition

Figure 4.36 depicts Concept-9's first and second stage tool, trim curve and the assembly. As the minimum edge radius for both of Concept-9's tools was 10 mm, the edge radius to element size was 1.25:1. A blank mesh refinement level of 3 was used which provided a final element size of 2 mm. Hence, the edge radius to element size was 5:1, which was deemed acceptable for the manufacturability assessment to continue. The five elements over an edge rule was a recommendation to capture the curvature of the form (Chen et al. 2014), (ESI Group 2018).

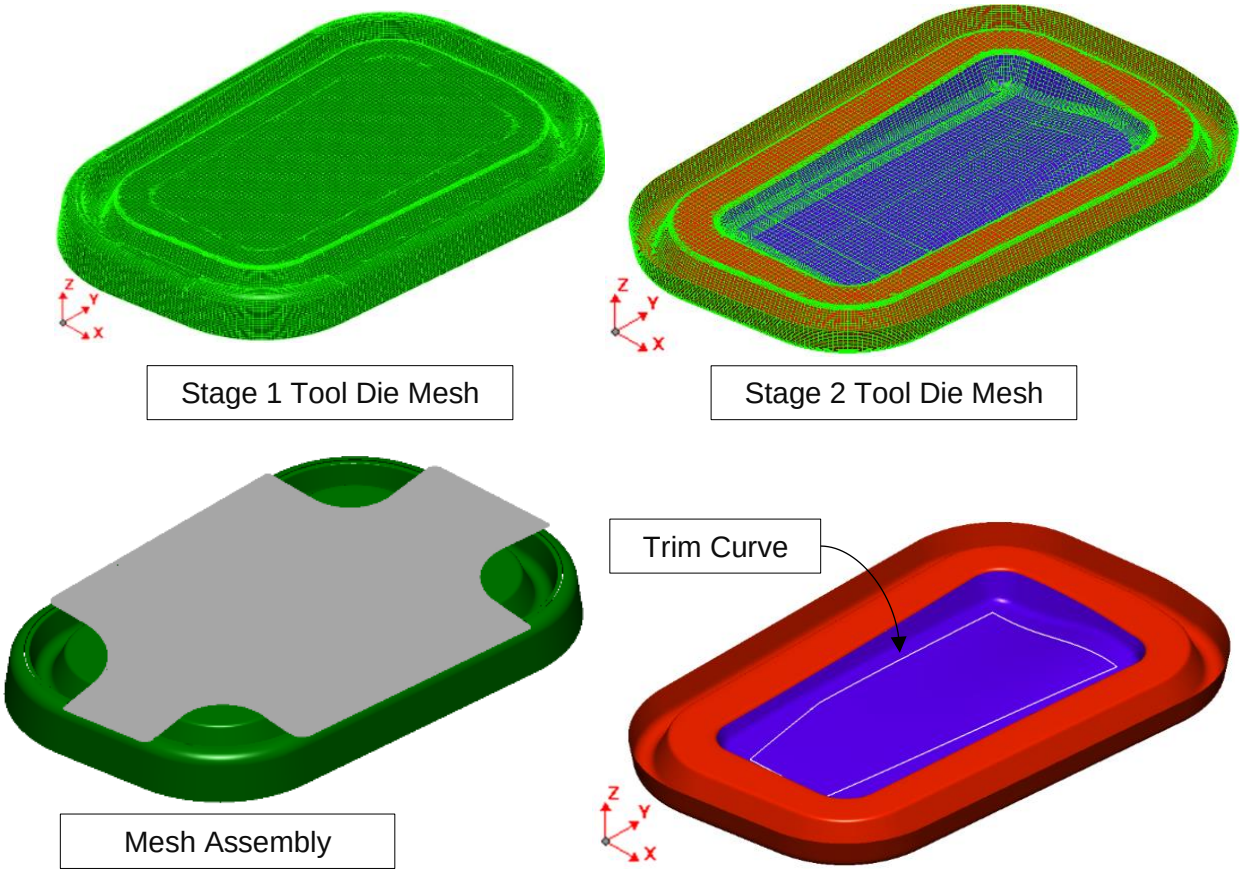

Figure 4.36: Concept-9 first & second stage tool, blank, trim curve and the assembly

The simulation set-up was:

1. The forming stage: a fluid cell forming operation of the first stage tool and the flat blank.
2. The springback stage: springback of the pre-form.
3. The forming stage: a fluid cell forming operation of the second stage tool and the pre-formed blank
4. The springback stage: springback of the formed component
5. The trimming stage: Trimming of the form to the final shape.

The total progression time of the two forming stages was limited to 30 seconds, with a maximum pressure of 80 MPa. Once the blank came into full contact with the tool, the forming stage completed. A state result was provided every 2.5 seconds. The material card used for this simulation was the Vegter yield locus lite plasticity law and the Yoshida-Uemori kinematic hardening law. A friction coefficient of 0.15 was applied.

Figure 4.37 depicts the first stage tooling, fitted with the pre-formed blank ready for the second forming stage.

Figure 4.37: Concept-9 First stage pre-form

The rollers were postulated to apply a restraint loading condition to the pre-formed blank during the forming process. The restraint load was assumed to increase as the fluid pressure increased during the forming process. Figure 4.38 (a) depicts the actual pressure loading condition. Figure 4.38 (b) depicts the fluid cell pressure loading, that was only applied to the blank and cannot be applied to the rollers. In order to apply a load to the roller, a blankholding force must be applied, as shown in Figure 4.38 (b). The loading applied was in effect double the applied loading to the blank, because of the loading from the roller and the fluid cell pressure.

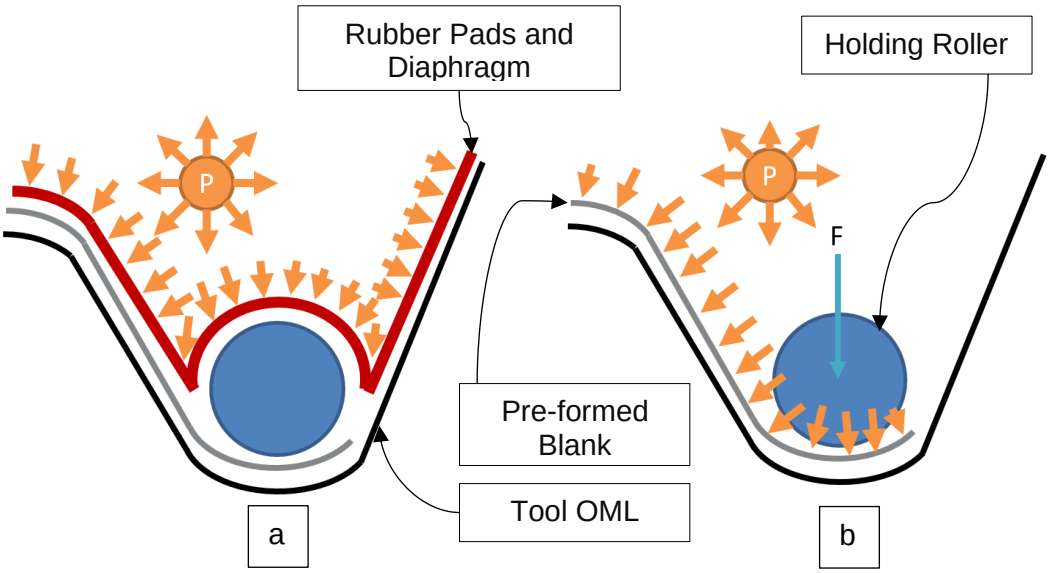

Figure 4.38: (a) Actual pressure loading condition (b) As-simulated loading condition

Figure 4.39 depicts the fluid cell pressure applied to the blank for the complete forming process. Due to the autostop contact area criterion, the maximum pressure applied was 0.031737 GPa.

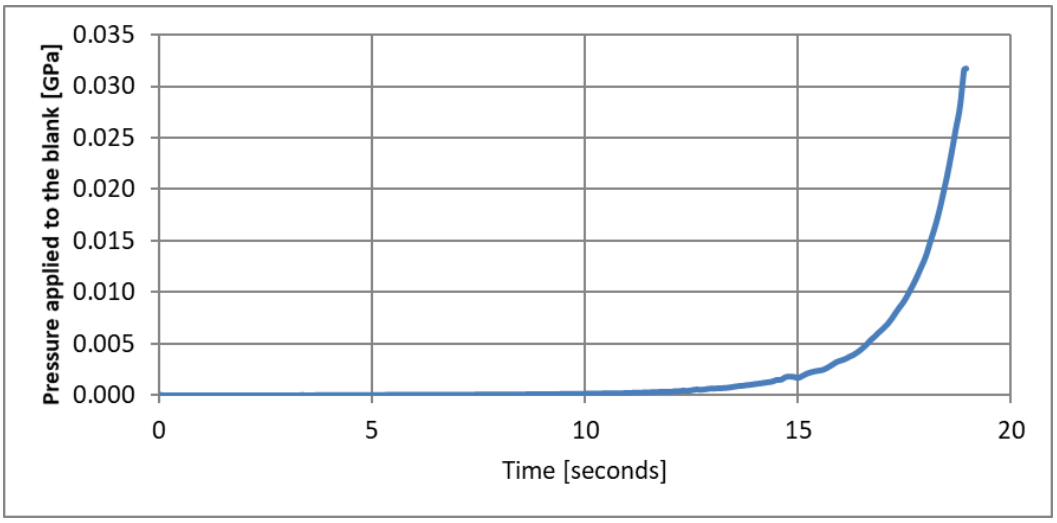

Figure 4.39: Concept-9 fluid cell pressure applied to the blank vs time

The rollers had a diameter of 40 mm and varying lengths of 653 mm, 223 mm, 675 mm and 190 mm. Using the cross-sectional area of the roller and the applied fluid cell pressure defined above, the holding roller force for each roller could be determined. For each holding roller, the loading time curve that was applied in the simulation is shown in Figure 4.40.

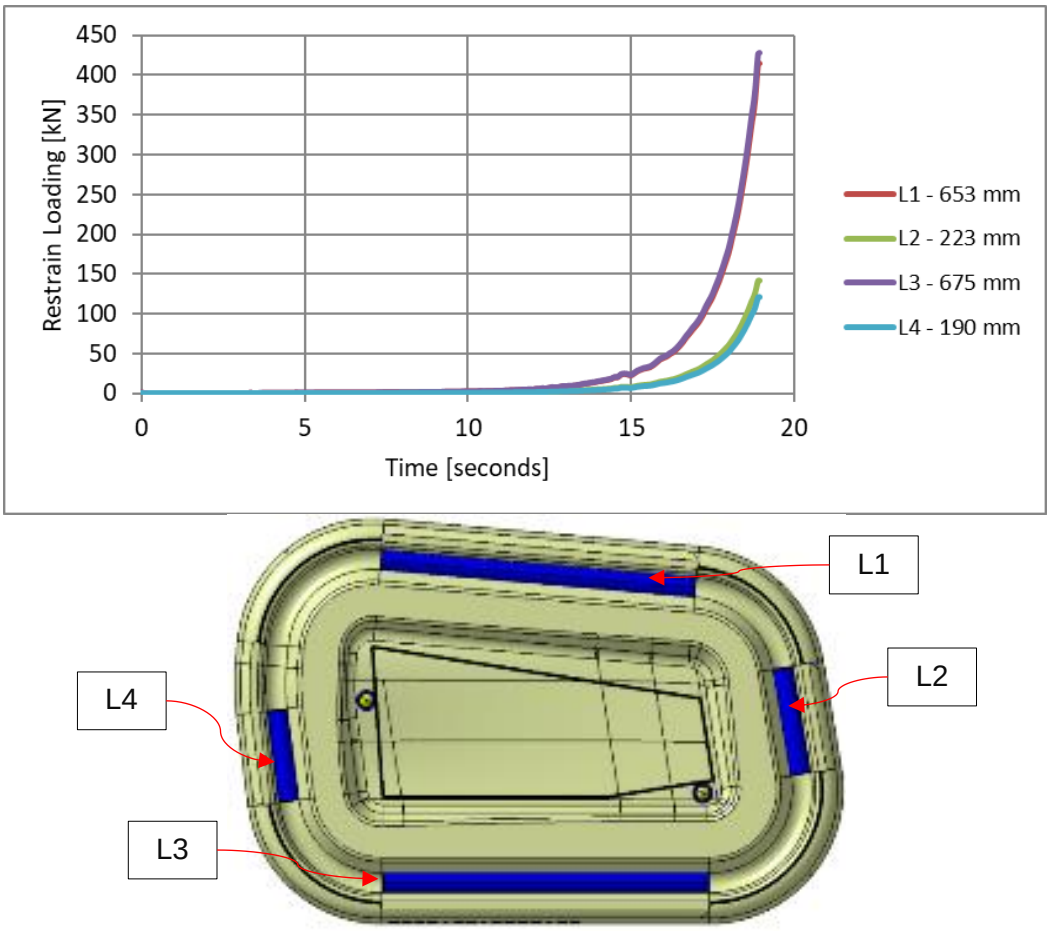

Figure 4.40: Concept-9 roller restraint force vs time

The results for Concept-9 AA2024-W temper condition material with rollers included are presented below. Figure 4.41 depicts the FLD, a zone quality overlay of the blank in the final form, the trimmed form at the trim stage and, the final form at the springback stage. The rollers had been incorporated in this simulation. No cracking was predicted, but the level of in-plane stretching achieved was not as high as expected.

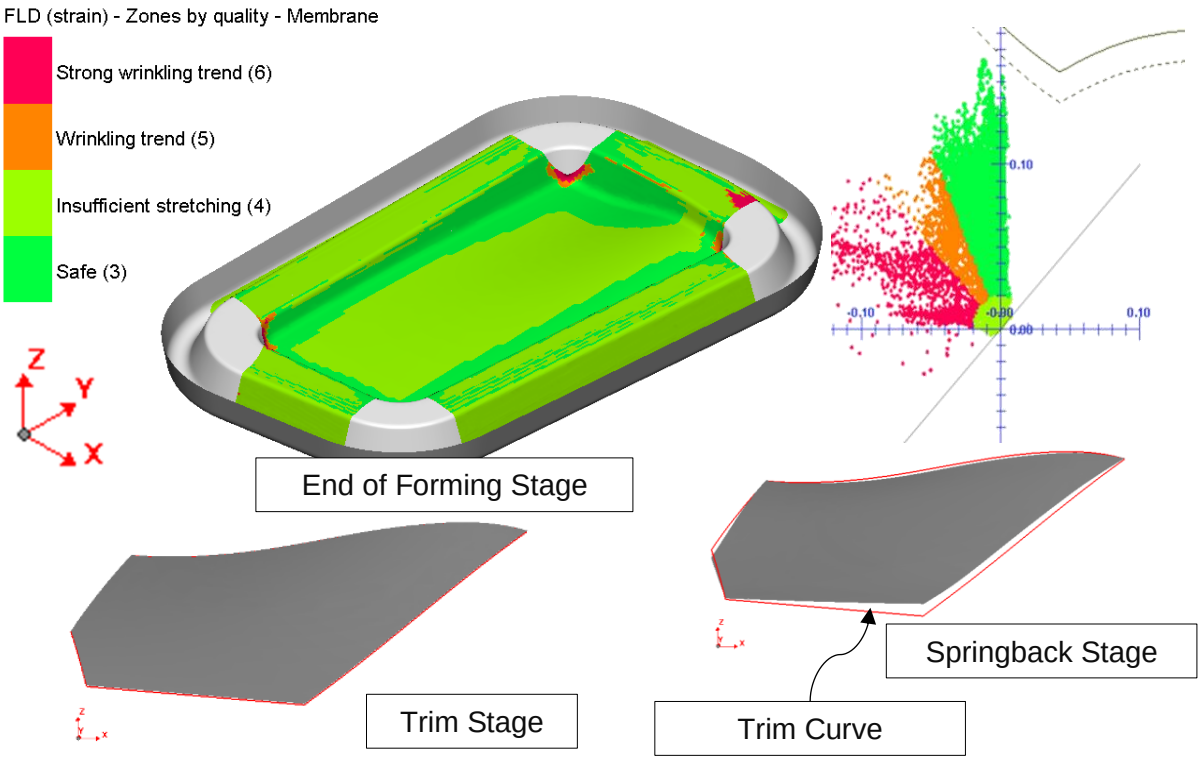

Figure 4.41: Concept-9 -W temper condition second stage with rollers FLD, zone quality overlay, & springback

Figure 4.42 depicts the final form compared to the desired shape. The simulation showed that the final component had a predicted distortion of 10.501 mm. The s-shaped curve was well defined with a predicted deviation of 1.5 mm. A flattened zone occurred and was predicted in the area of highest springback.

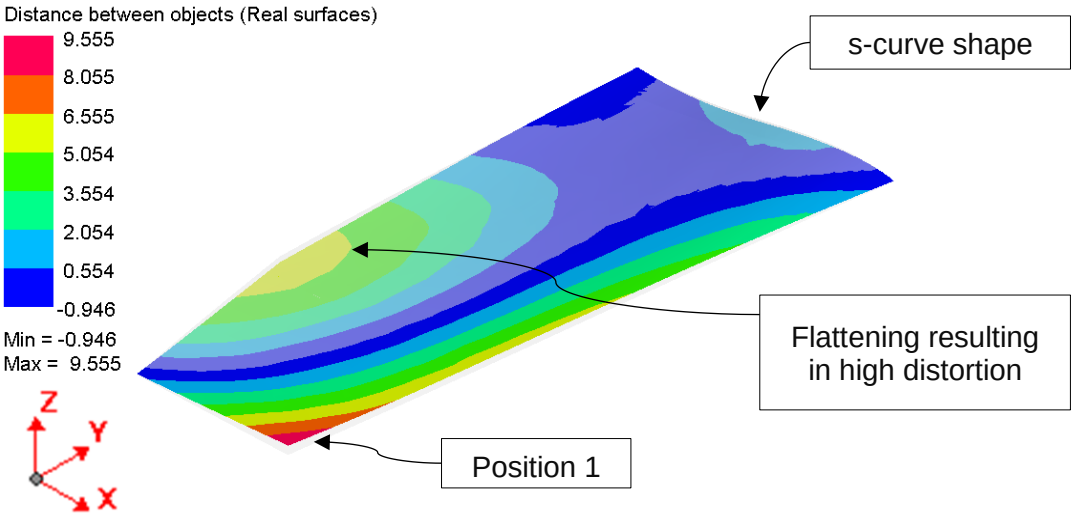

Figure 4.42: Concept-9 -W temper condition with rollers final simulation form vs component

The results for Concept-9 AA2024-W temper condition material without rollers included are presented below. Figure 4.43 depicts the FLD, a zone quality overlay of the blank in the final form, the trimmed form at the trim stage and, the final form at the springback stage. The rollers were not incorporated into this simulation. No cracking occurred, but the level of in-plane stretching was not as high as expected.

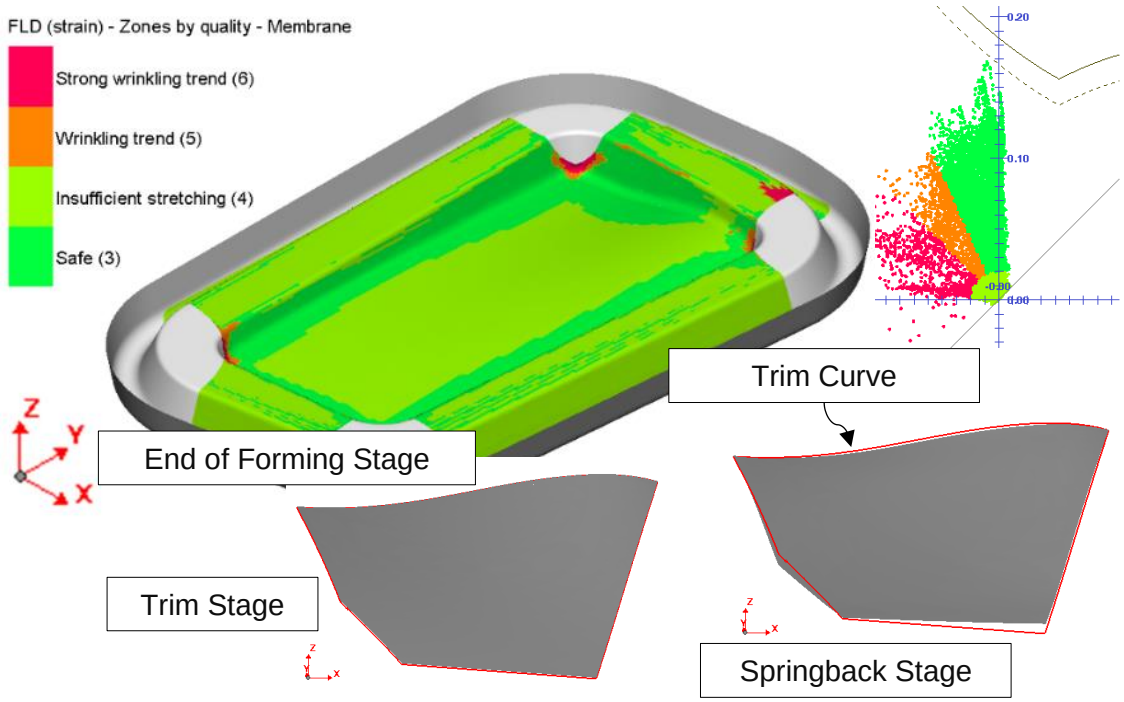

Figure 4.43: Concept-9 -W temper condition 2nd stage without rollers FLD, zone quality overlay & springback

Figure 4.44 depicts the final form compared to the desired shape. The simulation showed that the final component had a predicted distortion of 8.415 mm. The s-shaped curve was achieved with a predicted deviation of 1.202 mm. A flattened zone occurred and was predicted in the area of highest springback.

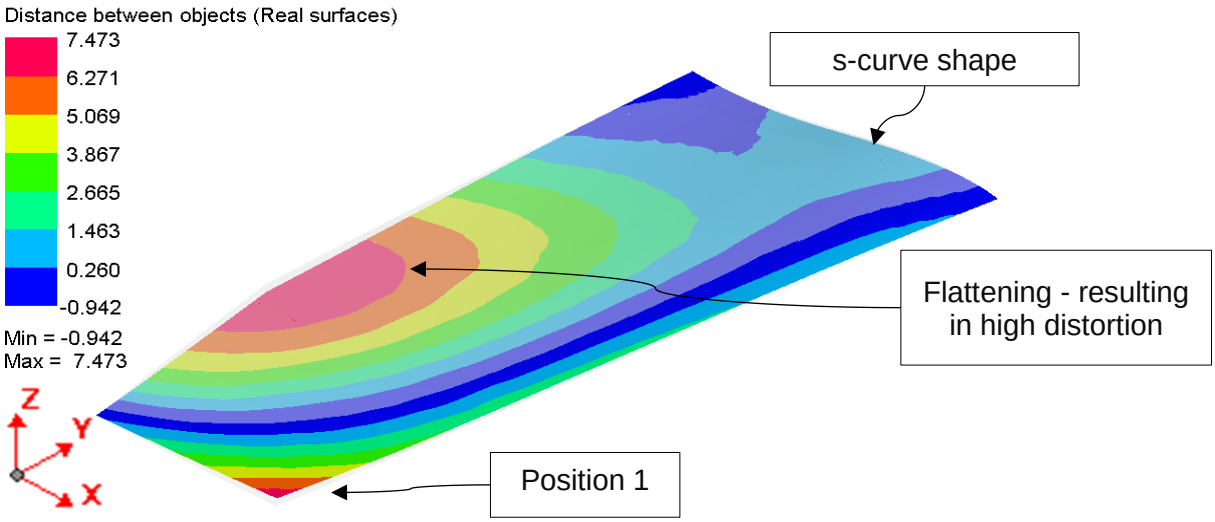

Figure 4.44: Concept-9 -W temper condition second stage without rollers final simulation form vs component

The simulation results indicated that manufacturing the component without the restraint rollers was predicted to give a better result compared to manufacturing with the rollers. Comparing Figure 4.42 and Figure 4.44, it was evident that the overall distortion of the part after the trimming stage was similar, except for the corner marked position 1. Concept-9 showed an improvement in the degree of in-plane stretching, compared to any of the other concepts. Thus, the Concept-9 component was predicted to have a better conforming shape with less springback to a flat blank.

The wrinkling that occurs in concepts 6 and 7 was avoided with the use of the sizeable overhanging edge flanges. The alignment features incorporated into Concept-9 would ensure perfect fitment of the blank during forming trials. Based on the results, no further investigations nor optimisation studies were conducted, and Concept-9 was accepted as the design solution to manufacture the aircraft skin panel.

Heat solution treating the AA2024-T3 sheet into the soft -W temper condition could not be conducted. An AA2024-O temper condition 2 mm sheet was to be simulated before proceeding to press trials. The -O temper condition sheet was softer than the -W temper condition and did not require solution heat treatment. Without the requirement to heat solution treat the blank, the press trial could proceed. Figure 4.45 depicts the FLD, a zone quality overlay of the blank in final form, the trimmed form at the trim stage, and the final form at the springback stage for the AA2024-O temper condition sheet. The rollers were used in this simulation. No cracking was predicted, but the level of in-plane stretching achieved was not as high as expected.

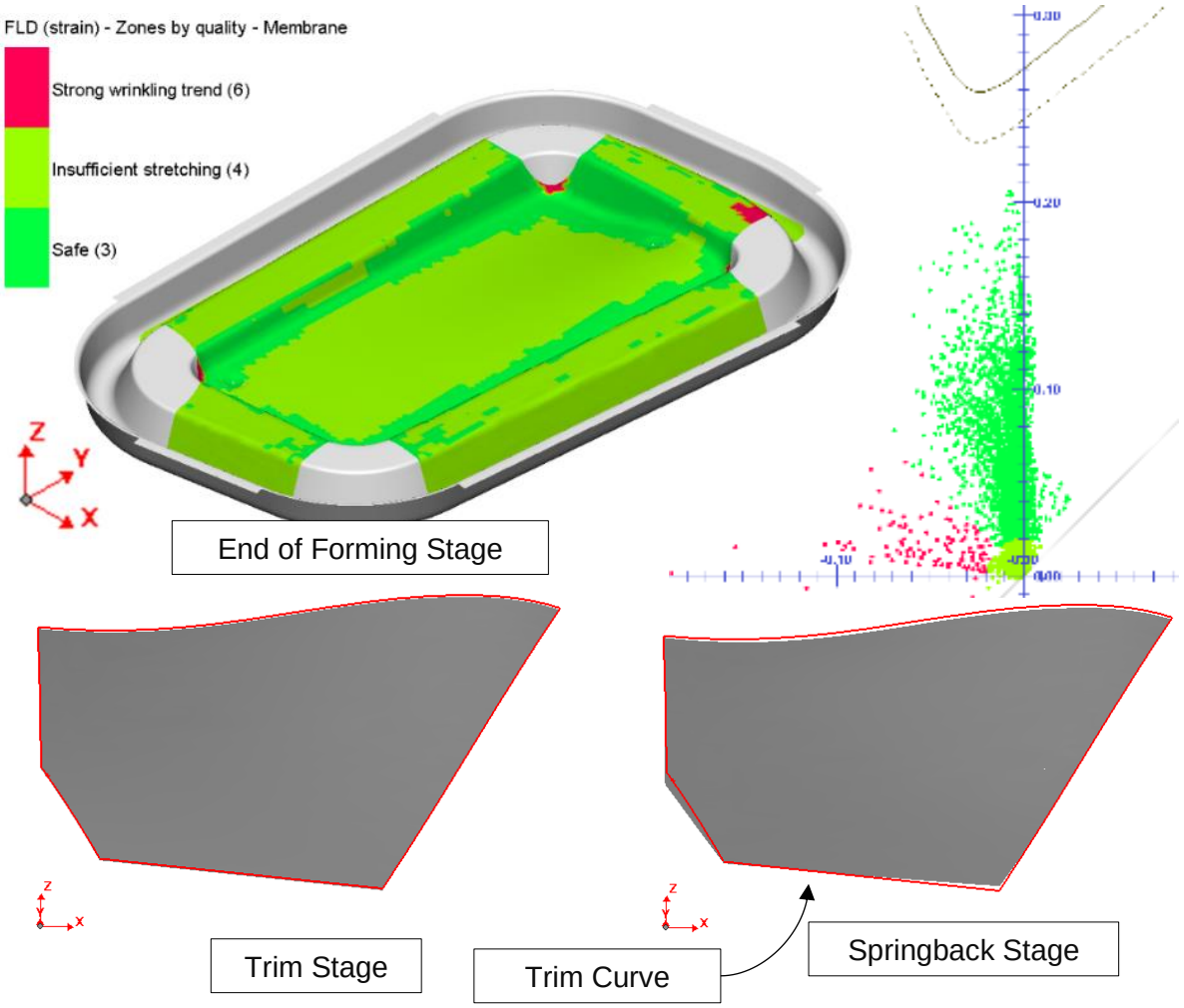

Figure 4.45: Concept-9 -O temper condition with rollers FLD, zone quality overlay, and springback

Figure 4.46 depicts the final form compared to the desired shape. The simulation showed that the final component had a predicted distortion of 7.932 mm. The s-shaped curve was well defined with a predicted deviation of 0.274 mm. A flattened zone occurred and was predicted in the area of highest springback.

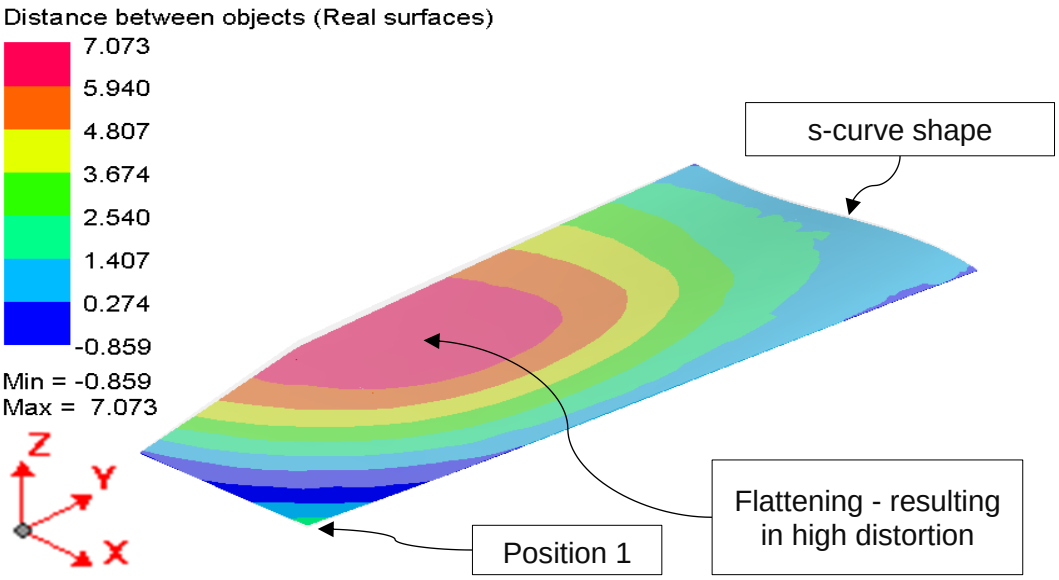

Figure 4.46: Concept-9 -O temper condition with rollers final simulation form vs component

The results for the Concept-9 AA2024-O temper condition material without rollers included are presented below. Figure 4.47 and Figure 4.48 depicts the FLD, a zone quality overlay of the blank in final form, the trimmed form at the trim stage, and the final form at the springback stage for the AA2024-O temper condition sheet. The rollers were not incorporated into this simulation. No cracking was predicted, but the level of in-plane stretching achieved was not as high as expected.

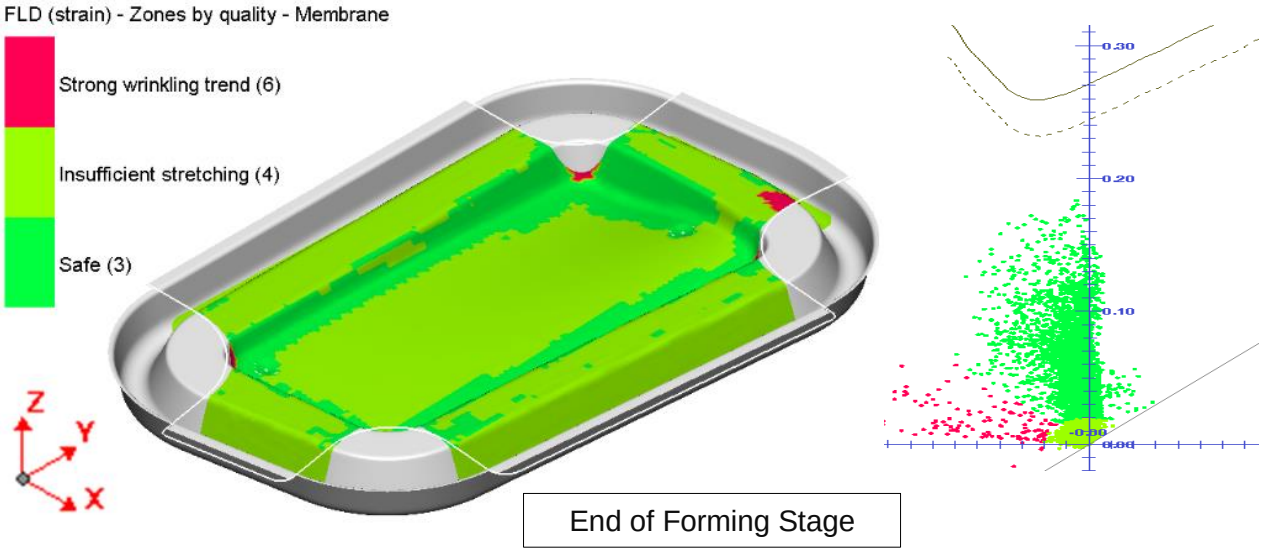

Figure 4.47: Concept-9 -O temper condition without rollers FLD, zone quality overlay

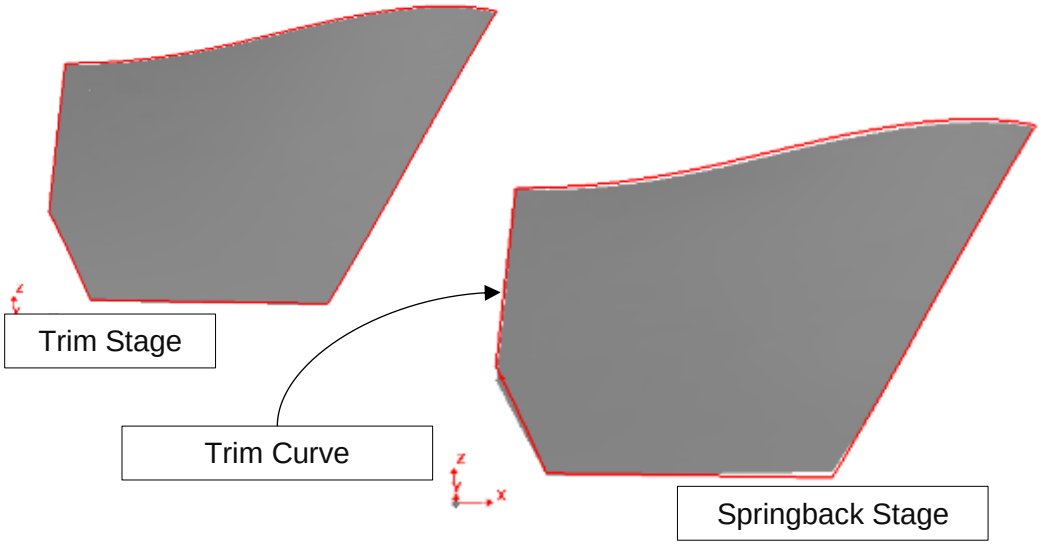

Figure 4.48: Concept-9 -O temper condition without rollers final trim and springback

Figure 4.49 depicts the final form compared to the desired shape. The simulation showed that the final component had a predicted distortion of 8.392 mm. The s-shaped curve was well defined with a predicted deviation of 0.331 mm. A flattened zone occurred and was predicted in the area of highest springback. It can be concluded that the -W temper condition and the -O temper condition are expected to have similar results. Hence it was acceptable to deviate to the -O temper condition for press trials as heat solution treatment of the blank could not be completed.

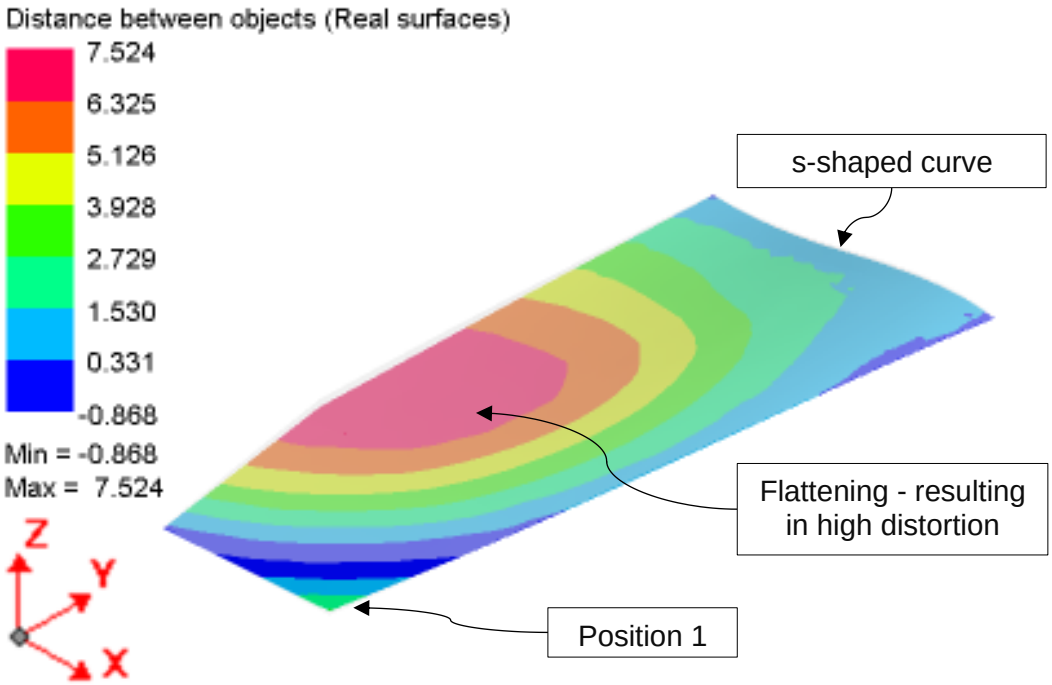

Figure 4.49: Concept-9 -O temper condition without rollers final simulation form vs component

Each concept's predicted distortion after the trimming and springback stage of the process is listed in Table 4-1. Concept-7 and 8 show better performance compared to Concept-9, but these concepts were not practical and could not be used to manufacture a component. Concept-7's compensated tool surface would require extensive CAD modelling to achieve the required geometry to manufacture the tooling successfully. Concept-8 performed significantly well but was infeasible to proceed with trials due to the blankholding set-up required. Concept-9 was designed with alignment features and was based on the findings from Concept-1 to Concept-8.

Table 4-1: Summary of the concept's distortion from the design

Concept	Component Predicted Maximum Distortion [mm]	Comment
1	26.757	Rejected due to excessive distortion
2	11.964	Rejected due to distortion
3	5.132	Rejected due to cracking
4	18.604	Rejected due to excessive distortion
5 (Tool A/Blank A)	20.512	Rejected due to excessive distortion
5 (Tool A/Blank B)	23.88	Rejected due to excessive distortion
5 (Tool B/Blank B)	26.094	Rejected due to excessive distortion
5 (Tool B/Blank C)	23.854	Rejected due to excessive distortion
5 (Tool C/Blank C)	27.01	Rejected due to excessive distortion
6	7.472	Rejected due to distortion
7 (Isotropic material)	4.621	Rejected due to distortion
7 (Kinematic material)	7.415	Rejected due to distortion
7 (Kinematic material Optimised tool)	3.671	Rejected as this is an optimisation concept
8	1.585	Blankholder force optimisation study, infeasible solution, showed increased edge restraint increased the degree of in-plane stretching.
9 (-W with rollers)	10.501	Accepted
9 (-W without rollers)	8.415	Accepted
9 (-O with rollers)	7.932	Accepted
9 (-O without rollers)	8.392	Accepted

4.6. Concept Validation

4.6.1. Component Manufacture

With a tool and blank design solution accepted, the tools and blank were manufactured to conduct press trials. AA2024-T3 blanks were manufactured, but solution heat treatment of the blank could not be conducted. AA2024-O temper condition blanks were manufactured and used for the trial. Before pressing the first stage, the selected lubricant (petroleum jelly) was applied to the tool and the blank. Figure 4.50 depicts the stage 1 tool and initial blank positioned accurately in the fluid cell press.

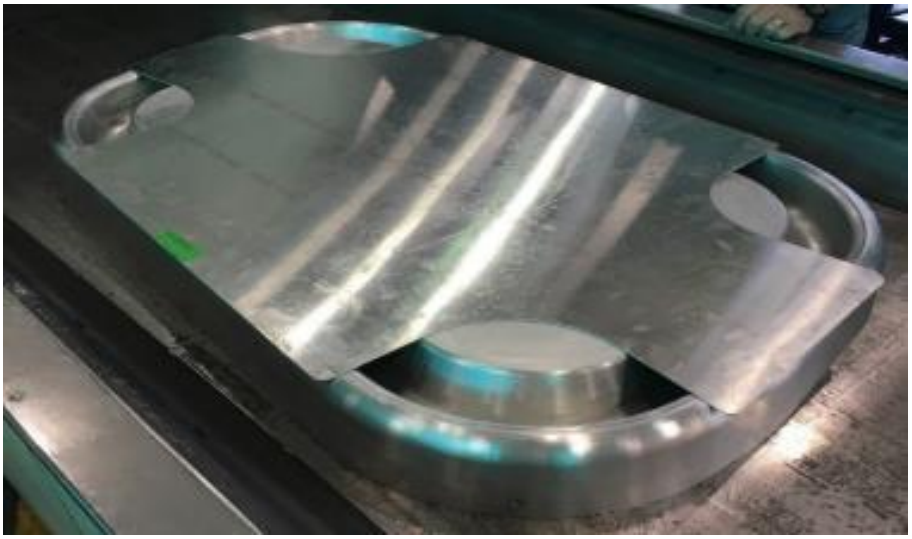

Figure 4.50: Stage 1 tool and the initial blank positioned in the fluid cell press

Figure 4.51 depicts the blank successfully pre-formed.

Figure 4.51: Stage 1 tool and pre-formed blank after pressing

Before loading the second stage tooling into the fluid cell press, the first pre-formed blank was placed into the tool for fitment check. Figure 4.52 depicts the second stage tool with the pre-formed blank fitted.

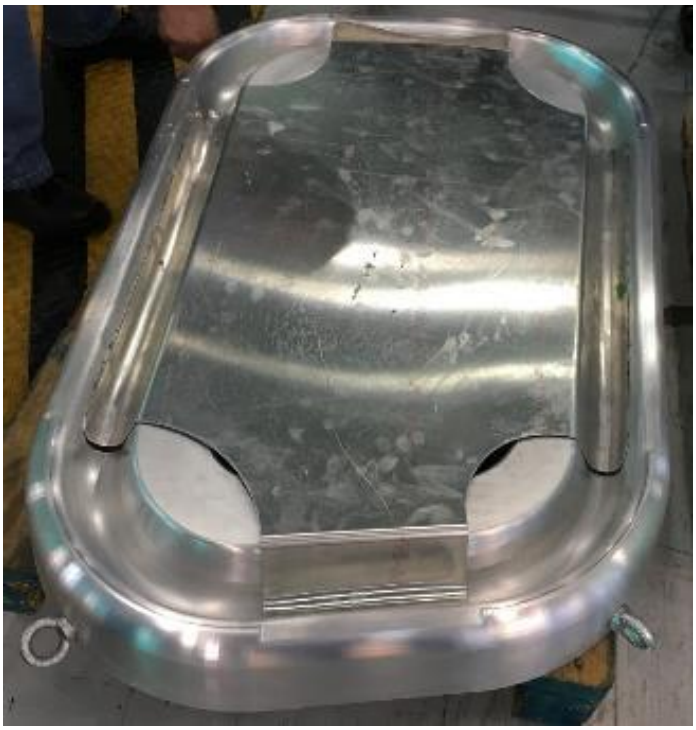

Figure 4.52: Stage 2 tool and the fitted pre-formed blanked

There was a concern with pressing at 800 bar (80 MPa / 0.08 GPa) and thus was reduced to 600 bar. The press trials were conducted without the rollers. Figure 4.53 depicts the successful pressing of the pre-formed blank into the final pre-trimmed form. Cracks were witnessed but not in the final part.

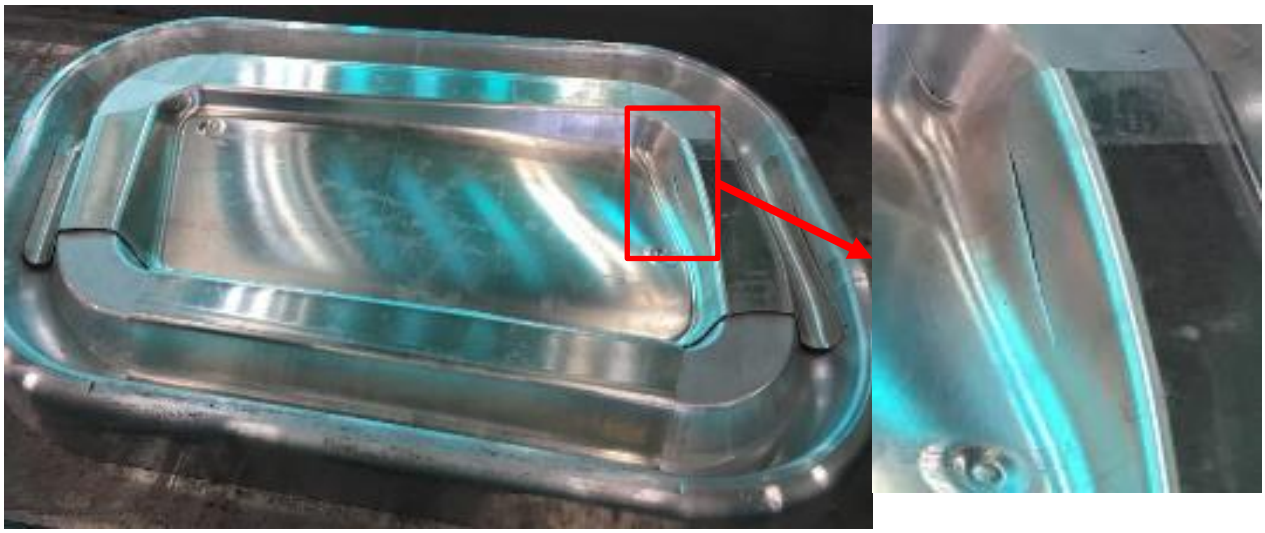

Figure 4.53: Stage 2 tool and the formed blank and minor cracking

In total, four blanks were pressed, as shown in Figure 4.54. Cracking in the blanks was experienced, as shown in Figure 4.53. One blank lost a complete flange edge due to a crack that ran the length of a tool's inner corner section. The cracks witnessed were far away from the component's edge and posed no risk to the final component's integrity. The lack of petroleum jelly lubricant that was applied to the second stage tool and the pre-formed blank was attributed to this failure of the first pressed component. More lubricant was applied to the second, third and fourth blanks and the tool are each pressing operation. No cracks were seen in the second, third and fourth components.

Figure 4.54: Four AA2024-O temper condition pre-trim formed components

The next stage of the manufacturing process was to trim to the final component. Typically, CNC machining of the component was conducted. The component was trimmed using laser cutting at the Council for Scientific and Industrial Research (CSIR) National Laser Centre (NLC). Figure 4.55 (a) depicts the simple holding fixture for positioning during the trimming process. Figure 4.55 (b) depicts the trim line of the final component after the laser cutting process had been completed.

Figure 4.55: (a) Laser trim holding fixture (b) Final component trim line

The final component was separated, deburred, and inspected using CMM. Figure 4.56 depicts the realised aircraft skin panel component that retained the desired form of the design. The s-shaped curve was well-defined and formed as predicted by the simulation studies (see Figure 4.48 and Figure 4.49).

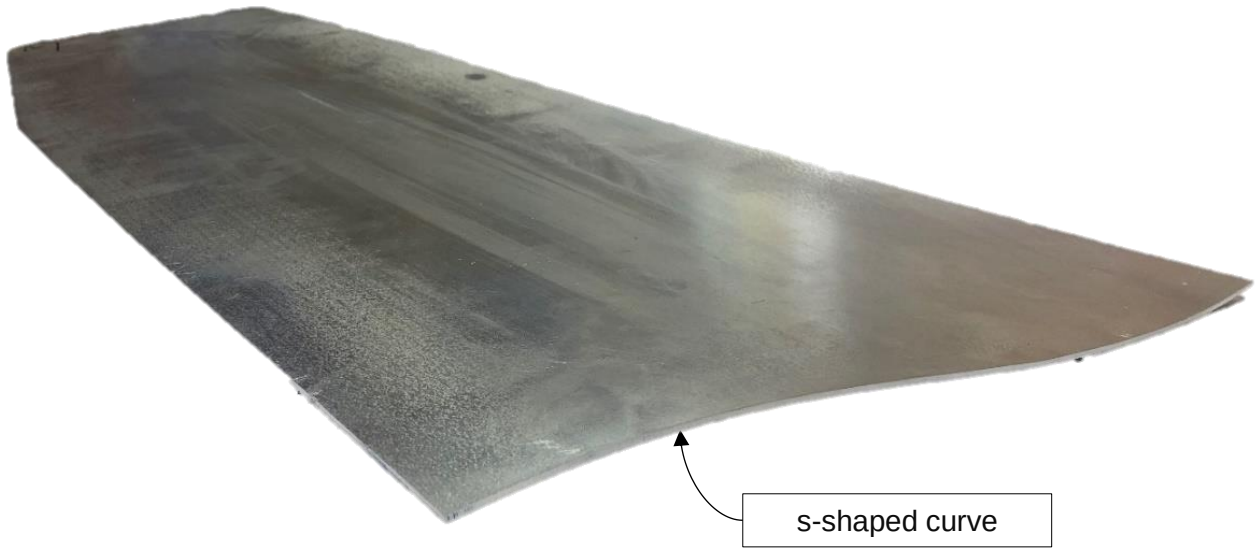

Figure 4.56: Realised aircraft skin panel component

4.6.2. Component Metrology

In order to validate the form of the four components were within the design tolerance limit of 1.4 mm, a visual inspection and detailed CMM metrology investigation were conducted. As this was an existing product, an inspection tool was available to clamp the panel down representing the final installation condition. The components were measured according to standard metrology procedures already used to validated the existing component using equipment calibrated according to ISO 10360-2:2009. Hence, multiple measurements were not conducted as the repeatability and performance of the equipment and measurement method was ensured through calibration.

All panels must be checked such that they met the design requirements before being permitted to proceed onto the next stage of the manufacturing process. An inspection check fixture was used to simplify the process without every panel being sent for a detailed CMM inspection. The inspection check fixture was accurately manufactured and met the surface profile tolerance of 1.4 mm. Thus, the component, when laid on the inspection check fixture, should fit without any gaps between the two interacting surfaces. The outer edges of the panel are clamped down.

The component was then tapped to determine if there was a gap between the panel and the inspection check fixture. If the component could be clamped without forcing it into position, and the sound that emanates when tapped was subtle, the panel was accepted. If a component failed to meet the design tolerances with minor deviation, a detail CMM inspection was conducted to determine to what extent the panel was out of tolerance. From the CMM results, the degree of distortion the component was determined and if it could be salvaged by rework or if it must be scrapped. If the component's failed to meet the design tolerances was major, it is scrapped outright.

Figure 4.57 depicts one of the aircraft skin panels with one corner clamped. All four of the panels fitted on the check fixture exceptionally well. A visual inspection of the panel's s-shaped curve edge showed a deviation of 3.5mm and the flattened zone a deviation of 2mm when measured with a ruler.

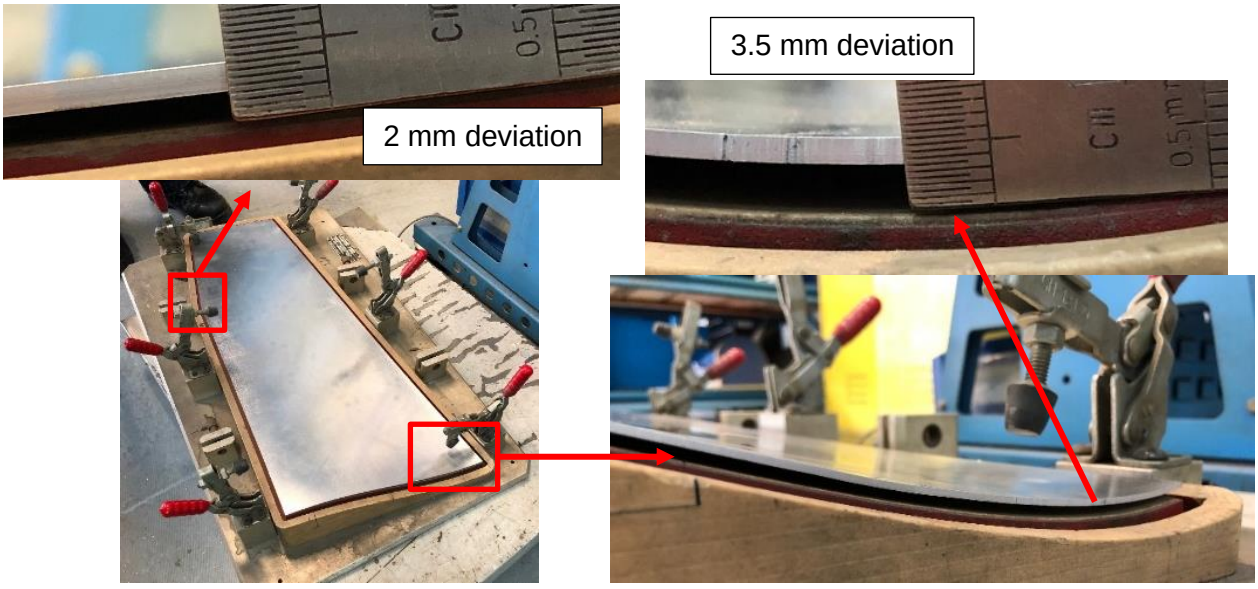

Figure 4.57: Aircraft skin panel component placed on the inspection check fixture

With all the edges of the component clamped, the visual inspection result rendered the panel acceptable. The CMM of the aircraft skin panel was measured in two configurations, unclamped and clamped. The unclamped condition with only the corner, as shown in Figure 4.57. Unclamped was used to determine the degree of distortion. The clamped condition represented the panel installation condition, which was the normal procedure for the CMM inspection.

The design specified a surface profile of 1.4 mm. Surface profile is defined as a sphere with a diameter of 1.4mm with its centre on the nominal surface (ISO 1101:2017). Offset surfaces were created above, and below the nominal surface, at a distance of 0.7 mm. These surfaces described the boundary upper and lower tolerance limits of the nominal surface. Figure 4.58 depicts the surface profile definition as described in ISO 1101:2017. The upper surface of the panel was nominal.

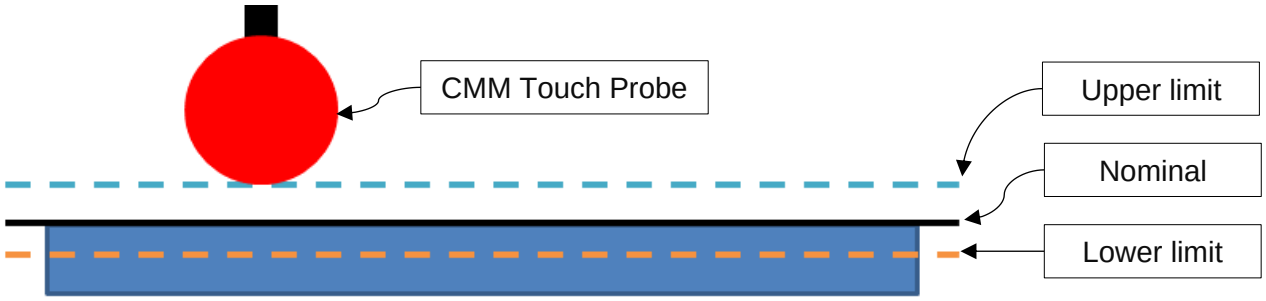

Figure 4.58: Surface profile definition as per ISO 1101:2017.

The CMM touch probe was programmed to measure 33 points distributed across the component, as shown in Figure 4.59. A total of 40 points were measured with points 1 to 7 used for alignment.

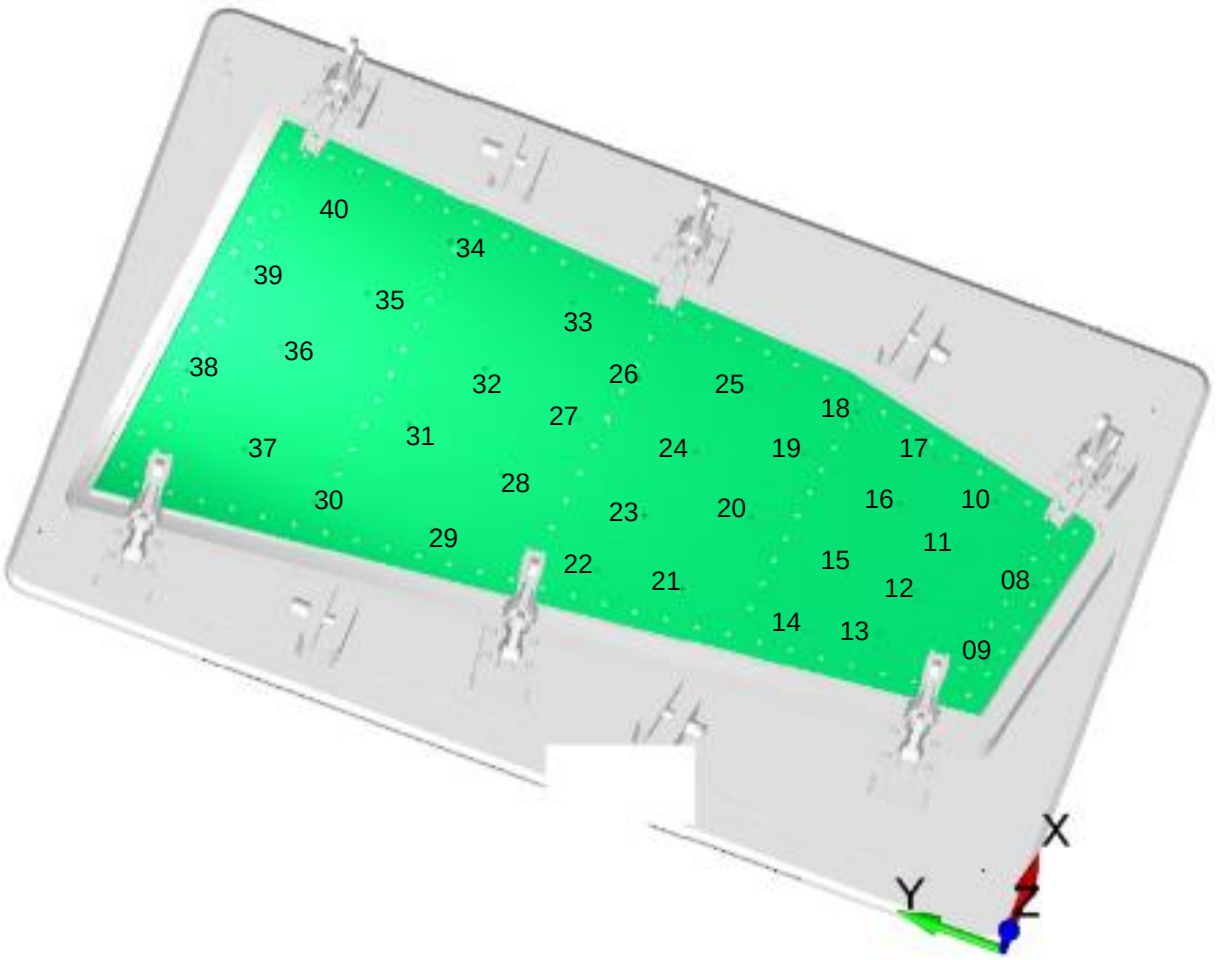

Figure 4.59: CMM point layout B: Panel CMM set-up

Figure 4.60 depicts the deviation of the actual component's surface from the nominal surface in the clamped condition. The panels met the design requirement with only one CMM point, exceeding the upper tolerance limit of 0.7 mm. Using the CMM points, the surface profile calculation was performed. The components achieve a surface profile of 0.483 mm, 0.505 mm, 0.478 mm, and 0.817 mm, respectively. Based on the results presented, the design solution was deemed a success. The CMM results are all positive as the component was measured on the inspection tool and cannot deviate negatively.

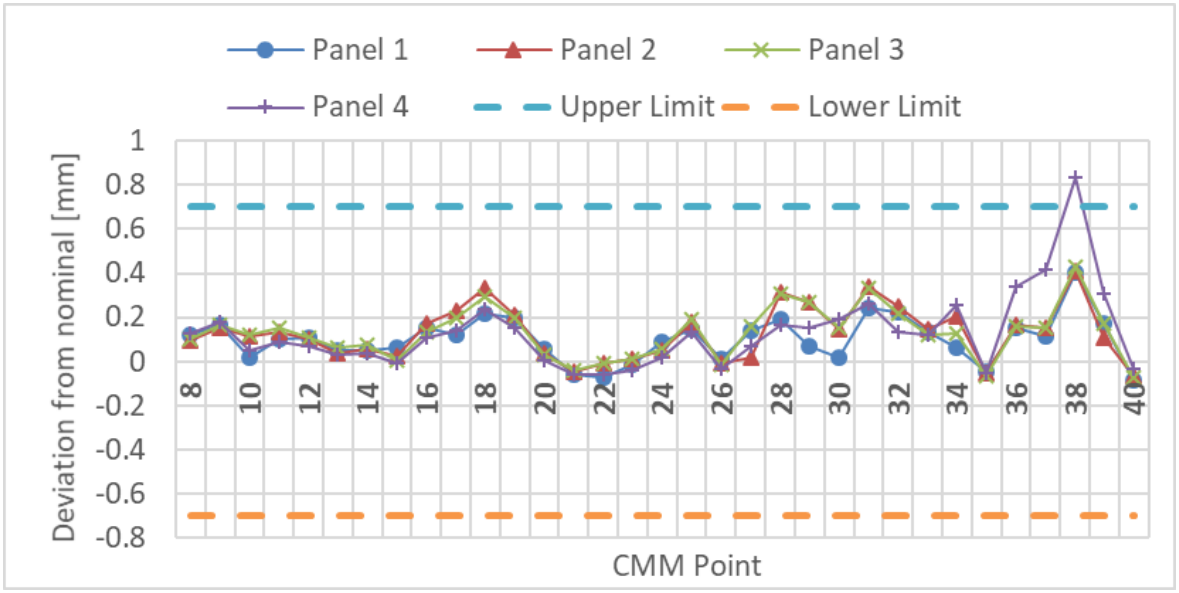

Figure 4.60: Aircraft skin panel CMM clamped results

Figure 4.61 shows the CMM results for the unclamped configuration. The panel was clamped on one side, and, hence, the panel distortion from the surface profile progressively worsened. This result was expected considering the distortion patterns seen in the simulation studies. Using the CMM points, the surface profile calculation was performed. The unclamped surface profile result for each panel was 1.927 mm, 2.153 mm, 2.329 mm, and 2.16 mm, respectively.

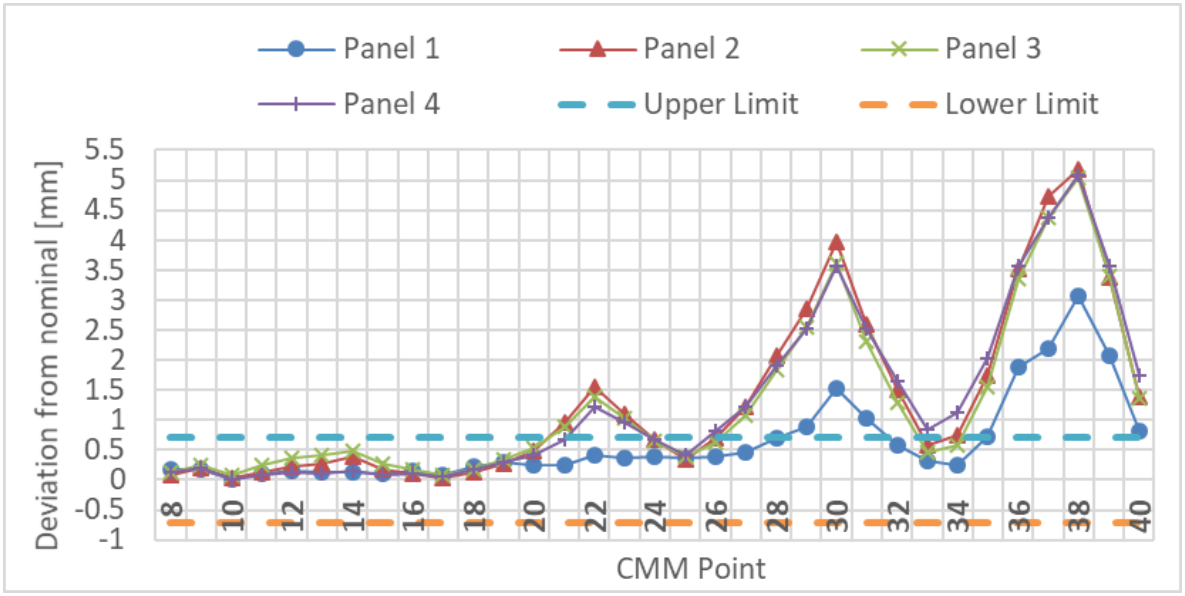

Figure 4.61: Aircraft skin panel CMM unclamped results

4.6.3. Simulation to Component Metrology Results Comparison

Correlation between the CMM and simulation results was explored. The process followed in the simulation to evaluate the anticipated final shape of the component did not match the CMM procedure used to measure the distortion from the manufacturing panel. The original position alignment of the simulation mesh and the nominal surface was used throughout the investigation and was the typical procedure seen in all the publications. PAM-STAMP did allow for a best-fit alignment of the mesh and the component surface. However, if the tool was distortion-compensated, or there was a deviation between the CAD and CAE models, the initial alignment of the mesh and nominal surface was required before using best-fit alignment.

Using either the original position or best-fit to do an alignment and assessment of the simulation result did not match the way the part was aligned in reality. To show the weak correlation Concept-9's result in Section 4.5 were compared with the results from the CMM study. In PAM-STAMP, the mesh and nominal surface were best-fit aligned, and the CMM points were added. The best-fit alignment distortion plot result is shown in Figure 4.62 (a). Figure 4.62 (b) is a line graph of the CMM and simulation results. A good correlation means the simulation trend and the CMM trend match. Figure 4.62 (b) shows no correlation between the simulation and CMM results. The weak correlation was assumed to be due to the way the alignment was done in the simulation.

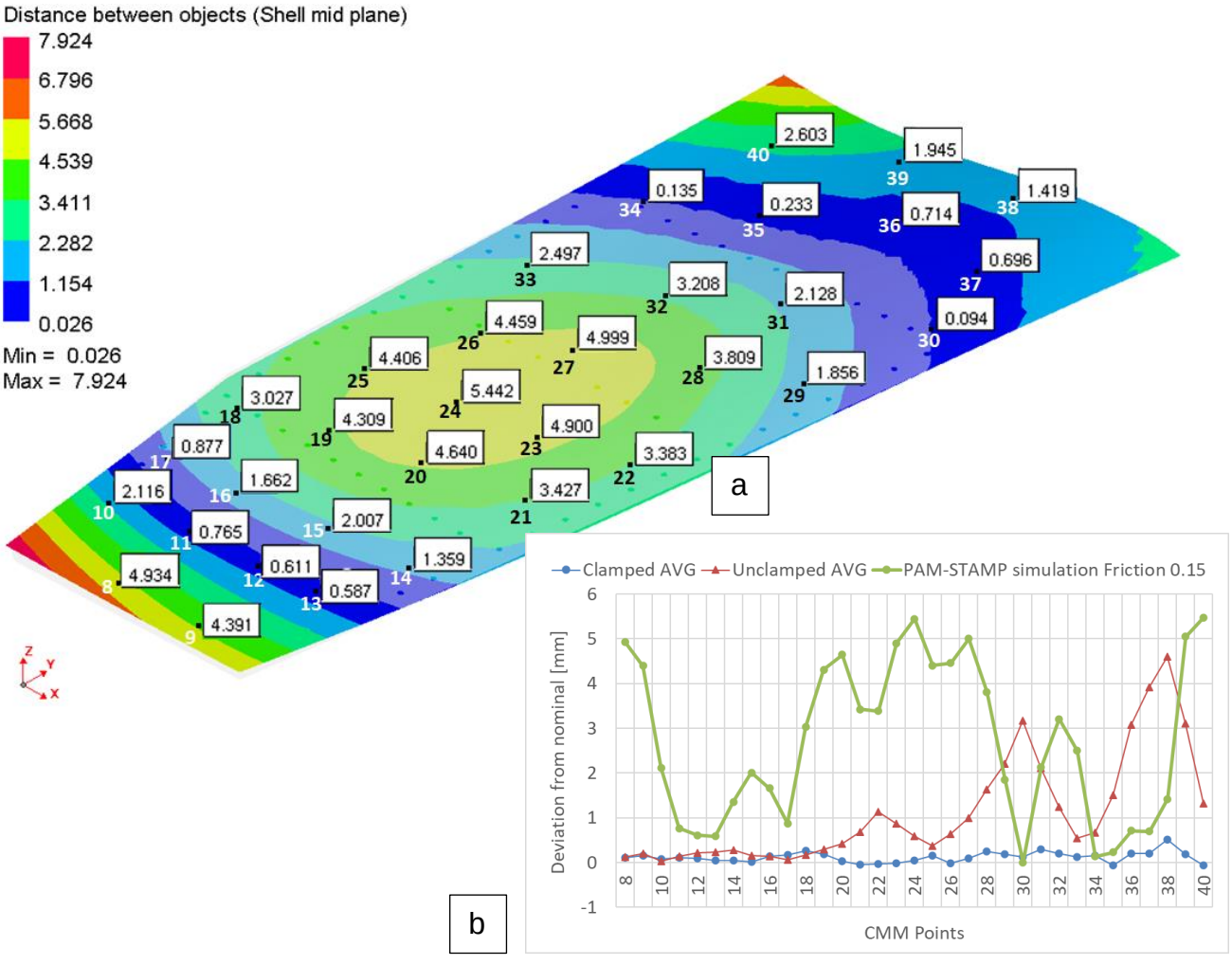

Figure 4.62: (a) Aircraft skin panel PAM-STAMP final springback best-fit alignment distortion plot result (b) Line graph of the averaged clamped and unclamped CMM results and the PAM-STAMP simulation panel distortion results (best-fit alignment)

PAM-STAMP only allowed for a best-fit alignment of the mesh and the nominal surface. In order to get a similar alignment to what was conducted in reality, an additional gravity step was proposed. The gravity step allowed for the panel to settle onto the nominal surface in a similar way the component settled on the inspection check fixture. This operation was considered similar to an assembly stage. With reference to the literature consulted for the presented study, the simulation ends after springback. The way the panel rests on a check fixture or fastened into an assembly is taken into consideration. Thus, the alignment of the component compared to reality is improved compared to just springback. Concept-9's simulation manufacturing stages were thus adapted from those defined in Section 4.4.1, as followings:

OP 1 – Pre-forming stage

OP 2 – Springback stage

OP 3 – Second forming Stage

OP 4 – Trim and springback stage

OP 5 – Gravity stage

Figure 4.63 depicts the PAM-STAMP springback distortion plot with the mesh aligned more realistically to how the panel was aligned and measured in reality.

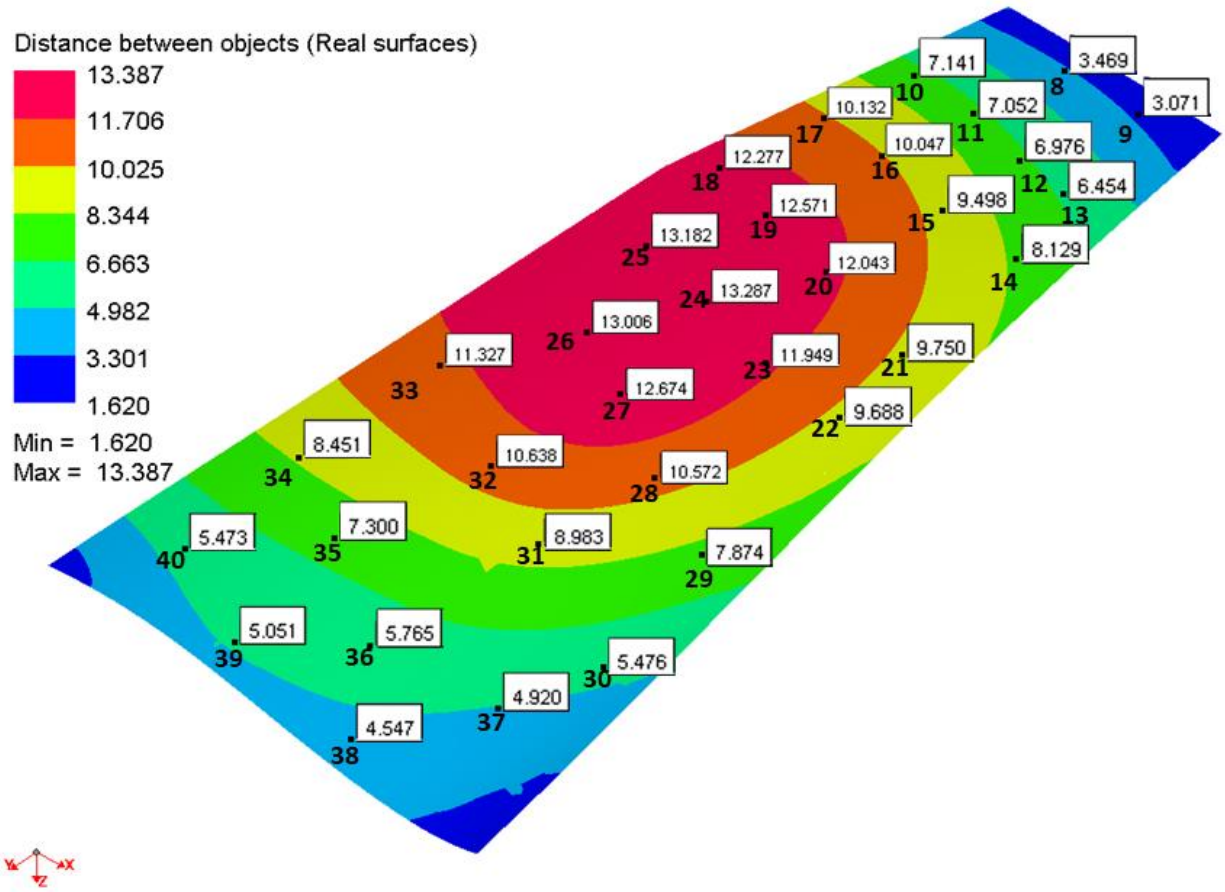

Figure 4.63: Aircraft skin panel PAM-STAMP final springback gravity step alignment distortion

Even with an improved alignment procedure, there was still a weak correlation between the simulation and CMM results, as shown in Figure 4.64. The lack of correlation is explored in detail in Chapter 5:.

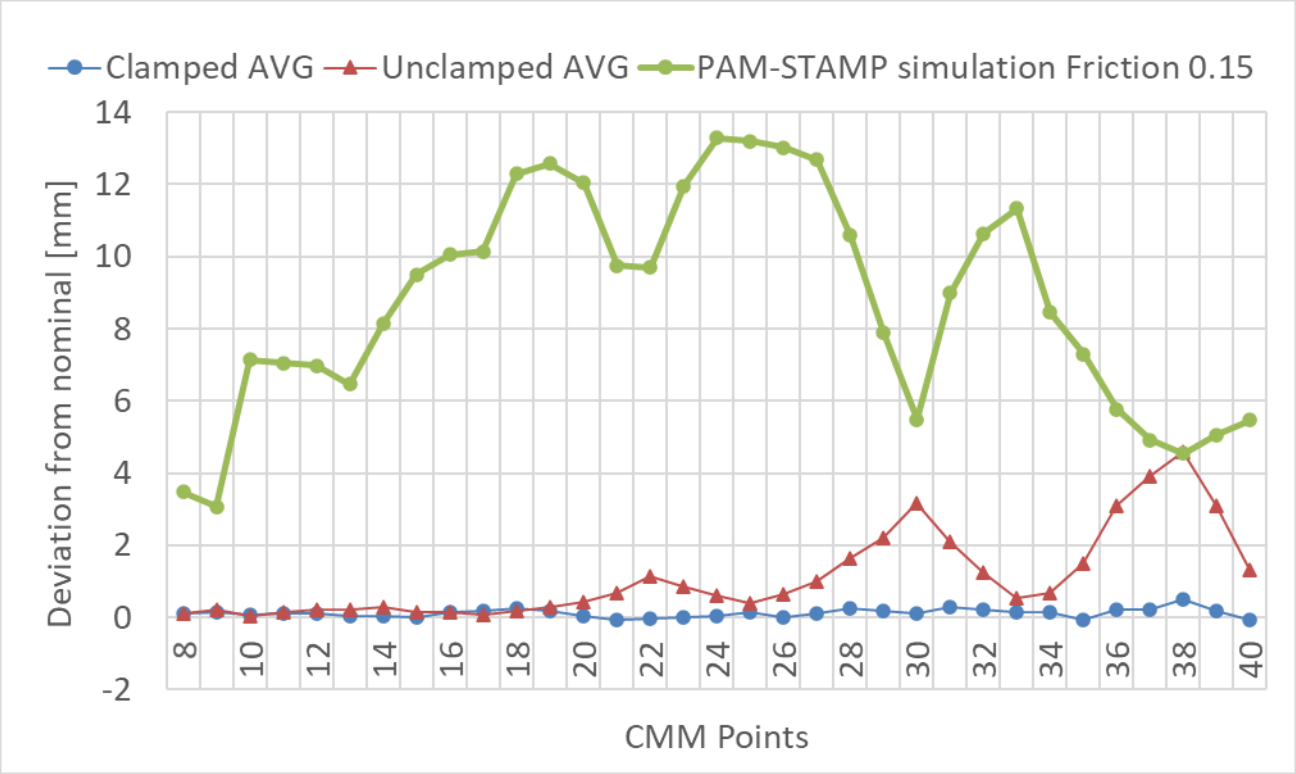

Figure 4.64: Line graph of the averaged clamped and unclamped CMM results and the PAM-STAMP simulation panel distortion results (gravity alignment)

Chapter 5: Simulation Model Validation

5.1. Introduction

Despite the final components having met the design tolerance requirements, the simulation results did not correlate to the CMM results, which was the purpose of the study. Section 3.4.2 discussed the material characterisation phase and the material cards that were available. As simulation material property data for any temper condition of AA2024 2 mm clad sheet was not publicly available, the only material or forming process parameters that could be altered was the friction coefficient. The work of Hatipoğlu et al. (2007) made use of a friction coefficient as high as 0.9. Whereas the friction coefficient used to simulate concepts 1 to 9 was a maximum of 0.19. Hence, forming simulations using ESI Group PAM-STAMP 2G were carried out to determine the influence of friction on the simulation result.

5.2. Variable Friction Study

The simulation set-up of Concept-9 in AA2024-O temper condition material, presented in Section 4.5, with the additional gravity step discussed in Section 4.6.3, was used to conduct a study to determine the influence of friction on the simulation results. The friction coefficient used for Concept-9 was 0.15 and only was applied to the blank and tool interface. The friction coefficients simulated were 0.15, 0.225, 0.45, 0.475, 0.485, 0.495, 0.5, 0.51, 0.525, and 0.55. As the gravity step simulation was used, the results were correlated to the CMM metrology results presented in Section 4.6.3.

As the friction coefficient was increased, the friction force between the blank and the tool increased. This, in turn, increased the in-plane stretching of the blank as it was drawn into the tool. Insufficient stretching resulted in a large springback instead of the component retaining the desired shape. The FLD diagrams for the friction simulations values of 0.15 and 0.5 are presented in Figure 5.1 and Figure 5.2, respectively. Each depicts the FLD zone quality results with angled views to depict the inner edge of the formed panel showing areas where cracking results from the increased edge restraint. Only the 0.15 and 0.5 friction simulation results are shown as 0.15 was the baseline model used in the study, and 0.5 was the best performing model in the friction study.

Figure 5.1 depicts the FLD zone quality result for the 0.15 friction coefficient model. The simulation result showed no signs of cracking. However, considering the cracking seen on the actual components (see Figure 4.27 and Figure 4.54), the friction of the system was greater than 0.15. The degree of in-plane stretching was insufficient and, hence, the springback of the panel was large.

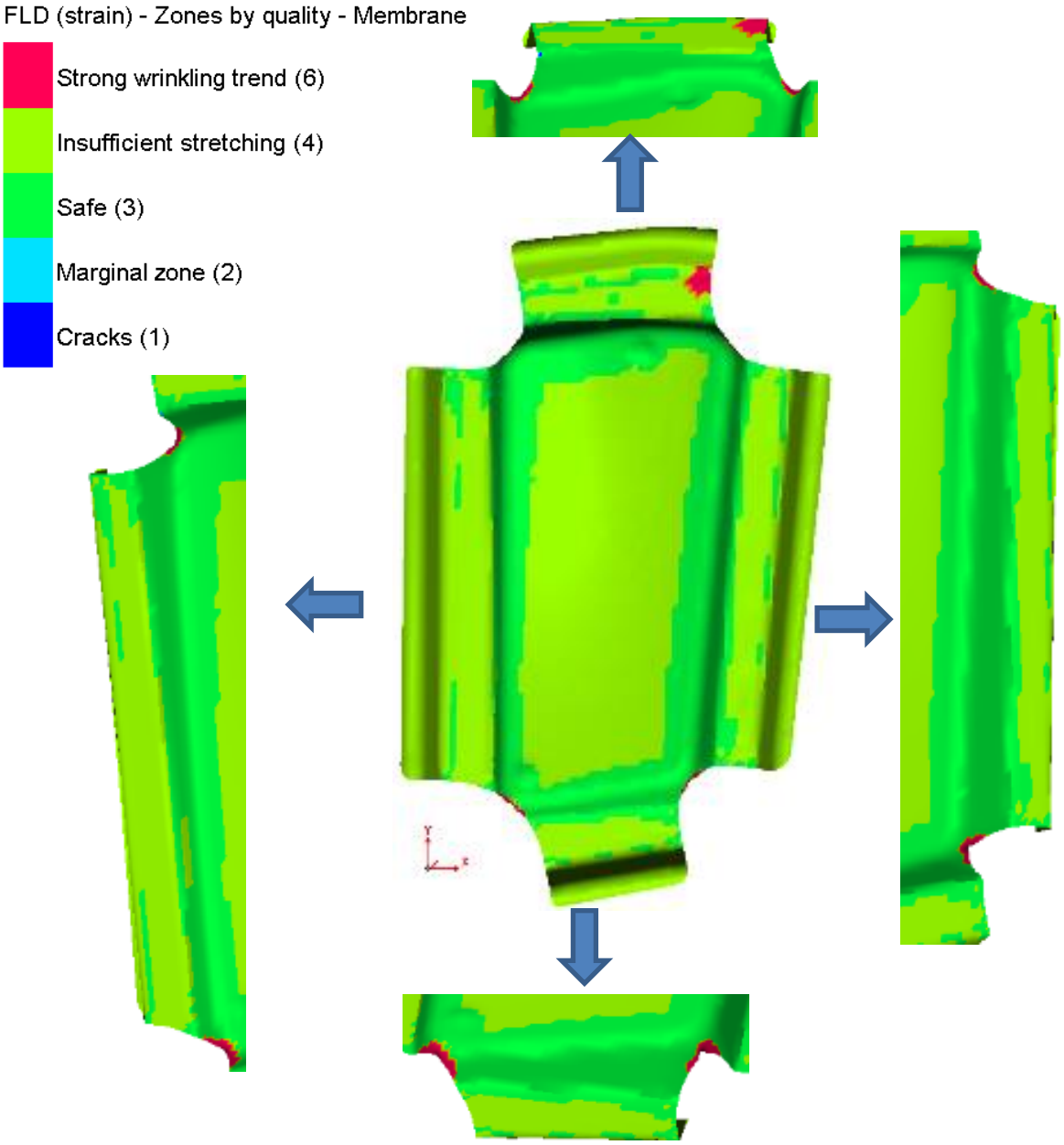

Figure 5.1: FLD zone quality results for the 0.15 friction coefficient simulation

Figure 5.2 depicts the FLD zone quality result for the 0.5 friction coefficient model. The simulation predicted cracking in all edges of the blank. However, considering the cracking seen on the actual components (see Figure 4.53 and Figure 4.54), the constant friction coefficient might not have been accurate.

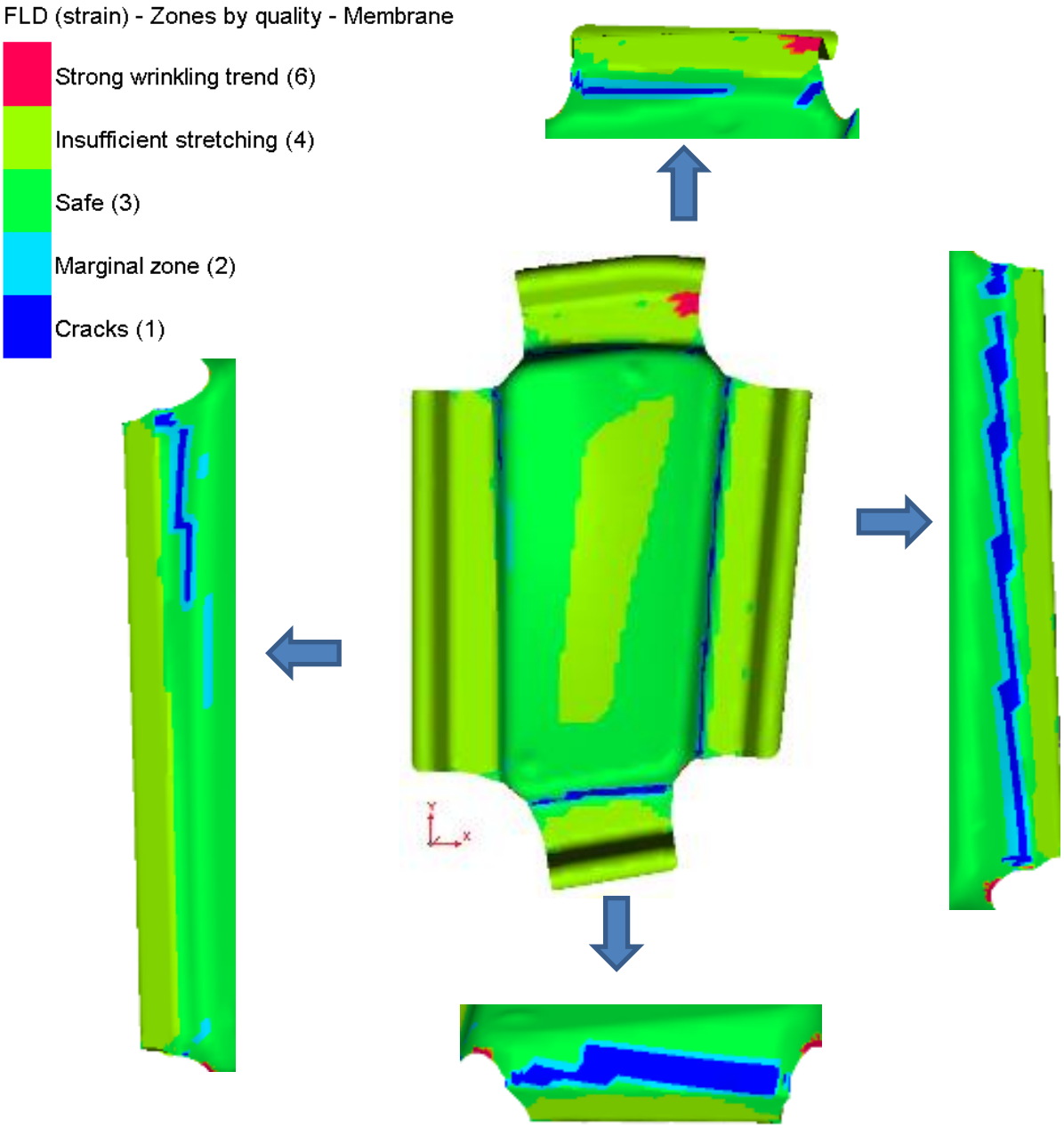

Figure 5.2: FLD zone quality results for the 0.5 friction coefficient simulation

Only one of the four panels completely cracked along the right-hand side edge. Cracking was seen in the other three components but was reduced in length, as the amount of lubricant used for those panels was increased. The bottom edge in the simulation was expected to separate, but this was not the case, as seen in Figure 4.53 and Figure 4.54.

The forming process presented in Section 4.4.1 was followed when preparing the results for the variable friction simulations. The gravity stage allowed the mesh to settle on top of the nominal surface in a similar way the component settled on the inspection check fixture. The distances between the final simulated shape and the nominal surface for the same CMM locations were extracted and are presented in Table 5-1 and Table 5-2.

Table 5-1: Distortion of the simulated panel and unclamped average CMM measurements from the nominal design surface profile – Friction values 0.15, 0.225, 0.45, 0.475, 0.485

CMM Point	Unclamped Average	Friction 0.15	Friction 0.225	Friction 0.45	Friction 0.475	Friction 0.485
8	0.132	3.469	3.801	4.32	0.942	2.552
9	0.21	3.071	1.833	2.186	1.064	1.7
10	0.02	7.141	7.63	5.443	1.139	3.146
11	0.092	7.052	6.934	4.142	1.347	2.905
12	0.124	6.976	5.45	2.935	1.386	2.437
13	0.098	6.454	4.345	1.382	1.354	1.831
14	0.143	8.129	5.42	0.827	1.677	1.915
15	0.08	9.498	7.377	2.626	1.78	2.674
16	0.106	10.047	8.828	4.784	1.889	3.599
17	0.063	10.132	10.136	6.065	2.13	4.162
18	0.168	12.277	11.309	6.41	2.914	4.863
19	0.299	12.571	10.705	4.777	2.762	4.096
20	0.417	12.043	9.45	2.979	2.604	3.282
21	0.675	9.75	6.84	1.064	2.587	2.582
22	1.215	9.688	6.702	0.747	3.402	2.932
23	0.955	11.949	8.6	2.207	3.174	3.326
24	0.677	13.287	10.396	3.778	3.107	3.903
25	0.425	13.182	11.233	5.528	3.292	4.696
26	0.813	13.006	9.927	4.279	3.548	4.293
27	1.215	12.674	9.093	3.036	3.797	3.979
28	1.908	10.572	7.292	1.796	4.318	3.739
29	2.531	7.874	4.68	0.667	5.053	3.708
30	3.569	5.476	2.698	0.455	6.235	4.356
31	2.515	8.983	5.713	1.949	5.14	4.078
32	1.639	10.638	7.204	2.973	4.299	4.054
33	0.838	11.327	8.587	4.871	3.868	4.649
34	1.118	8.451	5.936	4.394	4.35	4.608
35	2.015	7.3	4.608	3.077	4.978	4.328
36	3.573	5.765	3.247	2.415	6.476	4.949
37	4.363	4.92	2.296	1.051	6.935	4.819
38	5.08	4.547	2.206	2.355	8.201	5.903
39	3.574	5.051	3.055	3.618	7.392	5.621
40	1.745	5.473	3.127	3.43	4.648	4.154

Table 5-2: Distortion of the simulated panel and unclamped average CMM measurements from the nominal design surface profile – Friction values 0.495, 0.5, 0.51, 0.525, 0.55

CMM Point	Unclamped Average	Friction 0.495	Friction 0.5	Friction 0.51	Friction 0.525	Friction 0.55
8	0.132	4.661	0.577	1.199	2.387	1.87
9	0.21	2.46	0.802	1.411	2.088	2.055
10	0.02	5.853	0.299	1.439	3.106	2.699
11	0.092	4.587	0.173	1.831	3.186	3.083
12	0.124	3.324	0.098	1.951	3.005	3.178
13	0.098	1.656	0.069	1.943	2.516	2.951
14	0.143	1.042	0.051	2.386	2.986	3.607
15	0.08	2.968	0.014	2.455	3.453	3.857
16	0.106	5.305	0.192	2.504	4.139	4.118
17	0.063	6.668	0.612	2.678	4.557	4.479
18	0.168	7.131	0.909	3.696	5.67	5.89
19	0.299	5.294	0.438	3.482	5.033	5.44
20	0.417	3.246	0.085	3.298	4.332	4.942
21	0.675	1.102	0.069	3.387	3.801	4.668
22	1.215	0.719	0.599	4.199	4.226	5.245
23	0.955	2.258	0.422	3.943	4.506	5.329
24	0.677	4.058	0.454	3.903	5.02	5.687
25	0.425	6.112	0.839	4.093	5.752	6.259
26	0.813	4.6	1.027	4.316	5.374	6.066
27	1.215	3.326	1.266	4.479	5.058	5.841
28	1.908	1.613	1.919	4.994	4.863	5.82
29	2.531	0.447	2.903	5.721	4.931	6.081
30	3.569	0.32	4.738	6.732	5.323	6.496
31	2.515	1.564	3.243	5.617	5.083	6.034
32	1.639	2.878	2.312	4.914	5.037	5.846
33	0.838	5.345	1.769	4.59	5.603	6.263
34	1.118	4.697	2.953	4.914	5.305	5.97
35	2.015	2.843	3.86	5.5	5.159	5.973
36	3.573	1.667	5.746	6.985	5.867	6.863
37	4.363	0.424	5.99	7.395	5.673	6.621
38	5.08	0.994	8.013	8.759	6.913	8.119
39	3.574	2.773	7.176	7.571	6.506	7.467
40	1.745	3.451	4.136	5.051	4.69	5.401

The data from Table 5-1 and Table 5-2 is presented in Figure 5.3, Figure 5.4, and Figure 5.5 as line graphs. Figure 5.3 presents the results for friction coefficients 0.15, 0.225, 0.45, and 0.475. As the friction was increased, so the four friction coefficient lines began to move towards the unclamped average CMM data line.

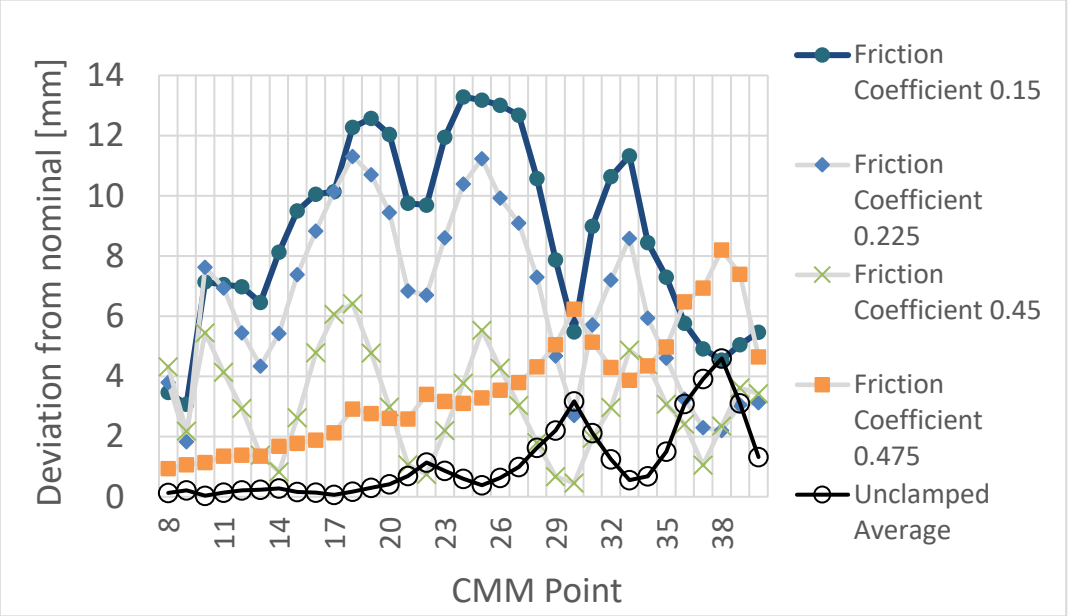

Figure 5.3: Line graph of the averaged unclamped CMM results and the several friction varied PAM-STAMP simulation models - panel distortion results

Figure 5.4 presents the results for friction coefficients 0.485, 0.495, 0.499, and 0.5. It was found that as the friction coefficient approached 0.5, a correlating trend with the unclamped averaged data was witnessed.

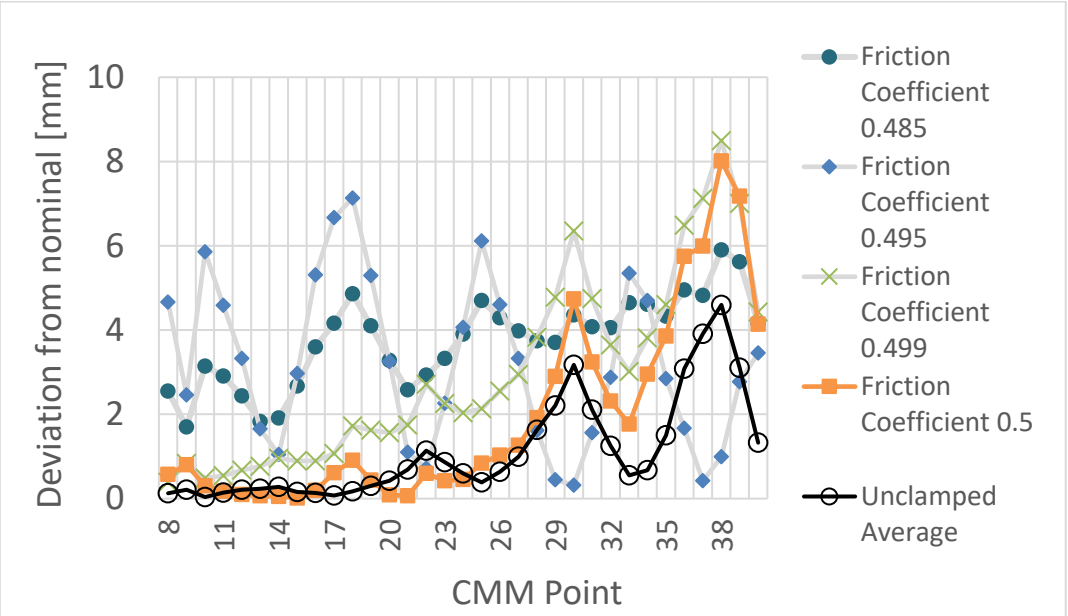

Figure 5.4: Line graph of the averaged unclamped CMM results and the several friction varied PAM-STAMP simulation models - panel distortion results

Figure 5.5 presents the results for friction coefficients 0.5, 0.501, 0.502, 0.525, and 0.5. As the friction coefficient increased above the 0.5 value, the trend deviates from the unclamped averaged CMM data line, thus rending 0.5 the optimal friction coefficient.

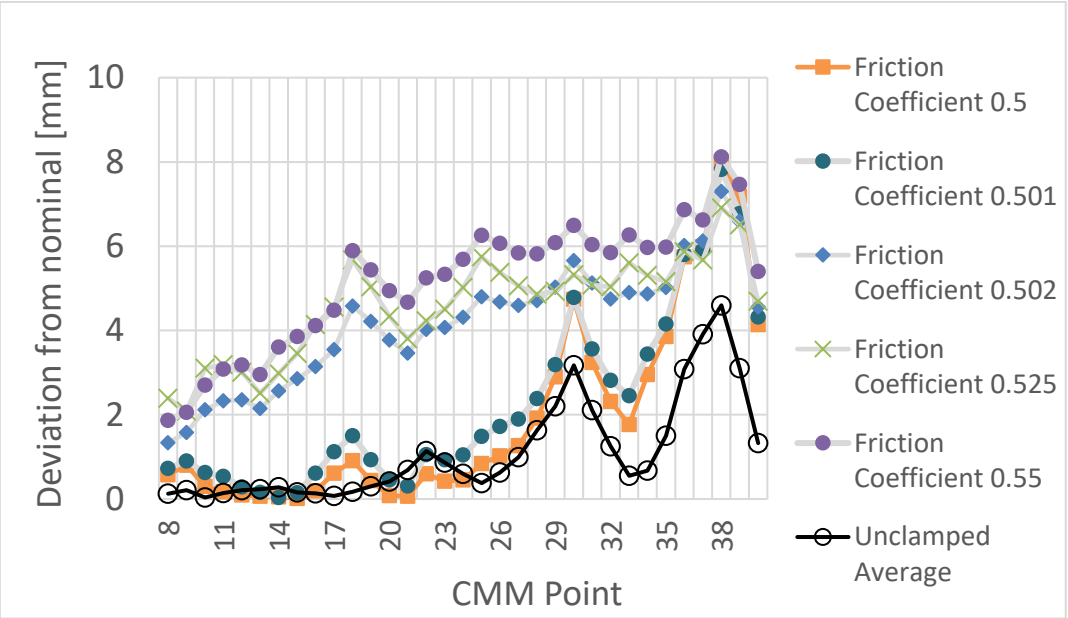

Figure 5.5: Line graph of the averaged unclamped CMM results and the several friction varied PAM-STAMP simulation models - panel distortion results

Figure 5.6 illustrates the surface profile of the 0.5 friction coefficient simulation model. Compared to the 0.15 friction coefficient simulation model, as shown in Figure 4.64 A, visually it appeared that the 0.5 friction model more closely aligned with the nominal surface.

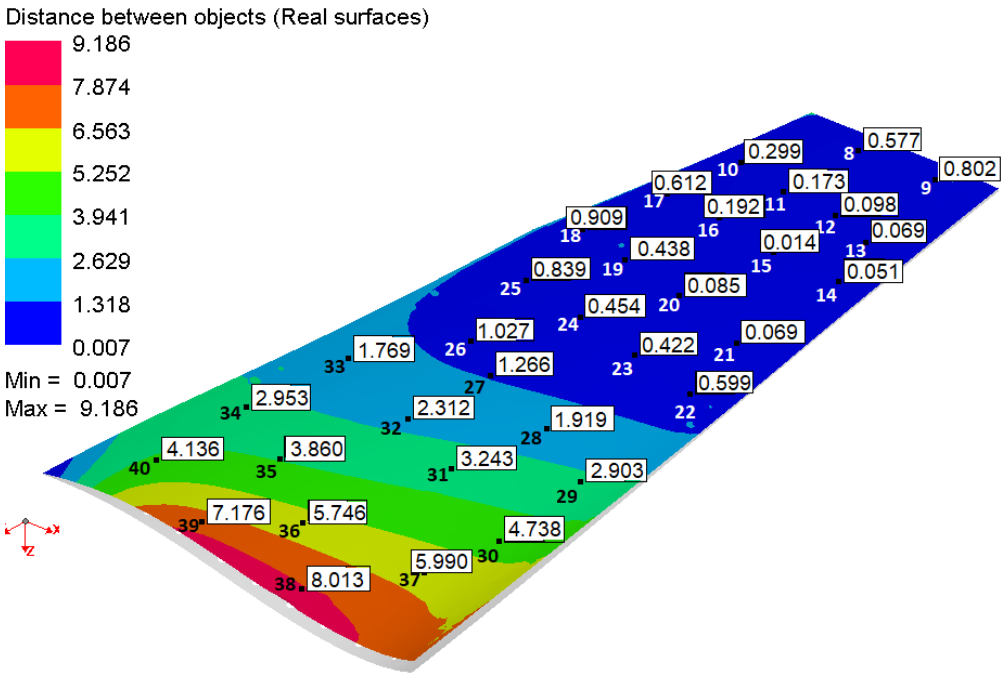

Figure 5.6: PAM-STAMP 0.5 friction coefficient model - final springback using the gravity stage alignment distortion plot

The line graph of the CMM and the simulation results for the 0.5 friction model is depicted in Figure 5.7. Compared with Figure 4.64 B and Figure 5.5, the 0.5 friction model showed a significant improvement but still deviated from the CMM results.

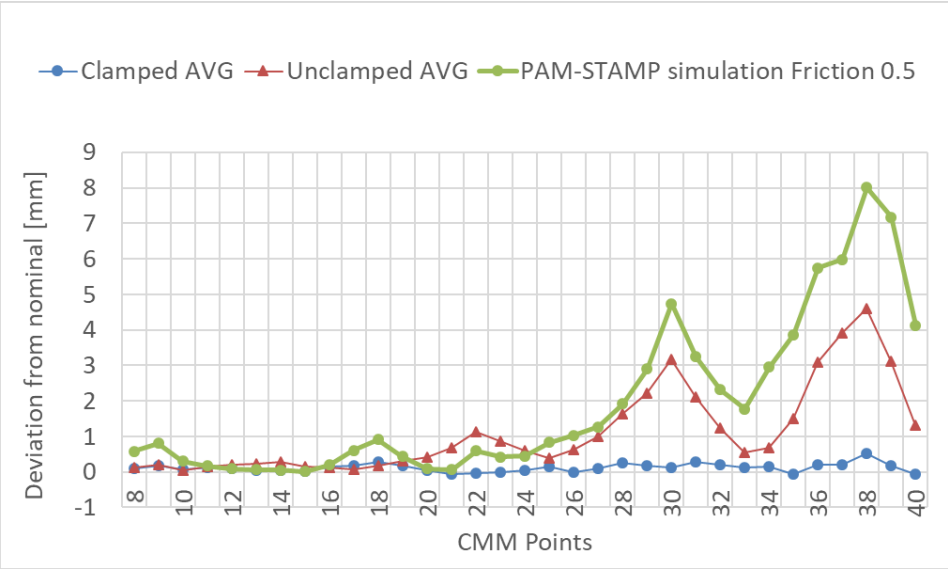

Figure 5.7: Line graph of the averaged clamped and unclamped CMM results and the PAM-STAMP 0.5 friction model distortion results (gravity alignment)

5.3. Metrology Results Comparison

In the variable friction study in Section 5.2, it was found that the 0.5 friction coefficient gave a better correlation to the manufactured component compared to the 0.15 friction coefficient simulation model. It was uncertain to what degree the surface profile tolerance of 1.4 mm was met using a line graph of the CMM points. The geometric dimensioning and tolerancing (GD&T) surface profile is defined in ISO 1101:2017, but the way it is calculated is not defined. Hence, a surface profile deviation of the simulation results could not be determined from the simulation results.

What was witnessed up this point was the lack of simulation software packages to draw a concrete comparison with the final component based on defined metrology measurement methodologies. The simulation ended with the panel distorting to a predicted final state after the final springback stage. However, in reality, it will be placed on an inspection fixture and subjected to gravity.

Section 4.6.3 provides the simulation operation where the gravity stage was introduced to improve the comparison between the manufactured component and the simulation studies. The evaluation methods currently utilised in most simulation software packages are inadequate at assessing the final form or the component.

This section will introduce a third-party software package, used to conduct a surface profile assessment conducted in accordance with the GD&T ISO 1101:2017 standard. GOM Inspect 3D Metrology software package was used to conduct three evaluations of the results achieved thus far:

1. Comparison of the simulation results with the nominal surface

2. Comparison of the manufactured components with the nominal surface

3. Comparison of the simulation results with the manufactured component.

The purpose of this section is to emphasis the degree of information missed in the current methods, especially in CAE simulation packages.

In order to conduct a comparison with the manufactured component, each had to be scanned, using a high definition 3D scanner. A Hexagon Romer scanner was used and provided a 3D point cloud of the four manufactured panels. The 3D scanner was calibrated according to ASME B89.4.22. A 3D point cloud consists of points on the surface of the item scanned in cartesian coordinates. This data was imported into the GOM 3D metrology software package, and a facetted mesh was created. The facetted mesh was then exported in a stereolithographic (.stl) file format.

Further processing of the mesh into a surface using CATIA V5 CAD software package was conducted to compare the simulation results with the manufactured component. The reason for creating a surface from the facetted mesh for conducting comparisons was the GOM 3D metrology software was a free version and not a commercially licenced version. The commercial license allowed for the two meshes (the simulation mesh and 3D scanned mesh) to be evaluated. The surfaces were generated using CATIA V5 CAD software package. The surface created from the facetted mesh had a maximum surface deviation of 0.3887 mm, a maximum free edge deviation of 0.7251 mm, and a mean surface deviation = 0.007681 mm. The deviations between the scanned mesh and reverse engineered mesh deemed acceptable.

Figure 5.8 shows the facetted mesh of panel number 3, which was converted into a surface. The final surface was then exported from CATIA in the IGS file format.

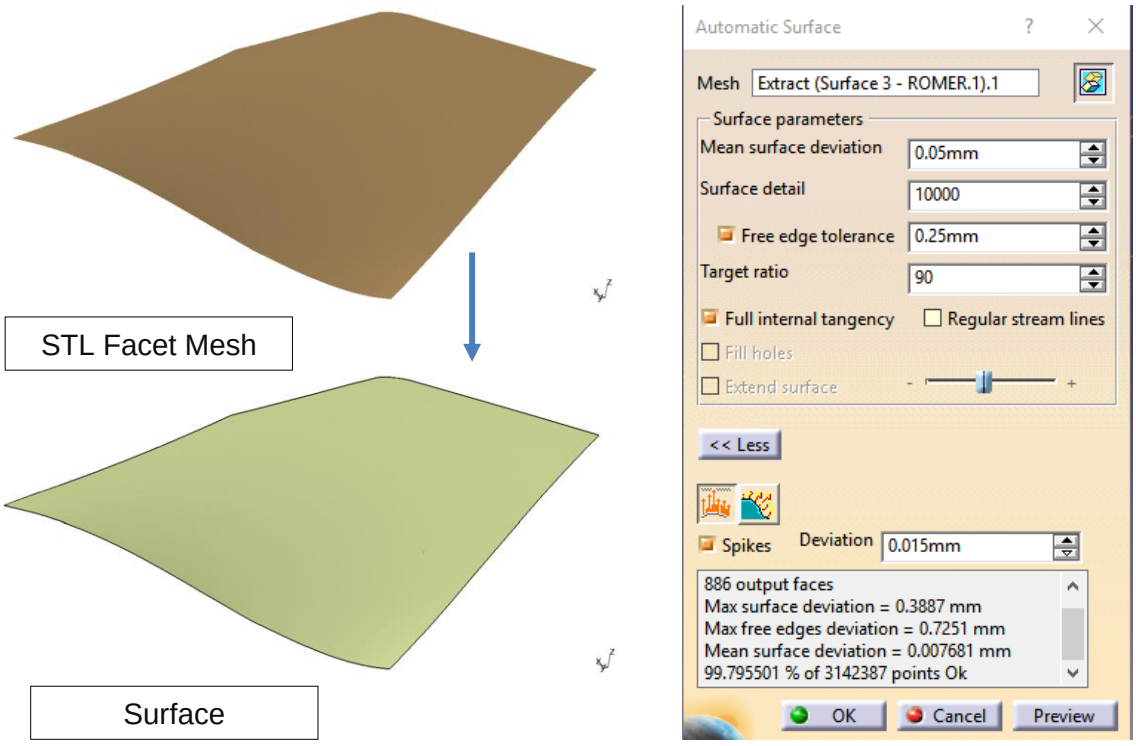

Figure 5.8: Facetted Mesh conversion into a surface

The benefit of using GOM to conduct an assessment of the various surfaces was the consistent method of aligning the components. A major challenge and downfall with many software packages was the inability to align the final result with the nominal surface definition and extract meaningful results.

5.3.1. Simulation to Nominal Surface Comparison

To compare the simulation result and the nominal surface, a .stl of the simulation results and a .igs model of the nominal surface was required. The igs surface geometry was first imported into the GOM 3D metrology software package and defined as the CAD part. The .stl mesh was exported from PAM-STAMP 2G at the gravity stage. This mesh was imported into the GOM 3D metrology software package and defined as the mesh part. Figure 5.9 depicts the simulation mesh and nominal surface as they were imported into the GOM 3D metrology software package before any alignment was conducted. The image shows that the two were well-aligned as the simulation mesh and nominal surface were based on the same coordinate system.

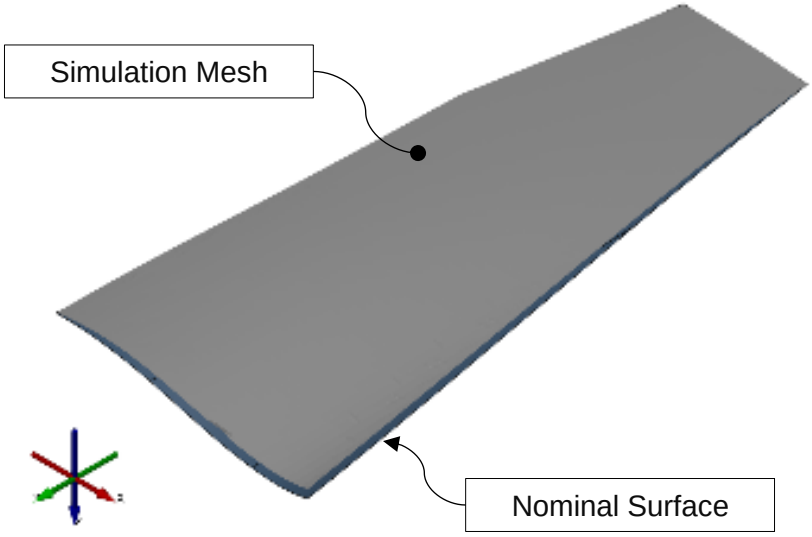

Figure 5.9: Simulated Mesh and Nominal Surface imported in the GOM 3D Metrology Software package before alignment has been conducted

Although the simulation mesh and the nominal surfaces aligned quite well, an alignment had to be created for the software to conduct a GD&T assessment. The 3-point alignment method was used based on the datum structure specified in the 2D drawing. Figure 5.10 shows the 3 points used to align the simulated mesh and the nominal surface. This alignment was used for all assessments using the GOM 3D metrology software package.

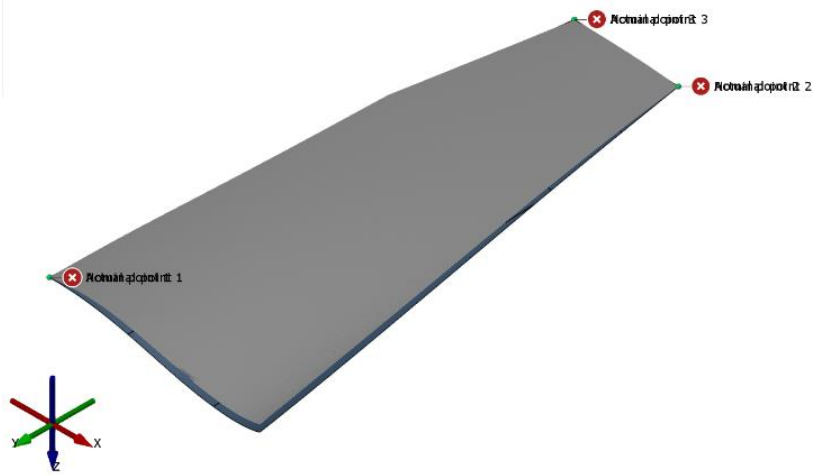

Figure 5.10: 3-point alignment of the simulated mesh and the nominal surface in the GOM 3D Metrology Software package

To conduct a GD&T inspection assessment, a measuring principle was required, serving as a link between a nominal element and the actual element. A nominal surface element from the CAD part was created. A fitted surface was created based on the meshed part. The GD&T check was then set-up with ISO 1101:2017 as the chosen assessment standard. In addition to the GD&T inspection check, a surface comparison was set-up to compare the deviation of the mesh surface from the nominal surface. The 33 CMM points have been included in this assessment.

Figure 5.11 depicts the GOM metrology software comparison of the 0.15 friction simulation result, compared with the nominal surface profile. Comparing the surface comparison contour plot of Figure 5.11 (a) (re-use of Figure 4.63) and (b), a correlation between the two was evident.

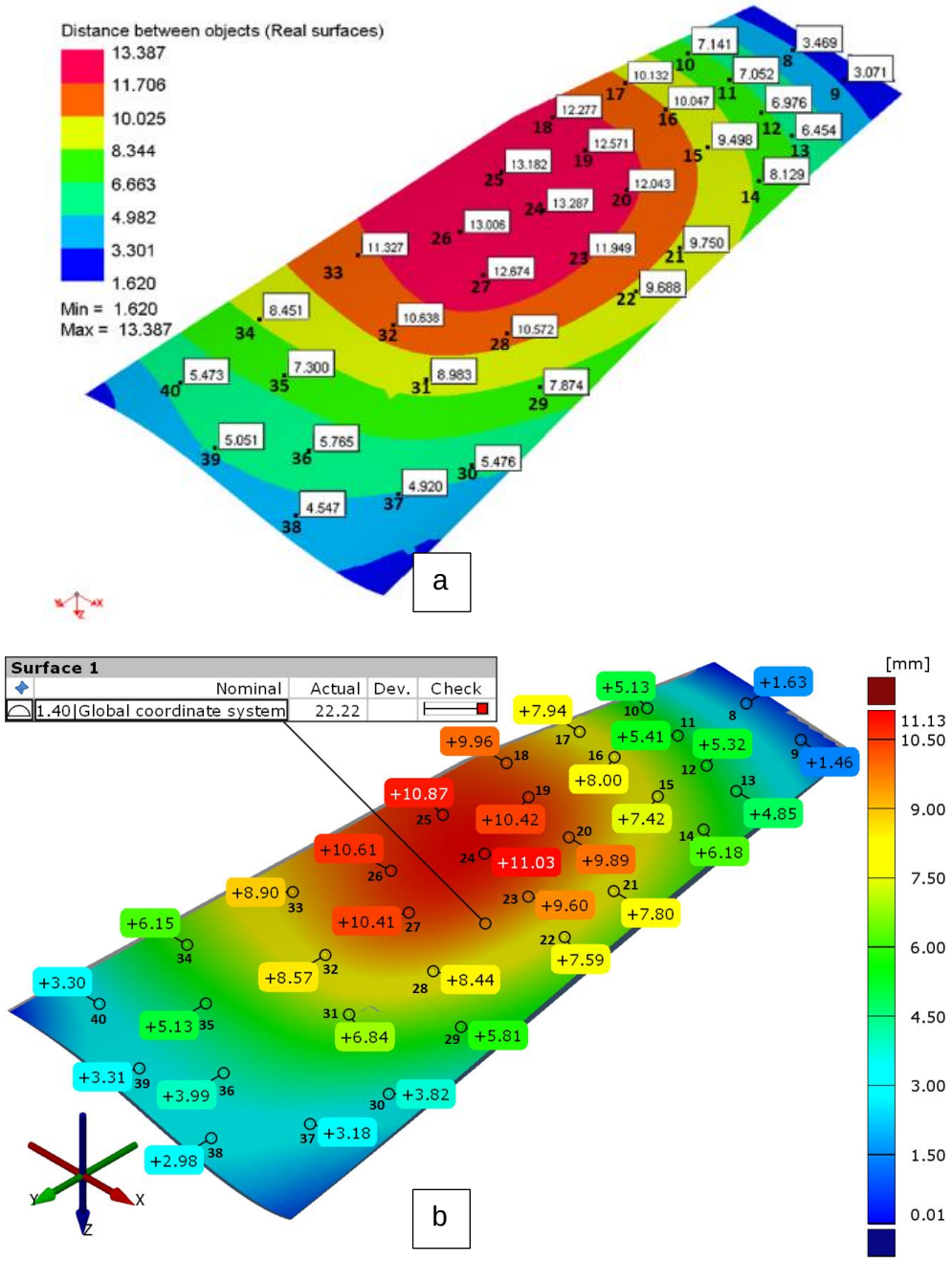

Figure 5.11: (a) PAMP-STAMP contour plot and (b) GOM 3D Metrology Software package GD&T surface profile and surface contour plot comparison of the 0.15 friction simulation result and the nominal surface

The correlation showed the gravity step in the simulation worked correctly for this model. However, if the misalignment of the mesh and the desired surface had been more complex than a single translation and required rotation transformation, proper alignment in the simulation software package would have been impossible.

Thus, the advantages of using the GOM 3D metrology software package was the simple and more consistent alignment method conducted in accordance with the component datum structure. The displacement contour plot gave a visual output of how well or poorly the panel conformed to the design. The most effective solution, using a metrology software package, in this case, was the GD&T surface profile calculation. Figure 5.11 shows that the 0.15 friction coefficient model had a surface profile of 22.22 mm. The design specification, as presented in Section 4.1, Figure 4.1, requires the manufactured component must meet a surface profile limit of 1.4 mm. Thus, the 0.15 friction coefficient model performs quite poorly as it deviates from the nominal by 20.82 mm.

Similarly, Figure 5.12 depicts the GOM metrology software comparison of the 0.5 friction simulation result, compared with the nominal surface profile. The surface profile of the 0.5 friction model did marginally better than the 0.15 friction coefficient model, achieving a result of 19.66 mm. As shown in detail A in Figure 5.12, a manufacturing flaw might have resulted from the panel trim line being too close to the trim location punch holes. This detail was not witnessed in the results presented in Sections 4.5 or 5.2. Removing the small flaw highlighted in Figure 5.12, detail A, the surface profile improved, resulting in a value of 6.01 mm.

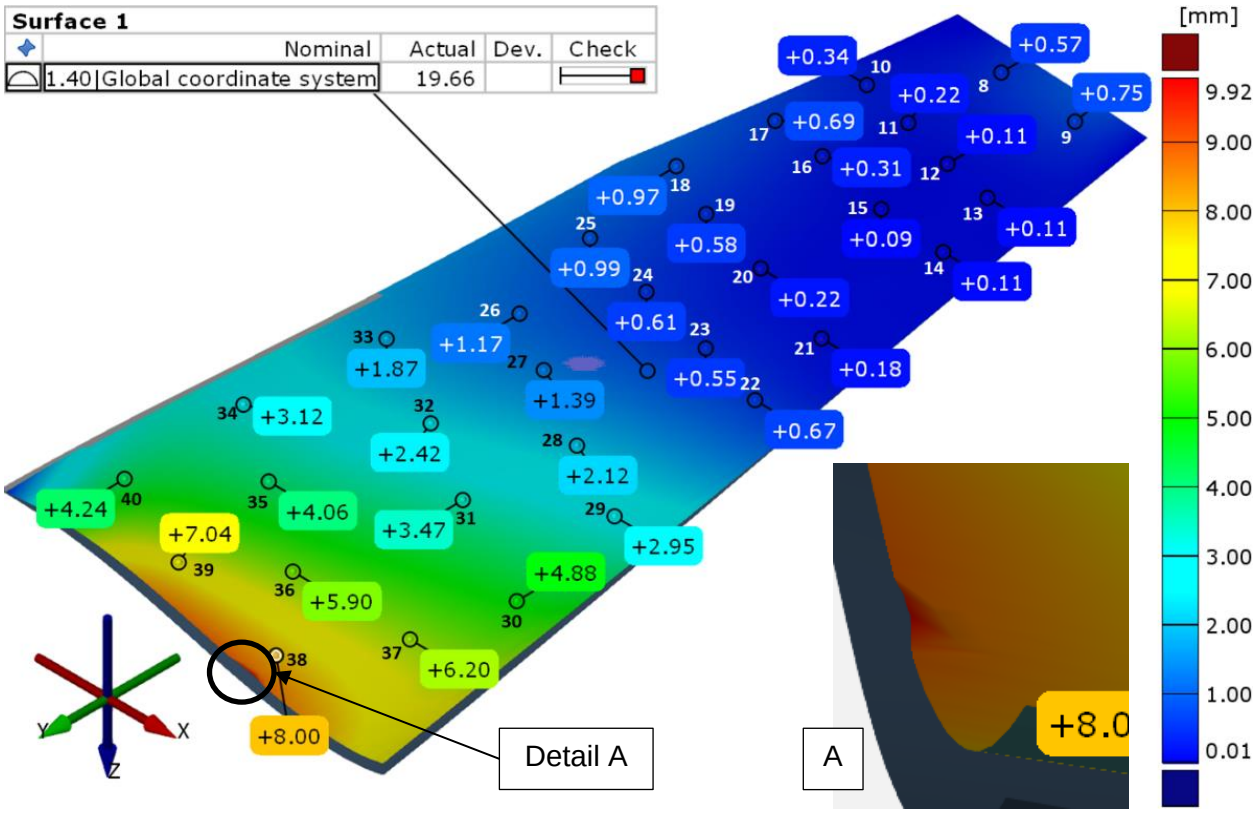

Figure 5.12: GOM 3D Metrology Software package GD&T surface profile and surface contour plot comparison of the 0.5 friction simulation result and the nominal surface

5.3.2. Manufactured to Nominal Surface Comparison

To compare the actual component and the nominal surface, a .stl of the actual component and a .igs model of the nominal surface was required. As conducted previously, the igs surface geometry was imported into the GOM 3D metrology software package and defined as the CAD part. The .stl mesh of the scanned panel, for this case panel number 3, was imported into the GOM 3D metrology software package and defined as the mesh part. Figure 5.13 depicts the actual component mesh and nominal surface as they were imported into the GOM 3D metrology software package before any alignment was conducted. The image shows the extreme misalignment of the two items in 3D space. Conducting an inspection in PAM-STAMP, or any CAE software package, was not possible.

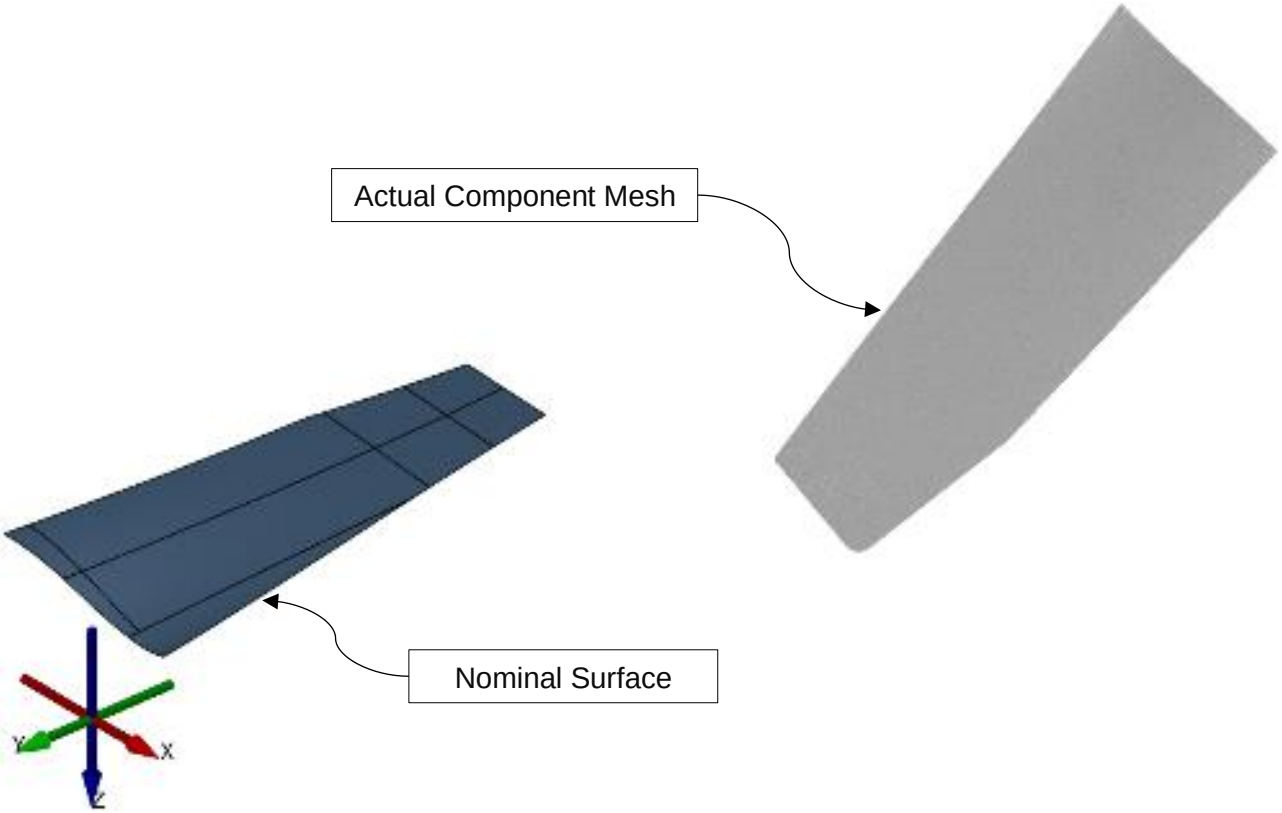

Figure 5.13: Actual Component Mesh and Nominal Surface imported in the GOM 3D Metrology Software package before alignment has been conducted

As conducted previously, a 3-point alignment was used to align the actual component mesh and the nominal surface. Figure 5.14 shows the 3 points used to align the actual component mesh and the nominal surface.

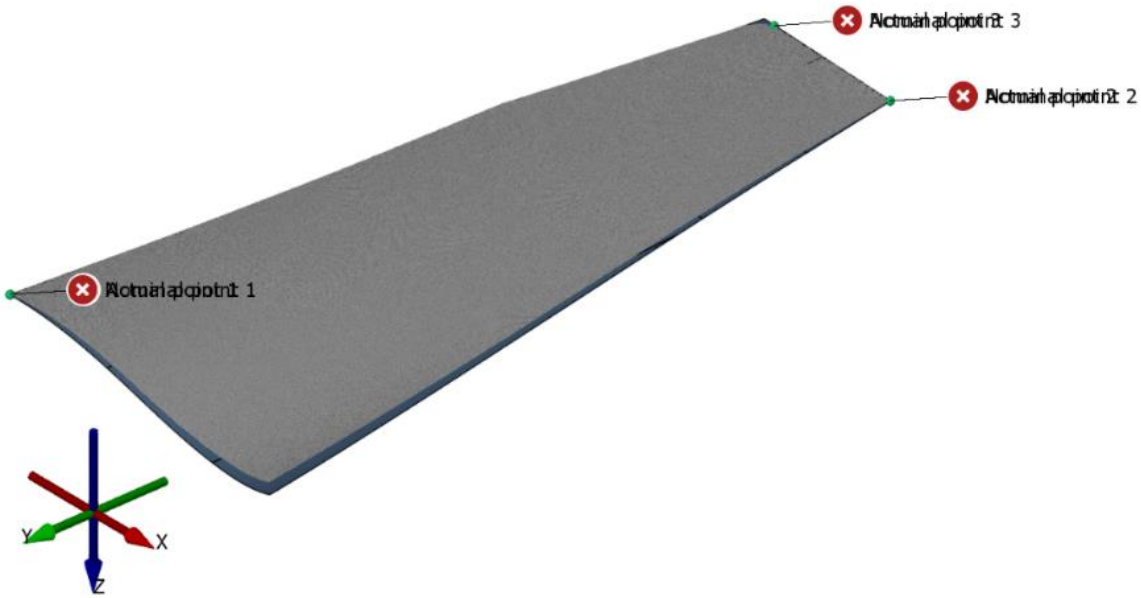

Figure 5.14: 3-point alignment of the actual component mesh and the nominal surface in the GOM 3D Metrology Software package

The actual component comparison with the nominal surface was conducted using the GOM 3D metrology software package, as depicted in Figure 5.15. The surface profile of the actual component compared to the nominal surface was 19.23 mm.

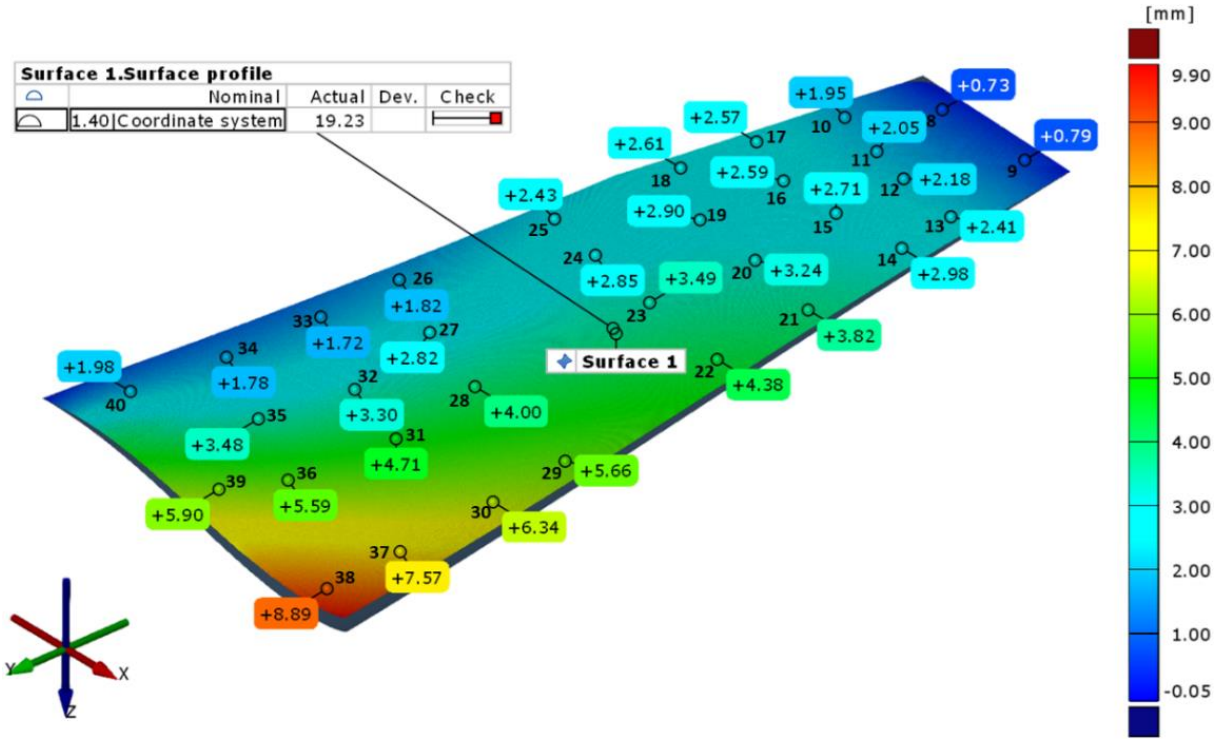

Figure 5.15: GOM 3D Metrology Software package GD&T surface profile and surface contour plot comparison of the actual component and the nominal surface

5.3.3. Simulation to Manufactured Component Comparison

To compare the actual component and the simulation result, a .stl of the simulation result and a .igs model of the actual component's surface from the .stl mesh was required. The creation of this surface was discussed previously. As conducted previously, the igs surface geometry was imported into the GOM 3D metrology software package and defined as the CAD part. The .stl mesh of the simulation result was imported into the GOM 3D metrology software package and defined as the mesh part. Figure 5.16 depicts the simulation result mesh, and the actual component surface before any alignment was conducted. The image shows the extreme misalignment of the two items in 3D space.

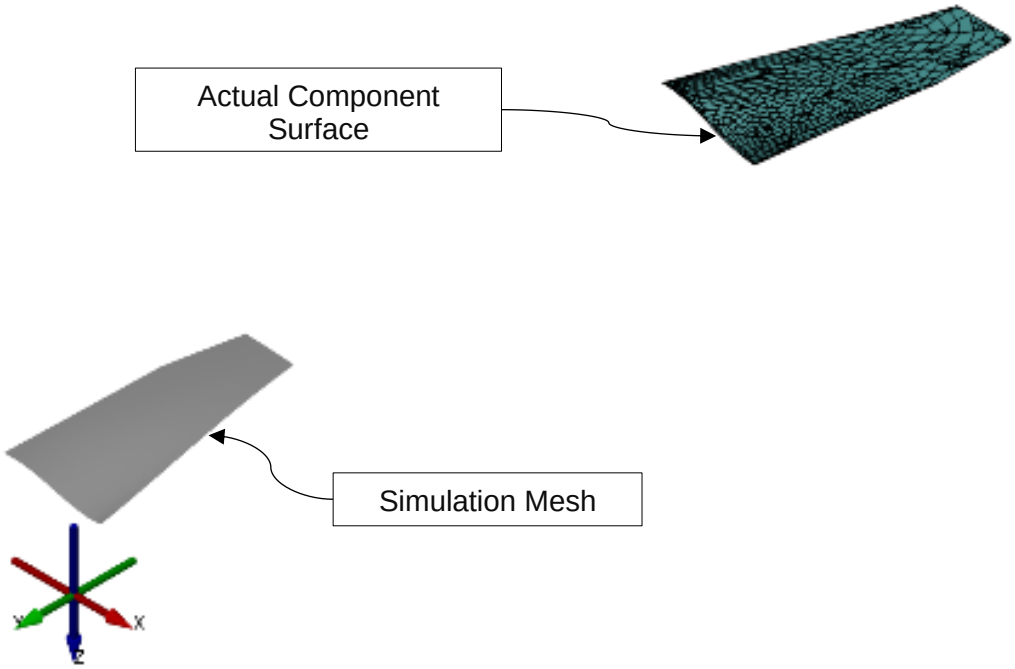

Figure 5.16: Simulation Result Mesh and Actual Component Surface imported in the GOM 3D Metrology Software package before alignment has been conducted

As conducted previously, a 3-point alignment was used to align the actual component mesh and the nominal surface. Figure 5.17 shows the 3 points used to align the simulation result mesh and the actual component surface.

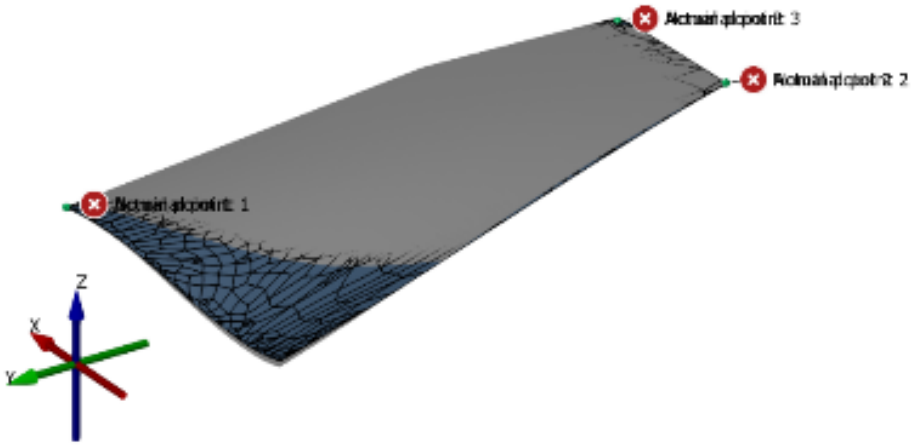

Figure 5.17: 3-point alignment of the simulation result mesh and the actual component surface in the GOM 3D Metrology Software package

The final comparisons of the 0.15 and 0.5 friction coefficient simulation model results were compared against the manufactured component. Figure 5.18 and Figure 5.19 depict the 0.15 and 0.5 friction coefficient simulation models compared the manufactured component, respectively.

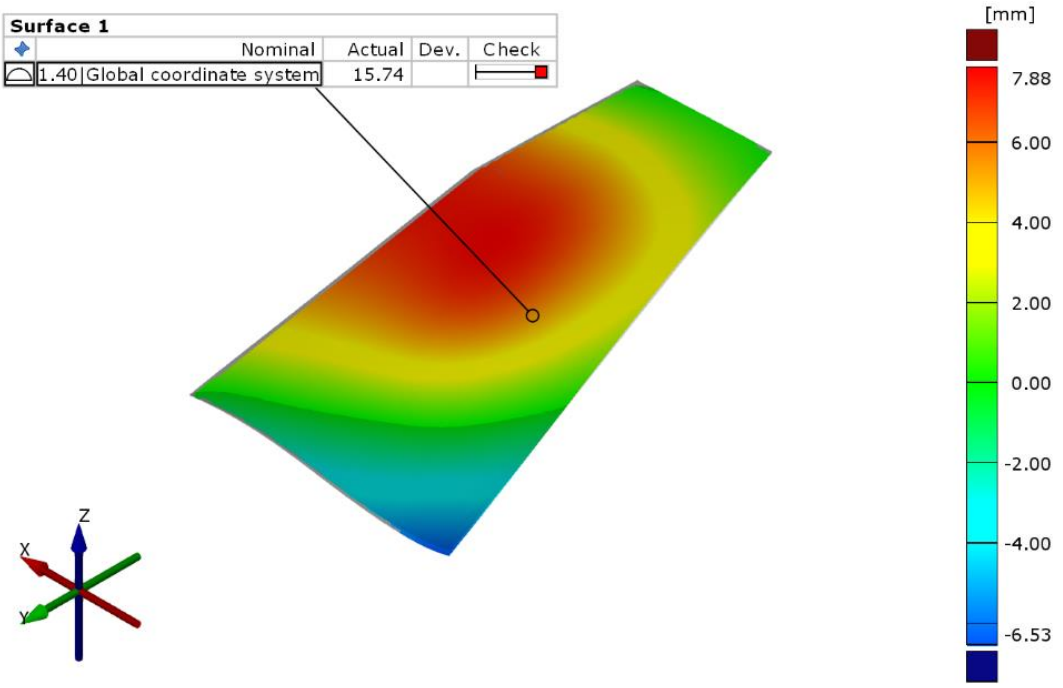

Figure 5.18: GOM 3D Metrology Software package GD&T surface profile and surface contour plot comparison of the 0.15 friction coefficient simulation model and the actual component surface

The 0.15 friction coefficient simulation achieved a surface profile measurement of 15.75 mm, whereas the 0.5 friction coefficient model achieved a surface profile measurement of 7.18 mm.

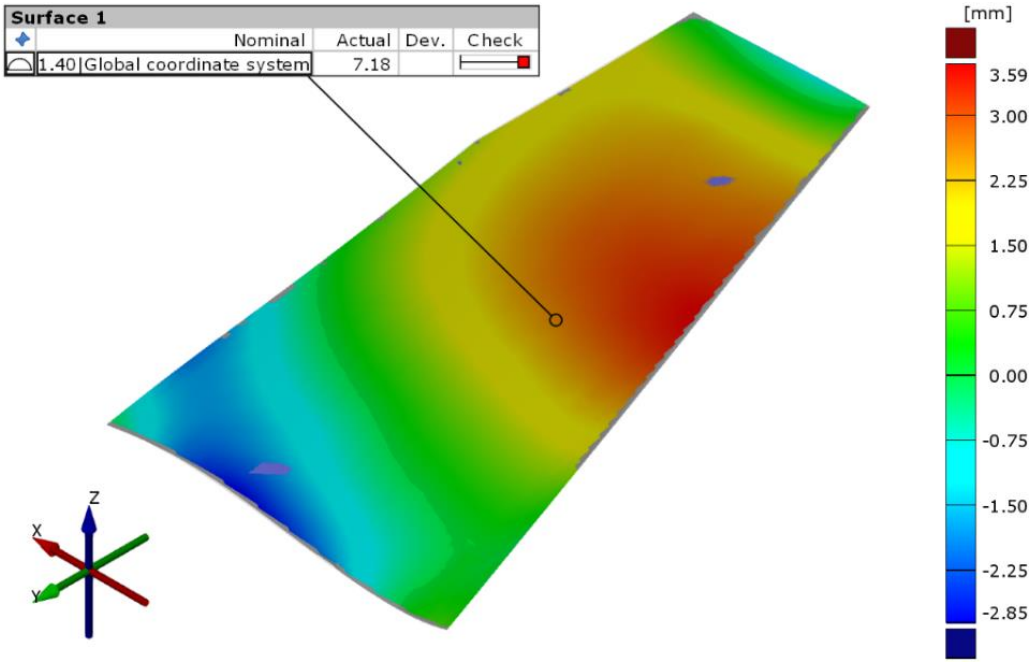

Figure 5.19: GOM 3D Metrology Software package GD&T surface profile and surface contour plot comparison of the 0.5 friction coefficient simulation model and the actual component surface

Chapter 6: Discussion

6.1. Introduction

The purpose of the study was to validate the simulation of die sheet hydroforming of a complex-shaped aluminium alloy component. The aluminium alloy aircraft panel selected for the study could not be manufactured by conventional stamp forming without further post-processing for it to meet the design requirements. A case study of the aircraft panel was conducted by systematically following the steps of the forming process conceptualisation cycle. A comprehensive materials testing campaign was conducted that provided accurate mathematical material laws to provide the most accurate predictions.

Several iterations of blank and tool designs were conceptualised and assessed using manufacturing simulations in ESI Group PAM-STAMP 2G forming simulation software package. A final concept was chosen, and tool proofing was conducted with four components successfully manufactured. Even without springback compensating the tool, the final shape of the components all met the 1.4 mm surface profile design requirement. This achievement deemed the manufacturing of the component a success.

However, in order to answer the research question, step 5 of the research objective had to be completed. To determine the accuracy of PAM-STAMP's ability to accurately predict the final form of a die sheet hydroformed component, the simulated and manufactured components were compared. Initial comparisons showed no correlation and further investigations were undertaken. As the material properties were based on test data, the only parameter that could be altered was the friction coefficient. The comprehensive friction simulation study yielded positive results when assessed using CMM results. 3D scanning and metrology were introduced to provide a more detailed assessment of the friction study results. The study yielded two main findings and two additional findings, which are discussed in detail in the sections to follow.

6.2. The Importance of Rubber-to-Metal Friction

It was found that simulation was useful in providing insight into how well or poorly a blank and tool concept would perform. The forming limit diagram proved to be extremely useful in evaluating defects such as buckling and cracks. Most notably, the in-plane stretching condition of the blank that must be sufficient for springback to be minimised. A major parameter that was found to have influenced the result was the rubber-to-metal friction condition.

The opted route taken was to conduct the simulation study without rubber similar to the work of Leacock et al. (2016) and Carlsson and Vrijhof (2018), where the rubber throw pads and diaphragms were not modelled. The software developer, ESI Group, recommended simulating the process without modelling the rubber. The omission of rubber elements was further substantiated by how the fluid cell forming pressure load was applied to the blank in accordance with the PAM-STAMP user guide (ESI Group, 2018).

The omission of rubber elements meant less material characterisation costs were incurred. In addition, the added cost computationally due to the need for solid rubber elements which increased the solving time dramatically. As the rubber elements were not modelled, neither was the rubber-to-friction tribological testing conducted.

Kang et al. (2004), Hatipoğlu et al. (2007), Chen et al. (2014), Chen et al. (2015), Lee et al. (2018), Păunoiu et al. (2019), Muñoz-Rubio et al. (2019), and Zhang et al. (2019) all modelled the rubber diaphragm and the rubber-to-metal friction coefficient. Hatipoğlu et al. (2007) and Muñoz-Rubio et al. (2019) were the only authors to make use of a rubber-to-metal friction coefficient that was greater than 0.3. Kang et al. (2004), Chen et al. (2014), Chen et al. (2015), Lee et al. (2018), Păunoiu et al.

(2019), and (2019), Zhang et al. (2019) all made use of low rubber-to-metal friction coefficients. The only exception was Muñoz-Rubio et al. (2019), who applied a friction coefficient of 0.5. However, this was a digital optimisation study, and the simulation results were not validated by practical forming trials.

The difference between the aircraft component considered in the presented study and that of previous die sheet hydroforming studies was the shape. Previous studies all investigated simple flanged components, compared to the compound curved component. Because of the nature of the components, the previous authors all showed that rubber friction had little impact on the manufacturing process. Where a similar, a more complex component was considered, as in the Muñoz-Rubio et al. (2019) study, the influence of rubber was found to be more significant.

In the presented study, friction was found to have a significant influence, as discussed in Section 5.2. As the friction coefficient was increased, so the correlation between the simulated surface and the nominal surface improved. This finding was attributed to the increased degree of edge restraint on the blank during forming, which increased the predicted degree of in-plane stretching. The best correlation between simulation and practical forming experiments was found with a 0.5 friction coefficient, which is consistent with the findings of Muñoz-Rubio et al. (2019). The friction coefficient was limited to 0.55 in the variable friction study as no further improvement was witnessed, and the FLD showed no cracks.

The complex nature of rubber-to-metal sliding (Gómez et al. 2013), cannot be accurately modelled in PAM-STAMP simulations as friction is modelled based on Coulomb's friction law (ESI Group, 2018). The hyperelastic deformability of the elements may improve the physics of rubber-to-metal friction condition. However, this will come at the cost of substantially increased computation time while the potential for improvement in the final result is unclear from previous studies, as discussed in Section 2.2.5. Nevertheless, based on the fact that the friction coefficient was found to be an important parameter in the presented study, further work to characterise the friction conditions in fluid cell metal sheet hydroforming and the potential of modelling the rubber diaphragm explicitly would seem to be warranted.

6.3. Simulation Metrology

3D metrology was introduced in the validation phase and is presented in Section 5.3. Typically, CMM is well established as the industry standard inspection method and was used to measure the final components in the studies the Leacock et al. (2016), Karaağaç (2016), Păunoiu et al. (2019), and Zhang et al. (2019) studies. Line graphs were used to provide a comparison between the simulation and manufactured components. The line graphs provided limited detail for surface components but are acceptable for simple components, such as flanged components.

Schneider el at. (2008) and Solfronk and Sobotka (2011) made use of optical measurement using the GOM ATOS software package. The panels received a grid pattern before forming and were only made use of for tool proofing purpose. The grid method was not a serial production inspection process. The process was useful in accessing the final component to validate the blank and tooling design solution and the simulation. The same technique was used to assess the results of the presented study, except the final components were 3D scanned. The laser created grid patterns or permanent markings, and the final shape was captured into a point cloud.

A 3D metrology software package, such as GOM, the alignment of any surfaces that were severely distant to one another, could be simply aligned according to the predefined datum structure. This was not achievable using PAM-STAMP. PAM-STAMP allowed for a displacement plot, where best-fit alignment was the only alignment method available. The displacement plot was an acceptable way of assessing the suitability of the final form to decide if the concept could be accepted. However, better assessment methods and processes are available.

The industry standard for geometric dimensioning and tolerancing (GD&T) of a surface profile is defined in ISO 1101:2017. The component investigated in the presented study had a defined surface profile tolerance of 1.4 mm. The component's fitness was measured against this specification and conformed to the design if within the desired tolerance band. A GD&T surface profile assessment was not available in PAM-STAMP. The digitalisation of the panels by 3D scanning and the use of GOM inspect, provided for a simple and standard method for comparing the various surfaces, in particular, the simulation to the manufactured component. Simulation metrology is a new area of research. It will provide a quantitative and standardised method of assessing simulation results.

6.4. Die Sheet Hydroforming Simulation – Gravity Stage

Another practical finding of the study was that an additional simulation operation needed to be applied to improve the correlation between the manufactured component and the simulation. This added step was a gravity stage that allowed the blank to settle onto the inspection fixture as it would in reality. This process was deemed an alignment step with three corners of the component interfacing the inspection tool in the same way the manufactured component does in reality. No evidence was found in the literature that this process has been applied previously as a means to assess the final results of a simulation study accurately.

Typically, the flanged components that were investigated by Kang et al. (2004), Hatipoğlu et al. (2007), Chen et al. (2014), Chen et al. (2015), Lee et al. (2018), Păunoiu et al. (2019), Muñoz-Rubio et al. (2019), Zhang et al. (2019) required no alignment as one half of the component was fixed to the tool. In the case of this study, the aircraft panel once the trim and springback stages were conducted, the panel was free to move in 3D space and thus not fixed like the flanged components. The lack of alignment for measuring results within the simulation is a significant limitation. The only disadvantage of the gravity step was the simulation time taken to complete the process.

What was missing in the sheet hydroforming simulation process was the final stage of manufacturing, assembly. As witnessed in the literature consulted for the presented study, all the authors finished the simulation study after springback. The gravity stage allowed for the alignment of the component onto the check inspection fixture. The check inspection fixture tool clamped the blank in a representative way it was fastened into the final assembly. The 1.4 mm surface profile tolerance was defined to accommodate the assembly process, where the component must be able to be installed without excessive force. By conducting a gravity stage, the fitness of the component will not only be validated for dimensional correctness, but suitability to meet installation requirements.

Digital manufacturing will greatly benefit from this added process step. The gravity stage improves the forming simulation process, which as stated, typically concludes after springback. Going further with the simulation and exploring the installation or inspection phase of the production process, provides a more detailed prediction of what the component's blank and tooling concept is capable of achieving before production equipment is manufactured. In addition, the way results are investigated and processed are more align to what the component must achieve in its final state, which in the assembly body.

6.5. Uncompensated tooling resulted in a good component

An interesting finding of the study was that the manufactured components met the design specification even though the tool surface was not compensated for springback. Compensated tooling is a pre-distorted surface from the nominal component surface profile to account for springback (ESI Group, 2018), to ensure that the shape of the component is close to the nominal design shape after forming. The final tool concept of this study did not receive tooling compensation and was identical to the nominal surface of the component. The results suggest that the component underwent sufficient plastic deformation during pressing to limit springback to a minimum. Moreover,

the comparison between the simulation and the manufactured components is based on the same surface definition and was thus sufficient to validate the simulation approach.

It was found that without compensation, the final components met the final design requirement of a surface profile of 1.4 mm. The panel was checked in two configurations in the inspection check fixture, unclamped and clamped state. Unclamped, the panel is clamped in one corner, versus all the edges of the panel clamped as it would be in the installed state. Section 4.6.2 presents metrology results.

The study aimed to manufacture the aircraft panel in the -W temper condition but was could only be manufactured in the annealed -O temper condition. As discussed in Section 4.3, the -O temper condition has a higher degree of formability which is directly correlated to the stiffness of the material. AA2024-W temper condition will naturally age to AA2024-T42 temper condition, which is stiffer. In addition, the material will work harden during the cold forming process (hence the need for kinematic hardening laws). The AA2024-O annealed temper condition is less stiff, will naturally age over a much longer time frame compared to -W temper condition, and does not undergo significant work hardening (Dowling, 2007). Thus, AA2024-O remains soft during the forming process and for some time after.

The low strength of the -O temper condition material is likely the reason for the exceptional conformance of the component, as the pressing operation resulted in sufficient plastic deformation to limit springback. The same results would not be expected for -W temper condition with the panel experiencing a much higher degree of springback and non-conformance. The AA2024-T3 temper condition would see even further distortion than -W temper condition, as witnessed in the Chen et al. (2015) study. In this case, compensation of the tool surface would need to be applied to compensate for the expected springback.

Chapter 7: Conclusions

7.1. Summary of Project Findings

This study aimed to investigate the process of conceptualising the blank and tools required to manufacture a complex-shaped aluminium aircraft skin panel, using die sheet hydroforming. Several investigations were conducted using ESI Group PAM-STAMP 2 simulation software package.

The forming process conceptualisation cycle showed to be a useful workflow, defining the steps to be taken from design concept model to realised component. The various steps of the cycle were followed explicitly and proved vital when deciding to proceed to the next step in the conceptualisation cycle.

It was found that even without the explicit modelling of the rubber elements, a successful die sheet hydroformed simulation result and a final component could be obtained. However, the rubber-to-metal friction coefficient must be incorporated appropriately, at a higher value than for conventional metal-to-metal press tooling.

In order to assess the final simulation result, it was found that the post-assessment procedures within a simulation software package required development. PAM-STAMP cannot assess a component according to standard metrology methods. A third-party software package, GOM inspect 3D metrology, was used to assess the component and determine if it was with the desired specification. This process is simulation metrology and is a new area of interest that should be incorporated into simulation software packages to offer the customer a standardised method to confirm the simulation output.

In addition to the forming, springback, and trimming stages of the digital manufacturing simulation process, an operation was introduced to align the two components in order to correlate the simulation and CMM results. The gravity stage has led to what is termed an assembly installation stage that provided a more accurate correlation to the manufactured component. The predicted capability of the blank and tool concept for manufacturing a component that is suitable for installation into the final assembly was realised with the gravity operation. The gravity stage or additional installation stages improves the forming simulation processes to become a complete digital manufacturing simulation investigation.

7.2. Future Research

Based on the findings from this research, the following further work is recommended:

1. The material characterisation campaign did not include the rubber characterisation and rubber-to-metal tribological testing. Future work should investigate the modelling of rubber elements, and rubber-to-metal friction data and its influence on a complex-shaped component such as the aircraft panel investigated in the presented study.

2. A third-party software package was used to assess the various surfaces. Future work is required to investigate and develop procedures and analysis methods that can be incorporated into commercial simulation software packages. This work should improve on the forming process conceptualisation cycle with accurate feedback about the state of the manufactured component. In addition, simulation metrology may result in commercial opportunities as it improves the current operational functions of the simulation investigations.

3. The AA2024-W temper condition sheet was not pressed due to complications during the study. Future work could investigate the simulation of the tool with tested rubber-to-metal friction coefficients and the manufacture of the AA2024-W temper condition component to validate blank and tool design for that material condition for comparison against the AA2024-O temper condition. This will require tool surface compensation to allow for springback since AA2024 aluminium alloy in the W temper condition has a higher strength than the -O temper condition that was used in the present study. In addition, it is proposed that in the future pressing trial, an appropriate strain measurement process be used to capture the stress and strain state of the blank in final form for comparison with the simulation results.

4. Further investigation is required into the gravity stage. The gravity stage has shown potential to effectively predicted the capability of blank and tool concepts with closer alignment to the actual final state of the component. The simulation of the final installation or inspection stages of manufacturing are not conducted in digital manufacturing simulation studies, and thus will have a significant benefit to the current forming feasibility and manufacturability simulation procedures and methodologies.

References

Abedrabbo. A., Zampaloni, M., Pourboughrat, F. 2005. Wrinkling control in aluminum sheet hydroforming. International Journal of Mechanical Sciences 47 (2005) 333–358.

Ahmetoglu, M., Hua, J., Kulukuru, S., Altan, T. 2004. Hydroforming of sheet metal using a viscous pressure medium. Journal of Materials Processing Technology 146 (2004) 97–107.

Altair Hyperform™ [Online]. https://altairhyperworks.com/product/hyperform. [2020, October 24].

Altan, T., Tekkaya, A. 2012. Sheet Metal Forming Fundamentals. ASM International, Volume 1.

Altan, T., Tekkaya, A. 2012. Sheet Metal Forming Processes and Applications. ASM International, Volume 2.

APB 3-1119. 2005. Heat treatment of aluminium. Process specification Airbus UK.

Armstrong, P.J., Frederick, C. O. 1996. A mathematical representation of the multiaxial Bauschinger e9ect. CEGB Report RD/B/N731, Berkeley Nuclear Laboratories; 1996.

Bagherzadeh, S., Mirnia, M. J., Mollaei Dariani, B. 2015. Numerical and experimental investigations of hydro-mechanical deep drawing process of laminated aluminum/steel sheets. Journal of Manufacturing Processes 18 (2015) 131–140.

Baosheng, L., Lihui, L., Yuansong, Z., Jianguo, L. 2012. Forming characteristic of sheet hydroforming under the influence of through-thickness normal stress. Journal of Materials Processing Technology 212 (2012) 1875– 1884.

Barlat, F., Brem, J.C., Yoon, J. W., Chung, K. Dick, R. E., Lege, D. J., Pourboghrat, F., Choi, S. H., Chu, E. 2003. Plane stress yield function for aluminum alloy sheets—part 1: theory. International Journal of Plasticity 19 (2003) 1297–1319.

Bell, C., Corney, J., Zuelli, N. Savings, D. 2020. A state of the art review of hydroforming technology. International Journal of Material Forming volume 13, pages 789–828 (2020).

Carlsson, B., Vrijhof, S. 2018. White paper on the successful simulation of flexforming processes at Quintus Technologies [Online]. Available: https://formingworld.com/quintus-technologies-flexforming/ [2020, July 12].

Chen, L., Chen, H., Guo, W., Chen, G., Wang, Q. 2014. Experimental and simulation studies of springback in rubber forming using aluminium sheet straight flanging process. Materials and Design 54 (2014) 354–360.

Chen, L., Chen, H., Wang, Q. Li, Z. 2015. Studies on wrinkling and control method in rubber forming using aluminium sheet shrink flanging process. Materials and Design 65 (2015) 505–510.

Cook, R., D., Malkus, D., S., Plesha, M., E., Witt, R., J. 2002. Concepts and Applications of Finite Element Analysis. 4th Edition, Wiley.

Curtis, M. A., Farago, F. T. 2013. Handbook of Dimensional Measurement. 5th edition. New York: Industrial Press Incorporated.

ESI Group. 2020. Determination of Krupkowsky parameters for hardening curve [Online]. Available: https://myesi.esi-group.com/resources/tips-tricks/determination-krupkowsky-parameters-hardening-curve. [2020, July 7].

Dirikolu, M. H., Akdemir, E. 2004. Computer aided modelling of flexible forming process. Journal of Materials Processing Technology 148 (2004) 376–381.

Dowling, N.E. 2007. *Mechanical Behavior of Materials: Engineering Methods for Deformation, Fracture, and Fatigue*. 3rd Edition. Pearson, New York, NY.

Elangovan, K., Sathiya Narayanan. C., Narayanasamy. R. 2010. Modelling of forming limit diagram of perforated commercial pure aluminium sheets using artificial neural network. Computational Materials Science, 47 (2010) 1072–1078.

ESI Group. 2013. Material Data Management.

ESI Group. 2018. PAM-STAMP sheet metal forming software user's guide.

ESI MAT-WIZARD [Online]. Available: https://myesi.esi-group.com/downloads/add-ons/esi-mat-wizard. [2020, July 7]

Ershov, A., Kotov, V., Loginov, Y. 2012. Calculation of the compensation of a stamping tool after springback in the software package PAM-STAMP. Metallurgist, Vol. 56, Nos. 7–8, November, 2012 (Russian Original Nos. 7–8, July–August, 2012).

Ershov, A., Loginov, Y. 2013. Using the inverse solver "inverse" in PAM-STAMP 2g to assess the formability of a part. Metallurgist, Vol. 57, Nos. 5–6, September, 2013 (Russian Original Nos. 5–6, May–June, 2013).

Ershov, A., Loginov, Y. 2014. Use of the program PAM-STAMP to study the effect of the as-received condition of a material on its formability during stamping. Metallurgist, Vol. 58, Nos. 3–4, July, 2014 (Russian Original Nos. 3–4, March–April, 2014).

ErtUrk, T. and Kazazoglu, E., "Effect of Aging on Bulk Formability of Aluminum Alloys," Formability of Metallic Materials—2000 A.D. ASTM STP 753. J. R. Newby and B. A. Niemeier, Eds., American Society for Testing and Materials, 1982, pp. 19-34.

Fallah, T., Sedighi, M., Hashemi, R. 2018. Effects of Natural Aging Treatment on Mechanical, Microstructural and Forming Properties of Al 2024 Aluminum Alloy Sheets. Iranian Journal of Materials Science & Engineering Vol. 15, No. 2, December 2018.

Frącz, W., Stachowicz, F., Pieja, T. 2013. Aspects of verification and optimization of sheet metal numerical simulations process using the photogrammetric system. Acta Metallurgica Slovaca, Vol. 19, 2013, No. 1, p. 51-59.

GOM Software. 2019. Inspection Basic Training – 3D Metrology.

Gómez, M. A., Gallardo-Hernández, E. A., Vite Tores, M. Peña Bautista, A. 2013. Rubber steel friction in contaminated contacts. Wear 302 (2013) 1421 - 1425.

Hama, T., Hatakeyama, T. Asakawa, M., Amino, H., Makinouchie, A., Fujimotoa, H., Takudaa, H. 2007. Finite-element simulation of the elliptical cup deep drawing process by sheet hydroforming. Finite Elements in Analysis and Design 43 (2007) 234 – 246.

Hatipoğlu, H. A., Polat, N., Köksal, A., Tekkaya, E. 2007. Modeling Flexforming (Fluid Cell Forming) Process with Finite Element Method. Key Engineering Materials Vol. 344 (2007) pp 469-476.

Hatipoğlu, H. A., Alkaş, C. O. 2016. Process modelling and die design concepts for forming aircraft sheet parts. Journal of Physics: Conference Series 734 (2016) 032088.

Hexagon Forming Technologies [Online]. Avialable: https://www.forming.com/. [2020, October 24]

Hexagon Simufact Forming [Online]. Available: https://www.simufact.com/module-sheet-metal-forming.html. [2020, October 24]

Hijazi, A., Yardi, N., Madhavan, V. 2004. Determination of forming limit curves using 3D digital image correlation and in-situ observation. Proceeds of SAMPE 2004 - Long Beach CA.

Hosseinzade, M., Mostajeran, H., Bakhshi-Jooybari, M., Gorji, A. H., Nourouzi, S., Hosseinipour, S. J. 2009. Novel combined standard hydromechanical sheet hydroforming process. Proceedings of the Institution of Mechanical Engineers, Vol. 224 Part B: Journal of Engineering Manufacture.

Hsu, C. W., Ulsoy, A. G., Demeri, M. Y. 2002. Development of process control in sheet metal forming. Journal of Material Processing Technology 127 (2002) 361 – 368.

International Organization for Standardization. ISO1101:2017. Geometrical Product Specifications (GPS) — Geometrical tolerancing - Tolerances of form, orientation, location and run-out. Switzerland: Case postale 56 • CH-1211 Geneva 20.

Kadkhodayan, M., Moayyedian. F. 2011. Analytical elastic–plastic study on flange wrinkling in deep drawing process. Scientia Iranica B, (2011) 18 (2), 250–260.

Kang, B., Son, B., Kim, J. 2004. A comparative study of stamping and hydroforming processes for an automobile fuel tank using FEM. International Journal of Machine Tools & Manufacture 44 (2004) 87–94.

Karaağaç, I. 2016. The experimental investigation of springback in V-bending using the flexforming process. Arabian Journal for Science and Engineering volume 42 (2017), 1853–1864.

Kumar, A., Kumar, S., Yadav, D. R. 2014. Review Of Rubber Based Sheet Hydro-Forming Processes. 5th International & 26th All India Manufacturing Technology, Design and Research Conference (AIMTDR 2014) December 12th–14th, 2014, IIT Guwahati, Assam, India.

Kumar, S., Amjith, T., Anjaneyulu, C. 2016. Forming Limit Diagram Generation of Aluminum Alloy AA2014 Using Nakazima Test Simulation Tool. Procedia Technology, 24 (2016) 386 – 393.

Kutz, M. 2013. Handbook of Measurement in Science and Engineering, Volume 1 - 1.3.6 B-WIM, WIM. John Wiley & Sons.

Lang, L., Danckert, J. Nielsen, K.B., Kang, D.C., Zhang, S.H. 2004. Key technologies of the simulation of the hydrodynamic deep drawing of irregular parts. Journal of Materials Processing Technology 150 (2004) 40–47.

Lang, L. Dankert, J., Nielsen, K.B. 2005. Multi-layer sheet hydroforming: Experimental and numerical investigation into the very thin layer in the middle. Journal of Materials Processing Technology 170 (2005) 524–535.

Lang, L., Gu, G., Li, T., Zhu, X. 2008. Numerical and experimental confirmation of the calibration stage's effect in multi-operation sheet hydroforming using poor-formability materials. journal of materials processing technology 2 0 1 (2 0 0 8) 97–100.

Lang, L., Wang, Y., Xie, Y., Yang, X., Xu, Y. 2012. Pre-bulging effect during sheet hydroforming process of aluminum alloy box with unequal height and flat bottom. Transactions of Nonferrous Metals. Society of China 22 (2012) s302−s308.

Leacock, A., Ling, D., Bergkvist, M. 2016. Industrial application and validation of forming simulation in the flexforming process. Journal of Physics: Conference Series 734 (2016) 032103.

Lee, J. H., Chun. B.S. 2005. Investigation on the variation of deep drawability of STS304 using FEM simulations. Journal of Materials Processing Technology 159 (2005) 389–396.

Lee, J., Park, H., Kim, S., Kwon, Y., Kim, D. 2018. Numerical investigation into plastic deformation and failure in aluminum alloy sheet rubber-diaphragm forming. International Journal of Mechanical Sciences 142–143 (2018) 112–120.

Lee, M., Korkolis, Y. P., Kim, J. H. 2015. Recent developments in hydroforming technology. Proceedings of the Institution of Mechanical Engineers, Part B: Journal of Engineering Manufacture 2015, Vol. 229(4) 572–596.

McGraw-Hill. 2003. Dictionary of Engineering. 2nd edition. Ney York, the McGraw-Hill Companies.

Metrology World [Online]. Available: https://www.3dmetrologyworld.net/. [2020, October 27]

MMPDS-13. 2018. Metallic Materials Properties Development and Standardization (MMPDS). Scientific Report. U.S. Department of Transportation, Federal Aviation Administration.

Muñoz-Rubio, A., Bienvenido-Huertas, D., Bermúdez-Rodríguez, F. J., Tornell-Barbosa, M. 2019. Design Optimization of the Aeronautical Sheet Hydroforming Process Using the Taguchi Method. Applied Sciences. 2019, 9, 1932.

Narayanasamy. R., Sathiya Narayanan. C. 2008. Forming, fracture and wrinkling limit diagram for if steel sheets of different thickness. Materials and Design 29 (2008) 1467–1475.

Niu, M. C. Y. 2011. *Airframe Stress Analysis and Sizing*. 3rd Edition. Hong Kong Conmilit Press Limited.

Paulk, M. C., Konrad, M. D., Garcia, S. M. 1995. CMM Versus SPICE Architectures. IEEE Software Process Newsletter, No. 3, Spring 1995, pp. 7-11

Păunoiu, V., Teodor, V. G., Susac, F. 2015. Researches regarding the hydroforming process of aluminum components. IOP Conf. Series: Materials Science and Engineering 95 (2015) 012016.

Păunoiu, V., Pereira, F., Teodor, V. G., Maier, C. 2019. Investigation of Hydroforming Technology for Manufacturing an Auto Complex Part. Materials Science Forum, 2019, Vol.957 (1), p.138-148.

Pearce, R., "4000 Years of Sheet Metal Forming," Formubility of Metallic Materials—2000 A.D. ASTM STP 753. J. R. Newby and B. A. Niemeier, Eds., American Society for Testing and Materials, 1982, pp. 3-18.

Samuel, M. 2004. Numerical and experimental investigations of forming limit diagrams in metal sheets. Journal of Materials Processing Technology 153–154 (2004) 424–431.

Schneider, M., Friebe, H., Galanulis, K. 2008. Validation and optimization of numerical simulations by optical measurements of tools and parts. International Deep Drawing Research Group, IDDRG 2008 International Conference.

Serfontein, J.L., Dimitrov, D., Gerber, W. 2019. Composite and metallic forming manufacturability criteria for incorporation into material selection methodology. International Conference on Competitive Manufacturing 337 – 345 (2019).

Sister, M., Slota, J. 2016. Material Model of AW 5754 H11 Al Alloy for Numerical Simulation of Deep Drawing Process. Acta Mechanica Slovaca 20 (2): 32 - 40, 2016.

Solfronk, P., Sobotka, J. 2011. Utilization of Forming Tool with Variable Blank holder Force for Drawing of Al Alloys. Physics Procedia, 22 (2011) 233 – 238.

Solfronk, P., Sobotka, J., Kolnerova, M., Zuzanek, L. 2016. Spring-back prediction for stamping from the thin stainless sheets. MM Science Journal, 1090 – 1094.

TUL. 2020. Laboratory of Mechanical Testing and Tribology [Online]. Avialble: http://www.ksp.tul.cz/laborator-mechanickych-zkousek-a-tribologie. [2020, October 2].

Thuillier, S., Manach, P.Y., Menezes, L.F. 2010. Occurence of strain path changes in a two-stage deep drawing process. Journal of Materials Processing Technology 210 (2010) 226–232.

Tolazzi, M. 2010. Hydroforming Applications in Automotive: A Review. International Journal of Material Forming (2010) Vol. 3 Suppl 1:307 – 310

Hexagon. 2020. Understanding Best Fit Alignments [Online]. Available: https://support.hexagonmi.com/s/article/Understanding-Best-Fit-Alignments-1527312042816#:~:text=A%20Best%20Fit%20alignment%20is,nominal%20location%20or%20theoretical%20counterpart. [2020, July 3].

Yershov, A., Kotov, V., Loginov, Y. 2012. Optimization of the Initial Form of a Semifinished Product in PAM-STAMP 2g. Metallurgist, Vol. 56, Nos. 3–4, 2012 231-235.

Yoshida, F., Uemori, T. 2003. A model of large-strain cyclic plasticity and its application to spring back simulation. International Journal of Mechanical Sciences 45 (2003) 1687–1702.

Yoshida, T. Isogai, E. Sato, K., Hashimoto, K. 2013. Springback Problems in Forming of High-Strength Steel Sheets and Countermeasures. Nippon Steel Technical Report No. 103 May 2013.

Zhang, L., Zhou, L., Wang, Z. Xu, Y. 2003. Technology of sheet hydroforming with a movable female die. International Journal of Machine Tools & Manufacture 43 (2003) 781–785.

Zhang, L., Zhou, S., Zhao, T., Zeng, Y. 2019. An Intelligent Method to Design Die Profile for Rubber Forming of Complex Curved Flange Part. International Journal of Precision Engineering and Manufacturing (2019) 20:111–119.

Ziaeipoor, H. Z., Moosavi, H., Menghari, H. G. Alves de Sousa, R. J. 2014. Investigation of Punch Nose Radius and Punch-Die Clearance on Thinning and Puckering in Hydro-Mechanical Deep Drawing Process. International Journal of Mechanic Systems Engineering. May 2014 Vol. 4, Iss. 2 PP. 16-21.

Appendix A: Metallic Sheet Case Study – Concept-1 to 8

Appendix A.1 Concept-1

The first blank and tool geometry developed as Concept-1 is depicted in Figure A.1. The purpose of this concept was to keep the tool and blank as simple as possible. To manufacture the tool and blank was not complex, and was done at a low cost. The component surface, as prepared as described in Section 3.4.1, was offset from the press bed. The tool side faces had a draft angle of 15°, a design feature to safeguard against rupture of the rubber bladder of the fluid cell press. The edge radius of the tool was 10 mm.

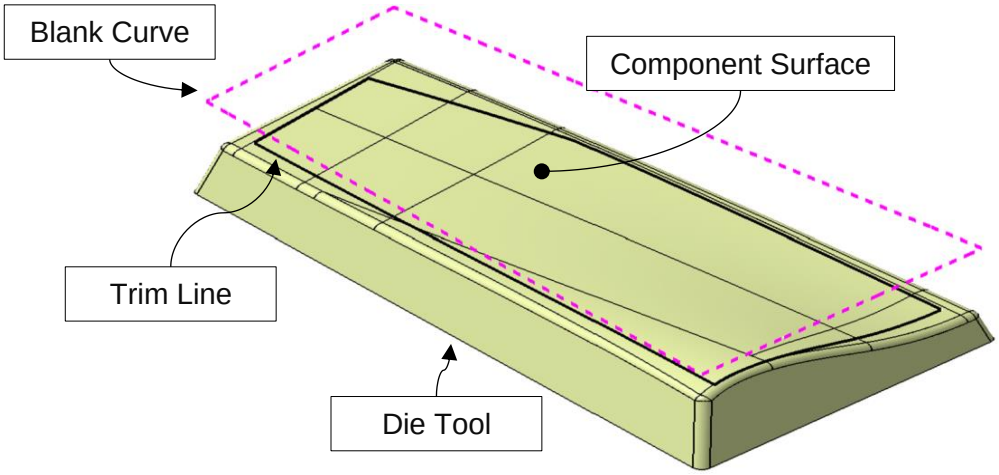

Figure A.1: Concept-1 Tool and Blank

The sheet metal blank was conceptualised by creating a sketch on the offset plane. The blank curve was created parallel to the outer edges of the part (solid black trim line) 25 mm away, see Figure A.2. The larger blank allowed for enough of the part to be trimmed from the form.

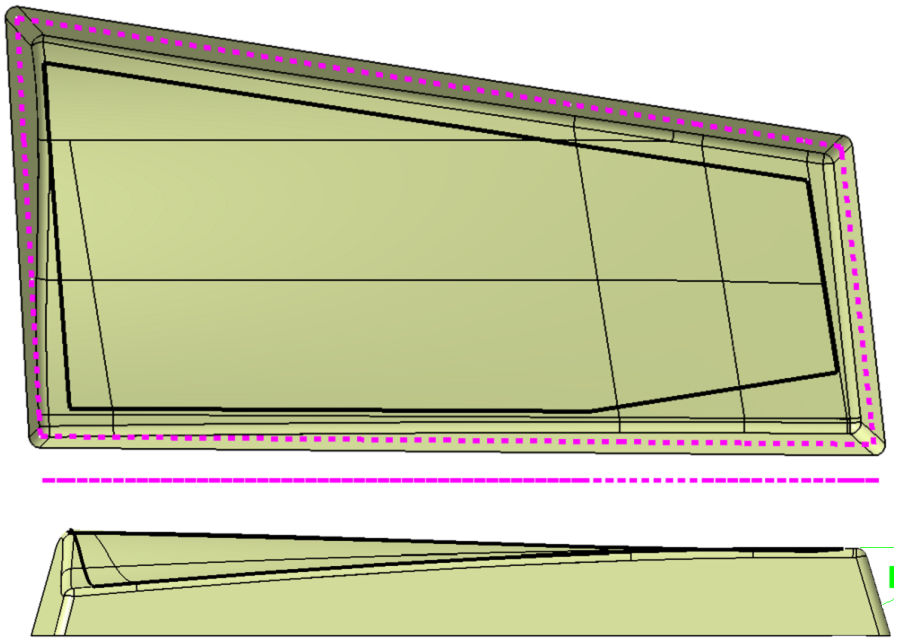

Figure A.2: Concept-1 Tool and Blank – Top and Side Views

Figure A.3 depicts Concept-1's tool, blank, trim curve and assembly FEM in PAM-STAMP 2G. The blank mesh had an element size of 8 mm. The sheet metal rolling direction was in the y-axis. As the minimum edge radius for Concept-1 was 10 mm, the edge radius to element size was 1.25:1. A blank mesh refinement level of 3 was used, providing an element size of 2 mm, where required. Hence, the edge radius to element size was 5:1.

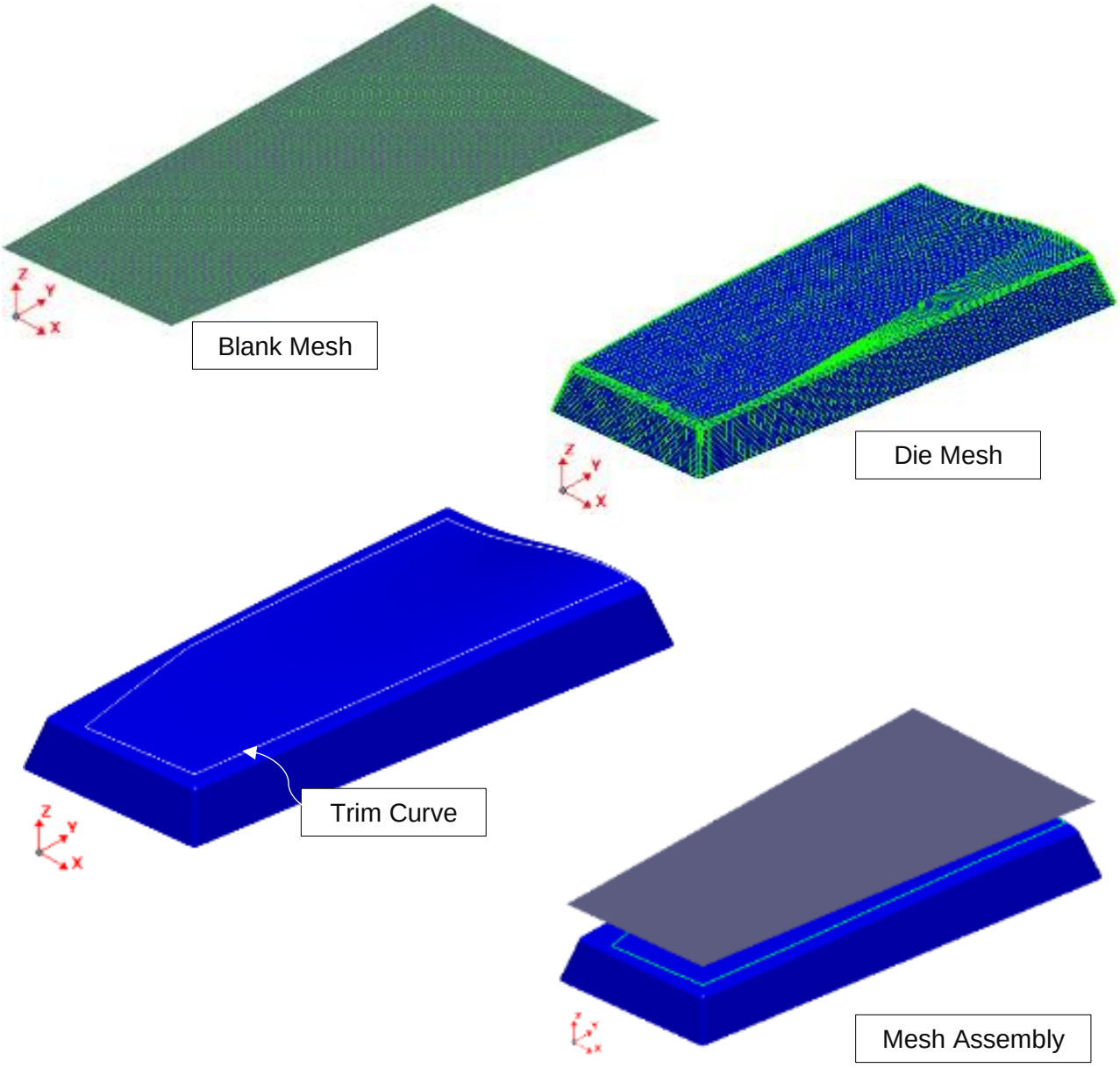

Figure A.3: Concept-1 tool, blank, trim curve and assembly FEM

The simulation set-up was a fluid cell forming stage, followed by a trimming and springback stage. Refer to Section 3.4.3 for a detailed breakdown of the simulation set-up. The total progression time was 30 seconds, with a maximum pressure of 80 MPa. The stopping criteria for the stage were the contact area. A state result was provided every 2.5 seconds. The material card used for this simulation was the Vegter yield locus lite plasticity law and the Yoshida-Uemori kinematic hardening law. The forming stage completed in 15.962 seconds. Figure A.4 depicts the FLD, a zone quality overlay on the blank in final form, the trimmed form at the trim stage and the final form at the springback stage. The degree of in-plane stretching was insufficient, resulting in the panel springing back to a near- flat state.

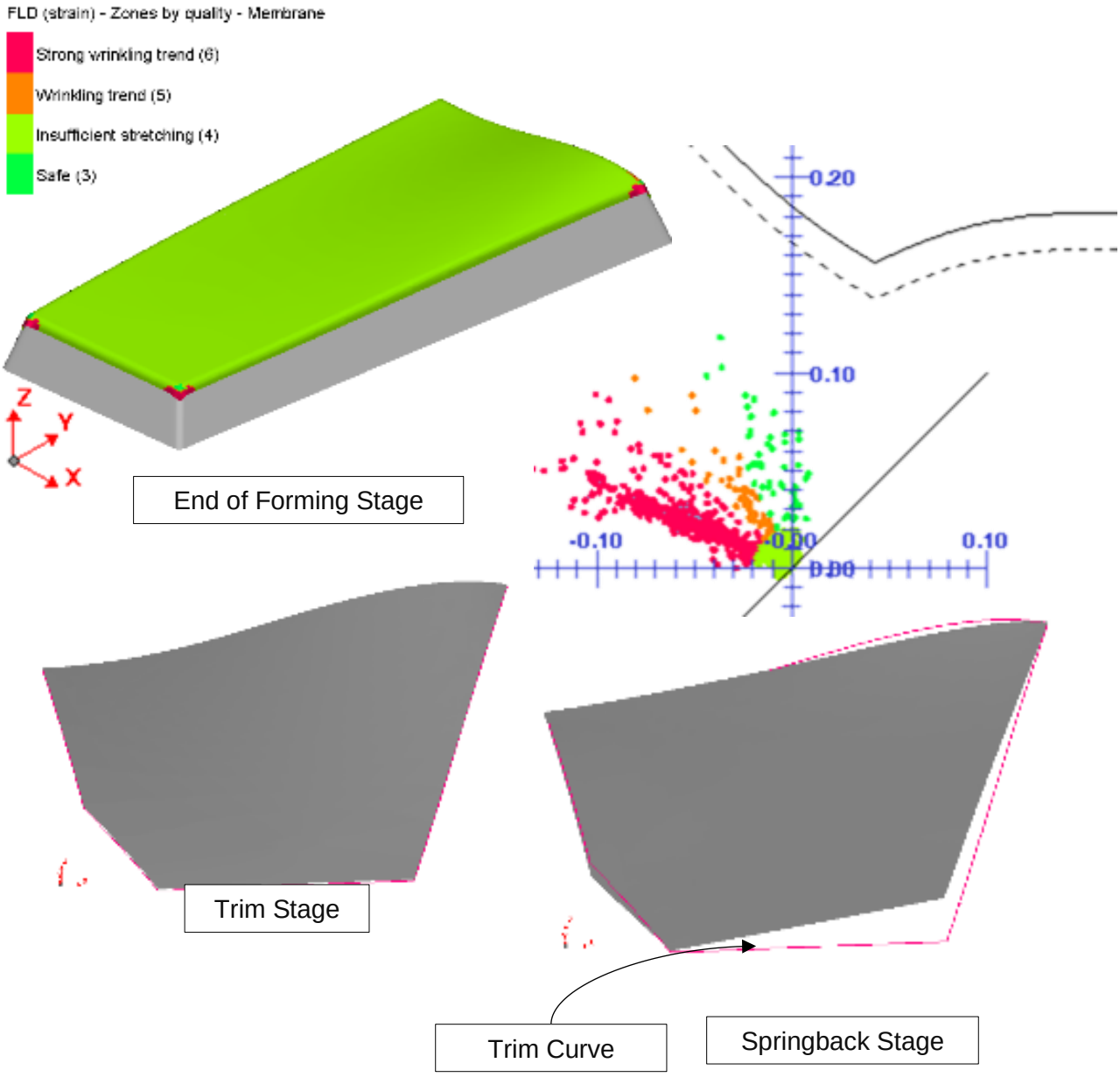

Figure A.4: Concept-1 FLD, zone quality overlay, and springback of the final form

Figure A.5 depicts the final form from the simulation versus the desired form of the component. The simulation showed that the final component might have a predicted distortion of 26.757 mm. Due to excessive distortion from the desired form, Concept-1 was rejected. To improve the in-plane stretching condition, the blank had to be constrained at the edges of the component. Concept-2 was designed with this perspective.

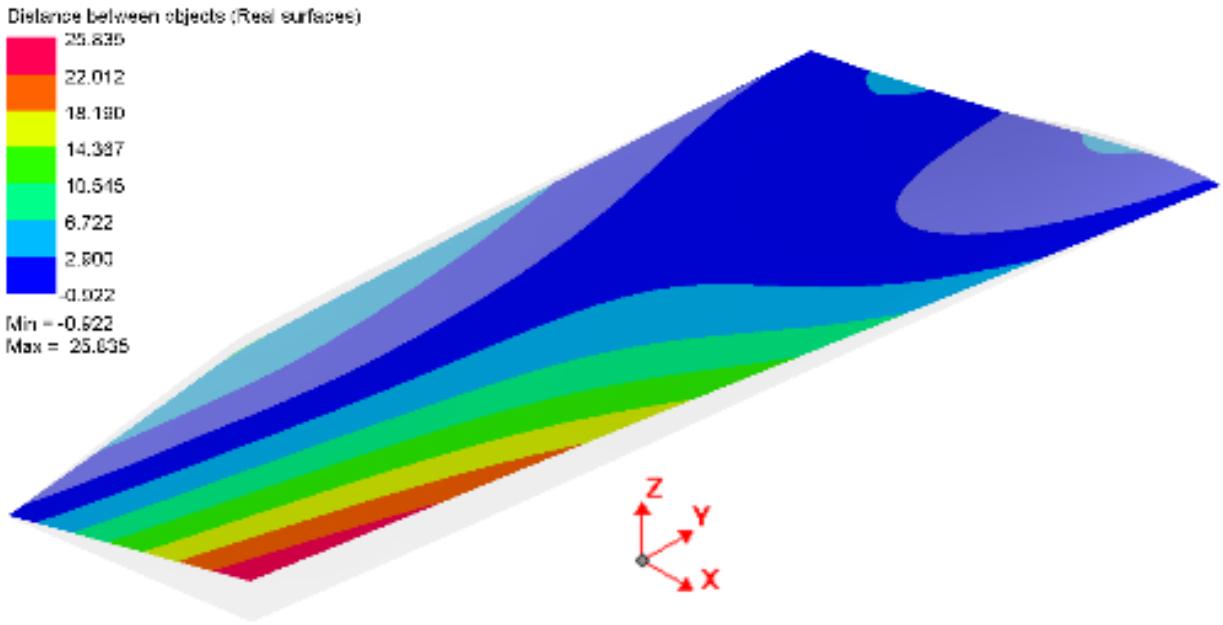

Figure A.5: Concept-1 final simulation form vs component

Appendix A.2 Concept-2

The blank and tool geometry developed for Concept-2 is depicted in Figure A.6. Based on the results from Concept-1's forming simulation, Concept-2 was created with the intent to increase the in-plane stretching by constraining the blank edges and deep drawing into the inner portion of the tool.

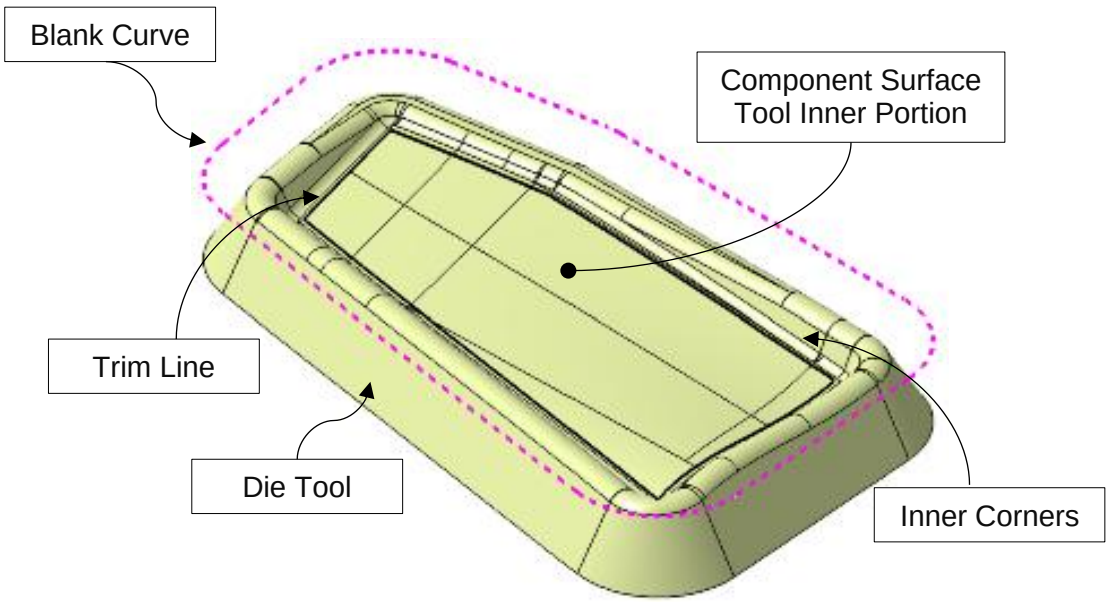

Figure A.6: Concept-2 Tool and Blank

The blank was assumed to wrap over the edge of sides of the tool. As the forming process continued, the frictional forces between the wrapped blank edges and the tool increased. The blank interfaced the surface with the assumption that in-plane stretching would be achieved as the blank was drawn deeper into the tool.

As the final stage of forming was reached, the blank pressed into the corners of the inner portion of the tool and the blank contouring the part definition. The minimum inner edge radius of the tool was 15 mm, and the outer top edge had a radius of 20 mm. The tool side face draft angle was increased to 30°, as depicted in Figure A.7.

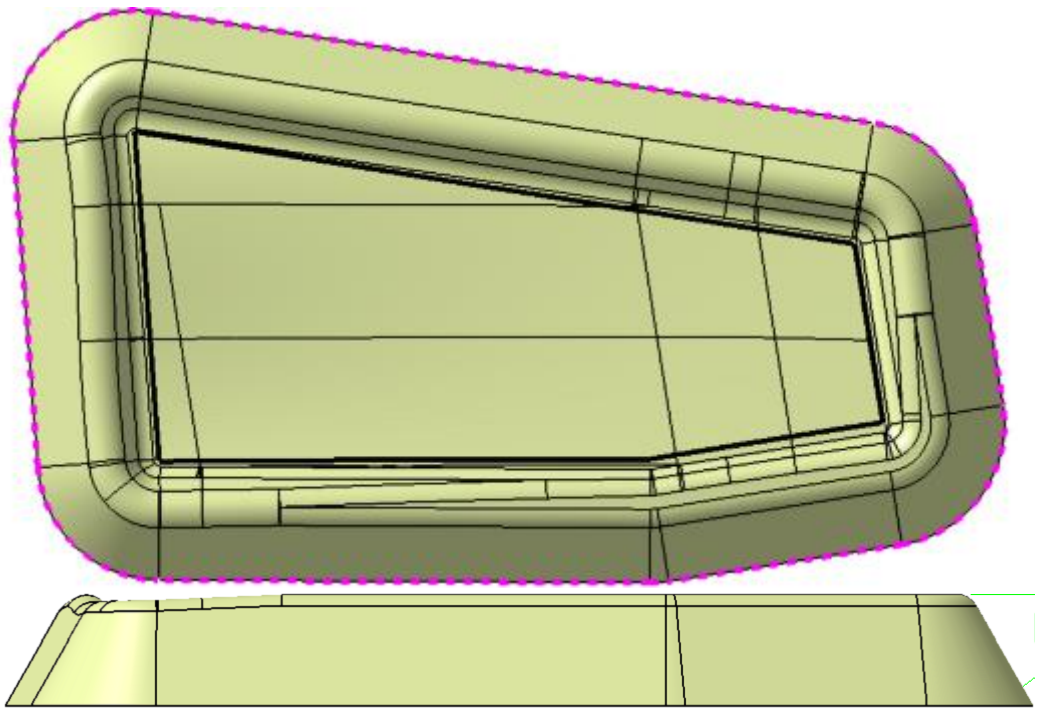

Figure A.7: Concept-2 Tool and Blank – Top and Side Views

Figure A.4 depicts Concept-2's tool, blank, trim curve and assembly FEM in PAM-STAMP 2G. The blank mesh had an element size of 16 mm. The sheet metal rolling direction was in the y-axis. As the minimum edge radius for Concept-2 was 15 mm, the edge radius to element size was 0.9375:1. A blank mesh refinement level of 3 was used, providing an element size of 4 mm. Hence, the edge radius to element size was 3.75:1, acceptable for a feasibility analysis.

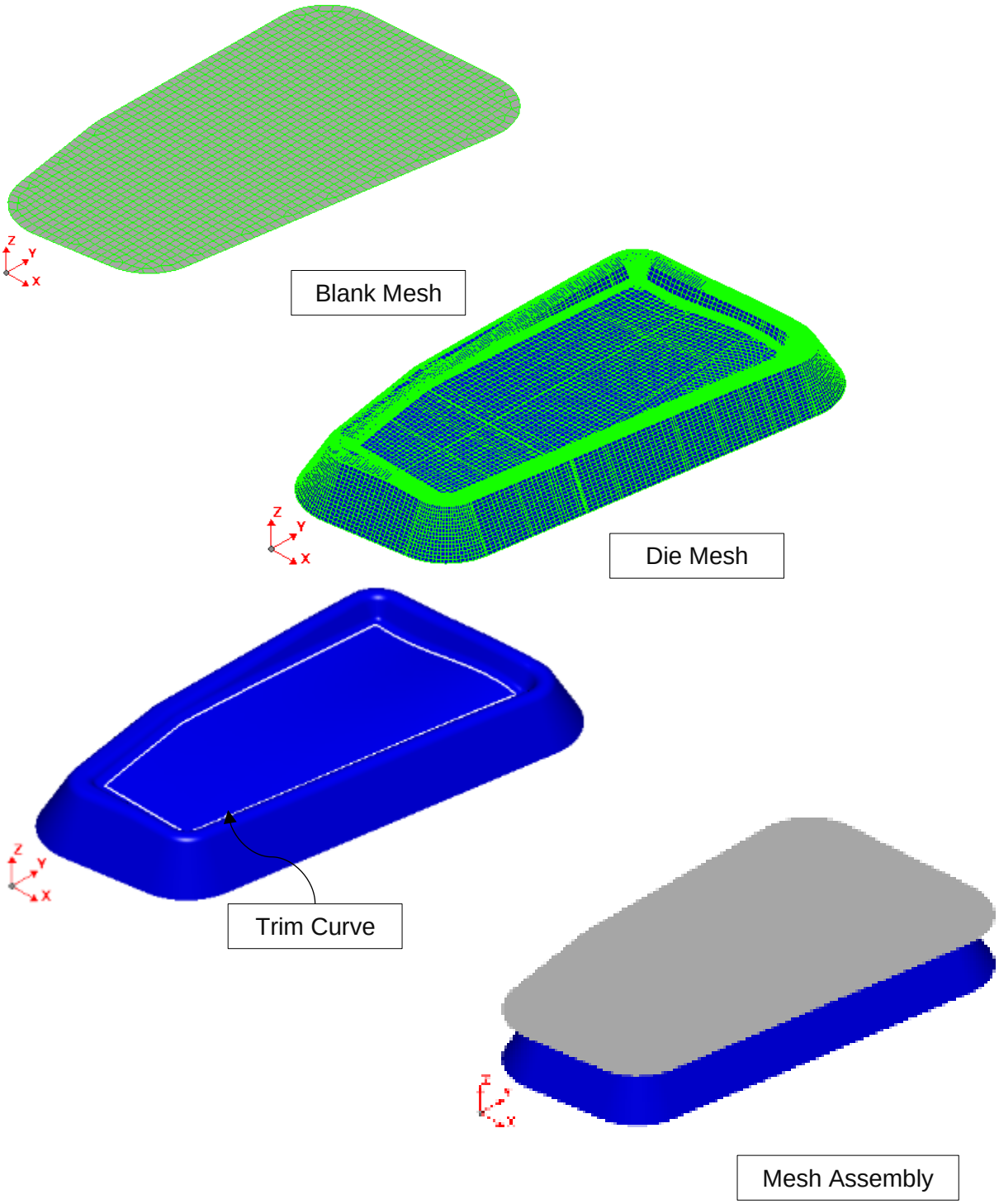

Figure A.8: Concept-2 tool, blank, trim curve and assembly FEM

The simulation set-up was a fluid cell forming stage, followed by a trimming and springback stage. Refer to Section 3.4.3 for a detailed breakdown of the simulation set-up. The total progression time was 30 seconds, with a maximum pressure of 80 MPa. The stopping criteria for the stage were contact area. A state result was provided every 2.5 seconds. The material card used for this simulation was the Vegter yield locus lite plasticity law and the Yoshida-Uemori kinematic hardening law. The forming stage completed in 23.2 seconds.

Figure A.9 depicts the FLD, a zone quality overlay on the blank in final form, the trimmed form at the trim stage, and the final form at the springback stage. Insufficient in-plane stretching was not achieved, resulting in the panel springing back to a near-flat state.

In comparison to Concept-1, more in-plane stretching was achieved in the corners of the tool. The improvement of the springback stage simulation form was seen by how close the edges of the simulation form contoured the trim line of the desired component, as shown in Figure A.9.

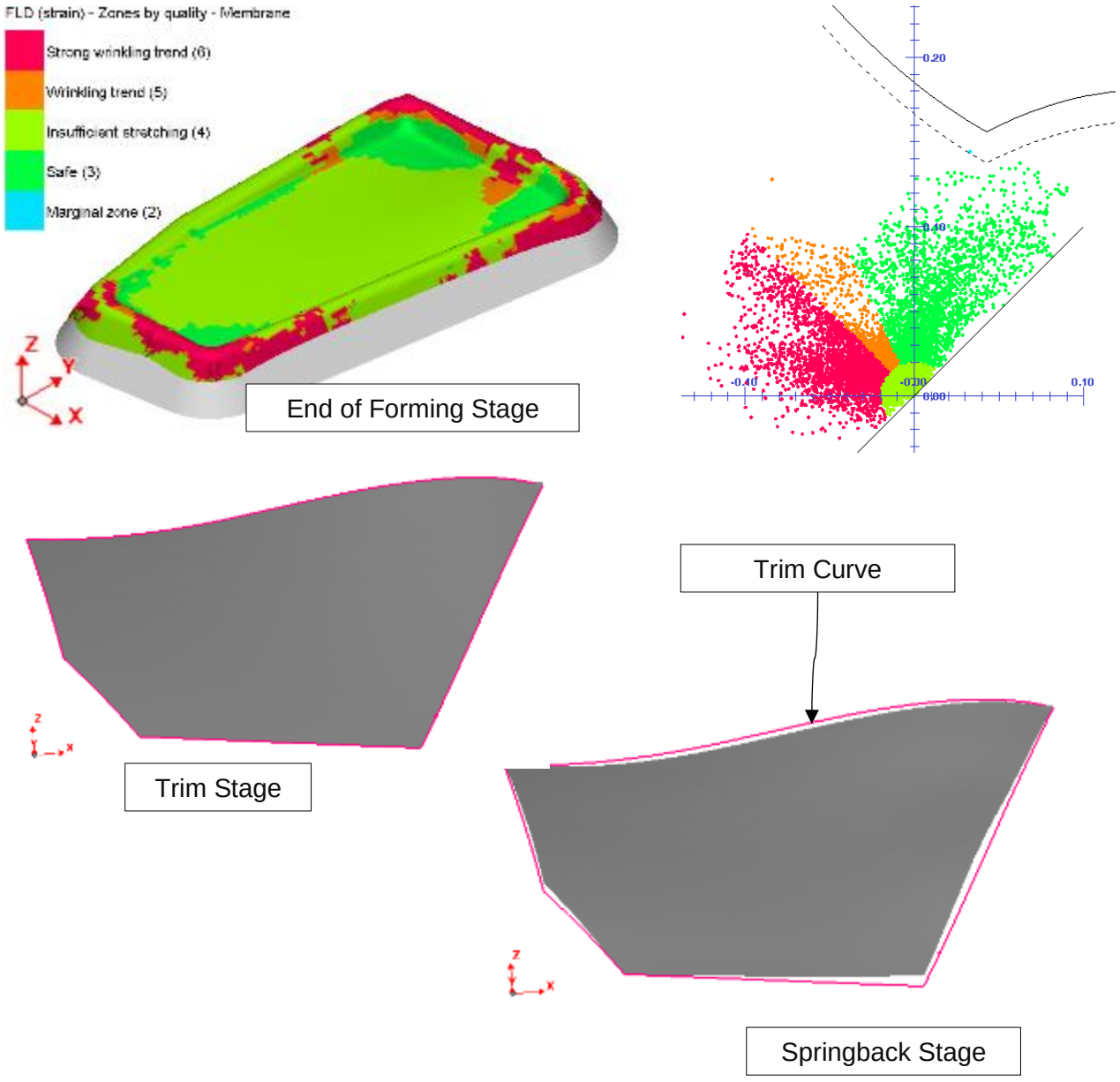

Figure A.9: Concept-2 FLD, zone quality overlay, and springback of the final form

Figure A.10 depicts the final form from the simulation versus the desired form of the component. The simulation showed the final component might have a predicted distortion of 11.964 mm, and an improvement of 55.4 %, compared to Concept-1. Comparing the distance contour lines of Figure A.5 with Figure A.10 shows Concept-2 did not springback as much as Concept-1, due to the increased in-plane stretching achieved.

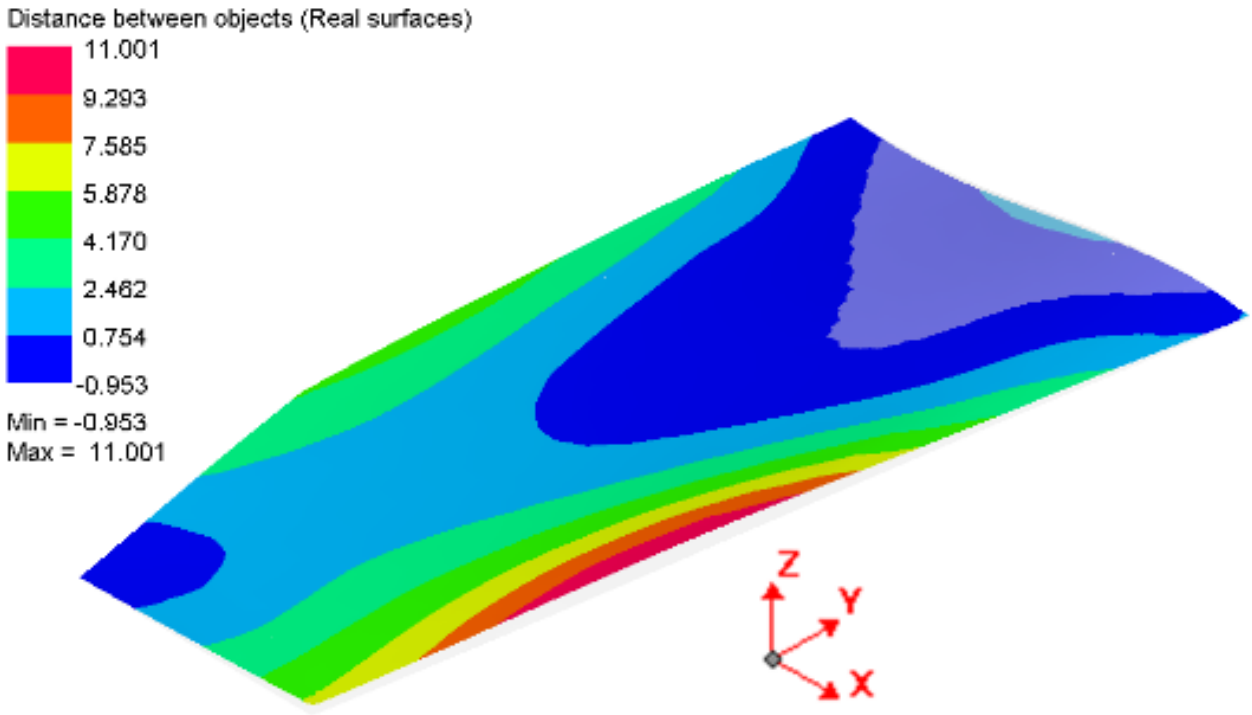

Figure A.10: Concept-2 final simulation form vs component

Due to excessive distortion from the desired form, Concept-2 was also rejected. To improve the in-plane stretching condition, the blank had to be constrained at the edges of the component. Concept-3 was designed with this perspective.

Appendix A.3 Concept-3

The blank and tool geometry developed for Concept-3 is depicted in Figure A.11. Based on the results from Concept-2's forming simulation, the strategy for Concept-3 was to further increase the draw depth to increase the in-plane stretching seen in Concept-2.

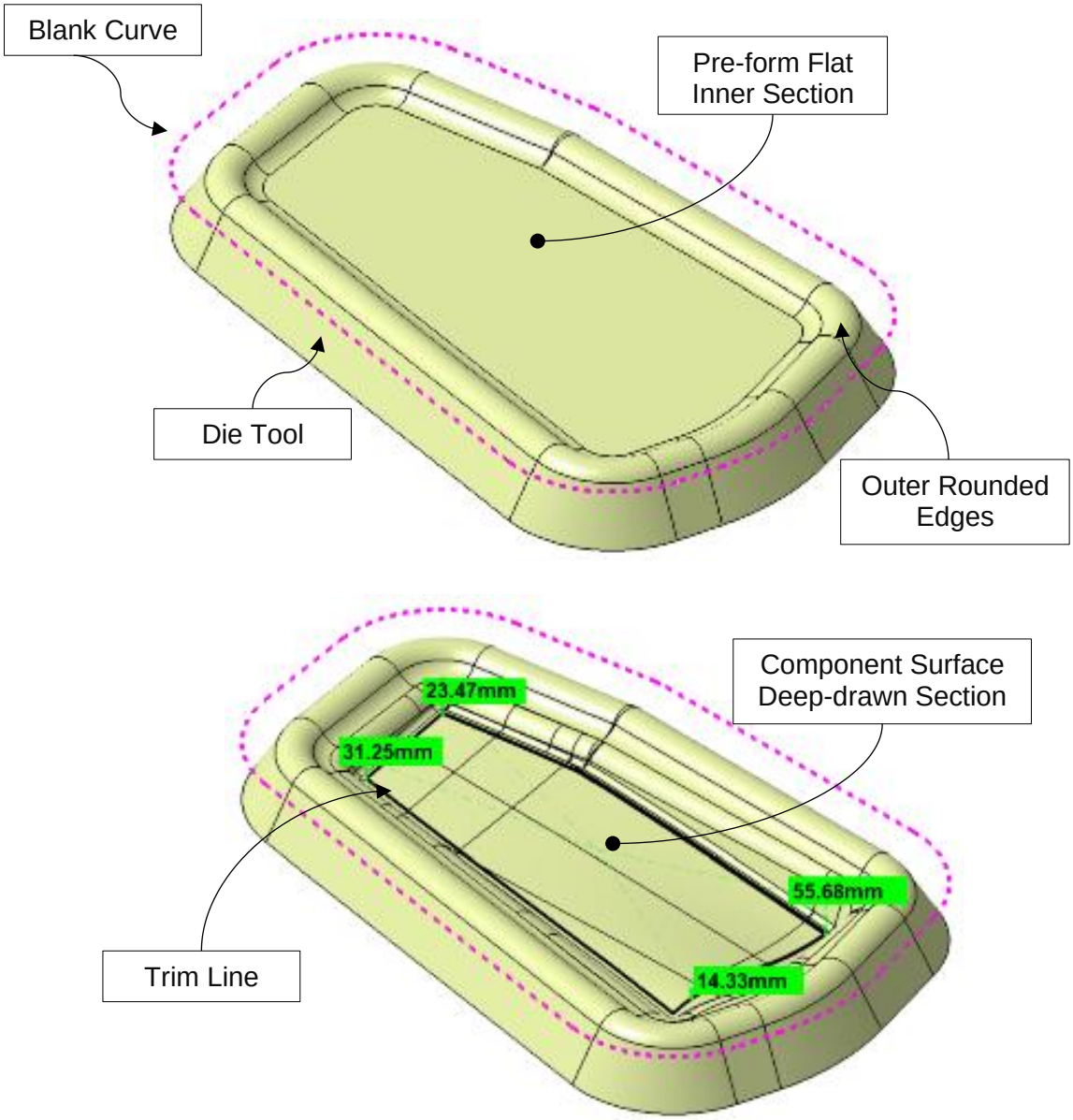

Figure A.11: Concept-3 Tool and Blank

Stage one of Concept-3 created a pre-form that contoured the outer rounded edges and a flat inner section. Stage two drew the blank deeper into the tool with the highest point 14.33 mm, and the lowest point 55.67 mm from the inner flat section of stage 1.

As the forming process continued during stage two, the frictional forces between the wrapped blank edges and the tool increased. The blank interfaced the surface with the assumption that in-plane stretching would be achieved as the blank was drawn even deeper into the tool compared to Concept-2.

As the final stage of forming was reached, the blank was pressed into the corners of the inner portion of the tool, and the blank contoured the part definition. The minimum inner edge radius of the tool was 10 mm and the outer top edge had a radius of 30 mm. The tool side face draft angle was 30°. Concept-3 had a new edge definition, as depicted in Figure A.12, which was assumed to improve the in-plane stretching along this edge, compared to Concept-2. This change affected the blank design which was also different compared to Concept-2.

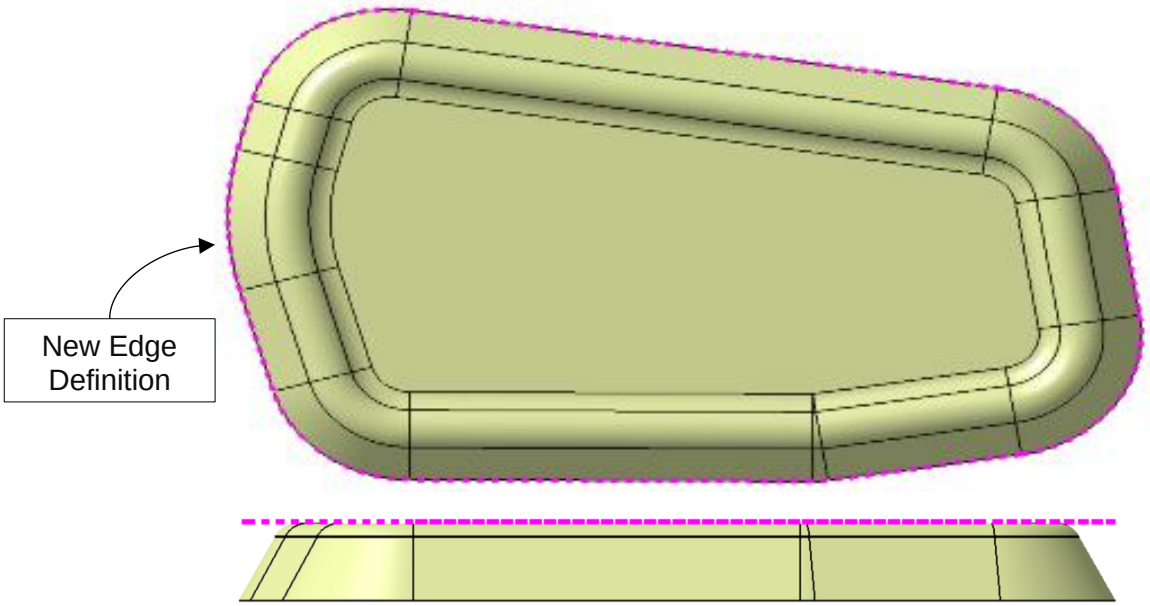

Figure A.12: Concept-3 Tool and Blank – Top and Side Views Stage One

Figure A.13 depicts the top and side view of Concept-3's second stage tool. The distance from the component trim edge to the inner corners was closer than Concept-2. This posed a risk to the curvature of the component edges. In addition, the depth of the draw might have resulted in cracks.

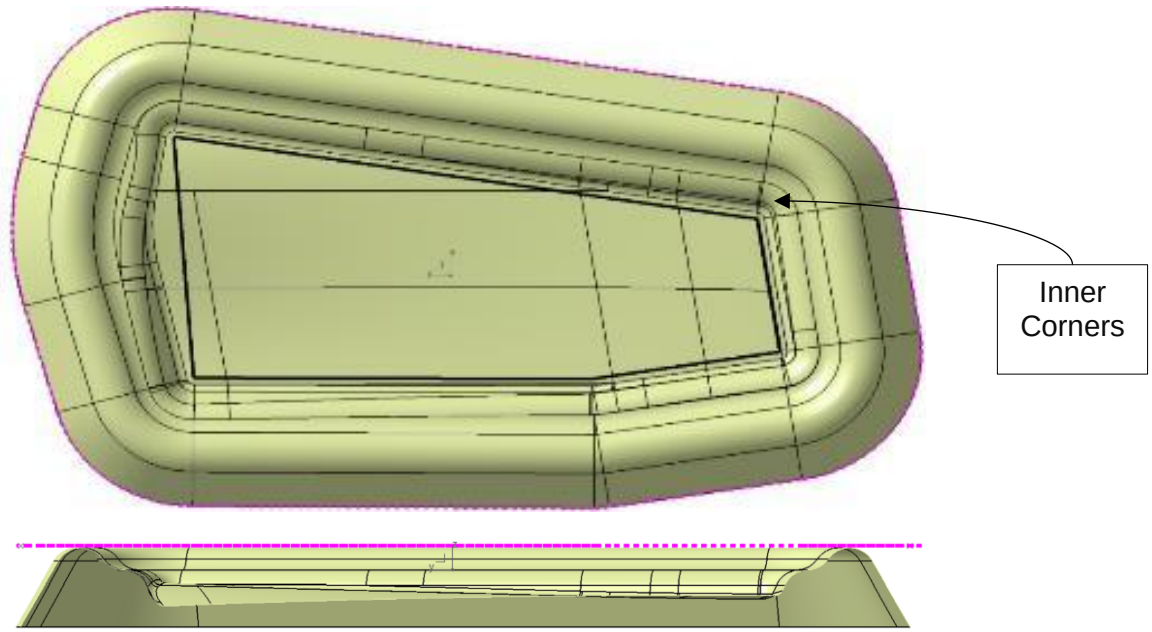

Figure A.13: Concept-3 Tool and Blank – Top and Side Views Stage Two

Figure A.14 depicts Concept-3's stage one tool, blank, trim curve and assembly FEM in PAM-STAMP 2G. The blank mesh had an element size of 22 mm. The sheet metal rolling direction was in the y-axis. As the minimum edge radius for Concept-3 stage one was 30 mm, the edge radius to element size was 1.363:1. A blank mesh refinement level of 3 was used which provided an element size of 5.5 mm. Hence, the edge radius to element size was 5.45:1, acceptable for a feasibility analysis.

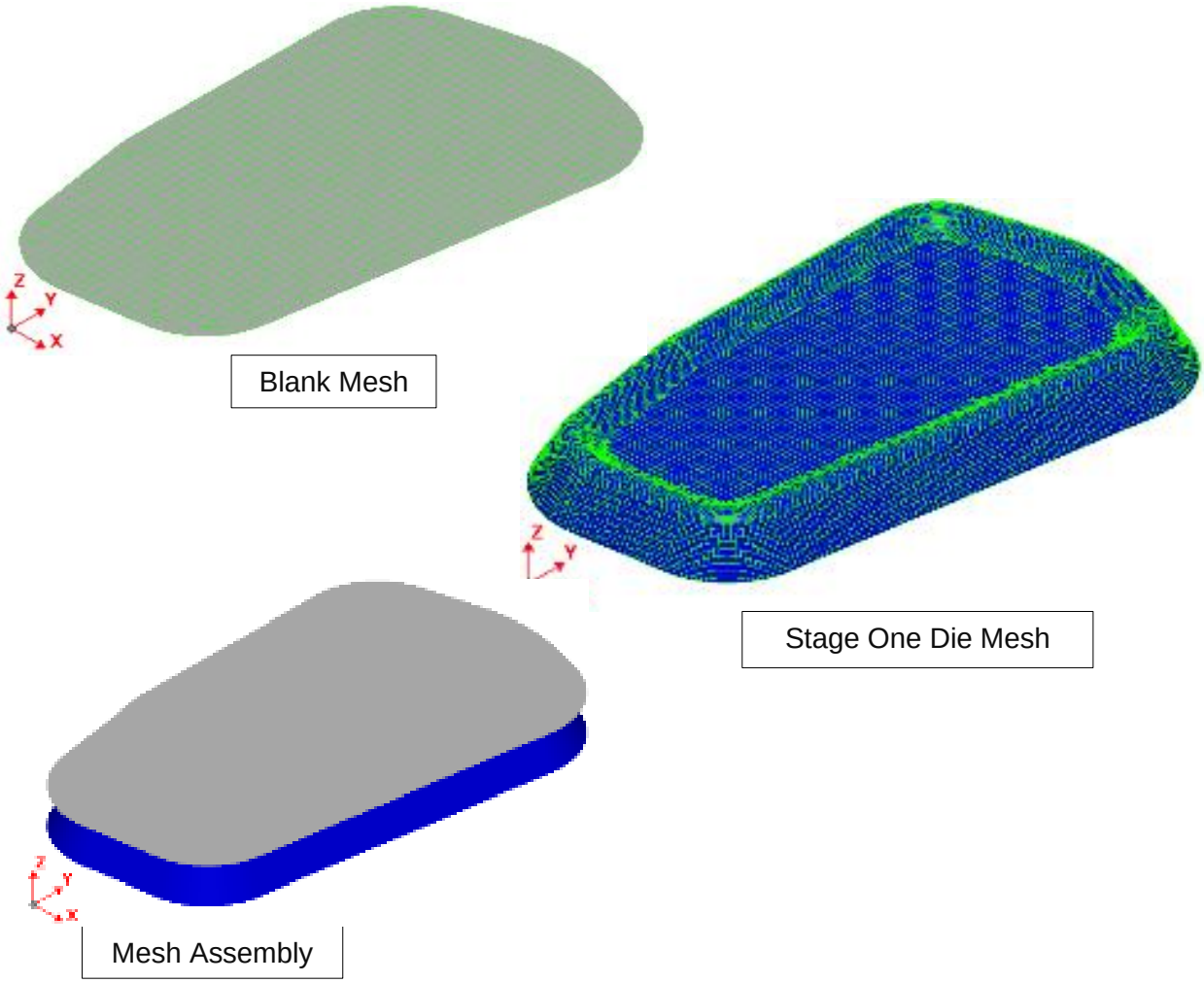

Figure A.14: Concept-3 stage one tool, blank, trim curve and assembly FEM

The complete simulation conducted the pressing of the first and second stages. The simulation process was a fluid cell forming stage, a springback stage of the pre-form, a second fluid cell forming stage, and, finally, a trim and springback stage. Refer to Section 3.4.3 for a detailed breakdown of the simulation set-up. The total progression time was 30 seconds with a maximum pressure of 80 MPa. The stopping criteria for the stage was contact area. A state was result provided every 2.5 seconds. The material card used for this simulation was the Vegter yield locus lite plasticity law and the Yoshida-Uemori kinematic hardening law.

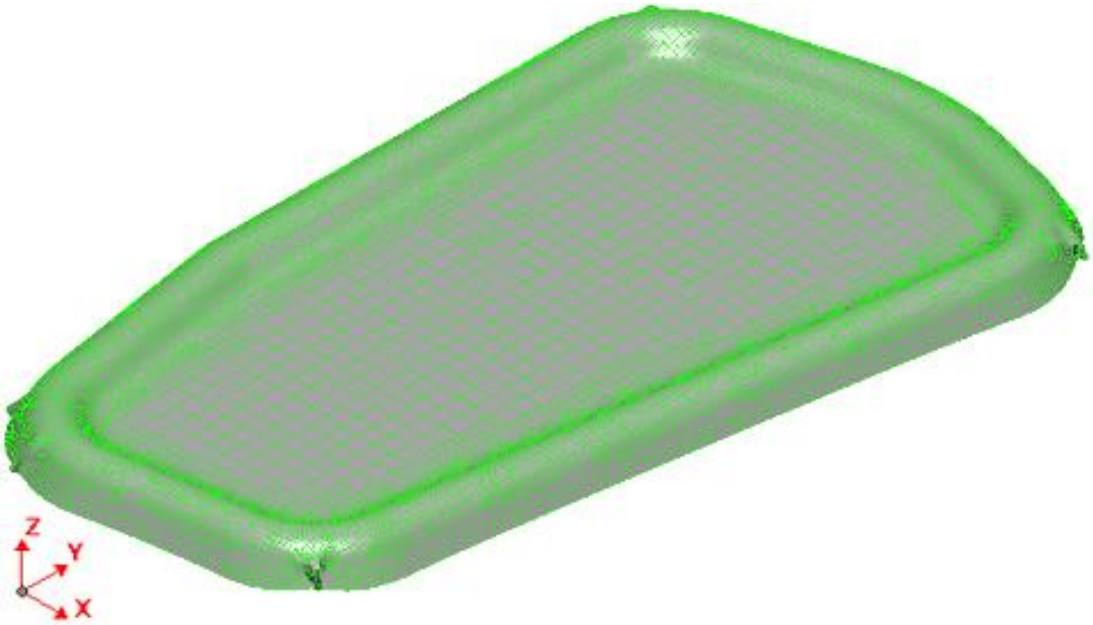

Figure A.15: Concept-3 stage one pre-form after springback

Figure A.15 depicts the pre-form blank after springback. The simulation then proceeded to the second phase of the simulation. Figure A.16 depicts the second stage die mesh and the trim curve. The stage two tool was loaded, and the pre-formed blank was formed into the final form. The form was then trimmed and, finally, a springback stage conducted to yield the final component.

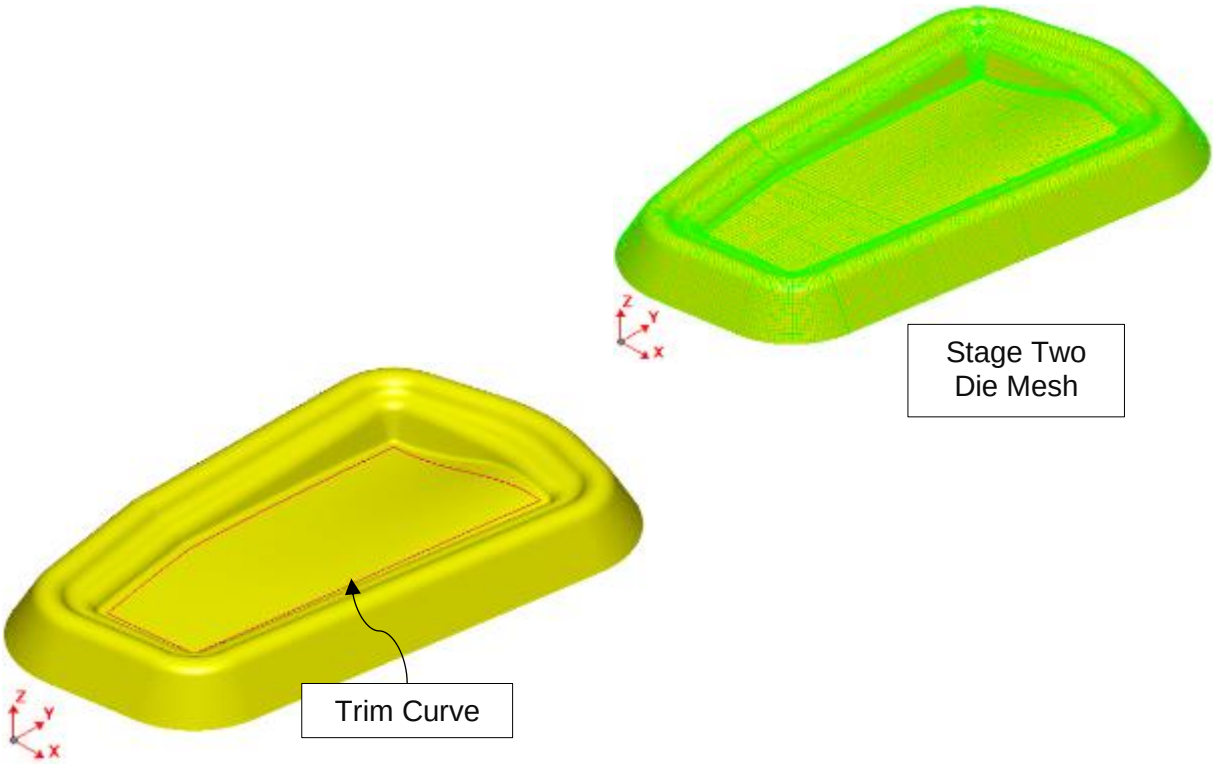

Figure A.16: Concept-3 stage two tool and trim curve FEM

Figure A.17 depicts the FLD, a zone quality overlay on the blank in final form, the trimmed form at the trim stage and, the final form at the springback stage.

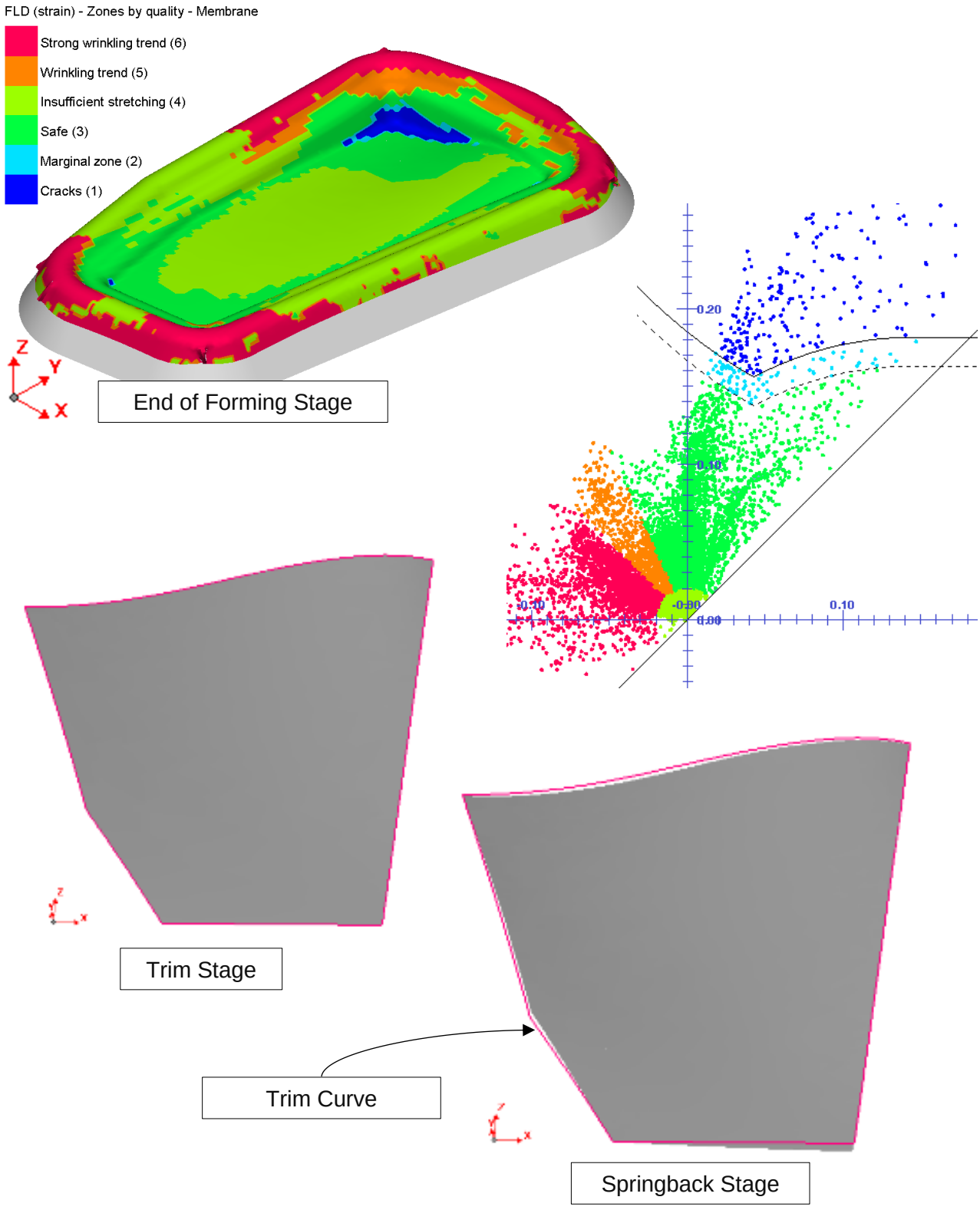

Figure A.17: Concept-3 FLD, zone quality overlay, and springback of the final form

Figure A.18 depicts the final form from the second stage simulation versus the desired form of the component. In comparison to Concept-2, further in-plane stretching was achieved. However, the concept showed cracking would occur in the deepest corner. The improvement of the springback stage simulation form was seen by how close the edges of the simulation form contoured the trim line of the desired component in Figure A.17.

The simulation showed the final component might have had a predicted distortion of 5.132 mm, and an improvement of 57.1 %, compared to Concept-2, and 80.8 %, compared to Concept-1.

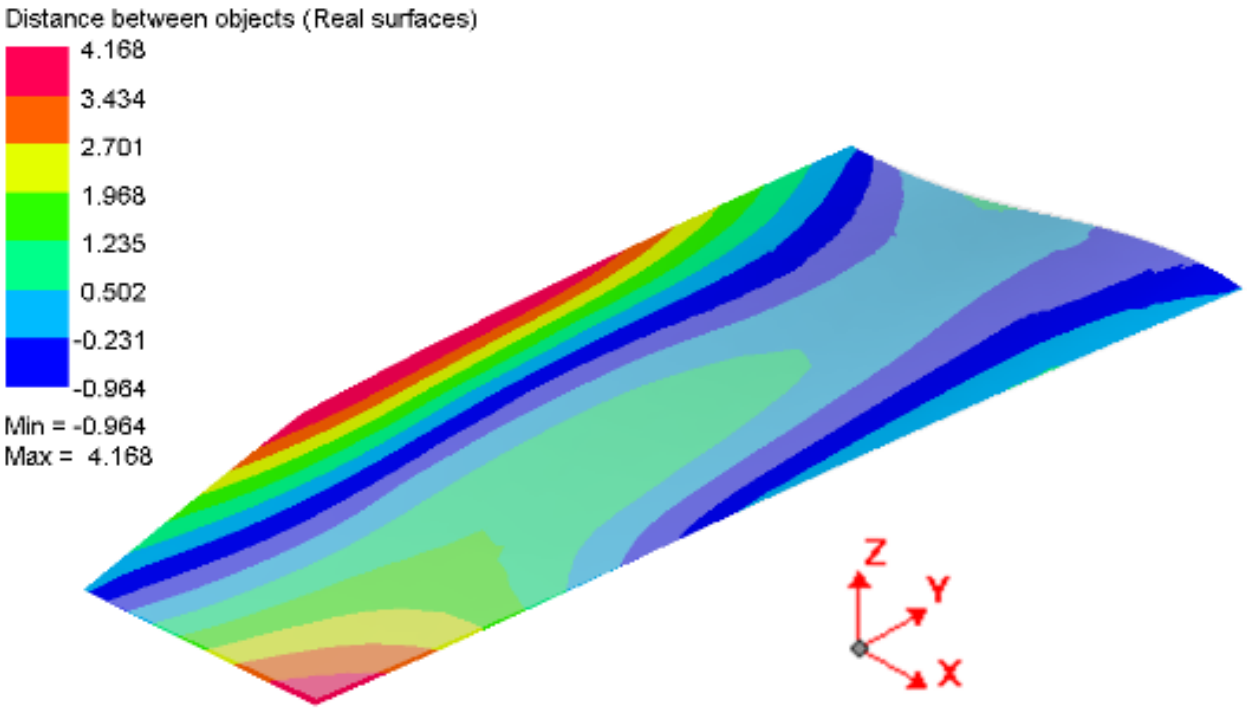

Figure A.18: Concept-3 final simulation form vs component

Even though the final predicted distortion of the blank from the final form was marginal, due to the blank cracking, Concept-3 was also rejected, even though the simulation showed the final distortion of the component was relatively small.

Appendix A.4 Concept-4

The blank and tool geometry developed for Concept-4 is depicted in Figure A.19. The strategy for Concept-4 was to reduce the draw depth design and make use of a larger overhanging blank to ensure the edge of the blank was constrained to ensure sufficient in-plane stretching would occur. An additional feature in this concept was a draw valley to draw the sheet further once it had contoured the component profile.

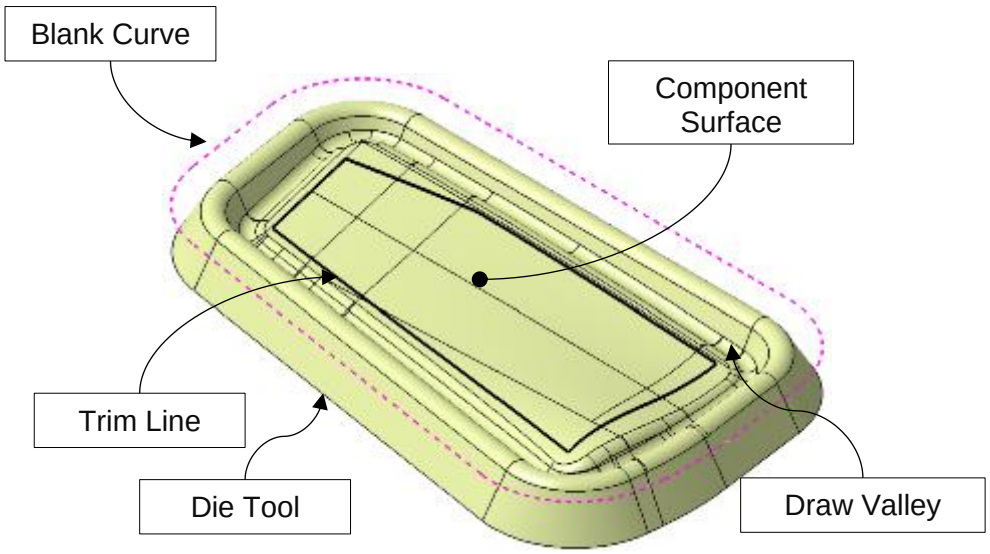

Figure A.19: Concept-4 Tool and Blank

The minimum edge radius of the tool was 20 mm. The tool side face draft angle was 30°. The draw valley had a radius of 15 mm. Concept-4 had a new edge definition, as depicted in Figure A.20.

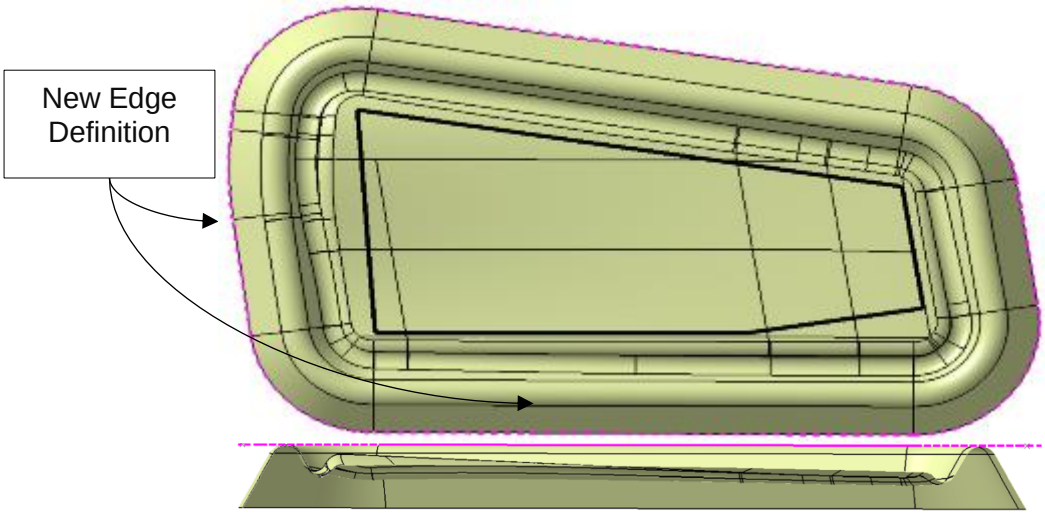

Figure A.20: Concept-4 Tool and Blank – Top and Side Views

Figure A.21 depicts Concept-4's tool, blank, trim curve and assembly FEM in PAM-STAMP 2G. The blank mesh had an element size of 24 mm. The sheet metal rolling direction was in the y-axis. As the minimum edge radius for Concept-4 was 20 mm, the edge radius to element size was 0.833:1. A blank mesh refinement level of 3 was used, providing an element size of 6 mm. Hence, the edge radius to element size was 3:1, acceptable for a feasibility analysis.

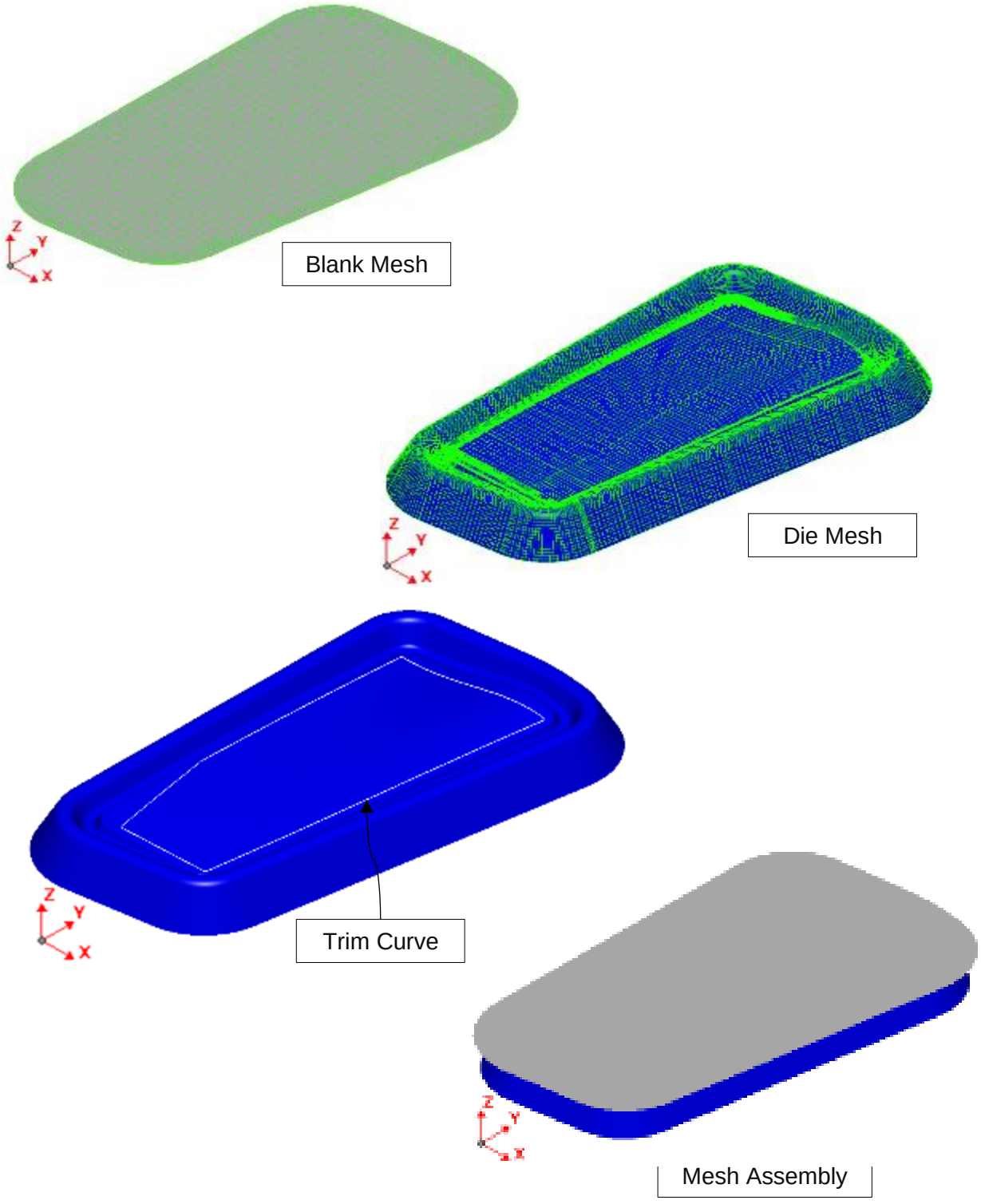

Figure A.21: Concept-4 tool, blank, trim curve and assembly FEM

The simulation set-up was a fluid cell forming stage, followed by a trimming and springback stage. Refer to Section 3.4.3 for a detailed breakdown of the simulation set-up. The total progression time was 30 seconds with a maximum pressure of 80 MPa. The stopping criteria for the stage was contact area. A state result was provided every 2.5 seconds. The material card used for this simulation was the Vegter yield locus lite plasticity law and the Yoshida-Uemori kinematic hardening law.

Figure A.22 depicts the FLD, a zone quality overlay on the blank in final form, the trimmed form at the trim stage and, the final form at the springback stage. The simulation showed the draw valley did not improve the in-plane stretching state of the sheet and resulted in the sheet cracking.

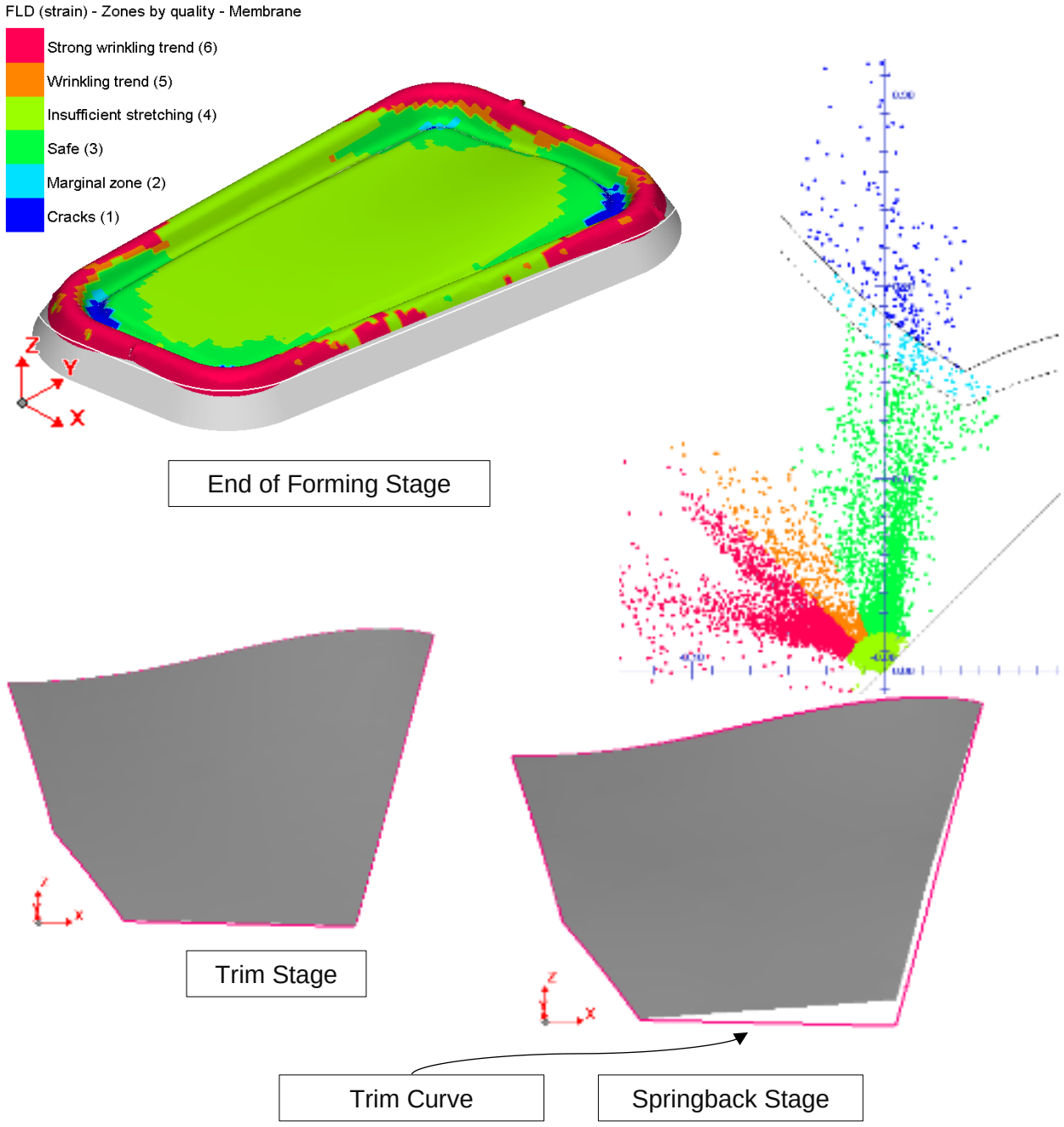

Figure A.22: Concept-4 FLD, zone quality overlay, and springback of the final form

Figure A.23 depicts the final form from the simulation versus the desired form of the component. The simulation showed the final component might have had a predicted distortion of 18.604 mm, which was worse than Concept-3. The distance contour lines showed Concept-4 would springback to a nearly flat shape one side, whilst maintaining the s-shaped curve on the opposite side.

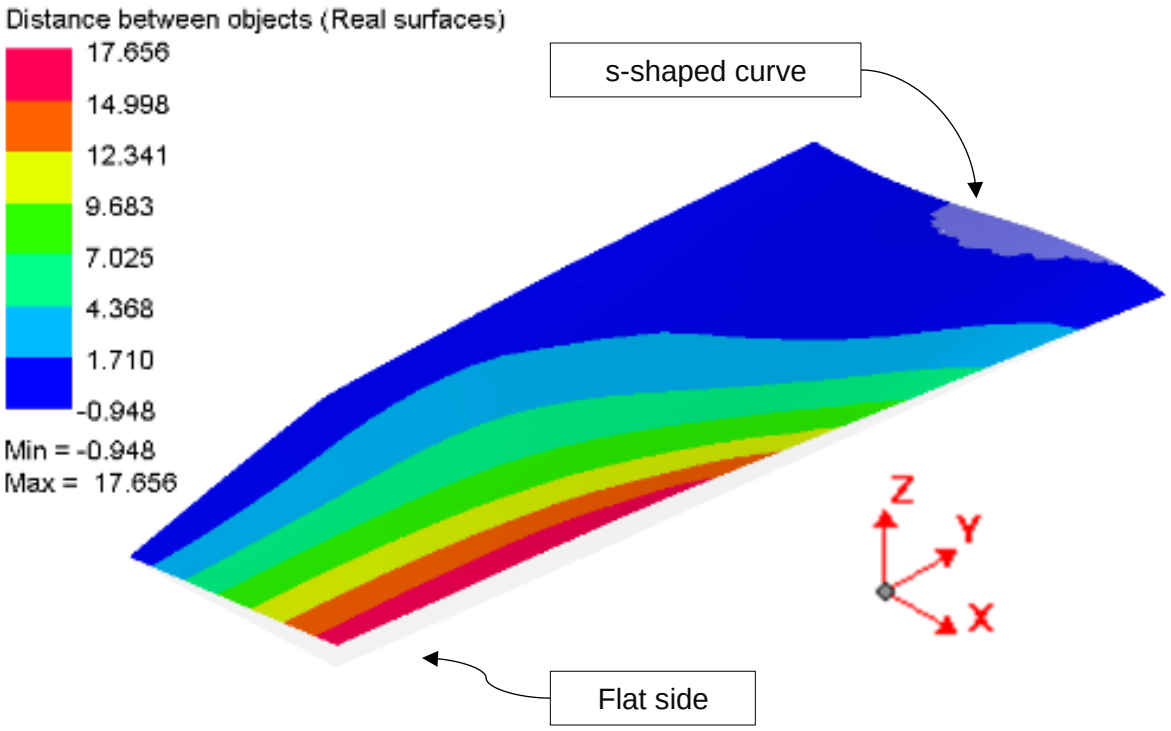

Figure A.23: Concept-4 final simulation form vs component

Based on the simulation results, Concept-4 was also rejected. The draw-valley strategy resulted in cracking, and did not improve the blank's state of in-plane stress.

Appendix A.5 Concept-5 – Tool A

Concept-3 was the best performing concept of the four proposed, thus far. The four maintained a similar outline shape with the internal section altered. Concept-5 was not a single blank and tool design investigation. Three tools and four blanks were conceptualised to investigate alternative shapes to those used previously.

Tool concepts 2 and 4 had shallow draw depths, whilst Concept-3 had deep draw depth. Concept-5 – tool A was designed with a much deeper draw depth than any of the previous concepts. Figure A.24 shows the deeper draw depth in Concept-5 tool A, compared to Concept-2 and 3. Concept-2 and 3 had draw depths of 15.116 mm and 24.103 mm, respectively. Concept-5 tool A had a draw depth of 37.161 mm. This was an effective draw depth increase of 59.3% and 35.1 %, compared to Concept-2 and 3, respectively.

The outer tool radii of Concept-5 tool A were smaller than the previous concepts. The smaller radius might have affected the way the blank was constrained and was investigated in this concept.

Concept-5's blank A and B for tool A differed from the blank concepts designed, thus far. The previous blanks were designed with large overhangs and no corners. Blank concepts 2, 3 and 4 could not be aligned on the tool accurately. Concept-5's blank A and B were designed with the intent of ensuring some form or alignment, if the concept was accepted as a solution. Figure A.24 depicts the design change implemented in blank A and B.

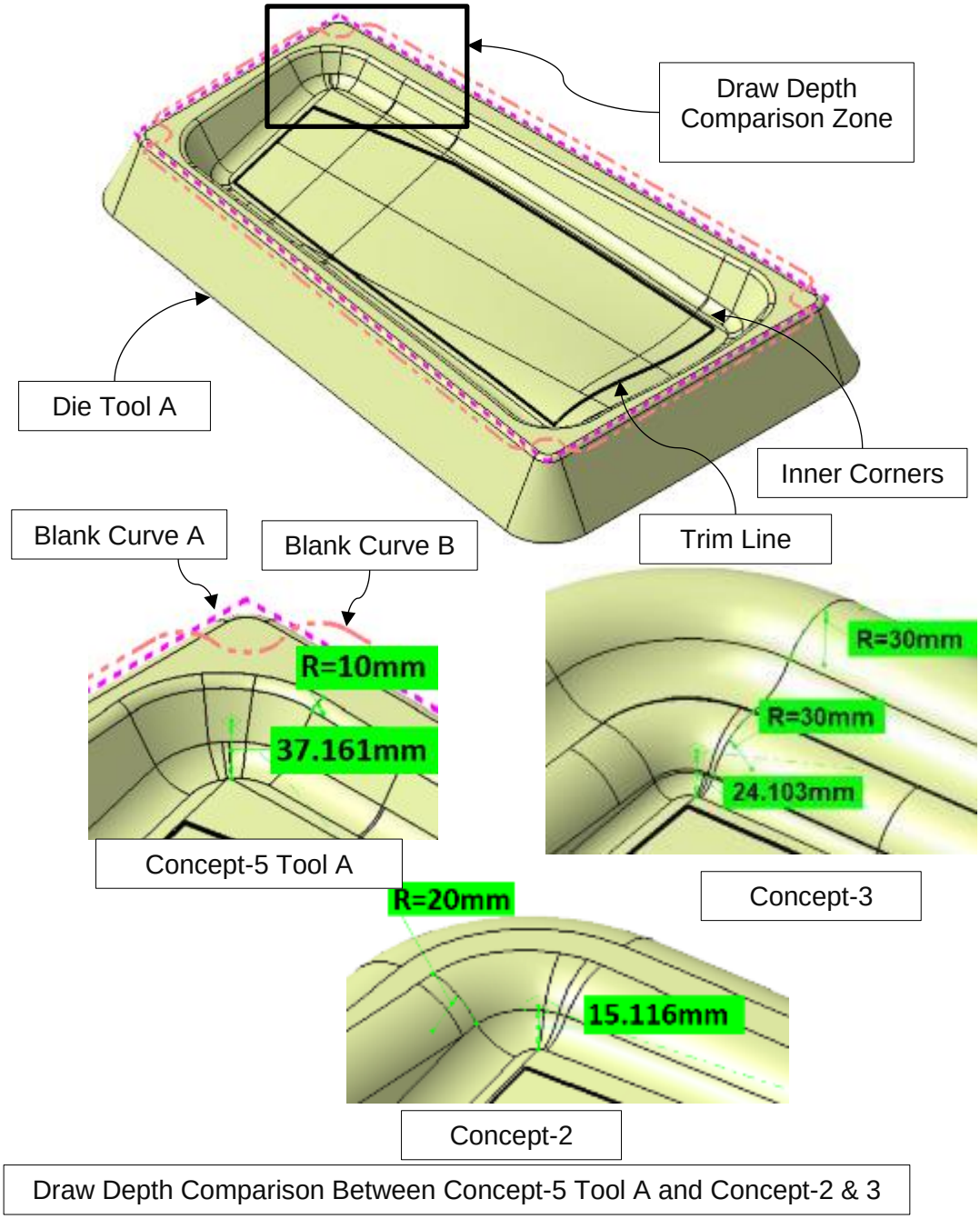

Figure A.24: Concept-5 Tool A and Blank A & B

Figure A.25 depicts the top and cut side view of Concept-5 tool A. The minimum edge radius of the tool was 10 mm. The tool side face draft angle was 25° and the inner portion draft angle was 25°.

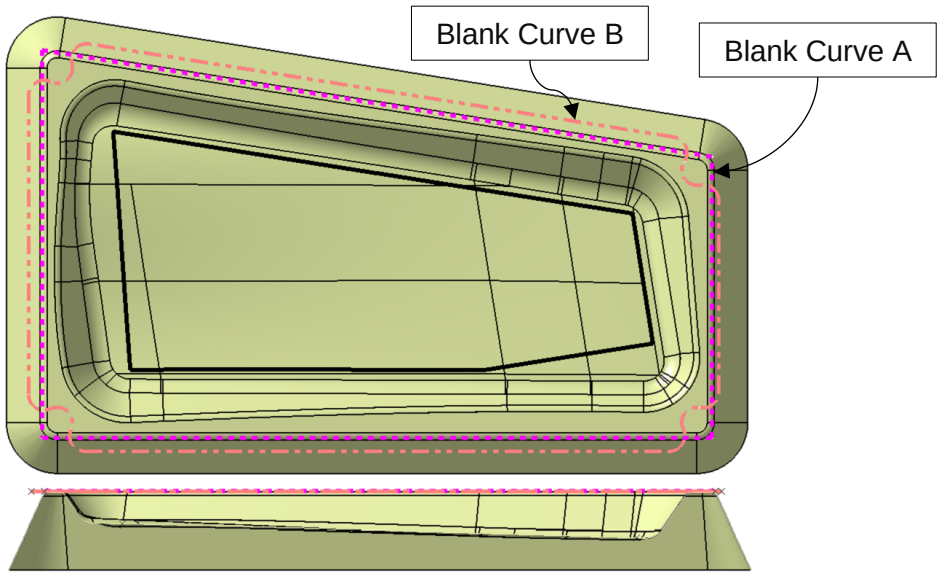

Figure A.25: Concept-5 Tool A and Blank A & B – Top and Side Views

Figure A.27 depicts Concept-5's tool A, blank A and B, and Figure A.27 depicts the tool die mesh, the trim curve and the two assembly configurations FEM in PAM-STAMP 2G. The mesh element size for blank A and B was 13 mm. The sheet metal rolling direction was in the y-axis. As the minimum edge radius for Concept-5 was 10 mm, the edge radius to element size was 0.769:1. A blank mesh refinement level of 3 was used, providing an element size of 3.25 mm. Hence, the edge radius to element size was 3.07:1, acceptable for a feasibility analysis.

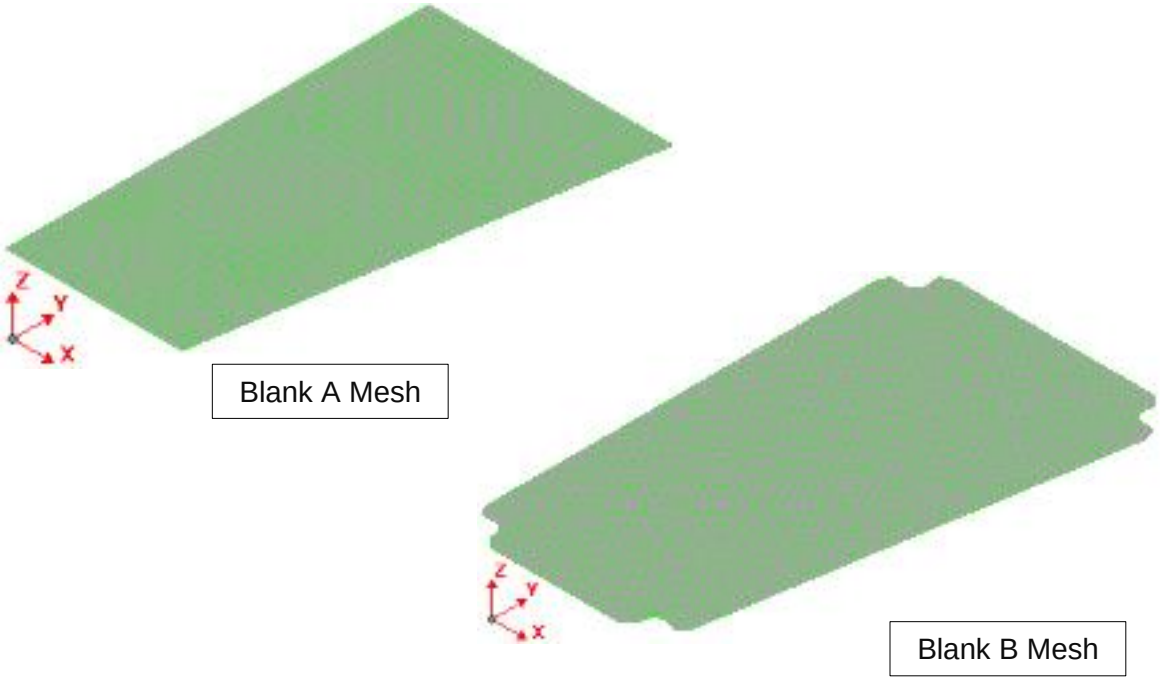

Figure A.26: Concept-5 Blank A and B FEM

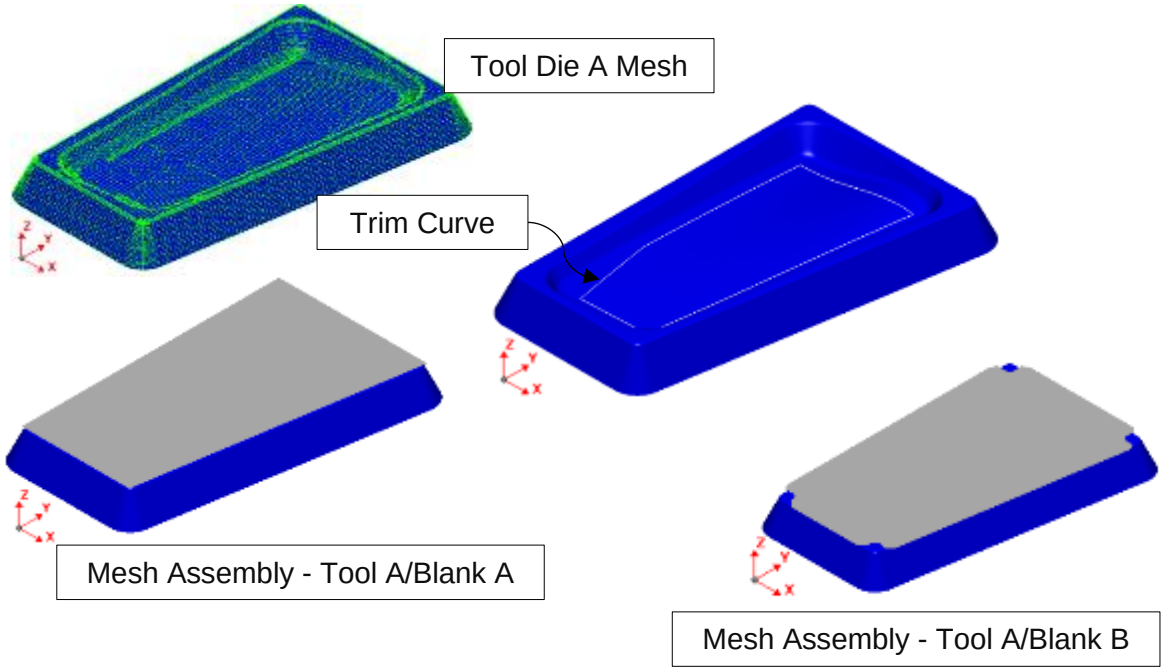

Figure A.27: Concept-5 Tool A, trim curve and the assemblies FEM

The simulation set-up was a fluid cell forming stage, followed by a trimming and springback stage. Refer to Section 3.4.3 for a detailed breakdown of the simulation set-up. The total progression time was 30 seconds with a maximum pressure of 80 MPa. The stopping criteria for the stage was contact area. A state result was provided every 2.5 seconds. The material card used for this simulation was the Vegter yield locus lite plasticity law and the Yoshida-Uemori kinematic hardening law. Figure A.28 depicts the FLD and a zone quality overlay on the blank in final form. The trimmed form at the trim stage and the final form at the springback stage are depicted in Figure A.29. Blank A did not have overhanging edges and collapsed into the inner section of the tool. The simulation showed in-plane stretching only occurred in the corners of the tool, hence the blank would not retain the desired form.

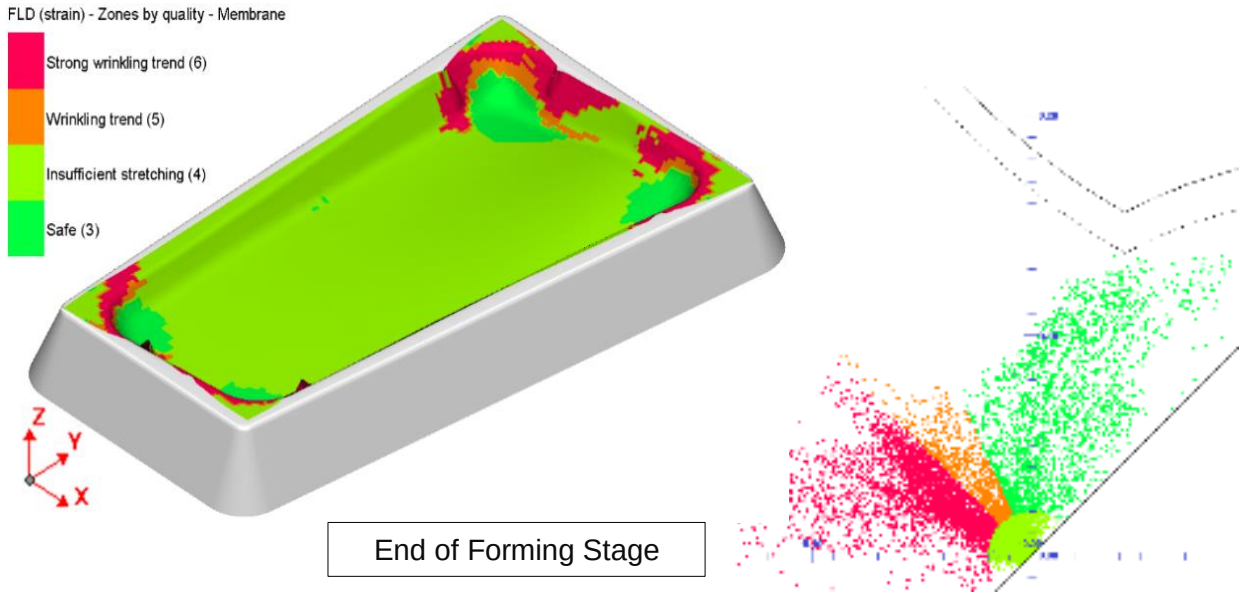

Figure A.28: Concept-5 Tool A, Blank A FLD and zone quality overlay

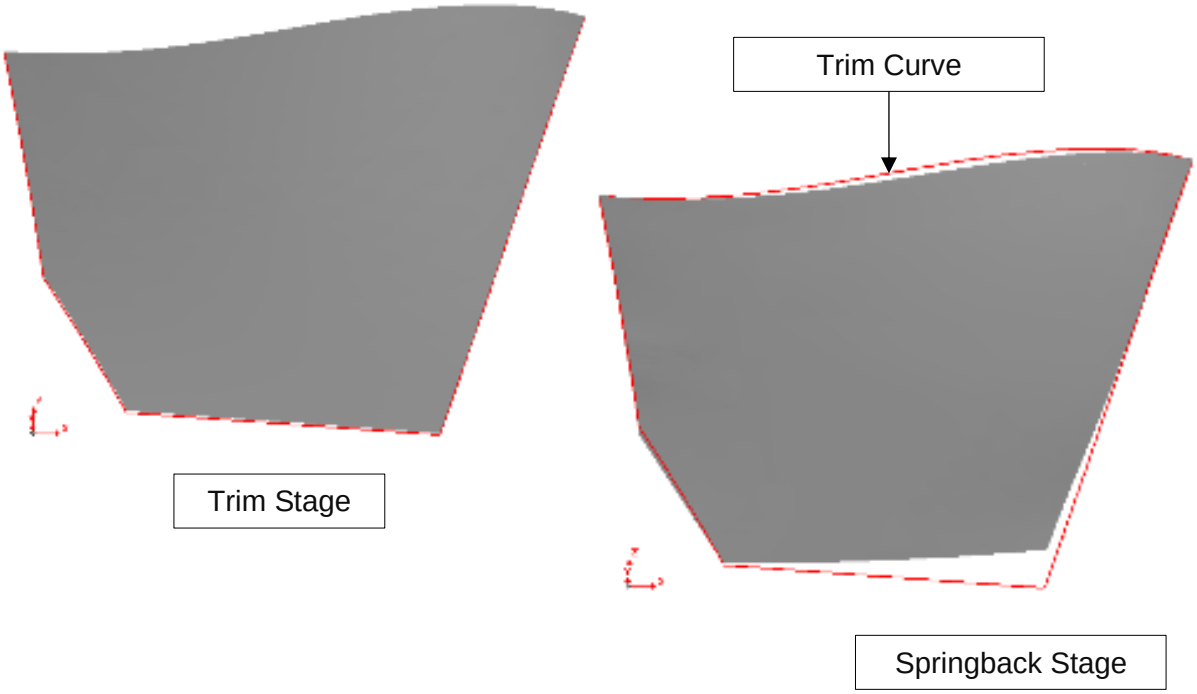

Figure A.29: Concept-5 Tool A, Blank A springback comparison

Figure A.30 depicts the final form from the simulation versus the desired form of the component. The simulation showed the final component might have had a predicted distortion of 20.512 mm. The distance contour lines showed Concept-5 Tool A Blank A would springback to a nearly flat shape.

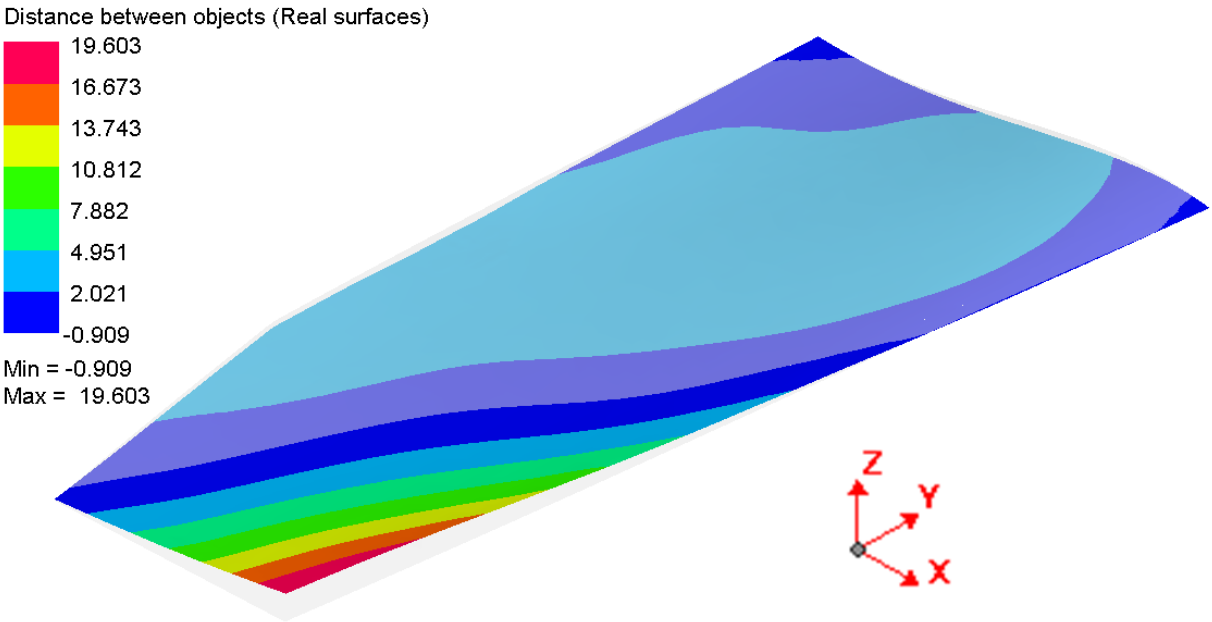

Figure A.30: Concept-5 Tool A Blank A final simulation form vs component

Figure A.31 depicts the FLD, a zone quality overlay on the blank in final form. Blank B did not have overhanging edges and collapsed into the inner section of the tool. The simulation showed in-plane stretching only occurred in the corners of the tool.

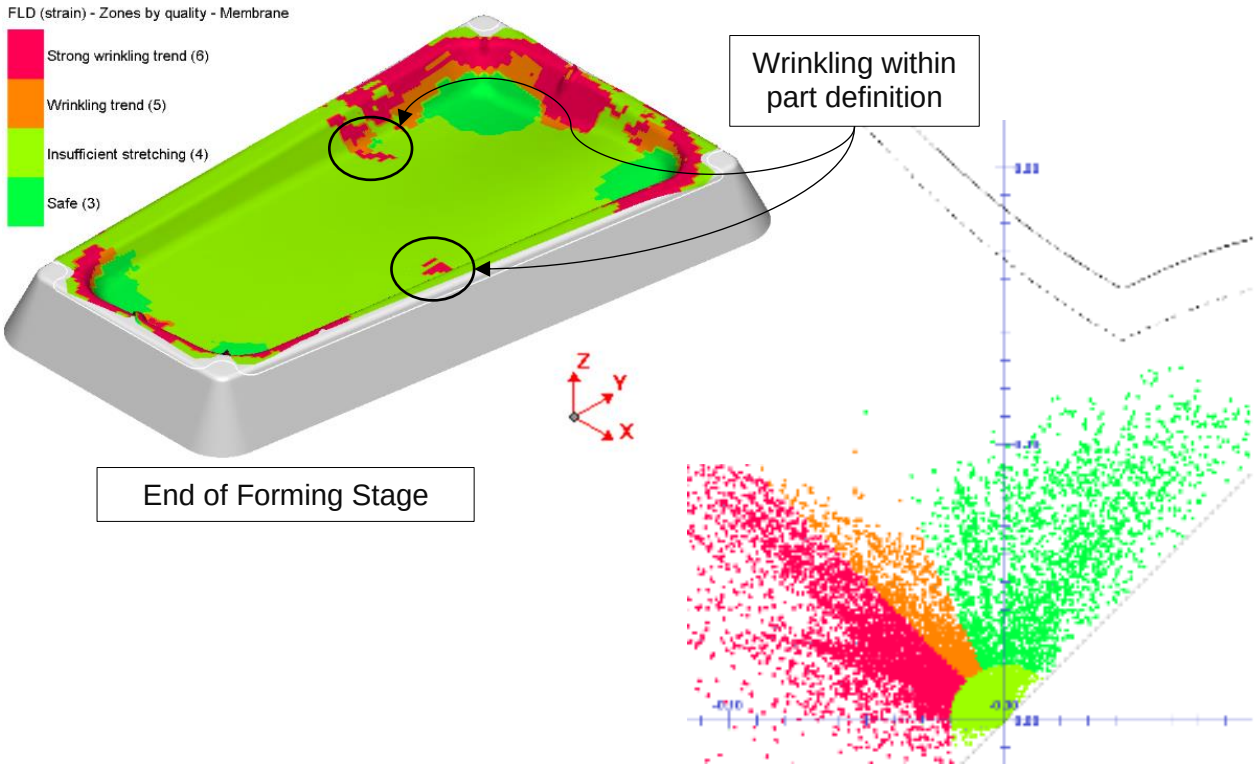

Figure A.31: Concept-5 Tool A, Blank B FLD and zone quality overlay

Figure A.32 depicts the trimmed form at the trim stage and the final form at the springback stage. The springback stage form showed the component deviated excessively from the final desired form of the component.

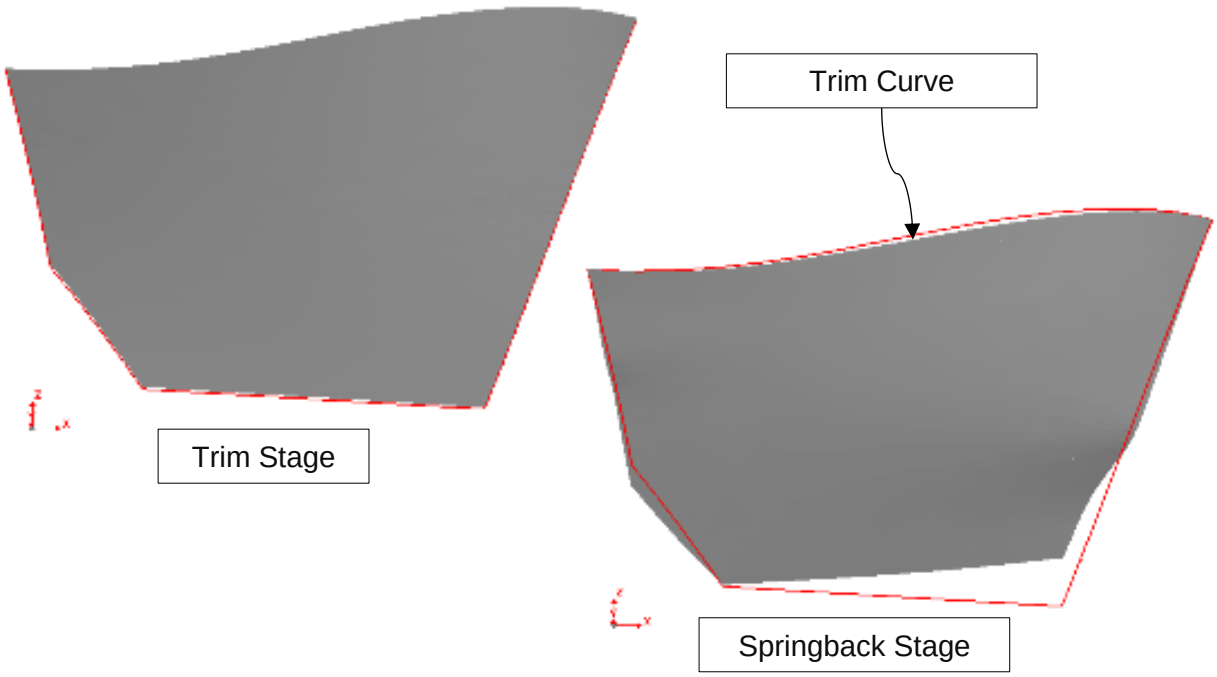

Figure A.32: Concept-5 Tool A, Blank B springback

Figure A.33 depicts the final form from the simulation versus the desired form of the component. The simulation showed the final component might have had a predicted distortion of 23.88 mm. Unlike the previous concepts, which distorted more towards the flat form, Concept-5 tool A blank B appeared to bend at a particular point, as shown in Figure A.33. This form was attributed to the wrinkling of the blank within the part definition, as shown in Figure A.32. The flanged edges of blank B did not overlap the side of tool A sufficiently, hence the blank drew into the tool before the flanges draped the sides of the tool. Tool A and blanks A and B were rejected due to the excessive distortion from the desired form.

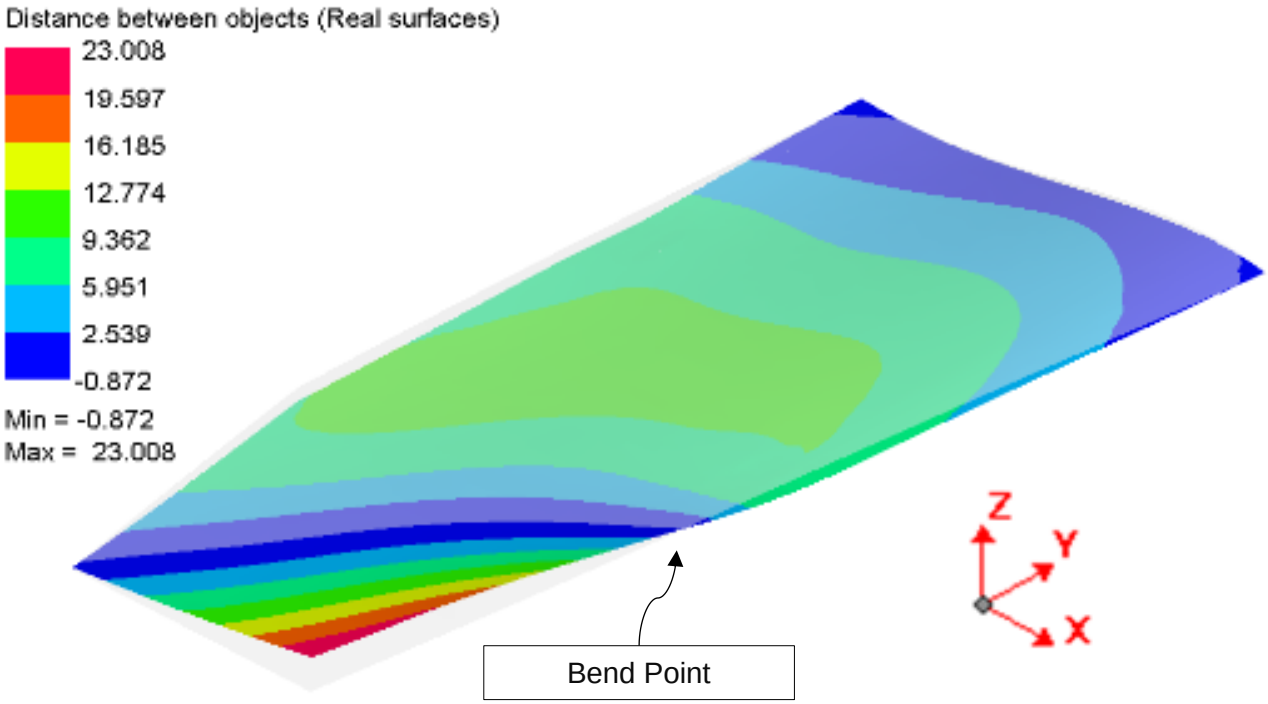

Figure A.33: Concept-5 Tool A Blank B final simulation form vs component

Appendix A.6 Concept-5 – Tool B

Figure A.34 depicts Concept-5 tool B. Tool A was designed with straight edges, whereas Tool B had curved segments. In addition, the distance from the inner corners to the edge of the final component was close, whereas this distance was larger in tool B. The curved segment design was introduced to omit the wrinkling seen in blank B in the previous investigation. Hence, blank B was used with tool B to investigate its feasibility of the tool to omit wrinkling. Blank C was introduced with a much larger overhang, compared to blank B, and used the blank shape definition used in concepts 2, 3 and 4.

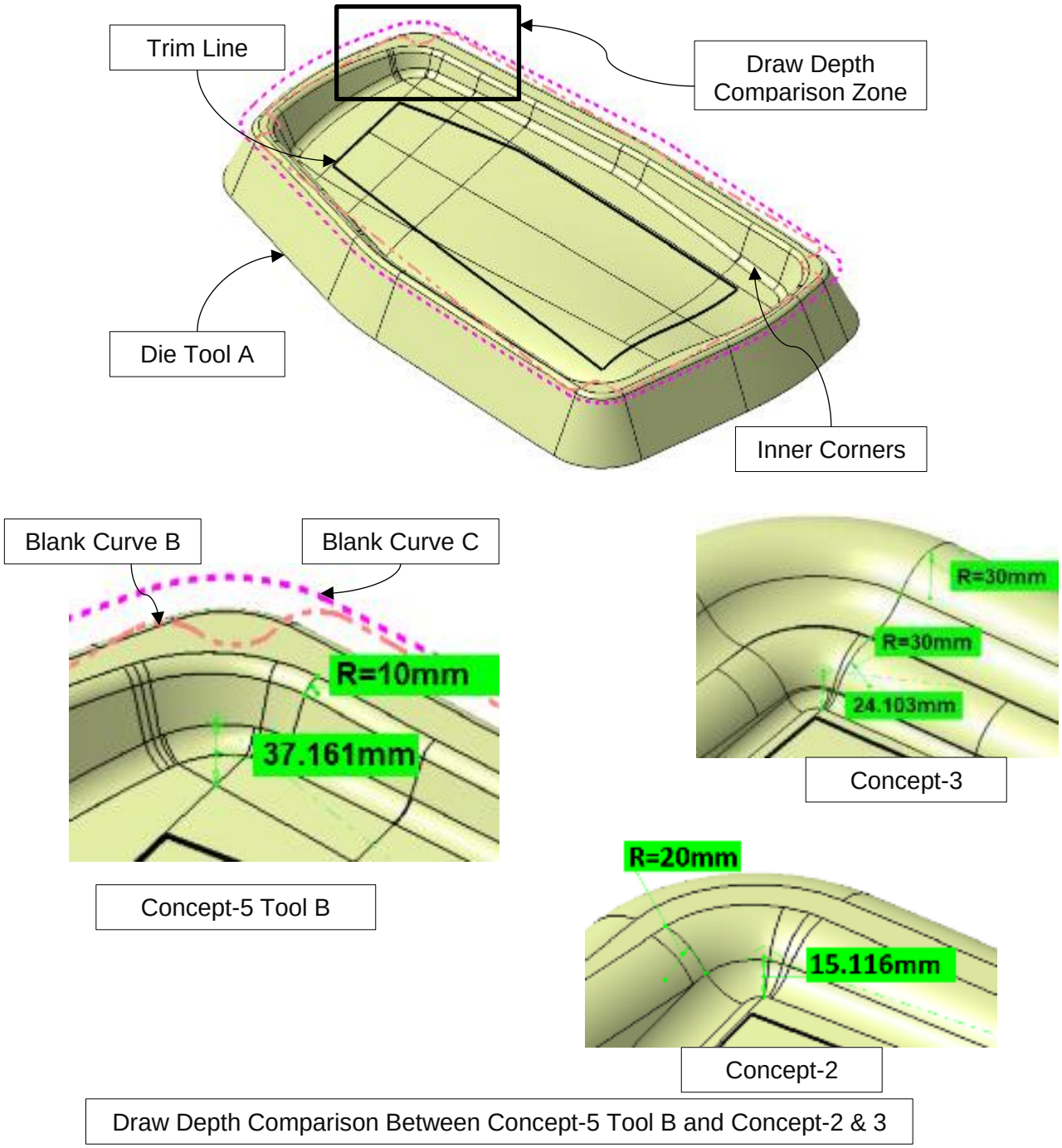

Figure A.34: Concept-5 Tool B and Blank B & C

Figure A.35 depicts the top and cut side view of Concept-5's tool B. The minimum edge radius of the tool was 10 mm. The tool side face draft angle was 25°, and the inner portion draft angle was 25°.

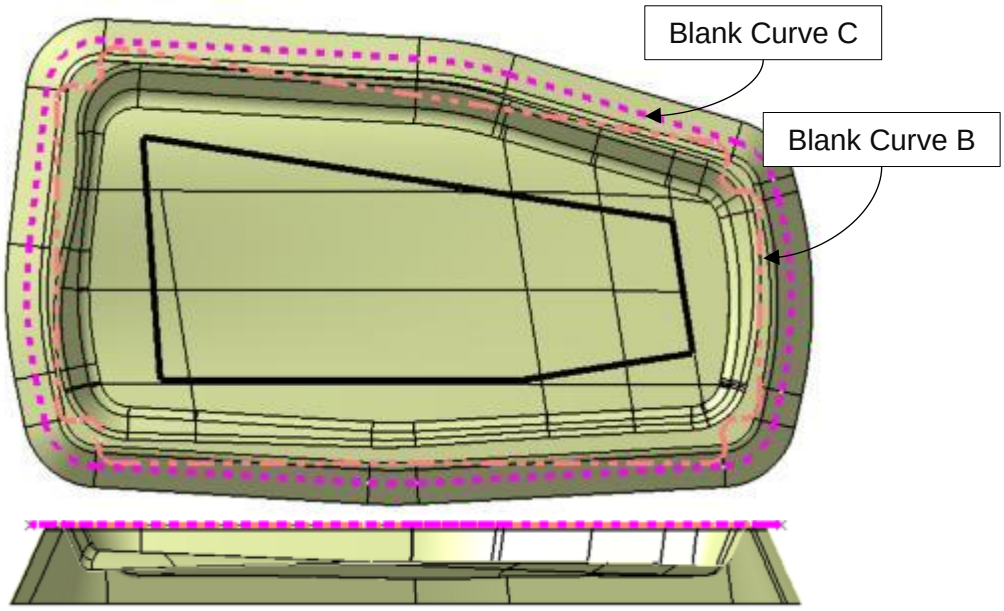

Figure A.35: Concept-5 Tool B and Blank B & C – Top and Side Views

Figure A.36 depicts Concept-5's tool B and blank C FEM mesh in PAM-STAMP 2G. The mesh element size for blank C was 16 mm. The sheet metal rolling direction was in the y-axis. As the minimum edge radius for Concept-5 tool B was 10 mm, and the edge radius to element size was 0.625:1. A blank mesh refinement level of 3 was used, providing an element size of 4 mm. Hence, the edge radius to element size was 2.5:1, acceptable for a feasibility analysis.

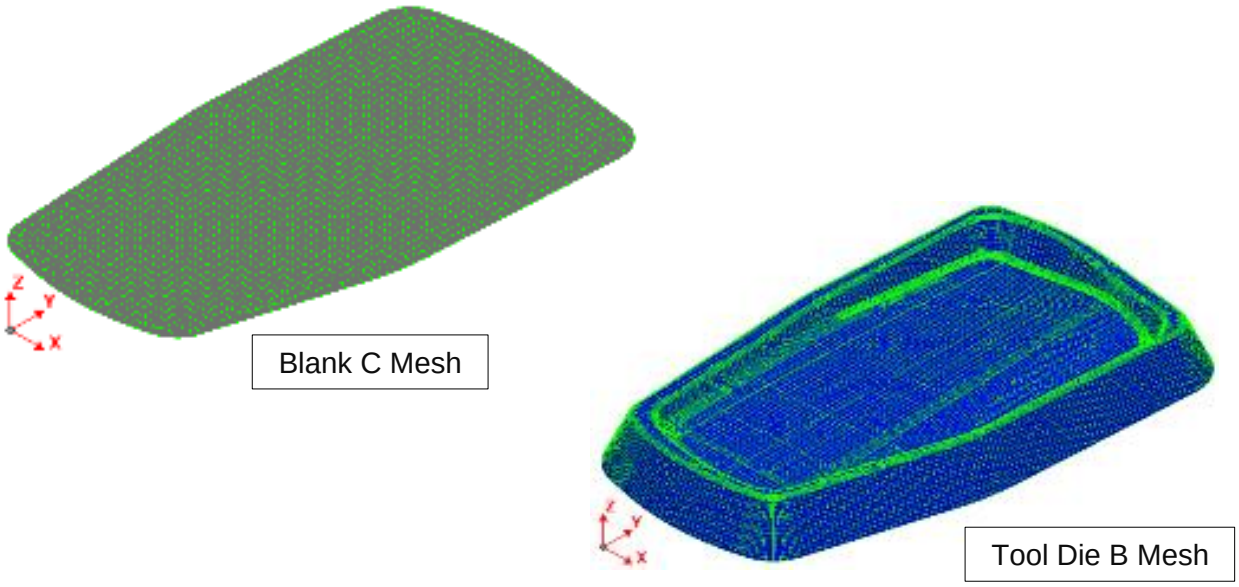

Figure A.36: Concept-5 tool B and blank C FEM mesh

Figure A.37 depicts Concept-5's tool B and blank C, trim curve and the assembly FEM in PAM-STAMP 2G. Blank B is shown in Figure A.27. The mesh element size for blank C was 16 mm. The sheet metal rolling direction was in the y-axis. As the minimum edge radius for Concept-5 tool B was 10 mm, and the edge radius to element size was 0.625:1. A blank mesh refinement level of 3 was used, providing an element size of 4 mm. Hence, the edge radius to element size was 2.5:1, acceptable for a feasibility analysis.

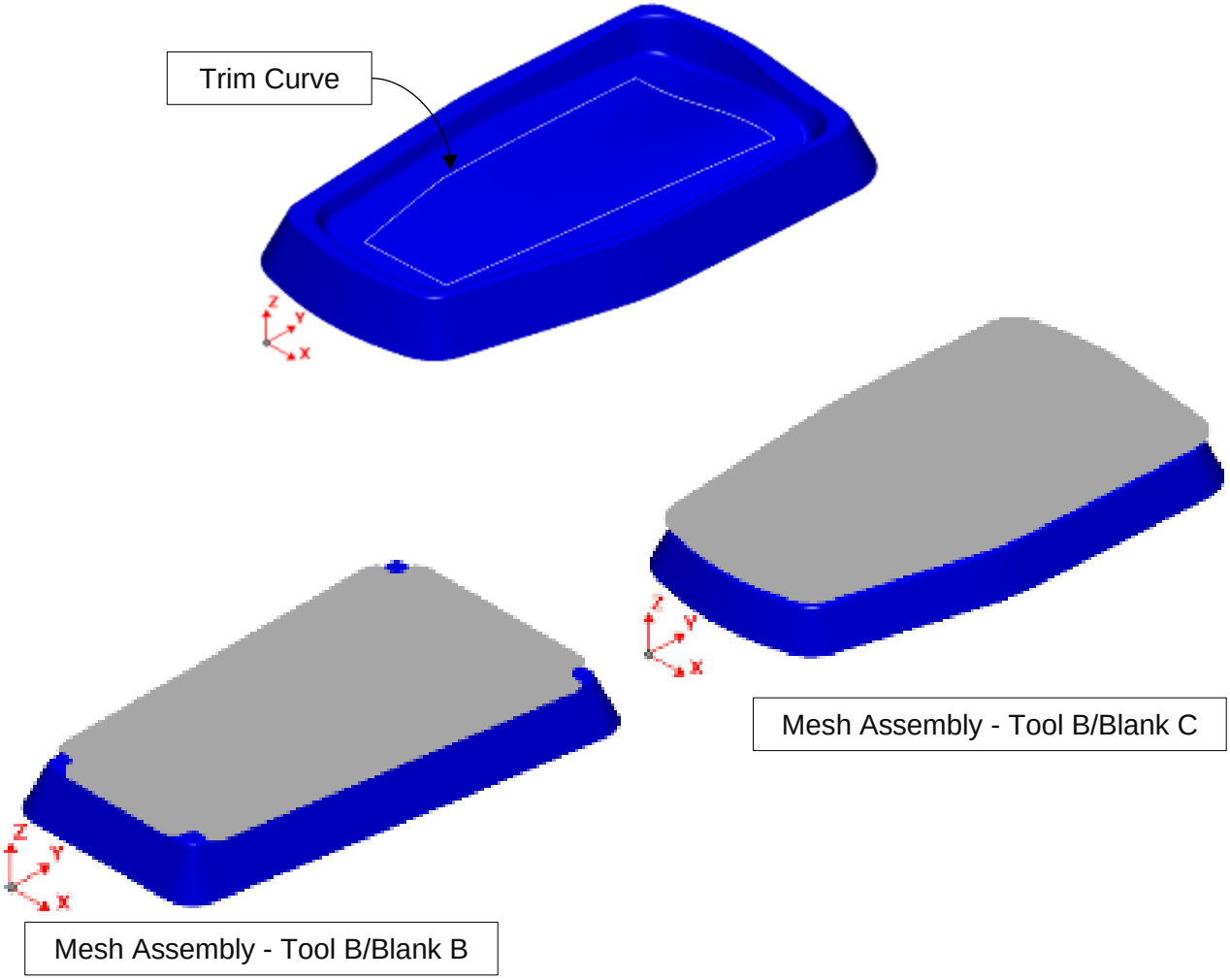

Figure A.37: Concept-5 tool B and blank C trim curve and FEM assemblies

The simulation set-up was a fluid cell forming stage, followed by a trimming and springback stage. Refer to Section 3.4.3 for a detailed breakdown of the simulation set-up. The total progression time for tool B blank B was 40 seconds with a maximum pressure of 80 MPa. The progression was increased as full contact was not achieved in 30 seconds. The stopping criteria for the stage was contact area. A state result was provided every 2.5 seconds. The material card used for this simulation was the Vegter yield locus lite plasticity law and the Yoshida-Uemori kinematic hardening law.

Figure A.38 depicts the FLD, a zone quality overlay on the blank in final form, the trimmed form at the trim stage and, the final form, at the springback stage. Blank B did not have overhanging edges and collapsed into the inner section of the tool. The simulation showed very low in-plane stretching only occurs in the corners of the tool, hence the blank would not retain the desired form. One edge of the blank was within the tool outer edge and slid past; at this edge no in-plane stretching occurred and the blank sprang back excessively.

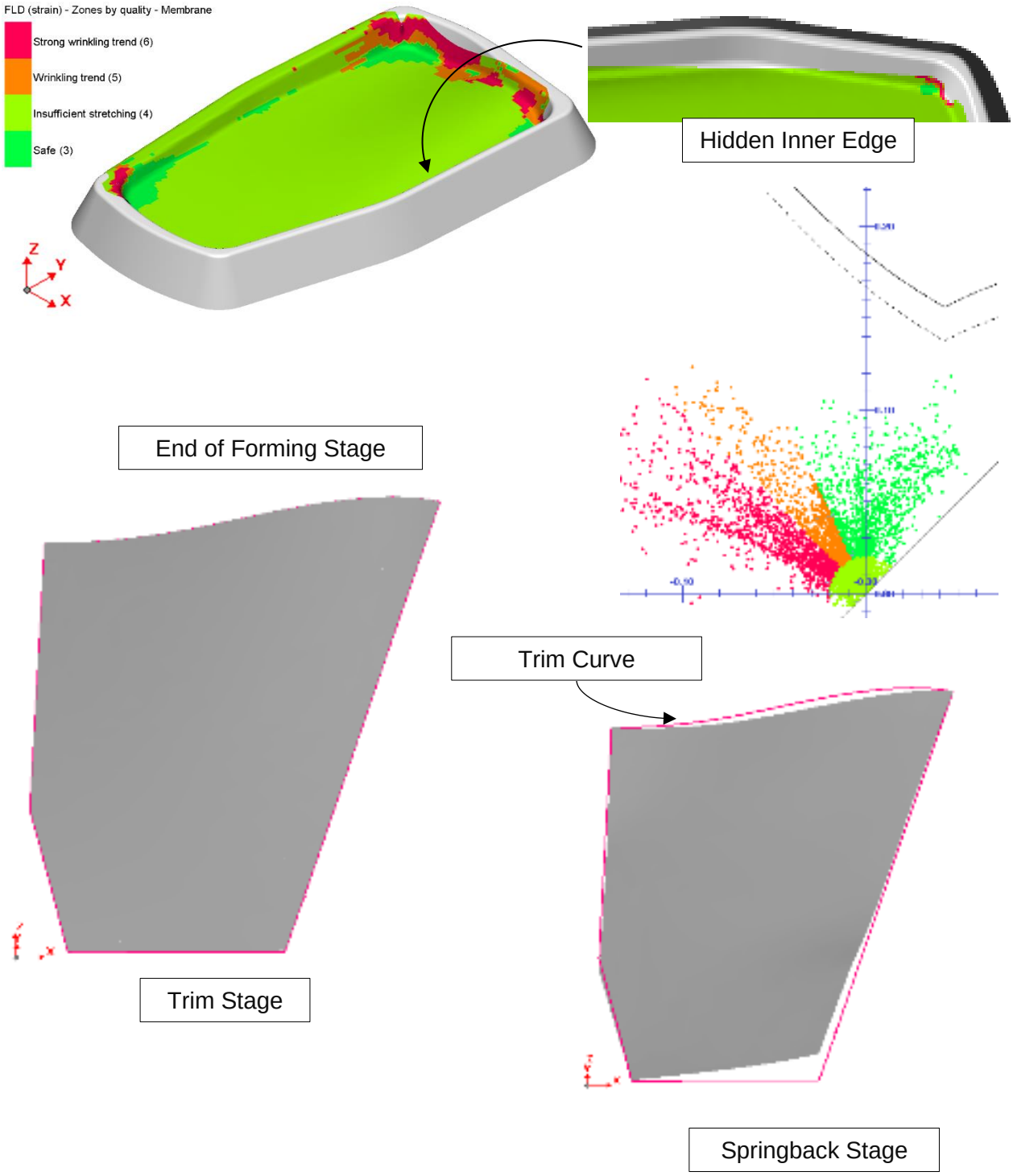

Figure A.38: Concept-5 Tool B, Blank B FLD, zone quality overlay, and springback

Figure A.39 depicts the final form from the simulation versus the desired form of the component. The simulation showed the final component might have had a predicted distortion of 26.094 mm, which was a worse-performing concept, and attributed to the edge of the blank lying within the tool outer edge.

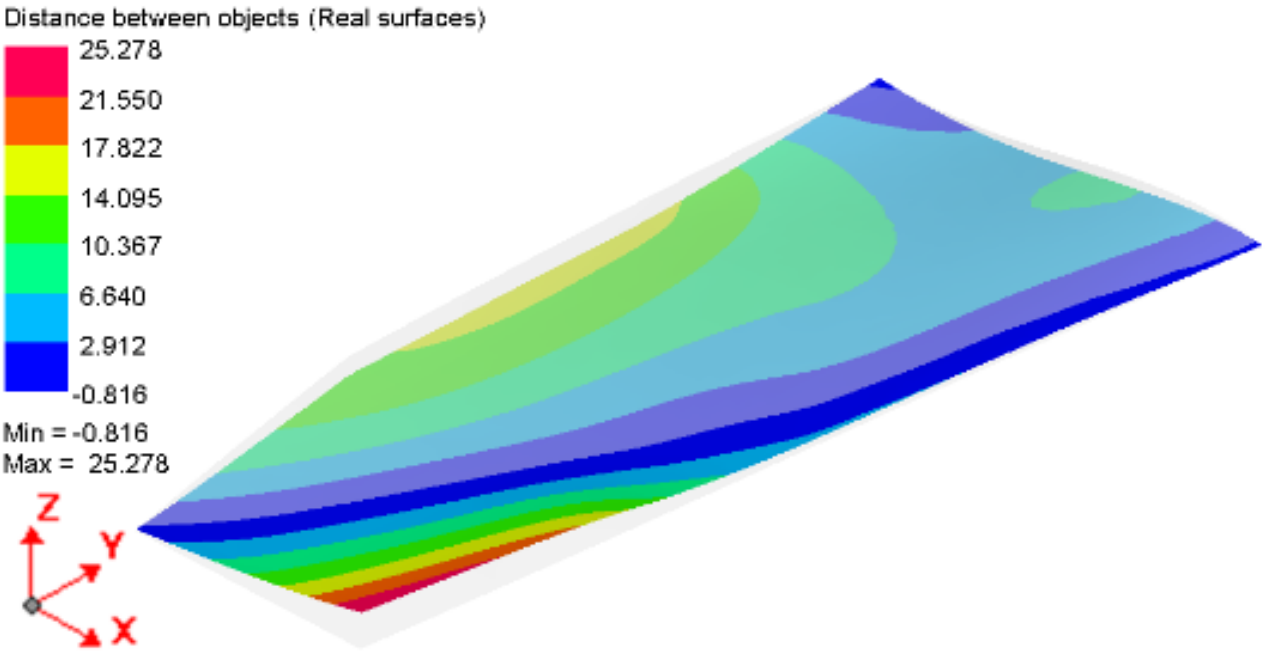

Figure A.39: Concept-5 tool B blank B final simulation form vs component

Concept-5 tool B blank B was rejected. What the poor performing concept showed was the need for the blank to lock over the edges of the tool before being drawn in. Compared with the previous concepts, where enough in-plane stretching had been achieved in the corners, the blank sprang back less.

For tool B blank C, the simulation set-up was a fluid cell forming stage, followed by a trimming and springback stage. Refer to Section 3.4.3 for a detailed breakdown of the simulation set-up. The total progression time was 30 seconds with a maximum pressure of 80 MPa. The stopping criteria for the stage was contact area. A state result was provided every 2.5 seconds.

Figure A.40 depicts the FLD, a zone quality overlay on the blank in final form, the trimmed form at the trim stage and, the final form, at the springback stage. Blank C had overhanging edges, but still collapsed into the inner section of the tool. The simulation showed improved in-plane stretching in the corners of the tool, but cracking in one corner had resulted. Due to cracking, the concept was rejected.

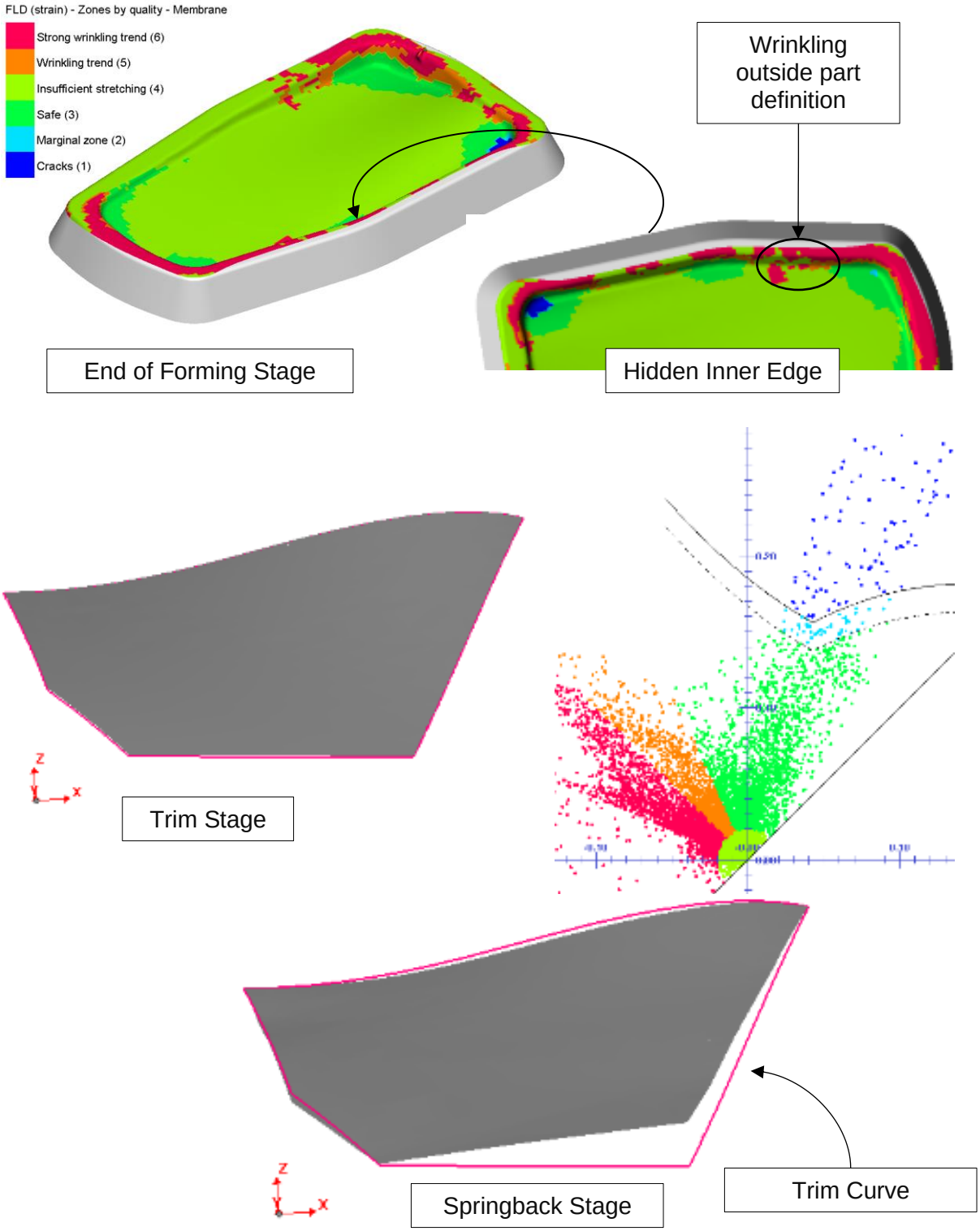

Figure A.40: Concept-5 Tool B, Blank C FLD, zone quality overlay, and springback

Figure A.41 depicts the final form from the simulation versus the desired form of the component. The simulation showed the final component might have had a predicted distortion of 23.854 mm. Blank C was an improvement from the results achieved for blank B. The s-shaped curve in the blank C concept was better than blank B, however concept C sprang back to a flattened shape on the other end of the component. Wrinkling near the component was seen, but it was outside of the component definition. The wrinkling and the lack of in-plane stretching were attributed to the concept high level of springback. Based on the results of the simulation, Concept-5 tool B was rejected. Tool B was revised into tool C, a more shallow tool compared to tool B.

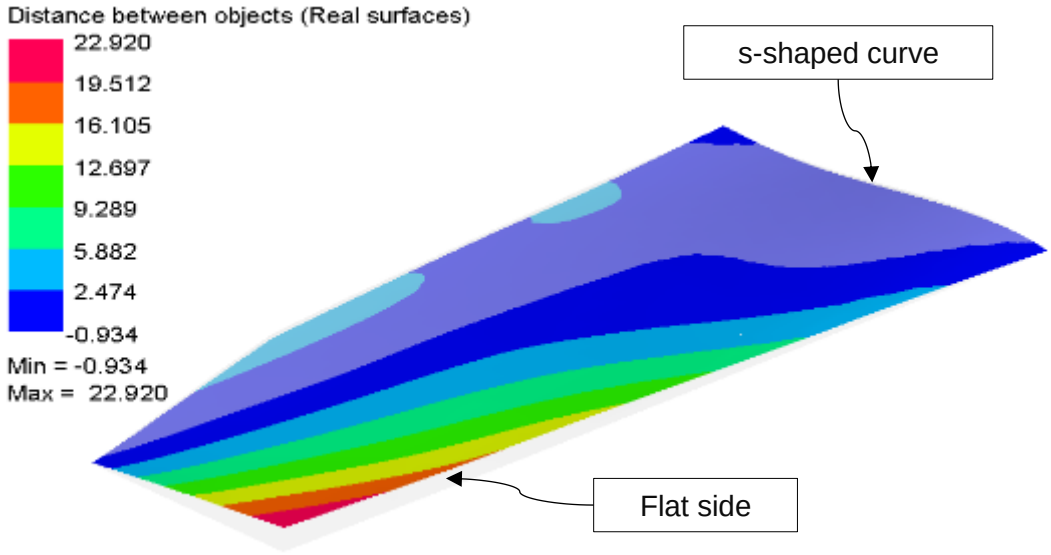

Figure A.41: Concept-5 Tool B Blank C final simulation form vs component

Appendix A.7 Concept-5 – Tool C

Figure A.42 depicts Concept-5 tool C and blanks C. Tool C had the same outline definition as tool B, except the outer section was reduced by 16 mm. Thus, the draw depth of tool C was less than tool B.

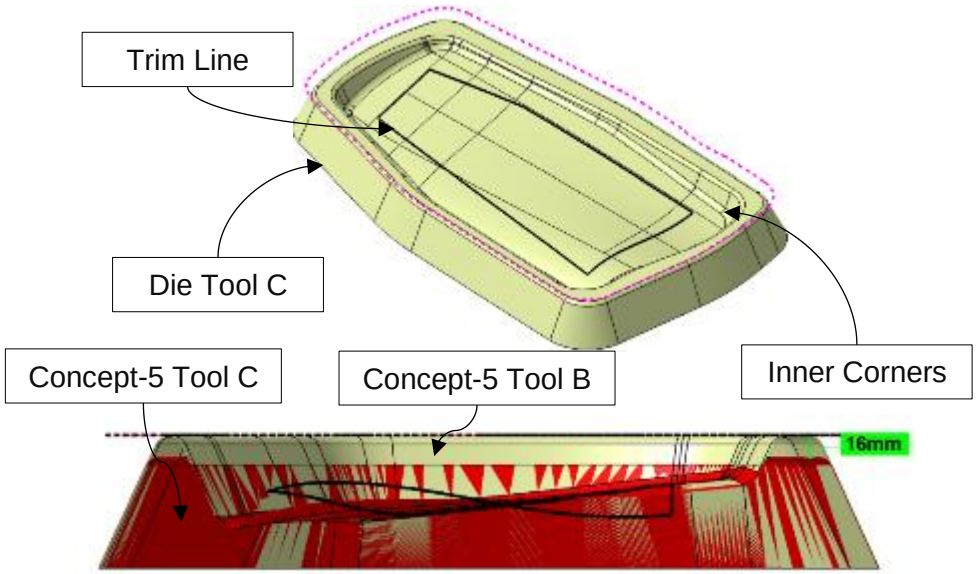

Figure A.42: Concept-5 Tool C and Blank D

Figure A.43 depicts the top and cut side view of Concept-5's tool C. The minimum edge radius of the tool was 10 mm. The tool side face draft angle was 25° and the inner portion draft angle was 25°.

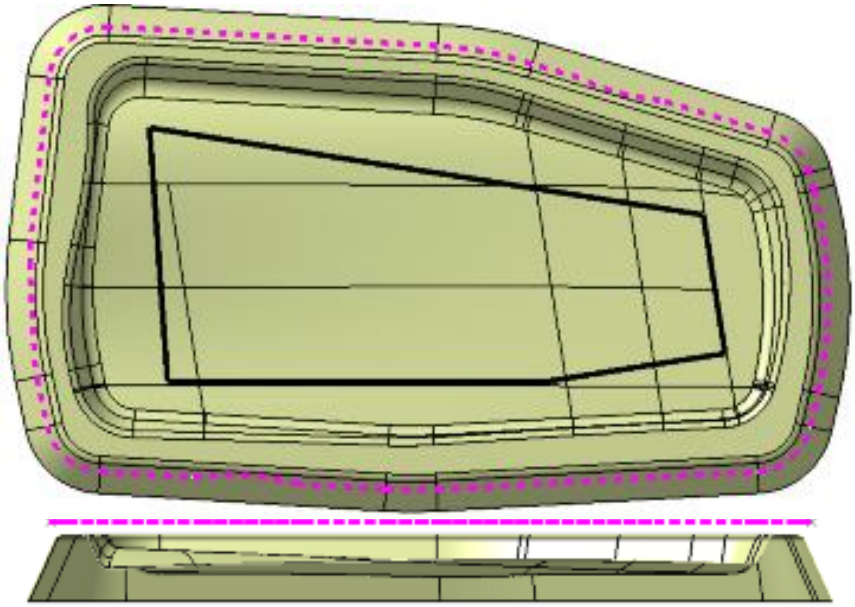

Figure A.43: Concept-5 Tool C and Blank C – Top and Side Views

Figure A.44 depicts Concept-5's tool C and blank C, and Figure A.45 depicts the trim curve and the assembly FEM in PAM-STAMP 2G. The mesh element size for blank C was 16 mm. The sheet metal rolling direction was in the y-axis. As the minimum edge radius for Concept-5 tool B was 10 mm, the edge radius to element size was 0.625:1. A blank mesh refinement level of 3 was used, providing an element size of 4 mm. Hence, the edge radius to element size was 2.5:1, acceptable for a feasibility analysis.

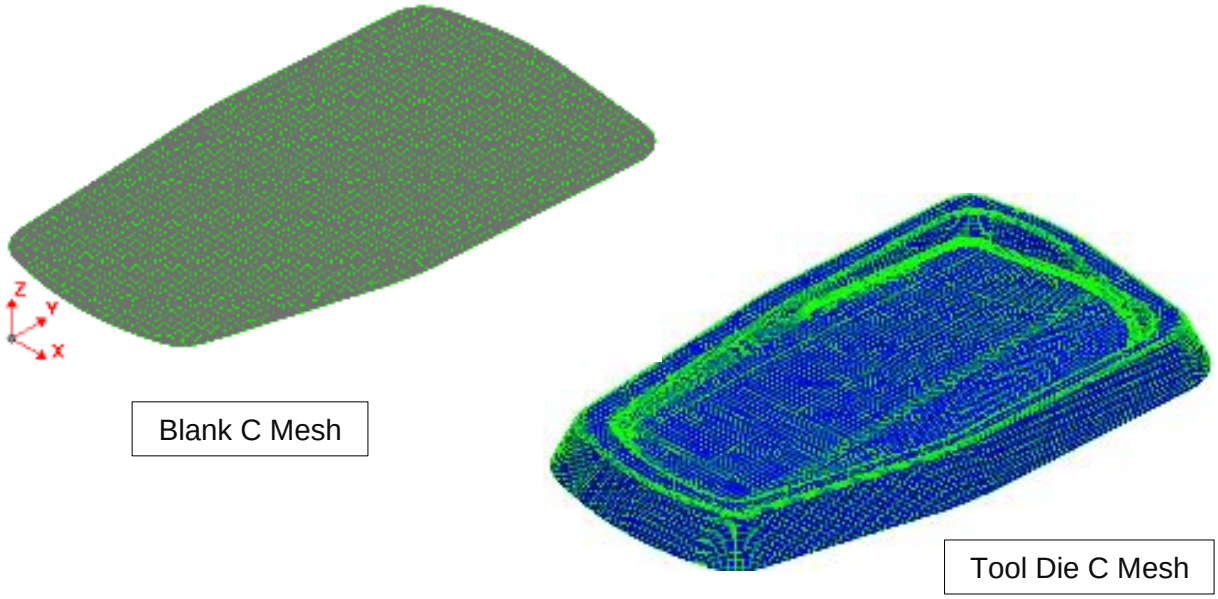

Figure A.44: Concept-5 tool C and blank C FEM

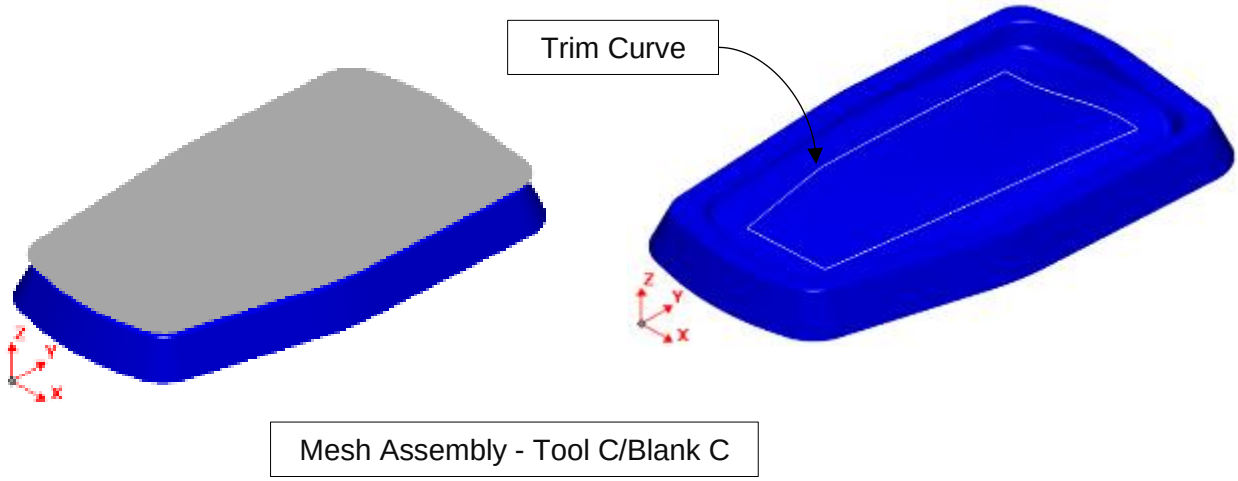

Figure A.45: Concept-5 tool C trim curve and assemblies FEM

The simulation set-up was a fluid cell forming stage, followed by a trimming and springback stage. Refer to Section 3.4.3 for a detailed breakdown of the simulation set-up. The total progression time for tool C blank C was 40 seconds with a maximum pressure of 80 MPa. The progression was increased as full contact was not achieved in 30 seconds. The stopping criteria for the stage was contact area. A state result was provided every 2.5 seconds. The material card used for this simulation was the Vegter yield locus lite plasticity law and the Yoshida-Uemori kinematic hardening law.

Figure A.46 depicts the FLD and a zone quality overlay on the blank in final form. Blank C did not have large overhanging edges and collapsed into the inner section of the tool. The simulation showed very low in-plane stretching in the corners of the tool, hence the blank did not retain the desired form.

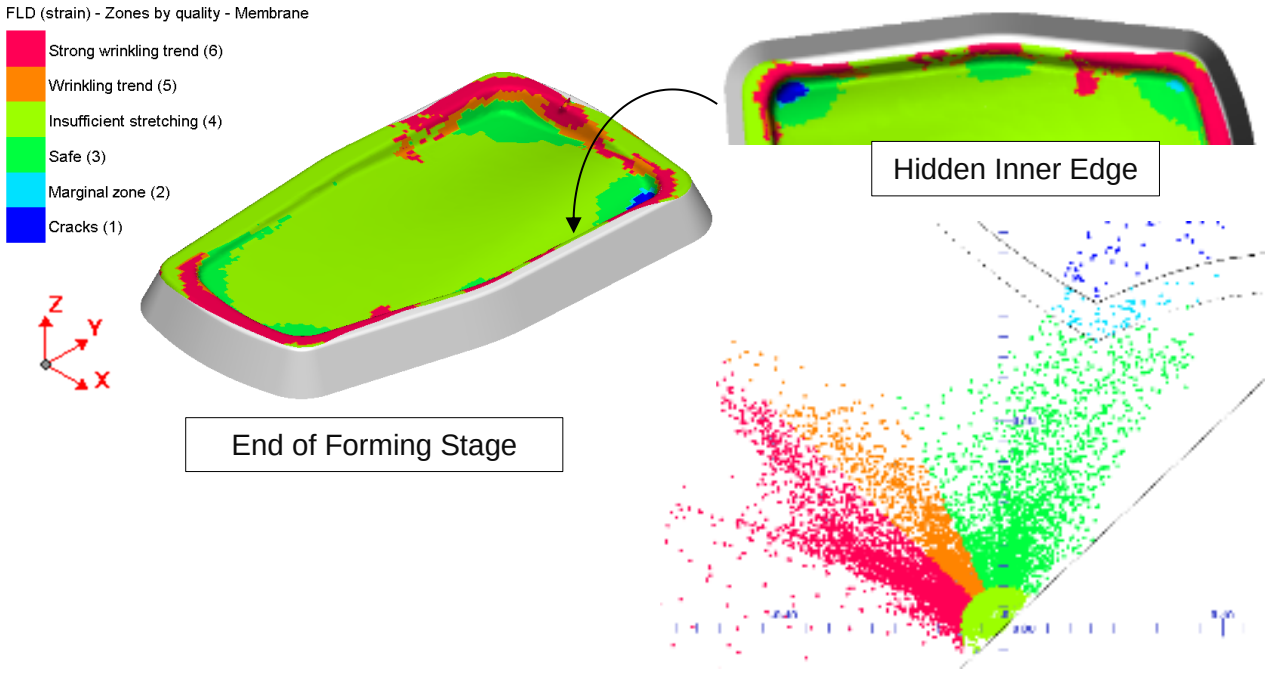

Figure A.46: Concept-5 Tool C, Blank C FLD, zone quality overlay, and springback

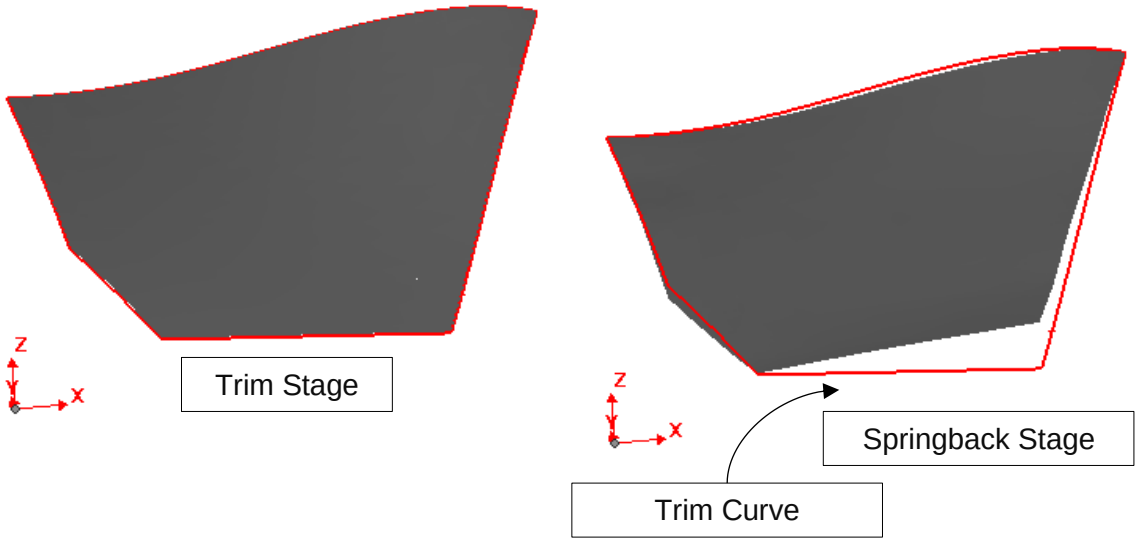

Figure A.47: Concept-5 Tool C, Blank C FLD, zone quality overlay, and springback

Figure A.47 depicts the final form contouring the trim curve and the component after the springback stage deviating from the trim curve. Figure A.48 depicts the final form from the simulation versus the desired form of the component. The simulation showed the final component might have had a predicted distortion of 27.01 mm, worse than tool B blank C's result. Cracking still resulted in the corner of the tool, but due to reduced the draw depth of the tool, less in-plane stretching resulted.

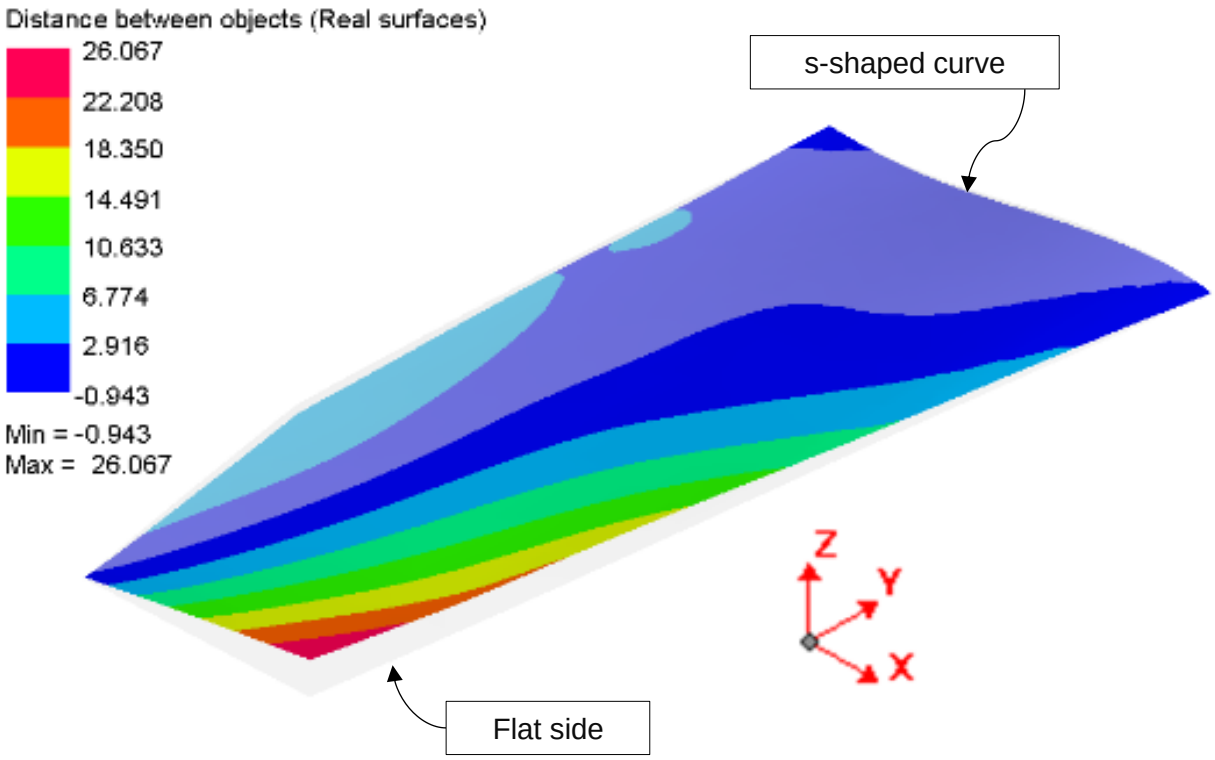

Figure A.48: Concept-5 tool B blank B final simulation form vs component

Appendix A.8 Concept-6

The deeper draw depths and large overhangs showed promising results. Concept-5 tool A's draw depth and the larger overhang blanks of Concept-2, 3 and 4 were used to conceptualise the Concept-6 design. The tool was adapted from the square shape as seen in Figure A.24. Figure A.49 depicts Concept-6's tool and blank definition.

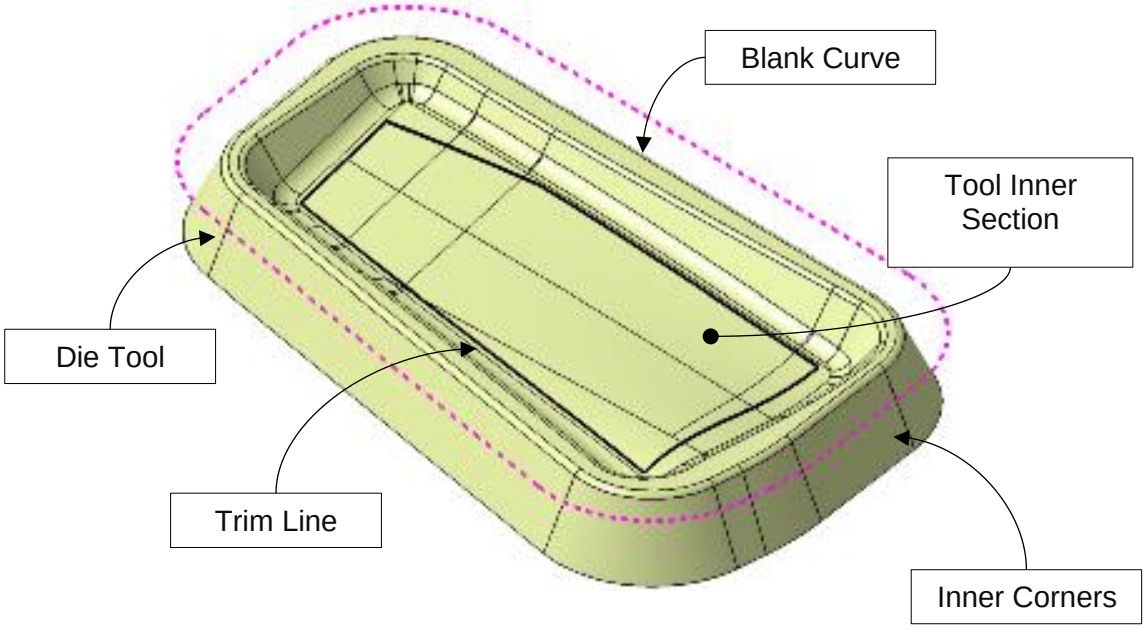

Figure A.49: Concept-6 tool and blank

Figure A.50 depicts the top and side view of Concept-6. The minimum edge radius of the tool was 10 mm. The tool side face draft angle was 25° and the inner portion draft angle was 37° The tool depth was 37 mm. The blank size was much larger than the tool and expected to drape over the sides during the forming process. As seen in the previous concepts, the blank was expected to bottom out on the inner tool section before the sides formed. However, the depth and large overhangs in this concept were not been investigated.

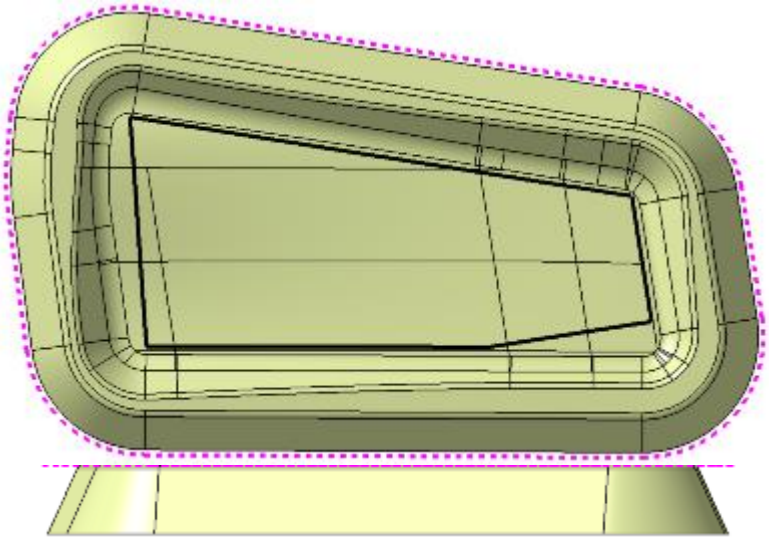

Figure A.50: Concept-6 tool and blank – top and side views

Figure A.51 depicts Concept-6's tool, blank, trim curve and the assembly FEM in PAM-STAMP 2G. The mesh element size for the blank was 22 mm. The sheet metal rolling direction was in the y-axis. As the minimum edge radius for Concept-6 tool was 10 mm, the edge radius to element size was 0.45:1. A blank mesh refinement level of 3 was used, providing an element size of 5.5 mm. Hence, the edge radius to element size was 1.8:1. The inner corner radius was 30mm, giving the edge to element size ratio of 3:1. The edge radius to element size after refinement was 5.45:1. The poor edge radius to element size on the outer corners was deemed acceptable for the feasibility assessment to continue.

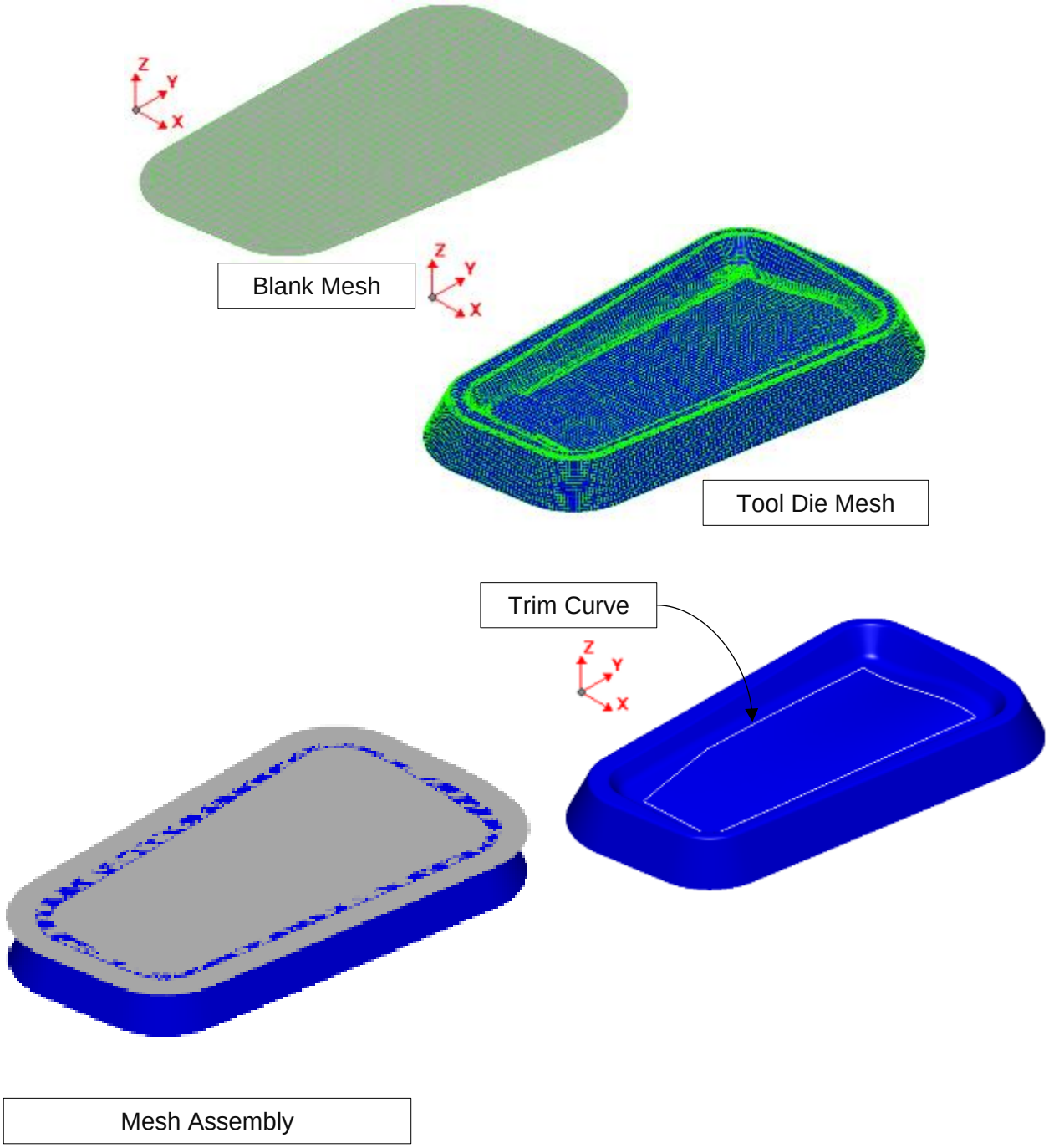

Figure A.51: Concept-6 tool, blank, trim curve and assembly FEM

The simulation set-up is a fluid cell forming stage, followed by a trimming and springback stage. Refer to Section 3.4.3 for a detailed breakdown of the simulation set-up. The total progression time

was 30 seconds with a maximum pressure of 80 MPa. The stopping criteria for the stage was contact area. A state result was provided every 2.5 seconds. The material card used for this simulation was the Vegter yield locus lite plasticity law and the Yoshida-Uemori kinematic hardening law.

Figure A.52 depicts the FLD, a zone quality overlay on the blank in final form, the trimmed form at the trim stage and, the final form, at the springback stage. The blank had a large overhang, but collapsed into the inner section of the tool, causing a wrinkle to form. The simulation showed that a greater degree of in-plane stretching occurred in the corners of the tool.

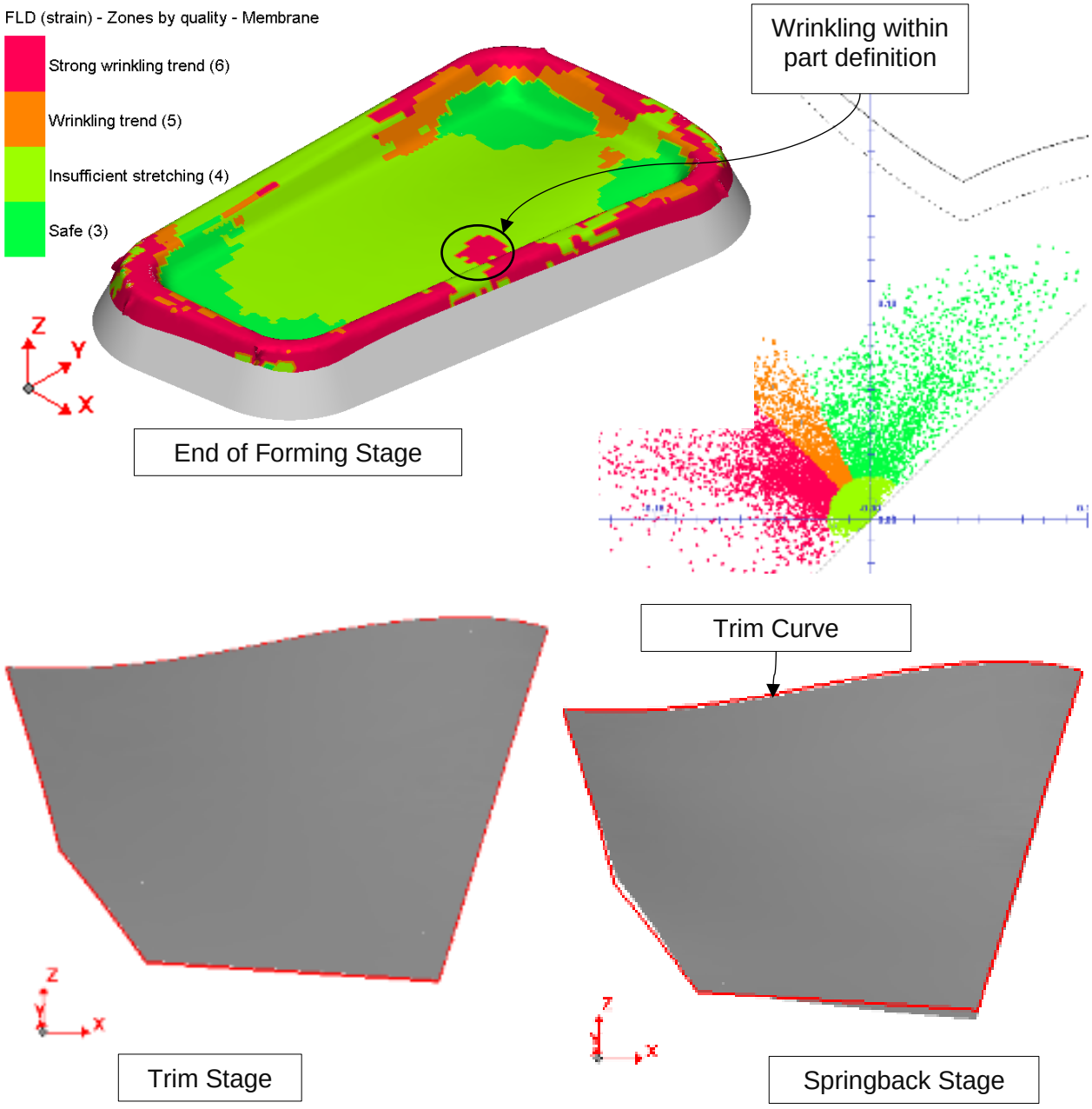

Figure A.52: Concept-6 FLD, zone quality overlay, and springback

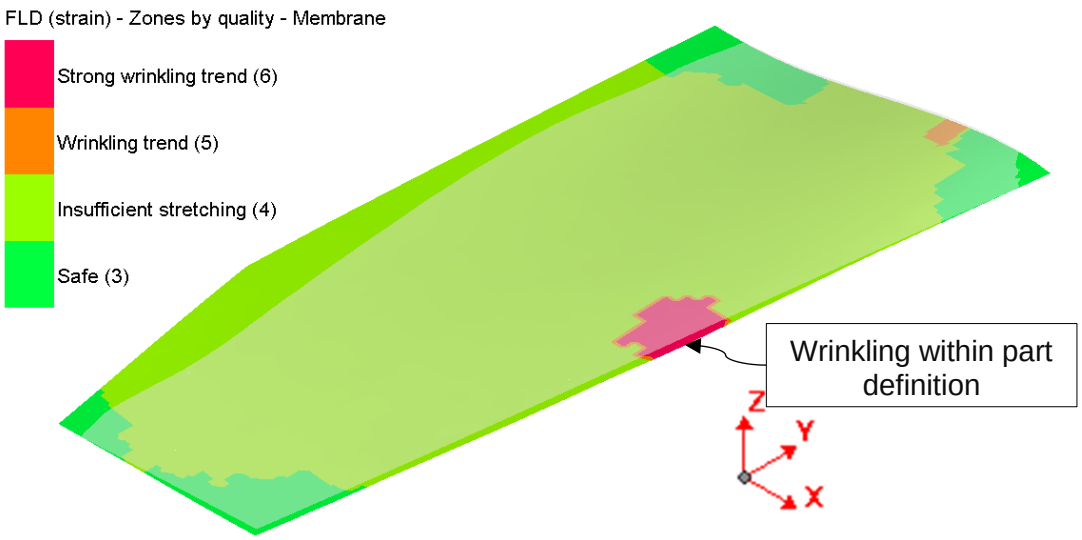

Figure A.53: Concept-6 final component zone quality overlay

Figure A.53 depicts the wrinkling in the component as a result of the blank bottoming out before the overhanging edges contoured the out corners to restrain the blank. Figure A.54 depicts the final form from the simulation versus the desired form of the component. The simulation showed the final component might have had a predicted distortion of 7.472 mm. This was an improvement on the result attained for Concept-4, and was marginally worse than Concept-3. The blank demonstrated less springback in this concept. The s-shaped curve profile conformed well to the desired design. Due to the wrinkling that occurred, the desired form was not attained. Based on the simulation results, the concept was rejected.

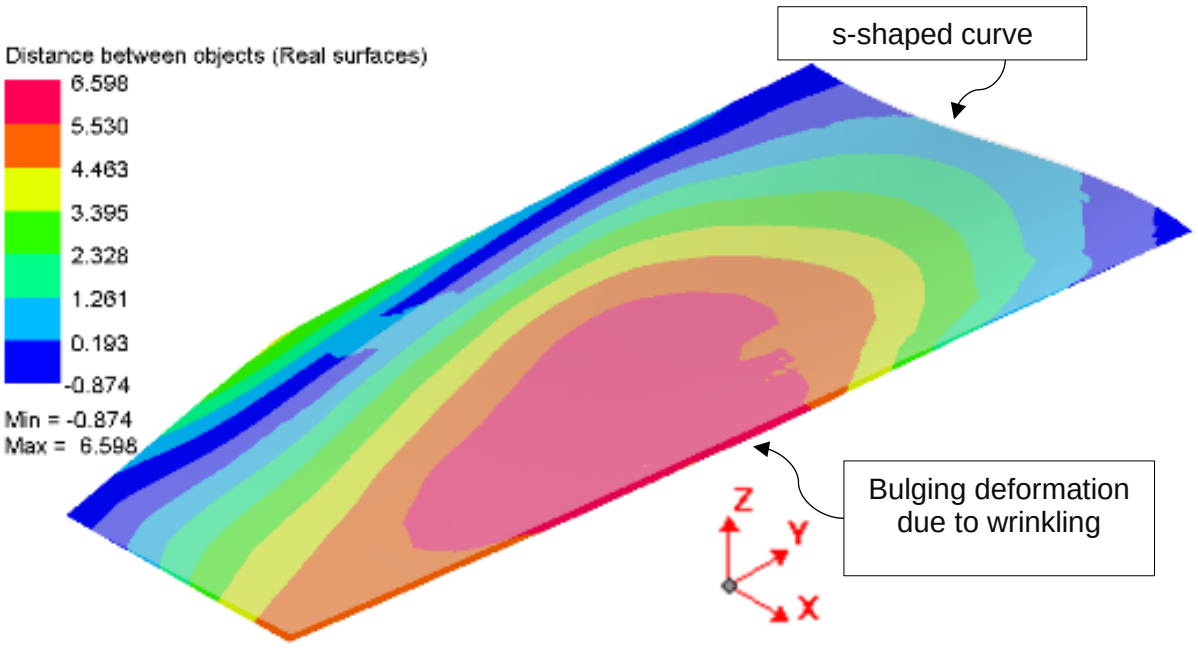

Figure A.54: Concept-6 final simulation form vs component

Appendix A.9 Concept-7

The promising results of Concept-6 were used in the development of Concept-7. The distance from the final part to the inner corner were increased to omit the wrinkle from the component. As there was no cracking seen in the previous concept, the draw depth remained the same. However, due to the s-shape curve, the form was expected to crack in the same place as seen in Concept-5 tool B, blank C and Concept-5 tool C, blank C, as shown in Figure A.40 and Figure A.46, respectively. Figure A.55 depicts the tool and blank for Concept-7.

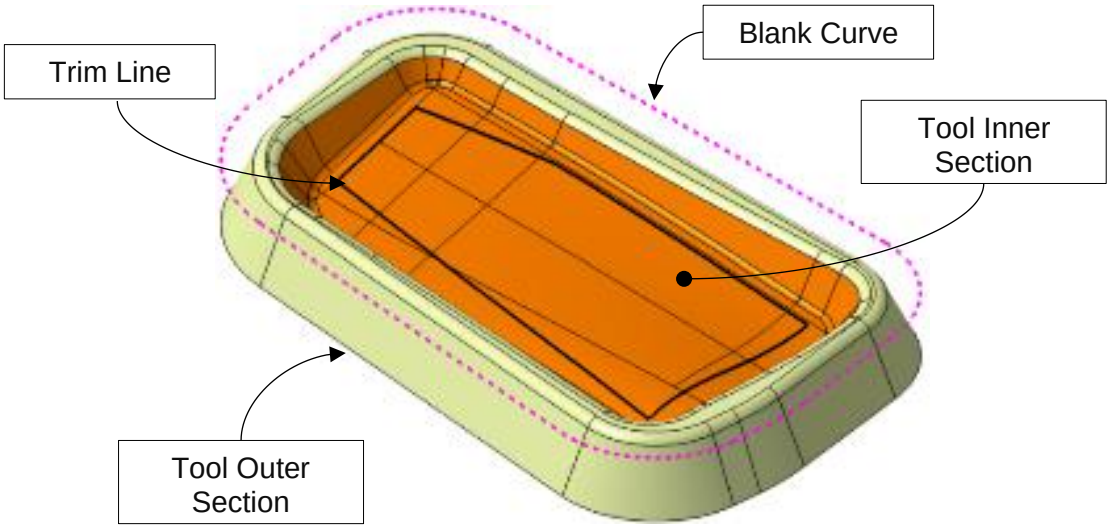

Figure A.55: Concept-7 tool and blank

Figure A.56 depicts the top and side view of Concept-7. The minimum edge radius of the tool was 12 mm. The tool side face draft angle was 25° and the inner portion draft angle was 35° The change in the inner corner radius and the inner portion draft angle allowed for the added distance between the edge of the component and the inner corner. The tool depth was 37 mm. The blank size was much larger than the tool to drape over the sides during the forming process. The inner and outer sections of the tool were now separate surfaces to conduct an optimisation study. The two were split as only the inner section was to be optimised and the outer section of the tool unchanged.

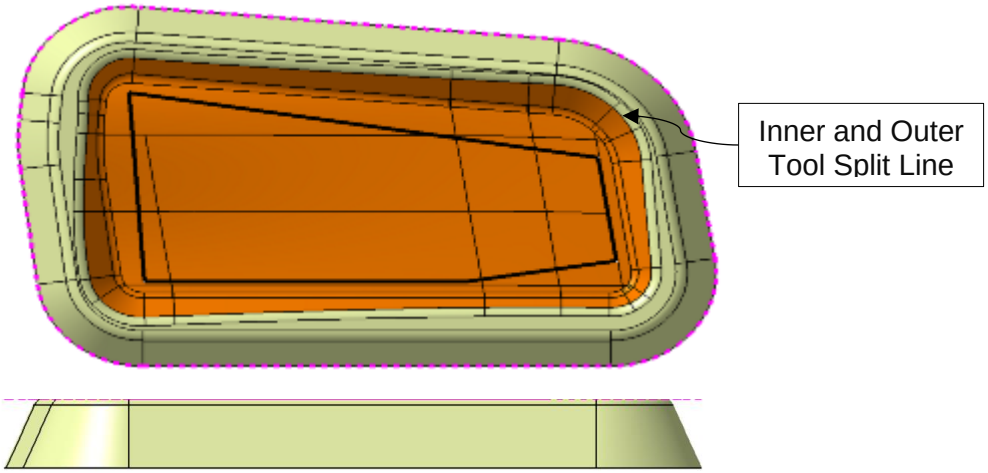

Figure A.56: Concept-7 tool and blank – top and side views

Figure A.57 depicts Concept-7's tool, blank, trim curve and the assembly FEM in PAM-STAMP 2G. The mesh element size for the blank was 13 mm. The sheet metal rolling direction was in the y-axis. As the minimum edge radius for Concept-7 tool was 12 mm, the edge radius to element size was 0.92:1. A blank mesh refinement level of 3 was used, providing an element size of 5.5 mm. Hence, the edge radius to element size was 3.69:1, deemed acceptable for the feasibility assessment to continue.

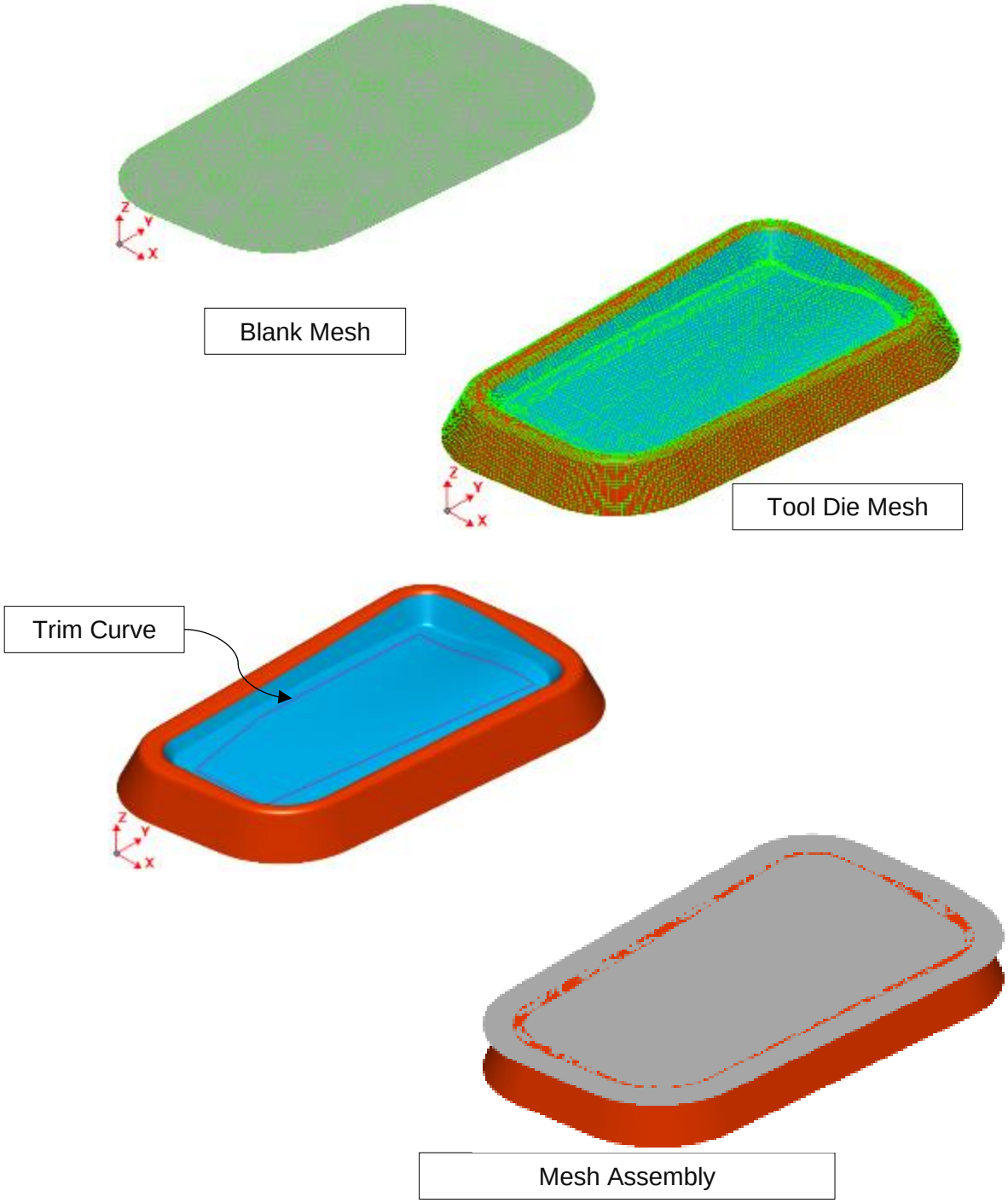

Figure A.57: Concept-7 tool, blank, trim curve and assembly FEM

The simulation set-up was a fluid cell forming stage, followed by a trimming and springback stage. Refer to Section 3.4.3 for a detailed breakdown of the simulation set-up. The total progression time

was 30 seconds with a maximum pressure of 80 MPa. The stopping criteria for the stage was contact area. A state result was provided every 2.5 seconds. In addition to the Vegter isotropic hardening material property, the Vegter kinematic hardening with friction was simulated. Figure A.58 depicts the FLD zone quality overlay of the blank in final form, using the Vegter Isotropic hardening material property card. Wrinkling and cracking occurred in the annotated areas.

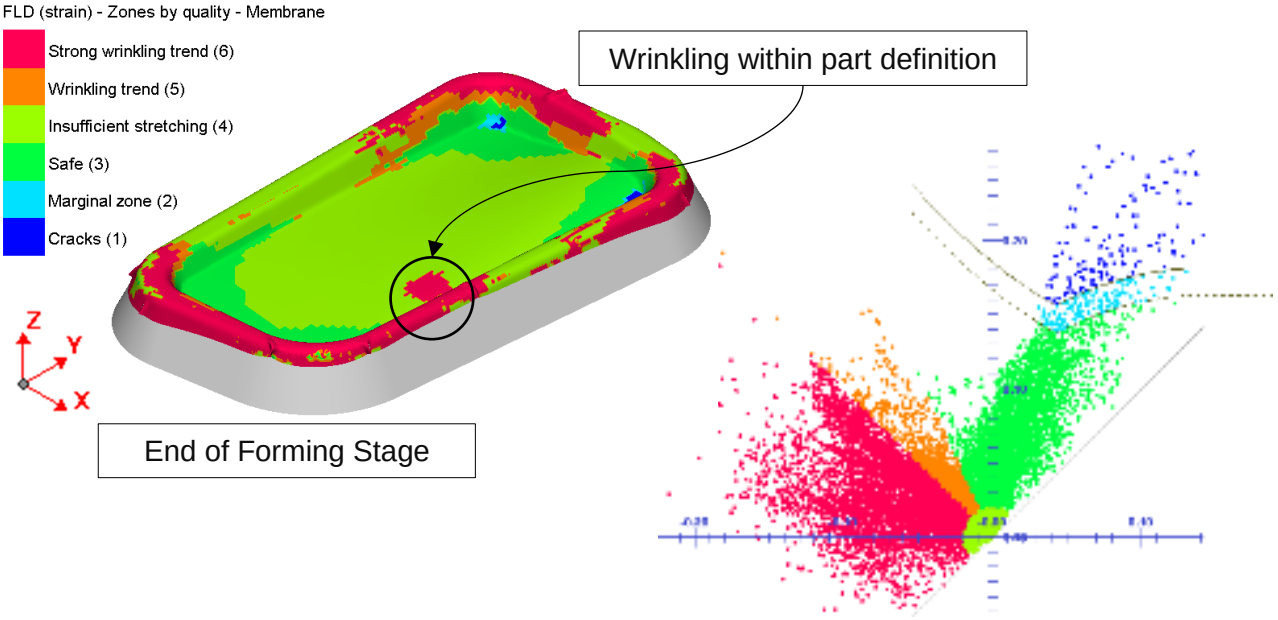

Figure A.58: Concept-7 Vegter-Iso Material FLD zone quality overlay

Figure A.59 depicts the FLD zone quality overlay on the blank in final form, using the Vegter kinematic hardening with friction material property card. Using the Vegter kinematic material card, the wrinkling did not change, but the crack that formed in the corners improved marginally.

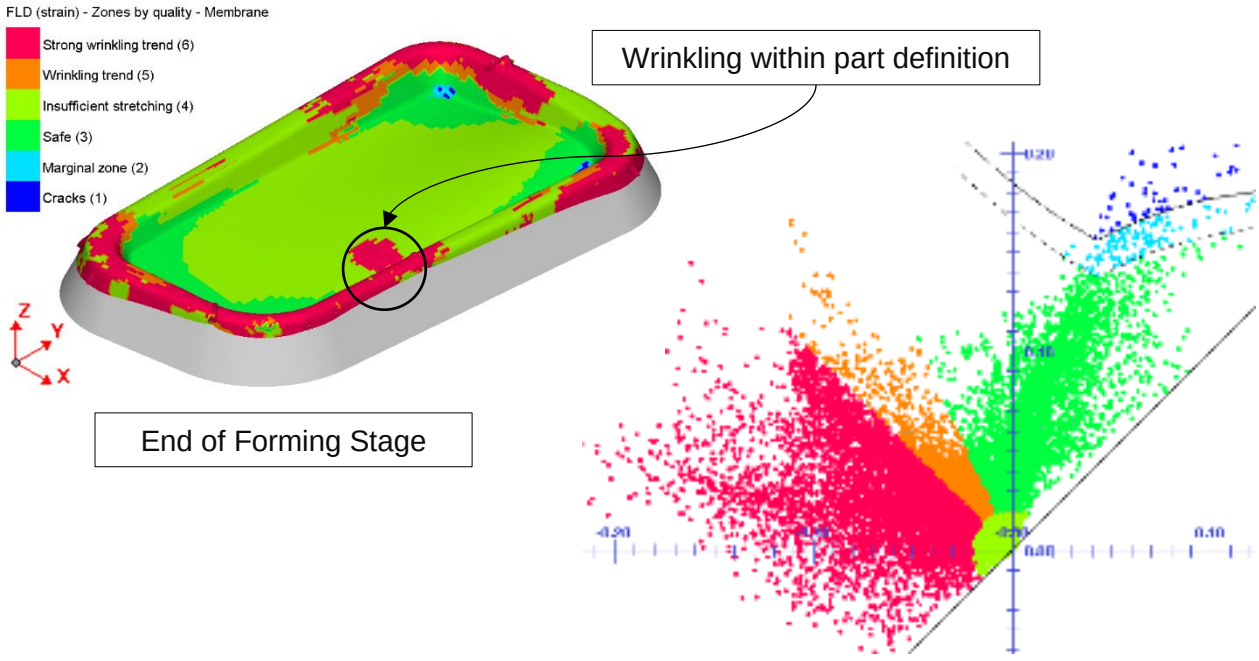

Figure A.59: Concept-7 Vegter-Kin Material FLD zone quality overlay

An optimisation study was conducted to improve the final form of the blank by compensating the tool die. The optimisation study was conducted on all the stages. In some cases, only certain stages was used in the optimisation study. The target was the blank geometry from the initial form. The optimisation compared the two blanks and aligned the two results using best-fit. The inner tool portion was compensated with a compensation factor of 1.0 and a thickness tolerance limit of 30%. The convergence criteria was a maximum displacement tolerance of 1 mm with the proportion of the blank below a limit of 95%. A maximum of 8 iterations was conducted. Modifications to the die were unlimited with the edges of the blank locked for alignment to the tool outer section. The result from the optimisation was exported in STL ASCII mesh facet geometry format.

Figure A.60 depicts a distance comparison plot of the compensated die from iteration 5 and the original tool die. The optimal result compensated the tool by further deepening the draw depth of the tool, but in the inner corners. The distance colour plot showed the draw depth was increased by 14.018 mm. However, the centre of the tool bulged, reducing the draw depth. Section cuts through the tool were provided to show the direction of compensation. The solid blank line was the original tool die and the red dashed line was the compensated tool die. During the forming process, the blank bottomed out on the centre bulge and then drew deeper into the corners of the tool.

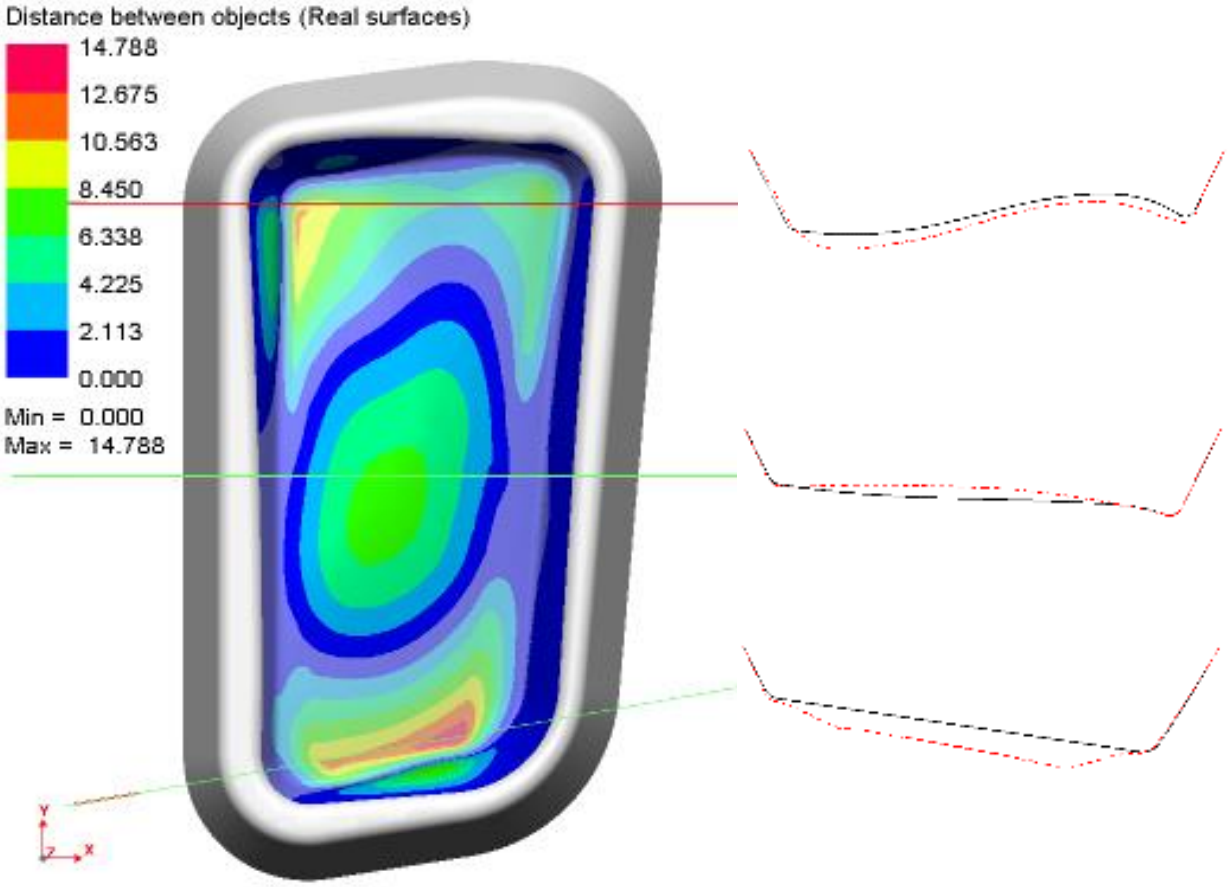

Figure A.60: Concept-7 optimisation iteration 5 distance plot and section cut views

Figure A.61 depicts the FLD zone quality overlay on the blank in final form, based on the optimised tool, using the Vegter kinematic hardening with friction material property card. The optimisation study showed the tool could be improved to reduce the cracking of the component in the corners. However, to omit the wrinkling, the tool and blank design would need to be changed.

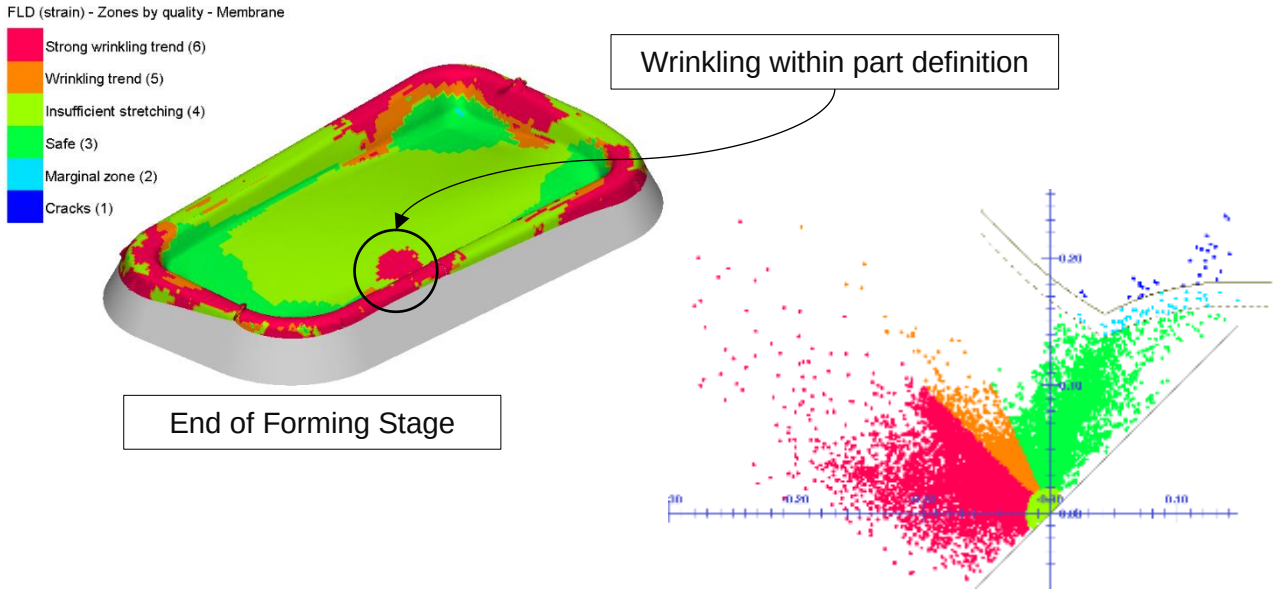

Figure A.61: Concept-7 Vegter-Kin Optimisation Iteration 5 FLD zone quality overlay

A top view of the three simulation results is depicted in Figure A.62. The image showed the FLC zone quality overlay for the Vegter isotropic hardening material property, the Vegter kinematic hardening property and the optimisation study in the final forming stage.

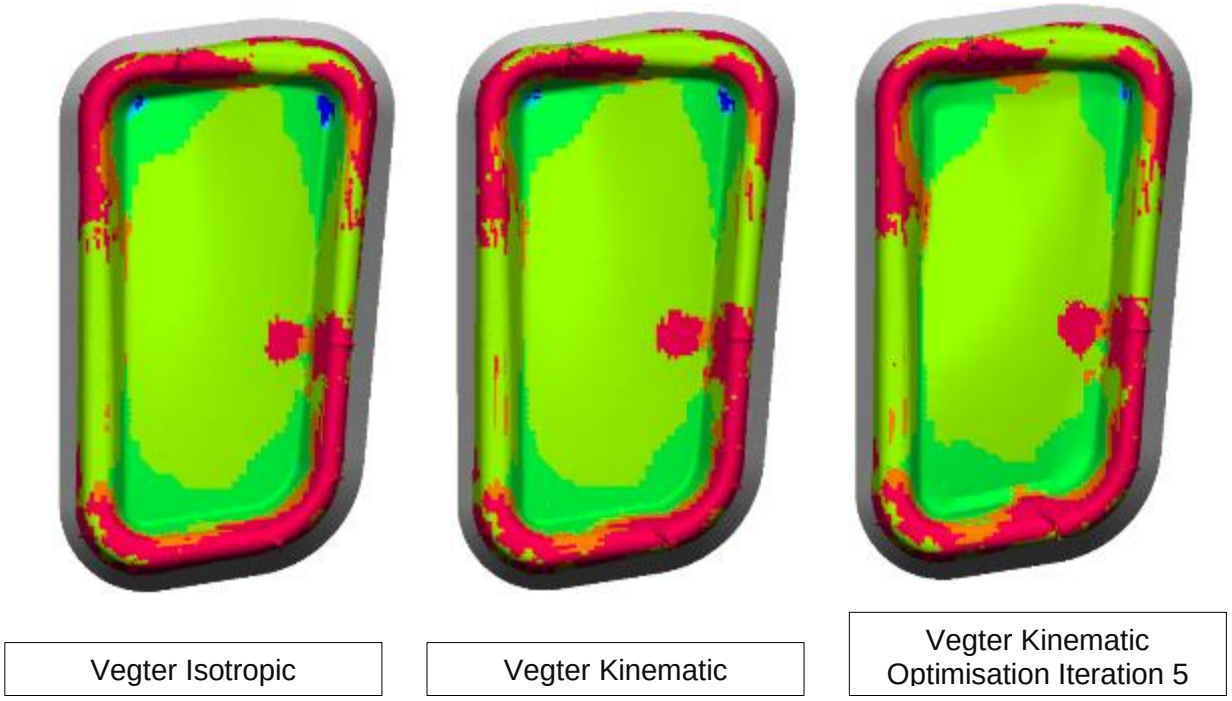

Figure A.62: Concept-7 Vegter-Iso/Kin/Optimisation FLD zone quality overlay comparison

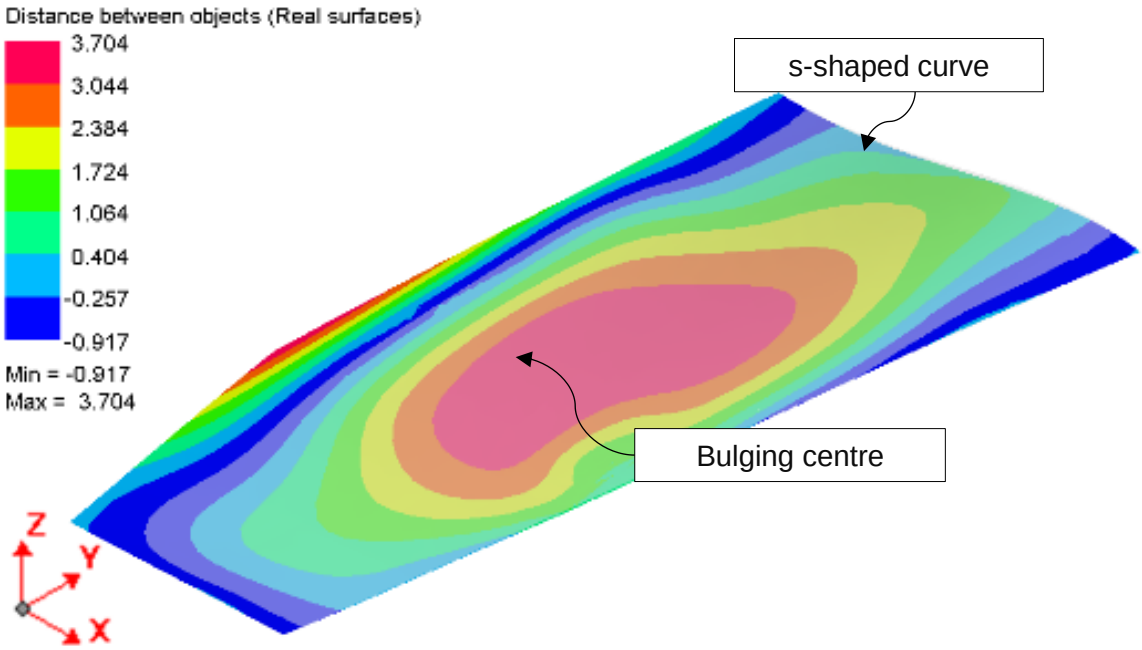

Figure A.63: Concept-7 Vegter-Iso final simulation form vs component

Figure A.63 depicts the final form from the simulation versus the desired form of the component simulated, using the Vegter Isotropic hardening material properties. The simulation showed the final component simulated might have had an expected distortion of 4.621 mm.

Figure A.64 depicts the final form from the simulation versus the desired form of the component simulated, using the Vegter Kinematic hardening with friction material properties. The simulation showed the final component might have had an expected distortion of 7.415 mm.

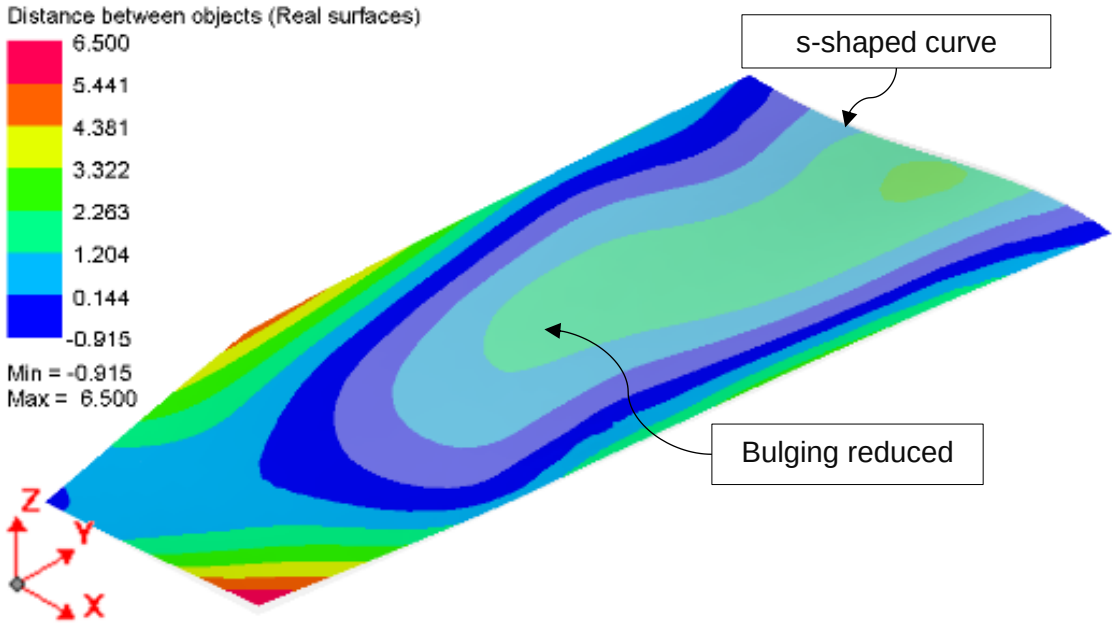

Figure A.64: Concept-7 Vegter-Kinematic final simulation form vs component

Figure A.65 depicts the final form from the optimised study versus the desired form of the component simulated, using the Vegter Kinematic hardening with friction material properties. The simulation showed the final component might have had an expected distortion of 3.671 mm.

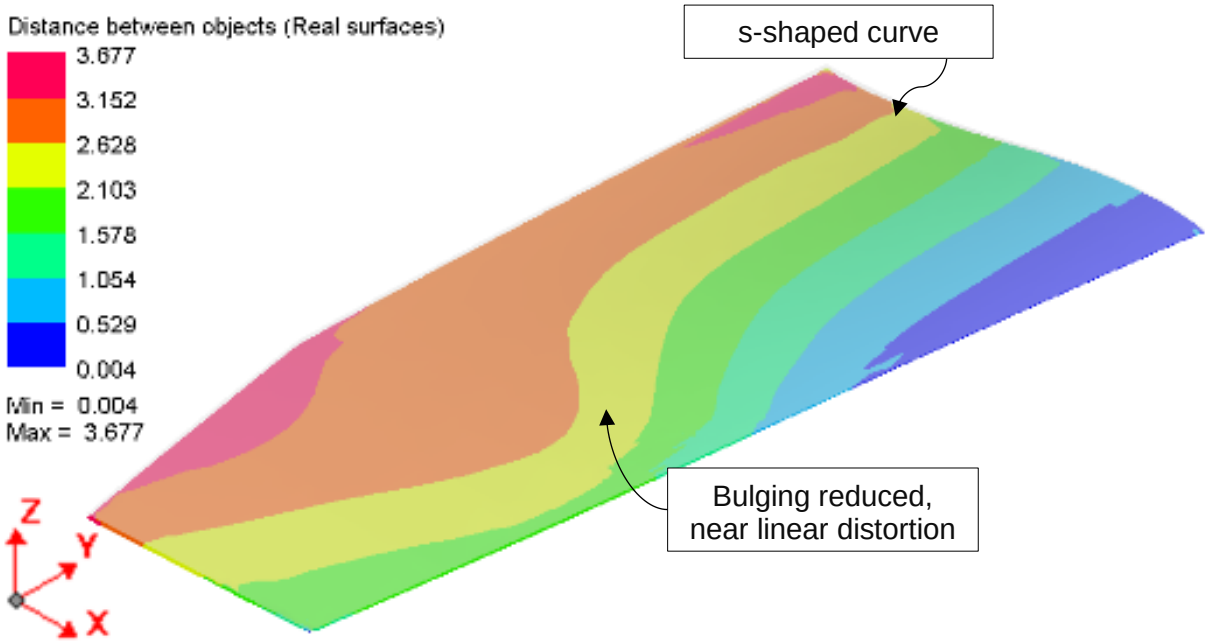

Figure A.65: Optimised Concept-7 Vegter-Kinematic final simulation form vs component

The bulging of the final component, as seen in Figure A.63, was more subtle when simulated, using the kinematic hardening material curve, as seen in Figure A.64. The s-shaped curve in the kinematic hardening-based simulation showed more springback. This was an expected outcome, as the kinematic material curve provided a more accurate result than the isotropic hardening curve.

The optimisation study yielded a compensated tool. The bulging in the centre of the component was reduced with a linear distortion, as seen by the bands in the distance colour plot in Figure A.65. Even with an improvement in the final form of the component, Concept-7 and the optimised tool were rejected. The blank and tool design were not suitable as a manufacturing solution, as ensuring accurate alignment of the blank in reality was not possible. In addition, the compensated tool was output in an STL ASCII geometry format which needed to be parameterised for it to be manufactured.

The conversion of an STL facetted body into a solid part body in a CAD tool such as CATIA was done using non-rational B-spline (NURB) surfaces. However, it is the author's opinion that the machining of NURB based part bodies can yield poor tooling surfaces. Hence, the compensated tool had to be re-designed parametrically for this tool be realised.

Appendix A.10 Concept-8

As the blank bottomed out on the inner tool portion before the blank's overhang sections formed to constrain the edges correctly was the focus of this concept. This was be accomplished by exploring the blank geometry design in Concept-5 blank B. The overhang size of Concept-5 blank B was extended to the distance of the overhang used for the continuous edge blanks. The extended overhang features were termed flanges. Three investigations were conducted:

1. A single-stage tool concept
2. A two-stage tool concept pre-forming the flanges in the first stage
3. Investigate the required blank holder force required to get complete in-plane stretching

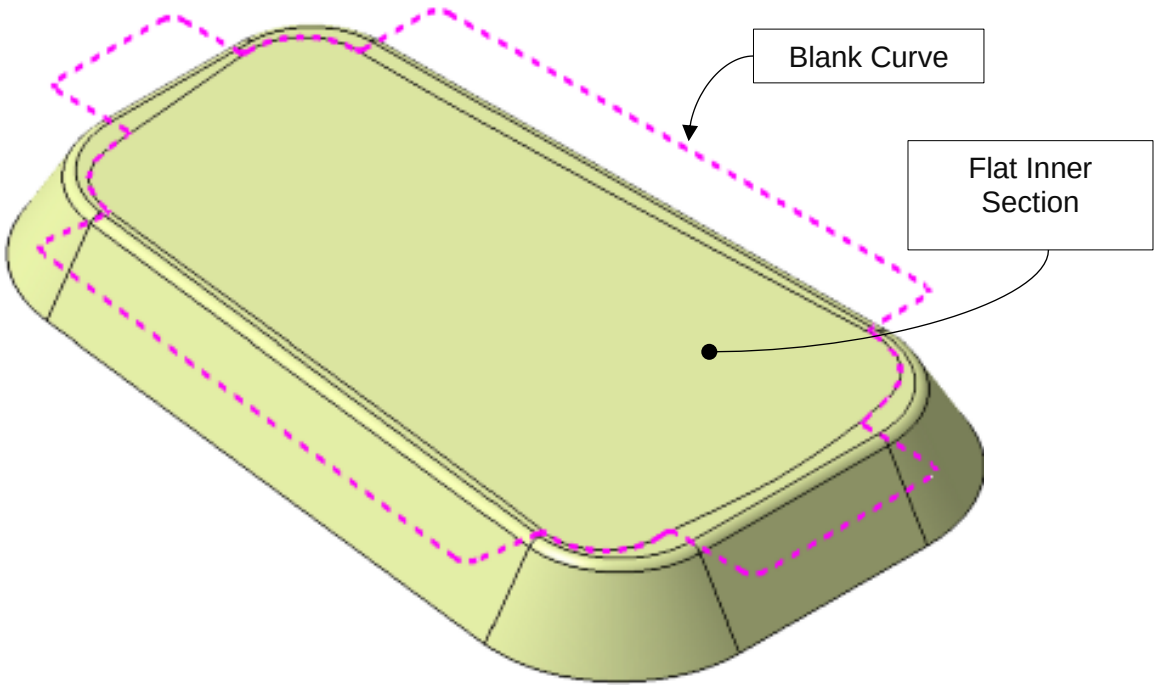

Figure A.66: Concept-8 first stage tool and initial blank

Figure A.66 depicts Concept-8's first stage tooling and the initial blank design. The purpose of the first stage tool was to pre-form the blank before proceeding to the second stage pressing. The flanges were flattened against the sides of the tool with the inner section remaining flat.

The blank was then placed on the second stage tool, where it formed into the final component shape. As the flange edge was pre-formed, constraining frictional force between the blank and the tool was increased with the increase in pressure during the forming process. As the blank was drawn into the tool, it was expected that the in-plane stretching would increase to the desired state to a reduced degree of springback. This process was the defined steps followed in the second investigation.

For the first investigation, the initial flat blank was pressed on the second stage tool. The blanks were not in the pre-formed state and, hence, a view of how the edge blank pre-form from a flat condition and the pre-formed condition could be compared. Figure A.67 depicts the second stage tool and initial flat blank for Concept-8.

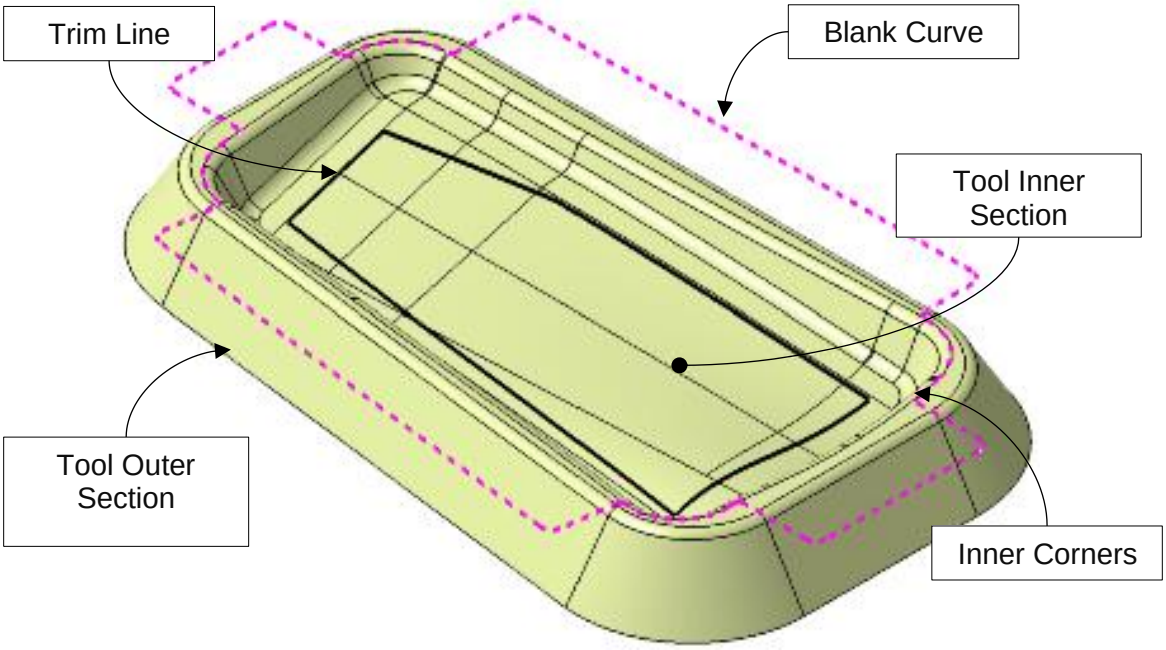

Figure A.67: Concept-8 second stage tool and initial blank

The minimum edge radius of the first and second stage tools was 15 mm. The tool side face draft angle was 32 °, and the inner portion draft angle was 30 °. The larger draft angles allowed for a larger surface area, and accommodated the length of the blank flanges. The tool depth was 34 mm. Figure A.68 depicts the top and side view of Concept-8.

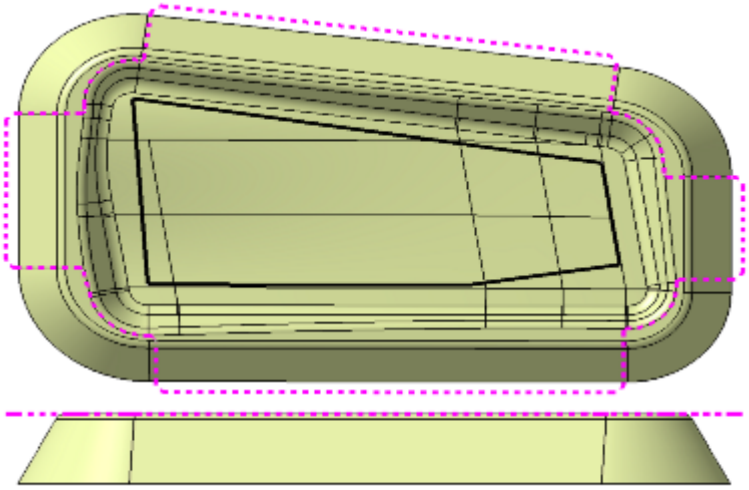

Figure A.68: Concept-8 second stage tool and initial blank - top & side views

Figure A.69 depicts the blankholders used for investigation three. Investigation two provided insight into the degree of in-plane stretching that could be achieved from the concept without initial force holding the pre-formed flanges down against the tool. Investigation three determined the required, blankholder force to constrain the blank flanges for sufficient in-plane stretching to be achieved.

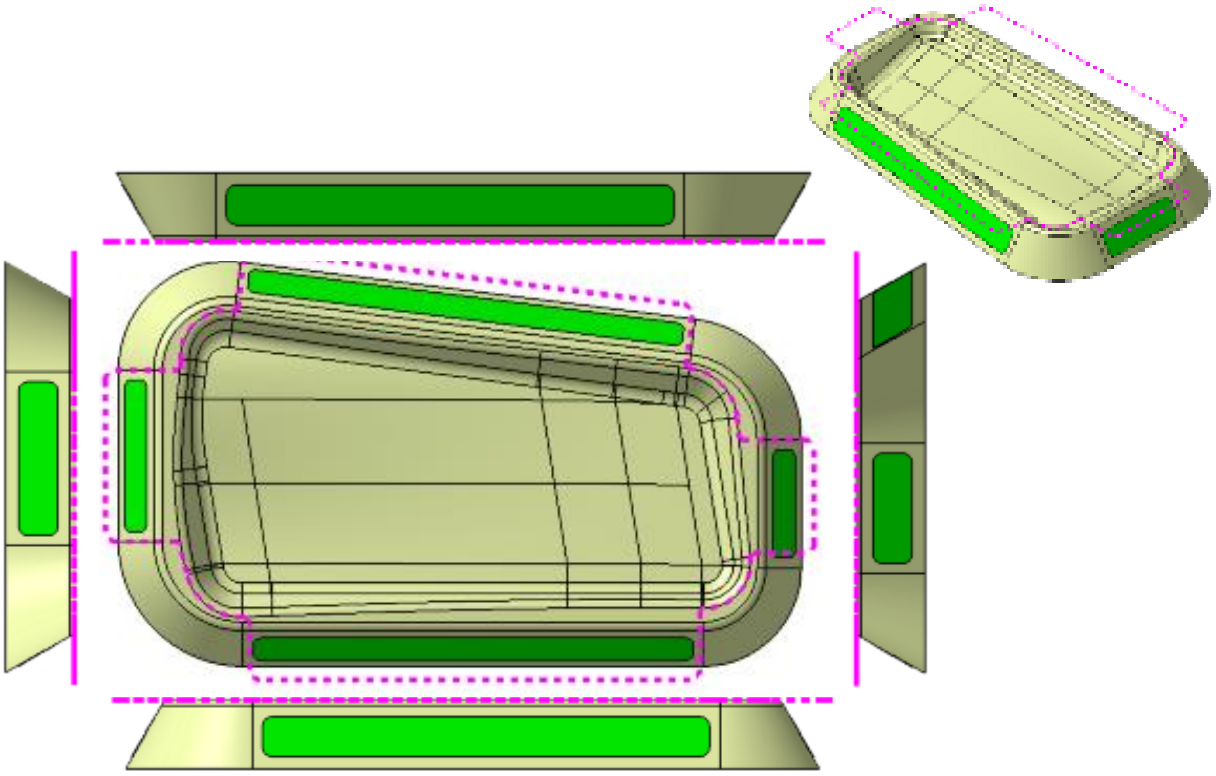

Figure A.69: Concept-8 second stage tool blankholders

Figure A.71 depicts Concept-8's second stage tool and initial blank. The mesh element size for the blank was 15 mm. The sheet metal rolling direction was in the y-axis. As the minimum edge radius for the Concept-8's second stage tool was 15 mm, the edge radius to element size was 1:1. A blank mesh refinement level of 3 was used, providing an element size of 5 mm. Hence, the edge radius to element size was 3:1, deemed acceptable for the feasibility assessment to continue.

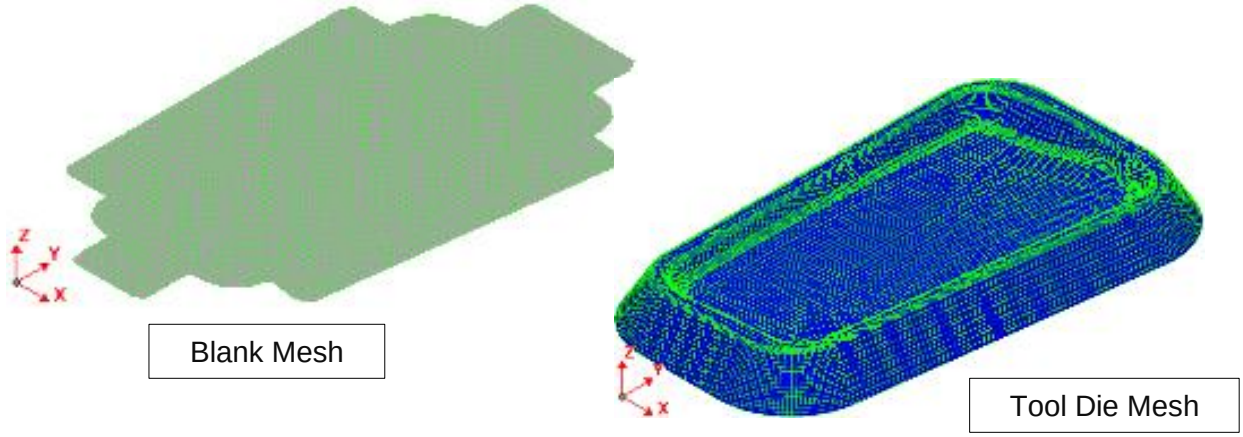

Figure A.70: Concept-8's second stage tool and the initial blank FEM in PAM-STAMP 2G

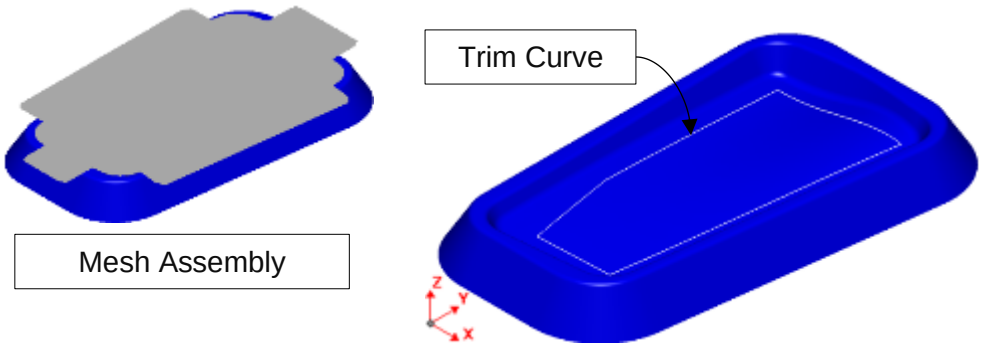

Figure A.71: Concept-8's second stage trim curve and assembly FEM

Figure A.71 depicts Concept-8's trim curve and the assembly FEM in PAM-STAMP 2G. The simulation set-up was a fluid cell forming stage, followed by a trimming and springback stage. Refer to Section 3.4.3 for a detailed breakdown of the simulation set-up. The total progression time was 30 seconds with a maximum pressure of 80 MPa. The stopping criteria for the stage was contact area. A state result was provided every 2.5 seconds. The material card used for this simulation was the Vegter yield locus lite plasticity law and the Yoshida-Uemori kinematic hardening law. Figure A.52 depicts the FLD, a zone quality overlay of the blank in final form, the trimmed form at the trim stage and, the final form, at the springback stage. No wrinkling of the blank occurred in the region seen in the previous concepts. This was attributed to the blank flanges folding over the edge as it was drawn into the tool. What was evident was the lack of in-plane stretching with only a single-stage operation.

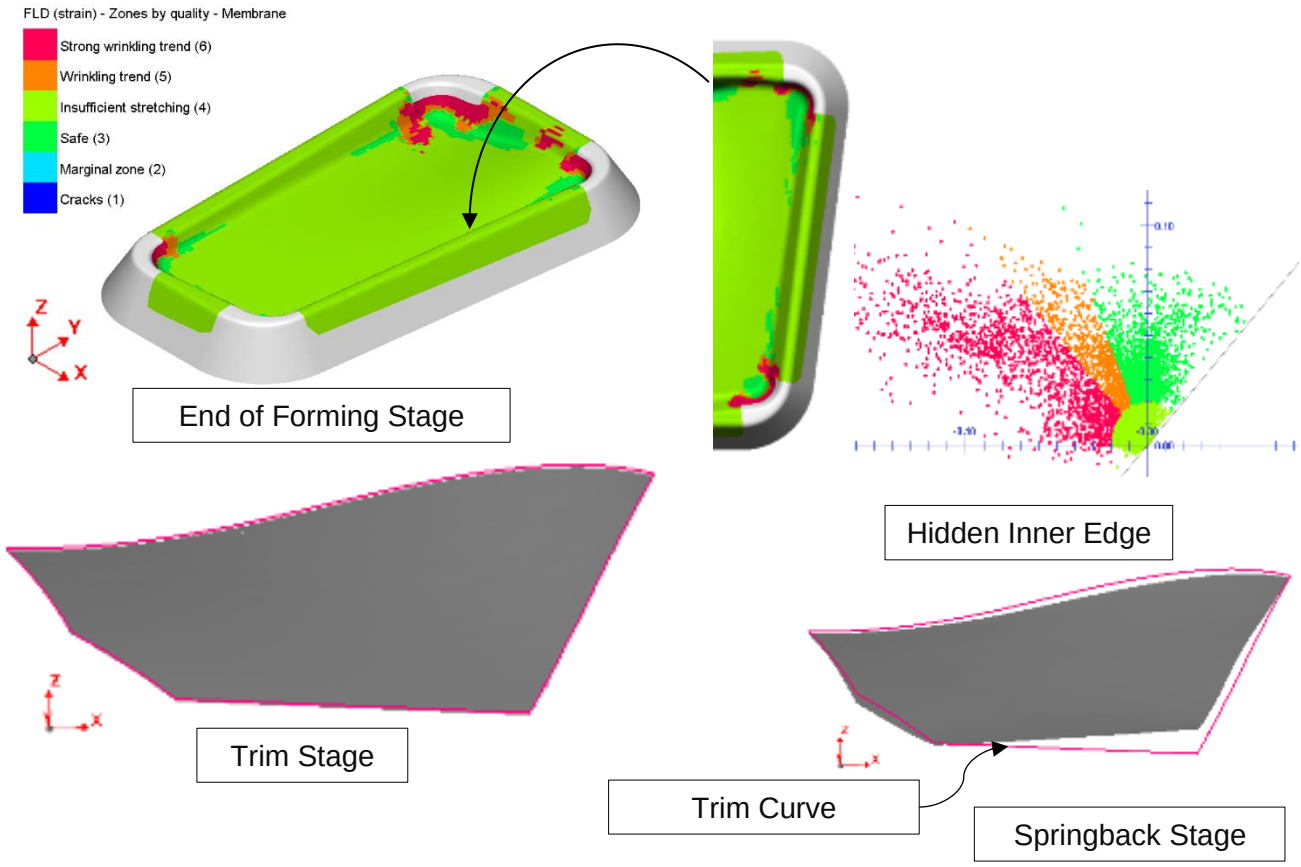

Figure A.72: Concept-8 FLD, zone quality overlay, and springback

Figure A.52 also depicts the final form contouring the trim curve and the component after the springback stage deviating from the trim curve. Figure A.73 depicts the final form from the simulation versus the desired form of the component. The simulation showed the final component might had an expected distortion of 15 mm.

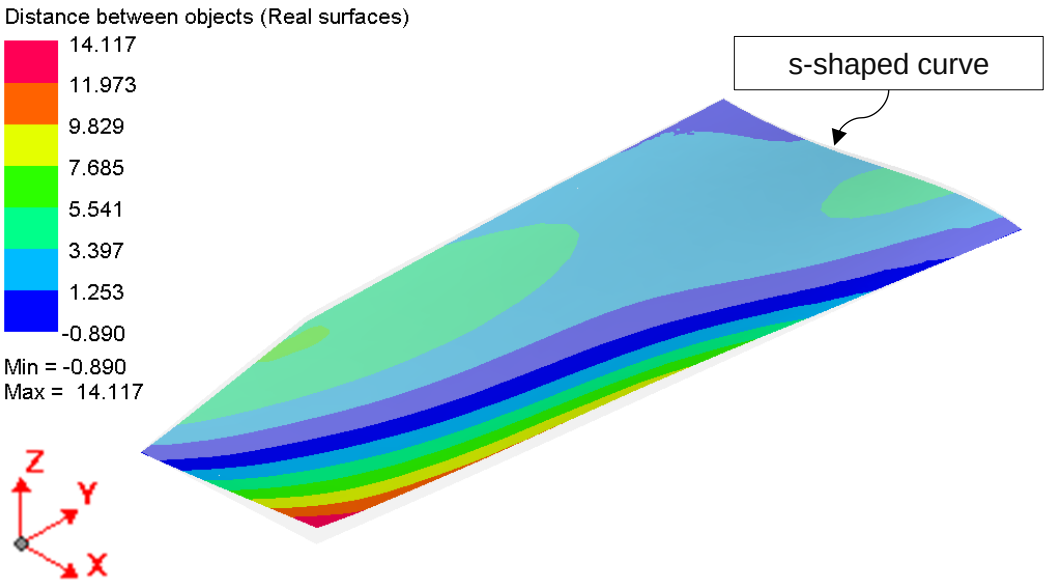

Figure A.73: Concept-8 single-stage forming final simulation form vs component

Figure A.71 depicts Concept-8's first stage tool and assembly FEMs in PAM-STAMP 2G. The mesh element size for the blank was 15 mm. The sheet metal rolling direction was in the y-axis. As the minimum edge radius for the Concept-8's second stage tool was 15 mm, and the edge radius to element size is 1:1. A blank mesh refinement level of 3 was used, providing an element size of 5 mm. Hence, the edge radius to element size was 3:1, deemed acceptable for the feasibility assessment to continue.

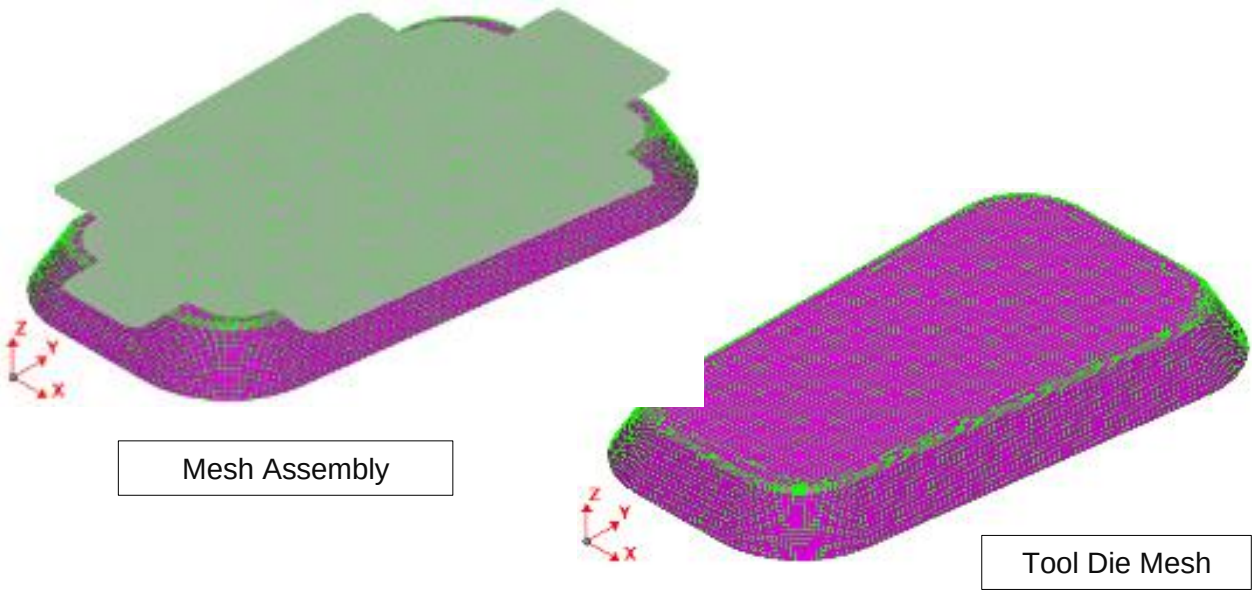

Figure A.74: Concept-8 first stage tool and assembly FEM in PAM-STAMP 2G

The simulation set-up was the first fluid cell forming stage, and then a springback stage of the pre-form. The second fluid cell forming stage was then conducted, followed by a trimming and springback stage. Refer to Section 3.4.3 for a detailed breakdown of the simulation set-up. The total progression time was 30 seconds with a maximum pressure of 80 MPa. The stopping criteria for the stage was contact area. A state result was provided every 2.5 seconds. Figure A.76 depicts the first stage pre-form springback condition and the positioning of the component for the second forming stage.

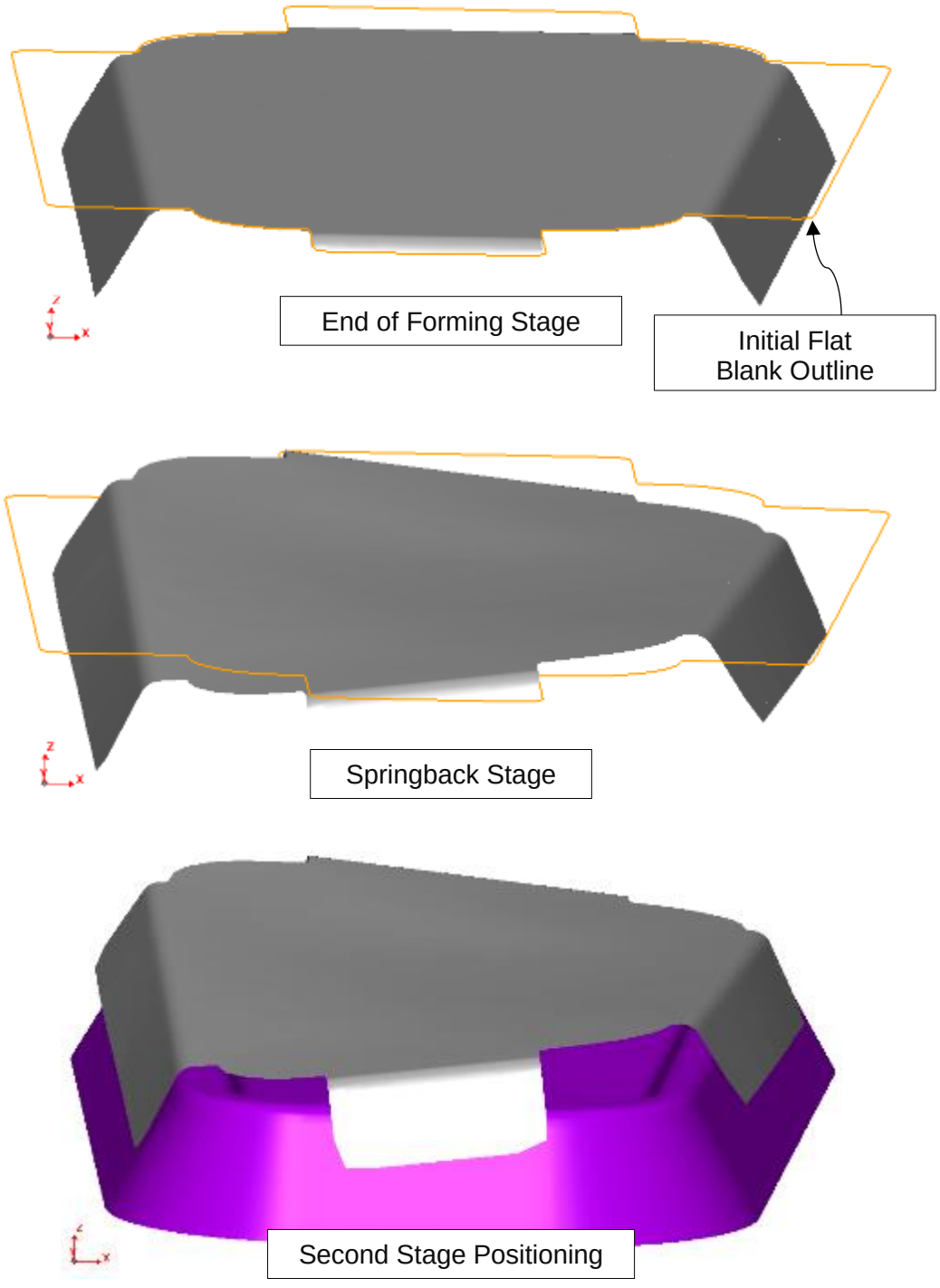

Figure A.75: Concept-8 first stage pre-form springback

Figure A.76 depicts the FLD, a zone quality overlay of the blank in final form, the trimmed form at the trim stage and, the final form, at the springback stage. Again, no wrinkling of the blank occurred in the region, as seen in the previous concepts. The pre-form already contoured the side of the blank. As seen in Figure A.75, the pre-form distorted excessively, but could be placed over the tool successfully. What was evident was the lack of in-plane stretching with only a single-stage operation. The final form contoured the trim curve well, however after springback, the component deviated from the trim curve significantly.

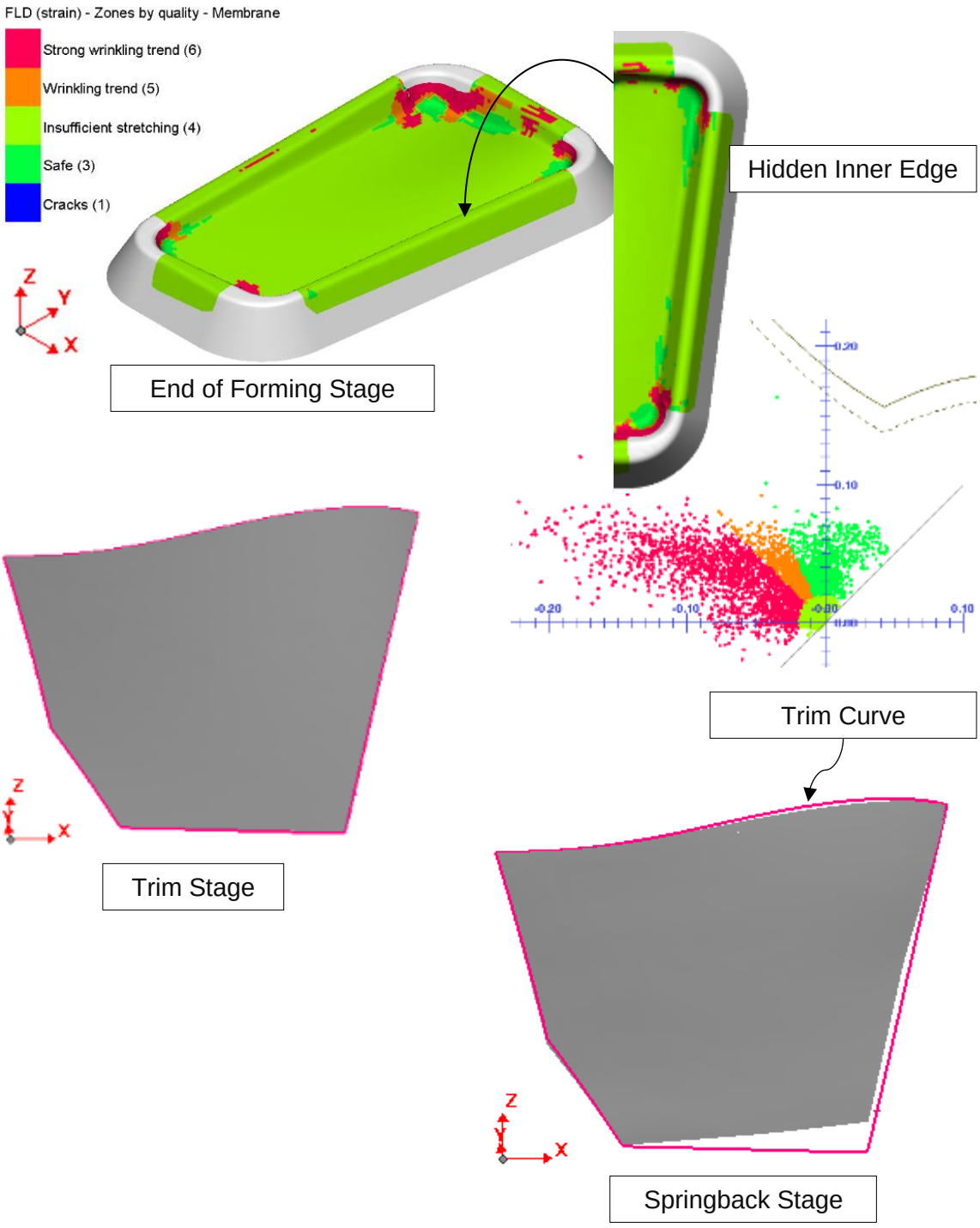

Figure A.76: Concept-8 FLD, zone quality overlay, and springback

Figure A.77 depicts the final form from the simulation versus the desired form of the component. The simulation showed the final component might have had an expected distortion of 12.292 mm. This is an improvement of 2.71 mm, compared to the single-stage forming operation. Little or no change in in-plane stretching was seen between the single-stage investigation and the two-stage forming investigation. This was attributed to the blank flanges not receiving any pressure from the fluid. As the process proceeded, the pressure on the flanges increased to a point where the frictional forces influenced the blank and increased the in-plane stretching. However, by this time, the blank would have bottomed out on the tool inner portion with no change in in-plane stretching. Thus, the third investigation was conducted.

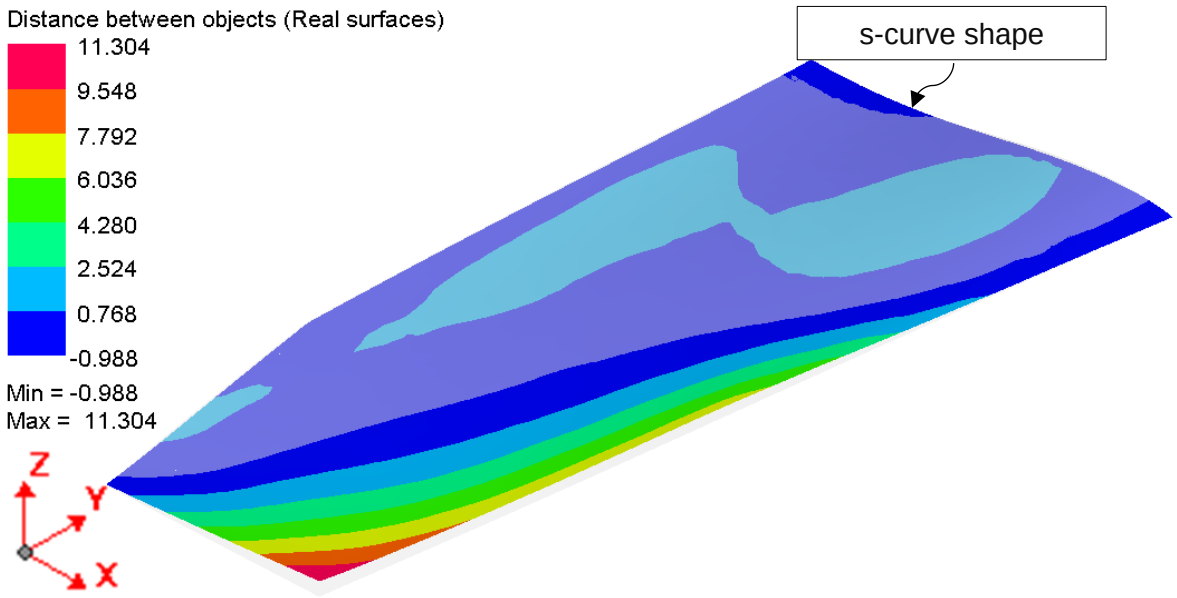

Figure A.77: Concept-8's two-stage forming operation final simulation form vs component

The third investigation utilised blank holders on the side of the tool, as shown in Figure A.69. The first stage was conducted to pre-form the blank into the required shape for the flanges to drape the sides of the tool. In the second stage of the forming process, the blankholders applied loading, starting from 50kN to 1000kN. The in-plane stretching and final distortion of the component relative to the desired form was determined and compared for each blankholder loading condition. Figure A.78 depicts Concept-8's second stage tool and the respective blankholders.

Figure A.78: Concept-8's second stage tool and the initial blank FEM in PAM-STAMP 2G

The simulation set-up was a fluid cell forming stage to pre-form the blank. The springback stage of the pre-formed blank was removed to ensure the alignment of the blank on the second stage tool could be done easily. The next stage was the positioning of the blankholders, followed by the second stage fluid cell forming stage, and, finally, the trimming and springback stage. Refer to Section 3.4.3 for a detailed breakdown of the simulation set-up. The total progression time was 30 seconds with a maximum pressure of 80 MPa. The stopping criteria for the stage was contact area. A state result was provided every 2.5 seconds.

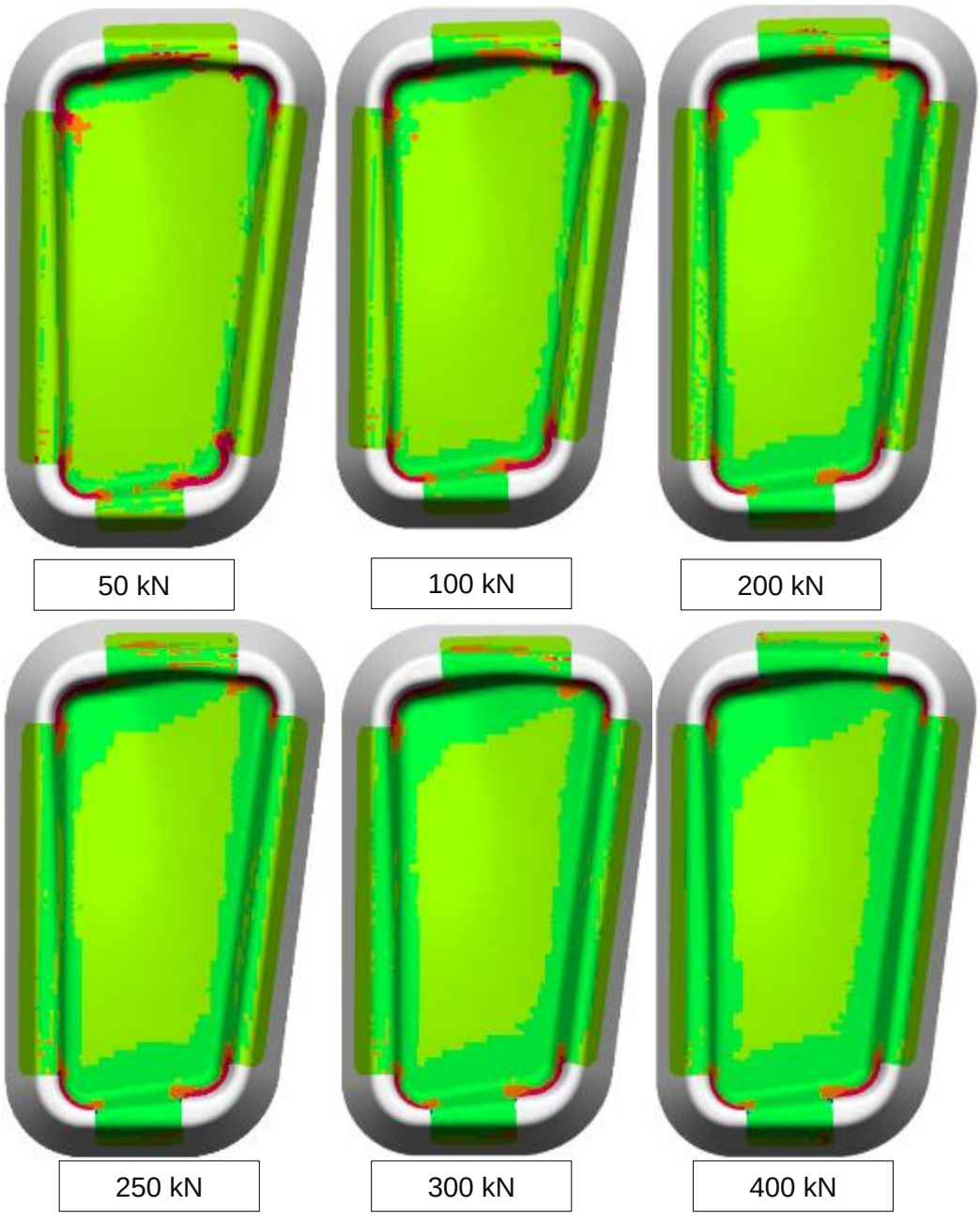

Figure A.79: Concept-8 FLD results for the 50kN to 400kN blankholder force

Figure A.79 and Figure A.80 depict the FLD results for the 50kN to 1000kN blankholder force. The force was applied normal to the side face of the tool clamping the flange of the blank. The purpose of a blankholder is to hold the blank in certain places, and generate a restraining force during the forming process. Drawbeads were features used to further increase the frictional forces between the blank, tool and the blankholder.

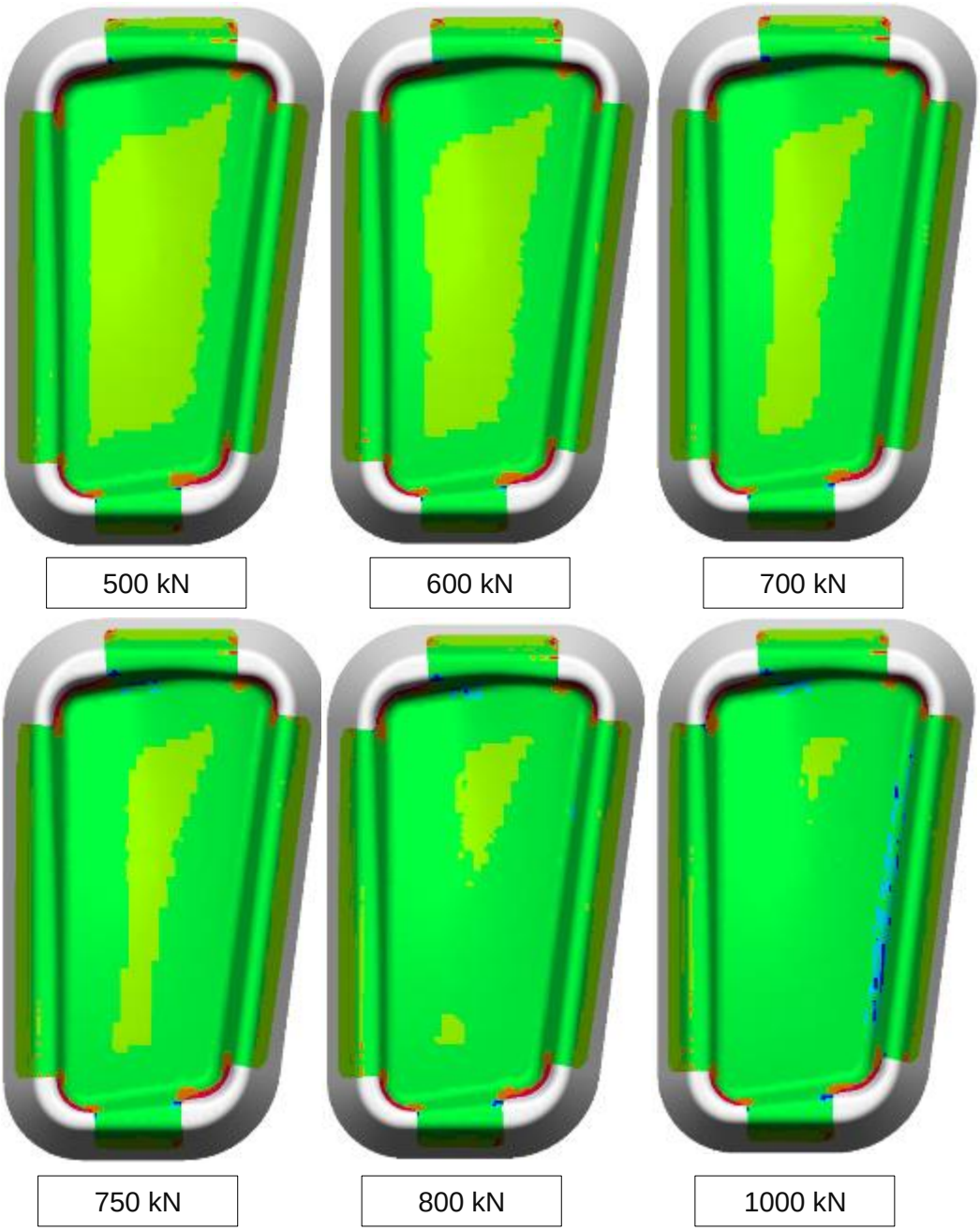

Figure A.80: Concept-8 FLD results for the 500kN to 1000kN blankholder force

The purpose of the blankholder study was to determine the amount of force required to restrain the blank flanges to increase the in-plane stretching of the component during the forming process. Figure A.79 and Figure A.80 show the increasing in-plane stress in the blank with an increase in blankholder force. The final simulation form distortion compared to the desired component form is shown in Figure A.81. With an increase in in-plane stress, the distortion of the component was reduced with the least distortion seen, using a blankholder force of 700kN. The overall distortion of the component was expected to be 1.585 mm. Figure A.82 depicts the final form from the simulation versus the desired form of the component.

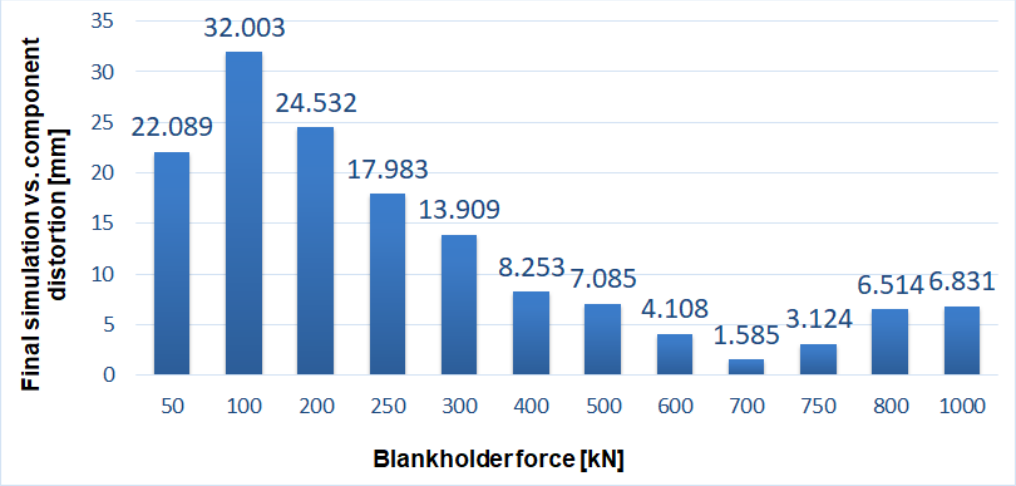

Figure A.81: Concept-8 blankholder force vs final simulation form distortion

The blankholder study provided an important aspect to the study which was the requirement to have enough in-plane stretching to minimise the springback of the component. Increasing the blankholder force improved the final results, but to a point after which negligible gains were to be seen. In this case, 700kN was the optimal blankholder force. Increasing the force above 700kN demonstrated worse springback of the component and cracking at 1000kN. Holding the blank flanges in this way was not feasible for fluid cell forming. A blankholder was needed to be fastened to the side of the tool, using at minimum 16 M16 bolts, tightened to 135Nm.

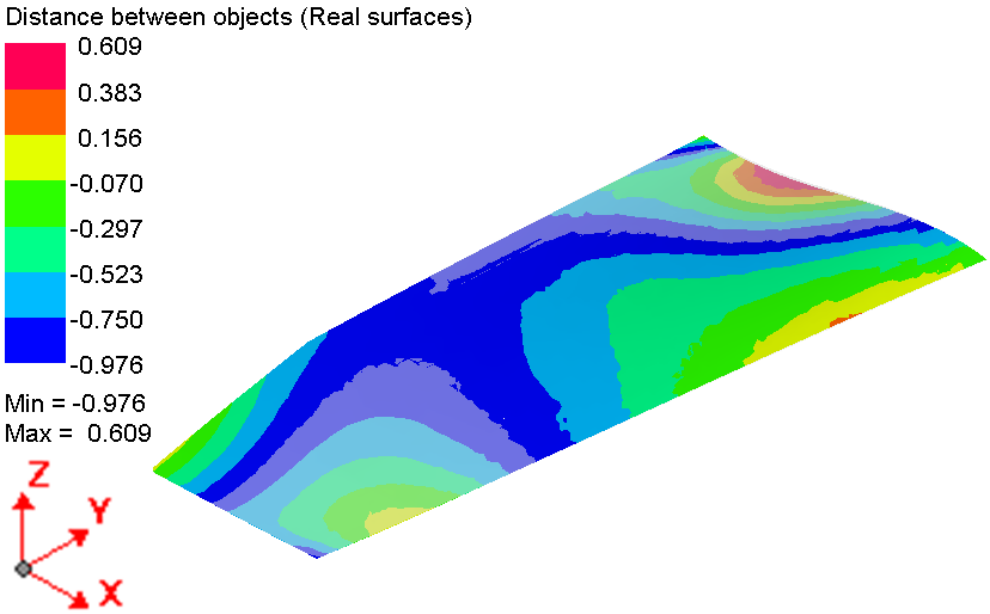

Figure A.82: Concept-8 700kN blankholder force final simulation form vs component